PROBABILISTIC CALIBRATION OF A SOIL MODEL

by

Zenon Medina-Cetina

A dissertation submitted to Johns Hopkins University in conformity with the requirements for the degree of Doctor of Philosophy.

Baltimore, Maryland
October of 2006

Abstract

A constitutive model is a relationship between material stimuli and responses. Calibration of model parameters within well-defined constitutive models is thus key to the generation of accurate model-based predictions. One limitation of traditional material calibration is that only a few standardized tests are performed for estimating constitutive parameters, which makes the calibration process eminently deterministic. Moreover, measurements taken during standardized tests are usually global readings, which implicitly assume a 'homogeneous' material composition, smearing out the influence of any local effects. This work introduces the Functional Bayesian (FB) formulation as a probabilistic methodology for the calibration of constitutive models that incorporates material random responses and local effects into the assessment of constitutive parameters. This particular calibration process is known as the probabilistic solution to the inverse problem. Estimates of the statistics required for the Bayesian solution are obtained from a series of standard triaxial tests which are coupled with 3-Dimensional (3D) stereo digital images allowing for the capturing of material local effects. In addition, the probabilistic method includes the spatial representation of elemental 'material' properties by introducing spatially varying parameters within a 3D Finite Element Model (3D-FEM) to reproduce to the extent possible the actual heterogeneous response of the material. The sampling of spatial 'material' realizations is performed by the Polynomial Chaos (PC) method, which permits the simulation of multi-dimensional non-Gaussian and non-stationary random fields. Integration of the random parameters is performed via Markov Chain Monte-Carlo and Metropolis-Hastings algorithms. The calibration of a soil

sample is presented as a case study to illustrate the applicability of the method when the soil response lies within the linear elastic domain. Calibration results show a probabilistic description of the spatially distributed parameters and of the coefficients of the chaos representation that defines it. Inferences retrieved from the MCMC sampling include the analysis of the 'material' properties and of the coefficients of the PC representation which enhances understanding of the randomness associated with the material composition and response.

Advisors:

Prof. Amy Rechenmacher

Prof. Roger Ghanem

Readers:

Prof. Lori Graham-Brady

Acknowledgements

Finally, I want to dedicate this work to my wife Maria Jose, who has shared with me this five-year journey, cheering and encouraging me with love and care so that I could complete this life-long milestone. Gracias Hon.

To Josefina

I dedicate this work to you.

Take it as your first lesson in life:

Rely in the providence of God our Lord to achieve your goals,

and always be thankful to the many people that will care freely for you.

Table of Contents

List of Tables

List of Figures

xiii

xv

1. Introduction

1.1. Problem Statement

A constitutive model is a mathematical formulation that defines a particular relationship between material stimuli and responses. The appeal of a constitutive model lies in its capacity to reproduce all possible combinations of the material stress-strain paths, to minimize the effort invested in parameter calibration, and to provide a clear physical understanding of parameter variation. In addition, when the model is embedded into analytical or numerical mechanistic predictive models such as Finite Elements, it is possible to extrapolate elemental material predictions to significantly more complex structures. Compared to the equilibrium and compatibility conditions, constitutive models are not as simple to define. Calibration of model parameters within a well-defined constitutive model is therefore a key process for the generation of accurate model-based predictions.

Traditional calibration is carried out by performing a limited number of standardized tests from which the constitutive parameters are estimated. This process is known as the solution to the inverse problem. The inverse problem is solved when parameter estimates generate predictions that are in good agreement with experimental observations. This means that the constitutive model is calibrated and that parameters estimates can be used to obtain predictions that go beyond the experimental conditions from which they were obtained. On the other hand, the forward problem is solved when the calibration consists

only in tuning constitutive parameters until model predictions are consistent with actual observations.

In this context, the calibration process is eminently deterministic in the sense that no statistical information is incorporated into the assessment of parameters. Moreover, in standardized tests, measurements such as axial stresses, axial strains, and global volumetric changes, represent global readings only. When these readings are used for the calibration of the constitutive parameters, a 'homogeneous' composition of the material is assumed smearing out the influence of any intrinsic local effects.

The present work introduces a different approach. Normally the experiment required for parameter calibration is repeated several times under identical conditions in order to determine to the extent possible the nature of the material response. However, if the material response is random, experimental uncertainty can be associated with the experiment observations. This uncertainty is usually associated with different sources including the inherent variation in the material, the variation due to the measuring devices, the variation induced by the operator, or a combination of these. Hence, in the presence of random observations it is expected that random constitutive parameters will be retrieved. This means that the solution to the inverse problem requires a probabilistic formulation.

One of the first probabilistic adaptations for the solution of inverse problems was the Bayesian paradigm (Dale, 1999). In this setting, the Bayesian paradigm defines the joint probability density function (pdf) of the material parameters using a-priori knowledge of

the constitutive parameters or prior, and the measure of the predictive model performance or likelihood; yielding the formulation of a joint pdf known as the posterior. The posterior can be interpreted as the probability of occurrence of the constitutive parameters once an update on observations has been introduced.

The Bayesian approach was not fully exploited until recently due to the unavailability of computational resources for its implementation when modeling multivariate phenomena. This limitation has been recently overcome with surging of more efficient numerical formulations. The most significant property of the Bayesian paradigm is that it introduces a complete solution for ill-posed problems by integrating the conjunction of a-priori information associated with experimental, theoretical and even subjective sources. This permits the probabilistic formulation of constitutive parameters. It is worth noting that the Bayesian approach can be applied only when the calibration of constitutive models makes use of reliable observations and a robust predictive model capable of generating accurate predictions. The conditions of existence, stability and non-uniqueness are also accounted for in the Bayesian solution. This yields a set of suitable parameters with particular marginal pdfs and correlation structure.

A unique feature of the probabilistic calibration approach is the final description of the model parameters. This is given by their corresponding pdfs and correlation structure as opposed to the results obtained with classical statistical methods such as least squares and maximum likelihood estimation, where parameters are interpreted as expected or mean values with uncertainty measures given by their variances. Hence, by following the Bayesian approach, the constitutive parameters are not considered deterministic entities.

3

Instead, they are random variables, which can also be referenced in space and time (random processes) carrying the uncertainties from the a-priori state of information throughout their final probabilistic descriptions.

Because of the difficulty in formulating multivariate posteriors, and considering the simplifications of the formulation of the Bayesian estimators with specific properties such as unbiasedness and minimum variance, Fitzpatrick (1991) proved the following. He showed that the Thikonov's regularization method (widely used for strongly ill-posed problems) and the Bayesian paradigm, converged when the Bayesian maximum a-posteriori is estimated under the assumption that errors between observations and the predictions show Gaussian properties and if they are independent of each other. This convergence is demonstrated by following a Bayesian weighted least squares form or what is known as the maximized posterior. The implementation is straightforward and allows for a smooth incorporation of multiple parameters that can be easily referenced in space and time if necessary.

In the case of multivariate processes, the representation of the parameters defining inherent Gaussian random fields may assume the form of finite series such as the Karhunen-Loeve's (K-L) expansions (Van Trees, 2001). The K-L expansions enable the simplification of the numerical implementation by using the process eigen-quantities. Taking advantage of these properties, McLaughlin and Townley (1996) re-parameterized the posterior by defining the parameters Gaussian field in terms of K-L expansions, and then maximizing it with respect to the series coefficients. This enabled the estimation of

a smooth parameter field and its marginal Gaussian pdfs by a functional form of the posterior.

The Functional Bayesian (FB) method introduces a generalized approach for the solution of inverse problems that allows for the representation of spatio-temporal non-Gaussian and non-stationary constitutive parameters, by using the Polynomial Chaos (PC) method (Sakamoto and Ghanem, 2002a and 200b) within a Bayesian framework. Multi-dimensional Hermite polynomials representing the fields of the constitutive parameters are embedded into the prior and likelihood definitions, such that the posterior integrates the series coefficients. This creates a sub-hierarchy of estimators (chaos coefficients) lying below the space of the constitutive model or 'physical' parameters. Consequently, more inferences about the calibration can be generated, enhancing the understanding not only of the constitutive parameters themselves but the estimators that control them.

The integration of the posterior is required to define the marginal pdfs of each of the constitutive parameters and to assess its correlation structure. For this purpose, it is necessary to define the a-priori marginal pdfs and the correlation structure of the constitutive parameters, so that the prior can be formulated. It is also necessary to define the covariance matrices of the observations and the predictions, so that the likelihood can be formulated. As mentioned above, these components of information rely on inferences from observations obtained from the same experiment that is repeated several times, and on the predictions of the same model based on multiple simulations. Once the prior and likelihood are properly defined, the posterior is integrated via Markov-Chain Monte

Carlo (MCMC) and Metropolis-Hastings (M-H) algorithms (Robert and Casella, 2004). Both of these are widely used because of their computational sampling efficiency. They have both been shown to be particularly useful for the integration of non-analytical and high dimensional posteriors.

In order to illustrate the applicability of the method, a case study is presented describing the probabilistic calibration of an elastic model used for simulating the behavior of a triaxial soil specimen. Estimates of the statistics of the observations required for the Bayesian formulation are obtained from a control-based experimental database. This database consists of a series of triaxial tests on sand specimens that populate both global and local spatio-temporal data. Estimates of the global material properties are obtained by measurements taken from standard triaxial device; local spatio-temporal data are captured over the samples surfaces by measurements taken from a 3D-Digital Image Correlation (3D-DIC) technique.

Estimates of the statistics corresponding to predictions are based on simulations of the soil response given by a 3D Finite Element Model (3D-FEM) that aims to reproduce the testing conditions to the extent possible. It does so by incorporating spatially varying constitutive parameters assigned to prescribed 'material' regions, and based on the actual test initial and boundary conditions. The displacement domain is chosen as the space where the calibration is performed (where observations and predictions are compared). This is delimited by the area where 3D-DIC captures the local deformations.

The case study first focuses on the linear elastic response of one particular test taken from the experimental database. The linear elastic constitutive model is chosen to reproduce the actual soil behavior. Additionally, constitutive parameters are spatially distributed following a prescribed spatial 'material' arrangement within the 3D-FEM. The Young's modulus is the only random parameter considered for the calibration, while the Poisson's ratio and density are assumed to be constant for all 'materials'. The initial guess of the prior is defined by assuming a random field of the Young's moduli within the specimen based on a-priori information, and it is assumed to be stationary (although this may change during the MCMC sampling). Since the correlation structure of the 'materials' is unknown, the correlation parameter is assumed to be random as well.

The FB method is a continuation of previous efforts that have explored the use of PC representations in the identification of non-random chaos coefficients associated with model parameters using the maximum likelihood approach (Desceliers et al., 2006), and for exploring the influence of the amount of information in the convergence of the parameter estimates using the updating feature of Bayes' theorem (Ghanem and Doostan, 2006). The emphasis of this work is therefore not on the evaluation of chaos parameters. Rather, it is on the methodological implementation of a generalized representation of random material fields defined by the PC, which are controlled by random chaos coefficients that permit the solution of the inverse problem.

1.2. Thesis Outline

Chapter 2 introduces the theoretical framework for the solution of inverse problems and presents the development of the Functional Bayesian (FB) method for the probabilistic calibration of constitutive models. Chapter 3 introduces the theoretical framework of the PC method for the simulation of multi-dimensional non-stationary and non-Gaussian process. It also presents three benchmark cases that explain in detail how to implement the PC method, including the sampling case used in the integration of the FB posterior. Chapter 4 introduces the experimental methods and results that conforms the database used to validate the FB Method. Chapter 5 introduces the numerical models developed for the model calibration making emphasis on the parameters considered for enhancing the model performance. It also presents a case that serves as a proof of concept for the implementation of the selected numerical model considered for the probabilistic calibration. Chapter 6 introduces the elements for the Bayesian formulation and the statistical estimates needed to integrate the case study presented in chapter 7. Chapter 7 introduces the case study that validates the applicability of the method for the probabilistic calibration of one test with spatially varying linear elastic constitutive parameters. And finally, chapter 8 introduces the conclusions of this work.

2. Inverse Problem Solutions

The practical purpose of solving an inverse problem as defined by the calibration of a constitutive model is to estimate the constitutive parameters $\boldsymbol{\theta}$ given some a-priori information. Common sources of a-priori information are experimental and theoretical, and even subjective. Regardless, a calibration method capable of transforming the actual state of information into the estimates of the constitutive parameters is required. This section introduces a scheme for the rational identification and quantification of the uncertainty present in the information sources, and the calibration methods that incorporate this uncertainty in the identification of solutions for inverse problems.

2.1. Uncertainty Quantification

In order to improve the definition of constitutive parameters, the probabilistic calibration approach includes a systematic identification and quantification of the uncertainty contained in a-priori information sources. This requires to identify and characterize the uncertainty associated with the displacement observations $\mathbf{d}_{obs}$ and the displacement predictions $\mathbf{d}_{pred}$, obtained from experimentation and numerical simulations respectively. Furthermore, $\mathbf{d}_{obs}$ and $\mathbf{d}_{pred}$ represent the two main sources of a-priori information. Hence, the quantification of their uncertainty becomes a key element in the calibration since it is expected to propagate throughout the solution of the inverse problem. Both $\mathbf{d}_{obs}$ and $\mathbf{d}_{pred}$ are random vectors and consequently the difference that each of them have with respect to the expected or actual displacements $\mathbf{d}$. This

9

means that the specimen displacements $\mathbf{d}$ can be defined with respect to the observations as:

$$\mathbf{d} = \mathbf{d}_{obs} + \Delta\mathbf{d}_{obs} \qquad\qquad (2.1)$$

where,

$\mathbf{d}_{obs}$ is a vector containing random experimental displacement fields measured during a test. Its randomness may be due to sample disturbance, sample manipulation, sample preservation, inaccuracy or imprecision of testing equipment, operator's inexperience, analyst's limited judgment, inherent variation of soil , or due to a combination of these

$\Delta\mathbf{d}_{obs}$ is the vector of random differences between $\mathbf{d}$ and $\mathbf{d}_{obs}$

Similarly, the specimen displacements $\mathbf{d}$ can also be defined with respect to the predictions as:

$$\mathbf{d} = \mathbf{d}_{pred} + \Delta\mathbf{d}_{pred} \qquad\qquad (2.2)$$

where,

$\mathbf{d}_{pred} = g(\boldsymbol{\theta})$ is a vector of random displacement predictions evaluated at the same spatio-temporal points as $\mathbf{d}_{obs}$ through a mechanistic predictive model g (analytical or numerical), which describes the physical behavior of the data given a set of random parameters $\boldsymbol{\theta}$. The evaluation of vector $\mathbf{d}_{pred}$ represents one realization of the forward problem. Its randomness may be due to model limitations such as under or over-

parameterization, numerical error of solver, parameter resolution (mesh size inadequacy), or due a combination of these

$\Delta \mathbf{d}_{pred}$ is the vector of random differences between $\mathbf{d}$ and $\mathbf{d}_{pred}$

Similarly, the expected vector of model parameters $\boldsymbol{\theta}$ is defined as follows:

$$\boldsymbol{\theta} = \hat{\boldsymbol{\theta}} + \Delta\hat{\boldsymbol{\theta}} \qquad (2.3)$$

where,

$\hat{\boldsymbol{\theta}}$ is a vector of random model parameters obtained either from global indirect measurements, from a deterministic inversion process (optimal solution), or from a non-informative function, all of these representing the inherent variability of the material

$\Delta\hat{\boldsymbol{\theta}}$ is the vector of random differences between $\boldsymbol{\theta}$ and $\hat{\boldsymbol{\theta}}$

When $\boldsymbol{\theta}$ is defined as a random field $\boldsymbol{\theta}(\mathbf{X})$, $\mathbf{X}$ represents a point coordinate in the spatial or spatio-temporal domain. In this case, equation 2.3 is rewritten as:

$$\boldsymbol{\theta}(\mathbf{X}) = \hat{\boldsymbol{\theta}}(\mathbf{X}) + \Delta\hat{\boldsymbol{\theta}}(\mathbf{X}) \qquad (2.4)$$

where $\hat{\boldsymbol{\theta}}(\mathbf{X})$ can be interpreted as the large-scale fluctuation component, and $\Delta\hat{\boldsymbol{\theta}}(\mathbf{X})$ can be interpreted as the small-scale fluctuation component of $\boldsymbol{\theta}(\mathbf{X})$.

From equations 2.1 and 2.2 it is possible to relate the two sources of uncertainty as:

$$\mathbf{d}_{obs} + \Delta\mathbf{d}_{obs} = \mathbf{d}_{pred} + \Delta\mathbf{d}_{pred} \qquad (2.5)$$

yielding four different uncertainty combinations. These possible states of information are presented in Table 1, where $\Delta\mathbf{d}_{obs} = 0$ implies a perfect measuring process free of uncertainty, and where $\Delta\mathbf{d}_{pred} = 0$ implies free modeling uncertainty.

Table 1. Schemes of uncertainty propagation

Case	Measurement Error	Modeling Error	Resulting Relationship
A	$\Delta\mathbf{d}_{obs} = 0$ $\mathbf{d}_{obs} = \mathbf{d}$	$\Delta\mathbf{d}_{pred} = 0$ $\mathbf{d}_{pred} = \mathbf{d}$	$\mathbf{d}_{obs} = \mathbf{d}_{pred}$
B	$\Delta\mathbf{d}_{obs} \neq 0$ $\Delta\mathbf{d}_{obs} = \mathbf{d} - \mathbf{d}_{obs}$	$\Delta\mathbf{d}_{pred} = 0$ $\mathbf{d}_{pred} = \mathbf{d}$	$\mathbf{d}_{obs} + \Delta\mathbf{d}_{obs} = \mathbf{d}_{pred}$
C	$\Delta\mathbf{d}_{obs} = 0$ $\mathbf{d}_{obs} = \mathbf{d}$	$\Delta\mathbf{d}_{pred} \neq 0$ $\Delta\mathbf{d}_{pred} = \mathbf{d} - \mathbf{d}_{pred}$	$\mathbf{d}_{obs} = \mathbf{d}_{pred} + \Delta\mathbf{d}_{pred}$
D	$\Delta\mathbf{d}_{obs} \neq 0$ $\Delta\mathbf{d}_{obs} = \mathbf{d} - \mathbf{d}_{obs}$	$\Delta\mathbf{d}_{pred} \neq 0$ $\Delta\mathbf{d}_{pred} = \mathbf{d} - \mathbf{d}_{pred}$	$\mathbf{d}_{obs} + \Delta\mathbf{d}_{obs} = \mathbf{d}_{pred} + \Delta\mathbf{d}_{pred}$ $\{\Delta\mathbf{d}_{obs} - \Delta\mathbf{d}_{pred}\} = [\mathbf{d}_{pred} - \mathbf{d}_{obs}]$ $\Delta\mathbf{d} = [\mathbf{d}_{pred} - \mathbf{d}_{obs}]$

Cases A and C represent ideal conditions where the measurements are free of uncertainties $\Delta\mathbf{d}_{obs} = 0$ (an assumption that is unrealistic in the case of geomaterials). A perfect modeling or $\Delta\mathbf{d}_{pred} = 0$ as represented by Case B can be more acceptable if it is assumed that the constitutive parameters are deterministic and if the uncertainty attributable to numerical calculations or to parameter resolution is minimal. Case D synthesizes both sources of uncertainty in only one term, where $\Delta\mathbf{d}$ can be interpreted as the component that encapsulates all possible states of uncertainty ranging from cases A through D. This state of information can be defined as:

$$\mathbf{d}_{obs} = \mathbf{d}_{pred} + \Delta\mathbf{d} \qquad (2.6)$$

Considering this particular state of information, the inverse problem solution is given by the estimate:

$$\hat{\boldsymbol{\theta}} = h(\mathbf{d}_{obs}) = h(\mathbf{d}_{pred} + \Delta\mathbf{d})$$
(2.7)

which is obtained by identifying an inverse operator h that maps the vector of observations $\mathbf{d}_{obs}$ into the vector of parameter estimates $\hat{\boldsymbol{\theta}}$.

2.2. Inverse Problem Solutions

Dale (1999) defined three different types of solutions for an inverse problem:

a) The exact solution, also known as the direct solution, aims to find the operator h that maps $\mathbf{d}_{obs}$ into $\hat{\boldsymbol{\theta}}$. Typical applications of this type of solution occur in the case of physical problems where the parameters are measured directly or have a linear dependence with the state variables. Another typical application is in the solution of systems of differential equations where the initial and boundary conditions are sufficient to reach a closed solution. Inverse problems that cannot be solved by the exact solution require a numerical approximation.

b) The optimal solution seeks an estimate $\hat{\boldsymbol{\theta}}$ by minimizing an objective function $h(\mathbf{d}_{pred}, \mathbf{d}_{obs})$. Some probabilistic assumptions may be used to define the form of the objective function, but the parameter estimates are considered deterministic. Typical methods identified with this type of solution are the least squares and maximum likelihood estimation approaches.

13

c) The complete solution presents the inversion results in the form of probability density functions. Typical applications of this type of solution include the Bayesian paradigm. Under specific circumstances, the optimal and complete solutions converge to each other.

2.2.1. Optimal Solutions

2.2.1.1. Least Squares Estimation (LSE)

A loss or objective function is defined by $L(d_{pred}, d_{obs}) = L(|\mathbf{d}_{pred} - \mathbf{d}_{obs}|)$, where $\mathbf{d}_{pred} = g(\hat{\boldsymbol{\theta}})$ is the theoretical solution for a fixed set of parameters $\hat{\boldsymbol{\theta}}$ given by a mechanistic predictive model g. A simple method to solve the inverse problem is Least Squares Estimation (LSE), which consists in minimizing the loss function defined by the weighted Euclidean distance function between the displacement observations and predictions:

$$
\begin{aligned}
h(L) &= \sqrt{\sum_{k=1}^{K} W_k \left[\frac{\left\{ (L)^T (L) \right\}_k}{\Gamma_k} \right]} \\
&= \sqrt{\sum_{k=1}^{K} W_k \left[\frac{\left\{ (\mathbf{d}_{pred} - \mathbf{d}_{obs})^T (\mathbf{d}_{pred} - \mathbf{d}_{obs}) \right\}_k}{\Gamma_k} \right]} \\
&= \sqrt{\sum_{k=1}^{K} W_k \left[\frac{\left\{ (g(\hat{\boldsymbol{\theta}}) - \mathbf{d}_{obs})^T (g(\hat{\boldsymbol{\theta}}) - \mathbf{d}_{obs}) \right\}_k}{\Gamma_k} \right]}
\end{aligned}
\tag{2.8}
$$

where,

Γ_k is a scale factor associated with displacement observations and predictions at the time or deformation stage k

W_k is a weight factor associated with the observed and predicted displacements at the time or deformation stage k

It is worth noticing that LSE considers no probability density function for the $\hat{\boldsymbol{\theta}}$ sampling, which makes this approach deterministic.

2.2.1.2. Maximum Likelihood Estimation (MLE) with Random Observations

The uncertainty introduced into the calibration by the difference between predictions and observations $\Delta\mathbf{d}$, is only due to the observations if the predictions from model g are assumed to be deterministic $\Delta\mathbf{d}_{pred} = 0$ and the observations are considered to be random $\Delta\mathbf{d}_{obs} \neq 0$ (Table 1 case B). In addition, if $\Delta\mathbf{d}_{obs}$ are spatially and temporally independent of each other, and if these are normally distributed with zero mean and covariance $\mathbf{C}_{\mathbf{d}_{obs}}$, then the best estimates of $\hat{\boldsymbol{\theta}}$ are those that maximize the occurrence of the observations relative to the predictions (Fadale et al., 1995). In that case, the best estimate is the one that maximizes the joint pdf of the observations given a set of parameter estimates $\hat{\boldsymbol{\theta}}$. This transformation is defined by the function $l(\boldsymbol{\theta};\mathbf{d}) = f(\mathbf{d}_{obs} | \boldsymbol{\theta})$ known as the likelihood function, which defines a joint pdf of a set of observations $\mathbf{d} = d_1, \quad d_2, \quad d_3, \quad \ldots, \quad d_{n,} \quad$ given $\quad$ a $\quad$ set $\quad$ of $\quad$ parameters $\quad \boldsymbol{\theta}$, $l(\boldsymbol{\theta};d_1,d_2,d_3,...,d_n) = f(d_1,d_2,d_3,...,d_n | \boldsymbol{\theta}) = f(\mathbf{d} | \boldsymbol{\theta})$, with the form:

$$f\left(\mathbf{d}_{obs} \mid \hat{\boldsymbol{\theta}}\right) =$$

$$\frac{1}{\sqrt{(2\pi)^{mk} \prod_{k=1}^{K} \left|\mathbf{C}_{\mathbf{d}_{obs}}\right|_k}} \exp\left[\sum_{k=1}^{K} -\frac{1}{2}\left(\mathbf{d}_{pred} - \mathbf{d}_{obs}\right)_k^T \left(\mathbf{C}_{\mathbf{d}_{obs}}\right)_k^{-1}\left(\mathbf{d}_{pred} - \mathbf{d}_{obs}\right)_k\right] = \qquad (2.9)$$

$$\frac{1}{\sqrt{(2\pi)^{mk} \prod_{k=1}^{K} \left|\mathbf{C}_{\mathbf{d}_{obs}}\right|_k}} \exp\left[\sum_{k=1}^{K} -\frac{1}{2}\left(g(\hat{\boldsymbol{\theta}}) - \mathbf{d}_{obs}\right)_k^T \left(\mathbf{C}_{\mathbf{d}_{obs}}\right)_k^{-1}\left(g(\hat{\boldsymbol{\theta}}) - \mathbf{d}_{obs}\right)_k\right]$$

where the covariance matrix of the observations at time k is defined as:

$$\left(\mathbf{C}_{\mathbf{d}_{obs}}\right)_k = E\left[\left(\Delta\mathbf{d}_{obs}\right)_k \left(\Delta\mathbf{d}_{obs}\right)_k^T\right] \qquad (2.10)$$

where $\left(\Delta\mathbf{d}_{obs}\right)_k = \left(\mathbf{d}_{obs}\right)_k - E\left[\left(\mathbf{d}_{obs}\right)_k\right]$.

Then, using a support function of the form,

$$h^*(\hat{\boldsymbol{\theta}}) = -2\ln f\left(\mathbf{d}_{obs} \mid \hat{\boldsymbol{\theta}}\right) =$$

$$mk\ln(2\pi) + \sum_{k=1}^{K}\ln\left[\left|\mathbf{C}_{\mathbf{d}_{obs}}\right|\right] + \left(\mathbf{d}_{pred} - \mathbf{d}_{obs}\right)_k^T \left(\mathbf{C}_{\mathbf{d}_{obs}}\right)_k^{-1}\left(\mathbf{d}_{pred} - \mathbf{d}_{obs}\right)_k = \qquad (2.11)$$

$$mk\ln(2\pi) + \sum_{k=1}^{K}\ln\left[\left|\mathbf{C}_{\mathbf{d}_{obs}}\right|\right] + \sum_{k=1}^{K}\left(g(\hat{\boldsymbol{\theta}}) - \mathbf{d}_{obs}\right)_k^T \left(\mathbf{C}_{\mathbf{d}_{obs}}\right)_k^{-1}\left(g(\hat{\boldsymbol{\theta}}) - \mathbf{d}_{obs}\right)_k$$

and minimizing it with respect to $\hat{\boldsymbol{\theta}}$, yields the same results as minimizing the objective function:

$$h_{\mathbf{d}}(\hat{\boldsymbol{\theta}}) = \sum_{k=1}^{K}\left(g(\hat{\boldsymbol{\theta}}) - \left(\mathbf{d}_{obs}\right)_k\right)^T \left(\mathbf{C}_{\mathbf{d}_{obs}}\right)_k^{-1}\left(g(\hat{\boldsymbol{\theta}}) - \left(\mathbf{d}_{obs}\right)_k\right) \qquad (2.12)$$

since the first two terms in the equation 2.11 remain constant during the optimization. A particularly appealing property of the likelihood function is that it allows for the finding of the best estimate of $\hat{\boldsymbol{\theta}}$ when the mapping function $\mathbf{d}_{pred} = g(\boldsymbol{\theta})$ is nonlinear.

2.2.1.3. Maximum Likelihood Estimation (MLE) with Random Observations and Random Predictions

A different likelihood function is defined if uncertainty is assumed to arise from both the observations and the predictions. Uncertainty due to modeling can be minimized by either increasing the resolution of the predictive model (e.g. finer mesh), by choosing an efficient numerical solver, or by using a better constitutive model. Yet variability inherent to the parameters cannot be minimized. Nevertheless, it can be included into the inverse problem solution by properly formulating the marginal pdfs. One way to incorporate the parameter variability into the inverse solution is by comparing the observations and the predictions, and by assuming that both of them carry uncertainty components (Table 1, case D). Consequently, the uncertainty associated with the observations and predictions can be defined as:

$$\Delta \mathbf{d} = \left[\mathbf{d}_{pred} - \mathbf{d}_{obs} \right] \tag{2.13}$$

If $\mathbf{d}_{pred}$ and $\mathbf{d}_{obs}$, and thus $\Delta \mathbf{d}$ are assumed to have Gaussian distributions, and $\mathbf{d}_{pred}$ and $\mathbf{d}_{obs}$ are assumed to be independent of each other, the likelihood function is formulated as:

$$f\left(\Delta \mathbf{d} \mid \hat{\boldsymbol{\theta}}\right)=$$

$$\frac{1}{\sqrt{(2\pi)^{mk}\prod\limits_{k=1}^{K}\left|\mathbf{C}_{\Delta\mathbf{d}}\right|_{k}}}\exp\left[\sum\limits_{k=1}^{K}-\frac{1}{2}\left(\Delta\mathbf{d}\right)_{k}^{T}\left(\mathbf{C}_{\Delta\mathbf{d}}\right)_{k}^{-1}\left(\Delta\mathbf{d}\right)_{k}\right]=$$

$$\frac{1}{\sqrt{(2\pi)^{mk}\prod\limits_{k=1}^{K}\left|\mathbf{C}_{\Delta\mathbf{d}}\right|_{k}}}\exp\left[\sum\limits_{k=1}^{K}-\frac{1}{2}\left(\mathbf{d}_{pred}-\mathbf{d}_{obs}\right)_{k}^{T}\left(\mathbf{C}_{\Delta\mathbf{d}}\right)_{k}^{-1}\left(\mathbf{d}_{pred}-\mathbf{d}_{obs}\right)_{k}\right]= \qquad (2.14)$$

$$\frac{1}{\sqrt{(2\pi)^{mk}\prod\limits_{k=1}^{K}\left|\mathbf{C}_{\Delta\mathbf{d}}\right|_{k}}}\exp\left[\sum\limits_{k=1}^{K}-\frac{1}{2}\left(g\left(\hat{\boldsymbol{\theta}}\right)-\mathbf{d}_{obs}\right)_{k}^{T}\left(\mathbf{C}_{\Delta\mathbf{d}}\right)_{k}^{-1}\left(g\left(\hat{\boldsymbol{\theta}}\right)-\mathbf{d}_{obs}\right)_{k}\right]$$

Using a support function similar to the equation 2.11 and minimizing it with respect to $\hat{\boldsymbol{\theta}}$, the objective function takes the form:

$$h_{\Delta\mathbf{d}}\left(\hat{\boldsymbol{\theta}}\right)=\sum\limits_{k}^{K}\ln\left\{\left|\mathbf{C}_{\Delta\mathbf{d}}\right|_{k}\right\}+\sum\limits_{k=1}^{K}\left(g\left(\hat{\boldsymbol{\theta}}\right)-\left(\mathbf{d}_{obs}\right)_{k}\right)^{T}\left(\mathbf{C}_{\Delta\mathbf{d}}\right)_{k}^{-1}\left(g\left(\hat{\boldsymbol{\theta}}\right)-\left(\mathbf{d}_{obs}\right)_{k}\right) \qquad (2.15)$$

Furthermore, if it is assumed that $E[\Delta\mathbf{d}]=0$, the covariance matrix of $\Delta\mathbf{d}$ is defined as:

$$\mathbf{C}_{\Delta\mathbf{d}}=E\left[\left\{\Delta\mathbf{d}-E(\Delta\mathbf{d})\right\}\left\{\Delta\mathbf{d}-E(\Delta\mathbf{d})\right\}^{T}\right]=E\left[\left\{\Delta\mathbf{d}\right\}\left\{\Delta\mathbf{d}\right\}^{T}\right]=$$
$$E\left[\left\{\mathbf{d}_{pred}-\mathbf{d}_{obs}\right\}\left\{\mathbf{d}_{pred}-\mathbf{d}_{obs}\right\}^{T}\right]= \qquad (2.16)$$
$$E\left[\left(\Delta\mathbf{d}_{pred}\right)\left(\Delta\mathbf{d}_{pred}\right)^{T}\right]+E\left[\left(\Delta\mathbf{d}_{obs}\right)\left(\Delta\mathbf{d}_{obs}\right)^{T}\right]=C_{\mathbf{d}_{pred}}+C_{\mathbf{d}_{obs}}$$

where $C_{\mathbf{d}_{pred}}$ and $C_{\mathbf{d}_{obs}}$ are the covariance matrices of the predictions and the observations respectively.

The covariance of the observations $\mathbf{C}_{\mathbf{d}_{obs}}$ was defined by equation 2.10. For the evaluation of $\mathbf{C}_{\mathbf{d}_{pred}}$ it is necessary to assume a-priori values $\boldsymbol{\theta}_{prior}$, with mean $E[\boldsymbol{\theta}_{prior}]$ and covariance $\mathbf{C}_{\boldsymbol{\theta}_{prior}}$. Therefore, the covariance of the predictions is defined as:

$$\mathbf{C}_{\mathbf{d}_{pred}} = E\left[\left(\Delta\mathbf{d}_{pred}\right)\left(\Delta\mathbf{d}_{pred}\right)^T\right] \qquad (2.17)$$

where $\Delta\mathbf{d}_{pred} = \mathbf{d}_{pred} - E[\mathbf{d}_{pred}] = g(\boldsymbol{\theta}_{prior}) - E[g(\boldsymbol{\theta}_{prior})]$.

From equations 2.9 and 2.14 it is observed that LSE is a particular case of Gaussian MLE, where the proper decomposition of the covariance matrix $\Delta\mathbf{d}$ may result in the factors Γ_k and W_k defined in equation 2.8.

2.2.2. Complete Solution

The complete solution to an inverse problem is expressed in the form of marginal pdfs and the covariance of $\boldsymbol{\theta}$. This work considers the Bayesian paradigm as the adequate venue to formulate a complete solution. The Bayesian approach makes inferences founded in statements that convey the integration of two main sources of information: the prior - derived from previous knowledge about the parameters, and the likelihood - based on the inferences assimilated by the data itself. Both of these are expressed in the form of probability density functions, which combined give a conditional joint probability function called posterior, which is itself the solution to the inverse problem.

2.2.2.1. Bayesian Paradigm

The Bayesian paradigm is an analytical formulation that naturally solves the inverse problem since it aims to retrieve the causes of the random observations generated by the constitutive parameters. The Bayes theorem defines the solution to the inverse problem as:

$$\pi(\boldsymbol{\theta}\,|\,\mathbf{d}_{obs},\mathbf{u}) = \frac{f(\mathbf{d}_{obs}\,|\,\boldsymbol{\theta})\pi(\boldsymbol{\theta}\,|\,\mathbf{u})}{\int f(\mathbf{d}_{obs}\,|\,\boldsymbol{\theta})\pi(\boldsymbol{\theta}\,|\,\mathbf{u})d\boldsymbol{\theta}} = \frac{f(\mathbf{d}_{obs}\,|\,\boldsymbol{\theta},g(\boldsymbol{\theta}))\pi(\boldsymbol{\theta}\,|\,\mathbf{u})}{\int f(\mathbf{d}_{obs}\,|\,\boldsymbol{\theta},g(\boldsymbol{\theta}))\pi(\boldsymbol{\theta}\,|\,\mathbf{u})d\boldsymbol{\theta}} \qquad (\,2.18\,)$$

where $\pi(\boldsymbol{\theta}\,|\,\mathbf{u})$ is the prior, which may be dependant on another set of parameters $\mathbf{u}$ known as hyper-parameters; $f(\mathbf{d}_{obs}\,|\,\boldsymbol{\theta})$ is the likelihood ; and $\pi(\boldsymbol{\theta}\,|\,\mathbf{d}_{obs},\mathbf{u})$ is the posterior. Descriptions of each of these components are discussed in the following sections.

2.2.2.2. Prior

The prior $\pi(\boldsymbol{\theta}\,|\,\mathbf{u})$ represents the a-priori state of information of the constitutive parameters, and the first of two main sources of information integrated into the solution of the inverse problem. Press (2003) identified three main types of priors. The most elemental is the one based on the principle of insufficient reason stated by Laplace, which suggests that in the absence of any reason to the contrary, all values of the unknown parameters should be taken to be equally likely. In those cases where there is less than total ignorance about a set of parameters, more rational procedures can be used to define them. Objective priors can be implemented when very little is known about the

parameters (e.g. Vague and Jeffrey's priors). Subjective priors can be implemented when there is enough evidence to build a distribution that reflects the analyst beliefs (e.g. conjugate, maximum entropy, empirical, hierarchical). In this work, it is proposed to explore the representation of the a-priori information over the parameters using conjugate priors such as the Gaussian and the log-normal distributions. These are then validated with experimental evidence.

The multivariate Gaussian prior is defined as:

$$\pi(\boldsymbol{\theta}) = f(\boldsymbol{\theta} - \boldsymbol{\theta}_{prior}) \propto \exp\left[-\frac{1}{2}(\boldsymbol{\theta} - \boldsymbol{\theta}_{prior})^T (\mathbf{C}_{\boldsymbol{\theta}_{prior}})^{-1} (\boldsymbol{\theta} - \boldsymbol{\theta}_{prior}) \right] \qquad (2.19)$$

where $\boldsymbol{\theta}_{prior}$ and $\mathbf{C}_{\boldsymbol{\theta}_{prior}}$ are the parameters mean vector and covariance matrix respectively.

The multivariate log-normal prior is defined as:

$$\pi(\boldsymbol{\theta}) = f(\boldsymbol{\theta} - \boldsymbol{\theta}_{prior}) \propto \exp\left[-\frac{1}{2}(\ln(\boldsymbol{\theta}) - \boldsymbol{\theta}^*_{prior})^T (\mathbf{C}_{\boldsymbol{\theta}^*_{prior}})^{-1} (\ln(\boldsymbol{\theta}) - \boldsymbol{\theta}^*_{prior}) \right] \qquad (2.20)$$

where $\boldsymbol{\theta}^*_{prior}$ and $\mathbf{C}_{\boldsymbol{\theta}^*_{prior}}$ are respectively the parameter's mean vector and covariance matrix of the underlying log-normal parameters $\boldsymbol{\theta}$.

2.2.2.3. Likelihood

The likelihood represents a measure of the predictive model performance, and the second one of the two main sources of information integrated into the solution of the

21

inverse problem. By definition it can take any particular shape according to the difference between observations and predictions. Nevertheless, a good model is expected to err following a simple and consistent response. Following a similar criteria for the prior definition, it is propose to explore simple representations which should be validated later. This is the case of the multivariate Gaussian-type likelihood introduced in sections 2.2.1.2 and 2.2.1.3 corresponding to two different states of information (equations 2.9 and 2.14).

2.2.2.4. Posterior

The posterior $\pi(\boldsymbol{\theta} \mid \mathbf{d}_{obs})$ is the joint probability function between the a-priori states of information associated with both the prior and the likelihood. Following the previous prior and likelihood assumptions, the posteriors for the Gaussian and log-normal priors are:

$$\pi(\boldsymbol{\theta} \mid \mathbf{d}_{obs})_G \propto$$

$$\exp\left[\begin{array}{c} \sum_{k=1}^{K} -\frac{1}{2}\left(g(\boldsymbol{\theta}) - \mathbf{d}_{obs}\right)_k^T \left(\mathbf{C}_{\Delta\mathbf{d}}\right)_k^{-1}\left(g(\boldsymbol{\theta}) - \mathbf{d}_{obs}\right)_k \\ -\frac{1}{2}\left(\boldsymbol{\theta} - \boldsymbol{\theta}_{prior}\right)^T \left(\mathbf{C}_{\boldsymbol{\theta}_{prior}}\right)^{-1}\left(\boldsymbol{\theta} - \boldsymbol{\theta}_{prior}\right) \end{array}\right]$$

(2.21)

and

$$\pi\left(\boldsymbol{\theta} \mid \mathbf{d}_{obs}\right)_{Log} \propto$$

$$\exp\left[\begin{array}{c} \sum_{k=1}^{K} -\dfrac{1}{2}\left(g(\boldsymbol{\theta}) - \mathbf{d}_{obs}\right)_{k}^{T}\left(\mathbf{C}_{\Delta\mathbf{d}}\right)_{k}^{-1}\left(g(\boldsymbol{\theta}) - \mathbf{d}_{obs}\right)_{k} \\[2mm] -\dfrac{1}{2}\left(\ln(\boldsymbol{\theta}) - \boldsymbol{\theta}^{*}{}_{prior}\right)^{T}\left(\mathbf{C}_{\boldsymbol{\theta}^{*}{}_{prior}}\right)^{-1}\left(\ln(\boldsymbol{\theta}) - \boldsymbol{\theta}^{*}{}_{prior}\right) \end{array}\right] \qquad (\,2.22\,)$$

respectively.

2.2.2.5. Maximum A-Posteriori

One particular case to the solution of the inverse problem is the Bayesian maximum a-posteriori approach, which defined under specific assumptions fulfills the form of the regularization algorithm developed by Thikonov (1995) for the solution of strongly ill-posed problems and the corresponding use of sophisticated optimization methods. This method is an extension of the effort of defining the posterior on a Bayesian setting, where it is maximized with respect to the unknown parameters $\hat{\boldsymbol{\theta}}$ (Fitzpatrick, 1991). When the observations are obtained from independent identically distributed (iid) Gaussian samples, the maximization of the posterior with respect to the parameters $\hat{\boldsymbol{\theta}}$ takes the form:

$$h_{\boldsymbol{\theta}\mid\mathbf{d}}\left(\hat{\boldsymbol{\theta}}\right) = \sum_{k=1}^{K}\left(g\left(\hat{\boldsymbol{\theta}}\right) - \mathbf{d}_{obs}\right)_{k}^{T}\left(\mathbf{C}_{\Delta\mathbf{d}}\right)_{k}^{-1}\left(g\left(\hat{\boldsymbol{\theta}}\right) - \mathbf{d}_{obs}\right)_{k} + \beta\left\|\hat{\boldsymbol{\theta}} - \boldsymbol{\theta}_{prior}\right\| \times \left\|\hat{\boldsymbol{\theta}} - \boldsymbol{\theta}_{prior}\right\|^{T} \qquad (\,2.23\,)$$

which is the generalized Thikonov's regularization function with:

$$\beta\left\|\hat{\boldsymbol{\theta}} - \boldsymbol{\theta}_{prior}\right\| \times \left\|\hat{\boldsymbol{\theta}} - \boldsymbol{\theta}_{prior}\right\| = \left(\hat{\boldsymbol{\theta}} - \boldsymbol{\theta}_{prior}\right)^{T}\left(\mathbf{C}_{\boldsymbol{\theta}_{prior}}\right)^{-1}\left(\hat{\boldsymbol{\theta}} - \boldsymbol{\theta}_{prior}\right) \qquad (\,2.24\,)$$

It is important to note that the parameter estimates in this case represent the MLE of the posterior, which means that they are not represented by a probability density function since its solution is a LSE type. Therefore, the maximum a-posteriori approach is a good proof about the generalization of the applicability of Bayesian methods for the solution of ill-posed problems with strongly non-linear mechanistic responses.

2.2.2.6. Functional Bayesian (FB)

In the case where constitutive parameters follow a prescribed spatial distribution, for instance, when regional 'materials' are allocated within a 3D-FEM (predictive model), the solution of the inverse problem given by the posterior is conditioned on the spatial parameters $\mathbf{X}$. Moreover, by using a functional representation of the $\boldsymbol{\theta}(\mathbf{X})$ field, such as the PC representation (Sakamoto and Ghanem, 2002a, 2002b), the solution of the inverse problem can be improved.

The benefits of this particular implementation are: the sampling of local 'material' heterogeneities that can extend to non-stationary and non-Gaussian conditions; the construction of a hierarchy of parameters, extending the statistical inferences from the constitutive parameters to the hyper-parameters (chaos coefficients) that govern them.

Under the previous assumptions, the posterior assumes a FB form, which in the case of Gaussian likelihood, and Gaussian and log-normal posteriors like those introduced in equations 2.21 and 2.22, evolve into the following expressions:

$$\pi(\boldsymbol{\theta}(\mathbf{X}) \mid \mathbf{d}_{obs})_G \propto$$

$$\exp\left[\sum_{k=1}^{K} -\frac{1}{2}\left(g(\boldsymbol{\theta}(\mathbf{X})) - \mathbf{d}_{obs}\right)_k^T (\mathbf{C}_{\Delta d})_k^{-1} \left(g(\boldsymbol{\theta}(\mathbf{X})) - \mathbf{d}_{obs}\right)_k \right. \\ \left. -\frac{1}{2}\left(\boldsymbol{\theta}(\mathbf{X}) - \boldsymbol{\theta}_{prior}(\mathbf{X})\right)^T \left(\mathbf{C}_{\boldsymbol{\theta}_{prior}(\mathbf{X})}\right)^{-1}\left(\boldsymbol{\theta}(\mathbf{X}) - \boldsymbol{\theta}_{prior}(\mathbf{X})\right)\right]$$

(2.25)

and

$$\pi(\boldsymbol{\theta}(\mathbf{u}(\mathbf{X})) \mid \mathbf{d}_{obs})_{Log} \propto$$

$$\exp\left[\sum_{k=1}^{K} -\frac{1}{2}\left(g(\boldsymbol{\theta}(\mathbf{u}(\mathbf{X}))) - \mathbf{d}_{obs}\right)_k^T (\mathbf{C}_{\Delta d})_k^{-1} \left(g(\boldsymbol{\theta}(\mathbf{u}(\mathbf{X}))) - \mathbf{d}_{obs}\right)_k \right. \\ \left. -\frac{1}{2}\left(\ln(\boldsymbol{\theta}(\mathbf{u}(\mathbf{X}))) - \boldsymbol{\theta}^*_{prior}(\mathbf{u}(\mathbf{X}))\right)^T \left(\mathbf{C}_{\boldsymbol{\theta}^*_{prior}(\mathbf{u}(\mathbf{X}))}\right)^{-1}\left(\ln(\boldsymbol{\theta}(\mathbf{u}(\mathbf{X}))) - \boldsymbol{\theta}^*_{prior}(\mathbf{u}(\mathbf{X}))\right)\right]$$

(2.26)

respectively.

2.2.2.7. Posterior Integration

The integration of the posterior becomes a challenge for a multivariate and multi-level Bayesian definition like equations 2.25 and 2.26 due to the number of samples needed to converge to the target joint pdf of $\boldsymbol{\theta}$. To overcome this problem, it is proposed to use the Markov Chain Monte Carlo (MCMC) method, which is a numerical procedure that allows for the sampling of a posterior. An important property of the MCMC method is that it converges to the target joint density as the sample grows. The decision rule that selects the samples is the Metropolis-Hastings (M-H), which is a generalized form of the Metropolis and Gibbs methods (Robert and Casella, 2005).

During the posterior integration, the MCMC 'state' of the chain at the s + 1 iteration is obtained by sampling a candidate point $\mathbf{Y}$ from a proposal distribution $q(\cdot \mid \hat{\boldsymbol{\theta}}_s)$. The latter is conditioned only by the previous set of parameters $\hat{\boldsymbol{\theta}}_s$ and can take any form subject to the regularity conditions of irreducibility and aperiodicity.

The candidate point $\mathbf{Y}$ is accepted or rejected as the next step of the chain with probability given by:

$$\alpha(\hat{\boldsymbol{\theta}}_s, \mathbf{d}_{obs}) = \min\left\{1, \frac{\pi(\mathbf{Y} \mid \mathbf{d}_{obs})q(\hat{\boldsymbol{\theta}}_s \mid \mathbf{Y})}{\pi(\hat{\boldsymbol{\theta}}_s \mid \mathbf{d}_{obs})q(\mathbf{Y} \mid \hat{\boldsymbol{\theta}}_s)}\right\} \qquad (2.27)$$

For the MCMC sampling the distribution of interest $f(\cdot \mid \mathbf{d}_{obs})$ appears as a ratio, so that the constant of proportionality cancels out. Also the evaluation of the posterior requires discarding the first iterations called the burn-in points, before it reaches the stationary condition, from which the statistical inferences are generated.

Metropolis-Hasting Algorithm

i) Initialize the chain with $\hat{\boldsymbol{\theta}}_0$ at $s = 0$

ii) Generate a candidate point Y from $q(\cdot \mid \hat{\boldsymbol{\theta}}_s)$

iii) Generate U from a uniform $(0,1)$ distribution

iv) If $U \leq \alpha(\hat{\boldsymbol{\theta}}_s, \mathbf{Y})$ then set $\hat{\boldsymbol{\theta}}_{s+1} = \mathbf{Y}$, else set $\hat{\boldsymbol{\theta}}_{s+1} = \hat{\boldsymbol{\theta}}_s$. This step implies that the forward problem should be solved for the candidate point Y and the previous point $\hat{\boldsymbol{\theta}}_s$ as part of the likelihood embedded in the posterior $f(\cdot \mid \mathbf{d}_{obs})$.

v) Set $s = s+1$ and repeat steps 2 through 5.

3. Simulation of Multi-Dimensional Non-Gaussian Non-Stationary Fields

The previous chapter introduced the Functional Bayesian (FB) method as an appropriate approach to solve inverse problems, where the constitutive model calibration permits the incorporation of local random effects as part of the a-priori information. This method relies on the spatial representation of the constitutive parameters as non-homogeneous 'material' compositions capable of reproducing the actual heterogeneous specimen deformation responses as captured by the digital images. This section introduces the PC method as an efficient approach to simulate multi-dimensional non-Gaussian non-stationary 'material' fields. The PC method significantly enhances the capacity of the FB solution due to the prior sampling flexibility to reproduce a wide range of random conditions (from stationary Gaussian to non-stationary non-Gaussian). After presenting the theoretical framework of the PC method, three benchmark cases with increasingly complex features are introduced to illustrate the implementation of the method. The third case is the representation of the spatially varying parameters used in the FB case study discussed in chapter 6.

3.1. Polynomial Chaos (PC) Method

The appealing formulation of the PC method is its ability to sample realizations of multi-dimensional non-stationry non-Gaussian random fields from the first order marginal pdfs and the second order correlation functions synthesized from the actual field

(Sakamoto and Ghanem, 2002a). Like other methods, the PC method involves a non-linear transformation of some underlying Gaussian process (Grigoriu, 1993, 1995; Shinozuka and Deodatis, 1991). This transformation is achieved by coupling the correlation function of the target field with the correlation function of an underlying non-stationary standard Gaussian field. The non-linear mapping relating both functions is found using the one dimensional PC decomposition of the target field and the Karhunen-Loève (K-L) representation of the non-stationary Gaussian field (Ghanem and Spanos, 1991). After the mapping between correlations functions is established, the target field is represented as a polynomial with uncorrelated Gaussian random variables.

For this purpose, consider $\Gamma_i(X)$ one-dimensional Hermite polynomials in the standard Gaussian random variable $\gamma(X)$ spatially or spatio-temporally referred to point X. Therefore, any target field or second-order random process $m(X)$ can be represented using a series expansion of the form (Sakamoto and Ghanem, 2002a):

$$
\begin{aligned}
m(X) = \sum_{i=0} U_i(X)\Gamma_i(X) = \\
U_0(X) + U_1(X)\gamma(X) + U_2(X)\left(\gamma(X)^2 - 1\right) \\
+ U_3(X)\left(\gamma(X)^3 - 3\gamma(X)\right) + U_4(X)\left(\gamma(X)^3 - 3\gamma(X)\right) + \ldots
\end{aligned}
\tag{3.1}
$$

where U_i are Fourier-type coefficients of the ith order that can be calculated using a Monte-Carlo sampling of the assimilated field $m(X)$ as:

$$
U_i(X) = \frac{\langle m(X)\Gamma_i\rangle}{\Gamma_i^2}
\tag{3.2}
$$

where $\langle\ \rangle$ denote the mathematical expectation.

The covariance function of the process $m(X)$ can be defined in terms of the series expansion introduced in equation 3.1 as:

$$Cov[m(X_2), m(X_1)] = \langle \widetilde{m}(X_2)\widetilde{m}(X_1) \rangle =$$
$$\sum_{i=1}\sum_{j=1} U_i(X_2)U_j(X_1)\langle \Gamma_i(X_2)\Gamma_j(X_1) \rangle \qquad (3.3)$$

where $\widetilde{m}(X) = m(X) - \langle m(X) \rangle$ is the residual field.

Due to the orthogonality of the Hermite polynomials with respect to the Gaussian measure, the cross-correlation of $\Gamma_i(X)$ is:

$$\langle \Gamma_i(X_2), \Gamma_j(X_1) \rangle = i!\langle \gamma_i(X_2)\gamma_j(X_1) \rangle \langle \Gamma_i(X_2)\Gamma_j(X_1) \rangle = 0 \qquad (3.4)$$

for $i \neq j$.

By substituting equation 3.4 into equation 3.3, the covariance $m(X)$ is redefined in terms of the Gaussian process $\gamma(X)$ as:

$$Cov[m(X_2), m(X_1)] = \sum_{i=1} U_i(X_2)U_i(X_1)i!\langle \gamma(X_2)\gamma(X_1) \rangle^i \qquad (3.5)$$

This system of algebraic non-linear equations can be solved iteratively after properly discretizing the spatial domain. Very similar results can be obtained by using the normalized covariance function or correlation function of the process $\rho(m(X_2), m(X_1))$

as the covariance function of the Gaussian process $\gamma(X)$, $\langle \gamma(X_2)\gamma(X_1)\rangle = \rho(m(X_2), m(X_1))$ (Sakamoto and Ghanem, 2002a and 2002b). The latter approach is less computationally intensive and easier to implement.

Once the covariance function of the Gaussian process $\gamma(X)$ is evaluated it follows to evaluated its corresponding K-L expansion. This is populated by sampling the Gaussian process $\gamma(X)$ as:

$$\gamma(X) = \sum_{i=1} \sqrt{\lambda_i} f_i(X)\xi_i \qquad (3.6)$$

where λ_i and f_i are the ith eigenvalues and eigenfunctions respectively, and $\{\xi_i\}$ are a set of uncorrelated Gaussian random variables, which will help to populate the process $m(X)$.

A representation of $m(X)$ as a series expansion in a set of uncorrelated random variables has the form:

$$m(X) = \sum_{i=0} u_i(X)\Psi_i(X) \qquad (3.7)$$

where $\{\Psi_i(X)\}$ represents a set of multi-dimensional Hermite polynomials with a set of standard Gaussian uncorrelated variables $\{\xi_i\}$.

By substituting the K-L definition into $\gamma(X)$ and setting equation 3.1 and 3.7 equal to each other, the chaos coefficients $u_i(X)$ are calculated using the expression:

31

$$u_i(X) = \frac{p!}{\langle \Psi_i^2 \rangle} U_p(X) \prod_{j=1}^{p} \sqrt{\lambda_{k(j)}} f_{k(j)}(X) \qquad\qquad (3.8)$$

where p is the order of the polynomial Ψ_i, $U_p(X)$ are the coefficients of the one-dimensional expansion introduced in equation 3.1, λ_k and f_k are the eigenvalues and eigenfunctions respectively of the Gaussian process $\gamma(X)$, and $\{\Psi_i(X)\}$ are the multidimensional Hermite polynomials.

Once both coefficients $U(X)$ and $u(X)$ of the one and multidimensional Hermite polynomials are evaluated, simulations of the process $m(X)$ can be populated by sampling the standard Gaussian uncorrelated variables $\{\xi_i\}$ as defined in equation 3.7.

3.2. PC Benchmark Case I: Simulation of a 1-D Field

The first benchmark case illustrates the applicability of the PC method for a 1D local variation field of data captured from a soil deforming specimen, where $X = y$ is the local spatial domain defined as the normalized vertical height of the soil specimen, and $m(X = y)$ is the random field under study defined as the average of the 3D vertical displacement field captured by the stereo digital images over the samples surface calculated along the specimen axial direction at 0.2 % of axial strain. A detailed explanation about the application of this particular field is given in section 5.4. The field $m(y)$ is measured in mm.

32

One data sample containing 13 observations is provided from which statistics are retrieved for the $m(y)$ field simulation (Figure 3.1). For computational simplicity each data profile is interpolated at 20 equally distributed points, which are considered enough as to capture local variations of the field and to facilitate the assessment of the spatial statistics.

The target values for estimating the field PC simulations are the data empirical first order marginal cumulative density functions (cdfs) and second order correlation statistics. The field profiles of the mean and standard deviations are presented in Figures 3.2 and 3.3 respectively. The mean shows a smooth monotonic behavior while the standard deviation captures different degrees of uncertainty showing local maximums and minimums, following an increasing trend from the bottom to the top of the spatial domain. The Non-Stationarity condition of $m(y)$ field is evidenced by the variability of both the mean and standard deviation along the spatial domain.

The field empirical covariance $Cov[m(y_2), m(y_1)]$ and the normalized covariance or correlation function $\rho(y_2, y_1) = Cov[m(y_2), m(y_1)]/\sqrt{Var[m(y_2)]}\sqrt{Var[m(y_1)]}$ are introduced in Figures 3.4 and 3.5 respectively. Both functions represent the linear correlation structure of $m(y)$ between any two points y_2 and y_1 along the spatial domain. In the covariance function, when both spatial reference points are the same (values lying over the diagonal), the square root of the covariance shows the same local maxima and minima as in the profile of the standard deviation presented in Figure 3.3. A similar interpretation can be applied to other coordinate combinations. In the case of the

correlation function, the highest values lie over the diagonal, meaning that the highest correlation is associated with the variation of the data values found at the same spatial position, whereas values close to zero are found between the farthest reference points, meaning that there is no recognizable pattern between the variations of data located at bottom and the top of the domain. For this particular field, it is shown that as the distance between any two data points y_2 and y_1 increases, the correlation decreases continuously from a maximum value of 1 to a minimum of 0.

One of the goals of this case it to contrast the ability of the PC method to simulate non-stationary non-Gaussian processes as compared with the Gaussian simulations only. With this purpose in mind, the spatial data ensemble (Figure 3.1) is assumed to follow a Gaussian behavior at each point over the space domain. Based on this assumption, the K-L expansion can be formulated to simulate the $m(y)$ field, such that $m(y) = \sum_{i=1} \sqrt{\lambda^*_i} f^*_i(y) \xi_i$, where λ^*_k and f^*_k are the eigenvalues and eigenfunctions respectively estimated from the empirical covariance function introduced in Figure 3.5. The eigenvalues and the corresponding first five eigenfunctions of $m(y)$ are presented in Figures 3.6 and 3.7 respectively, illustrating the order of magnitude and trends of the first set of eigen-quantities (5 eigenvectors only). Typical realizations obtained by the K-L expansion are introduced in Figure 3.8 showing good agreement with the actual observations (Figure 3.1). This can be corroborated in Figure 3.9, which shows the synthesized marginal cdf of the data ensemble and the synthesized K-L cdfs following

20,000 realizations at control points $y = 0.22$ and $y = 0.72$. By definition, the synthesized K-L covariance and correlation functions converge to the targets.

The PC expansion requires first that the eigen-quantities associated with the correlation function of the $m(y)$ field (Figure 3.5) be evaluated. As mentioned above, this assumption allows for the simplification of the non-linear mapping of the original correlation structure to the Gaussian-type process. The corresponding eigenvalues and the first five eigenfunctions are presented in Figures 3.10 and 3.11 respectively.

The second component required for the PC formulation is the definition of the first order marginal pdfs at each point over the spatial domain y. This allows for the coefficients $U_i(y)$ and $u_i(y)$ to be evaluated. In this example, the $U_i(y)$ coefficients are estimated using the raw data 'sample' as indicated by equation 3.2 for the first to the sixth polynomial order. Once the $U_i(y)$ coefficients are assessed, the $m(y)$ field is populated for each order to find the best one-dimensional expansion that fits the data marginal cdfs. For instance, Figures 3.12 and 3.13 show the marginal cdfs at control points $y = 0.22$ and $y = 0.72$ (as above) after performing 20,000 PC realizations for each polynomial order. From these figures it is observed that the sampling from the 'raw data', which represents the sampling of 'discrete' marginal functions weight the data behavior in a limited way, resulting in a poor representation of the observations. To overcome this problem, a continuous linear fit to the empirical data cdfs is proposed to smooth the data. By using a continuous linear fit of the empirical cdf, a new set of chaos coefficients are evaluated and new marginal densities are generated also following the generation of

35

20,000 PC realizations. The synthesized cdfs of the PC expansion at control points $y = 0.22$ and $y = 0.72$ are introduced in Figures 3.14 and 3.15 respectively. These show a significant improvement on the synthesized PC cdfs patterns.

Typical convergence behavior of the evaluation of the chaos coefficients $U_i(y)$ is presented in Figures 3.16 and 3.17 at control points $y = 0.22$ and $y = 0.72$ respectively. These figures show the evaluation of $U_i(y)$ for the PC expansions of orders $i = 0$, 1 and 2 (although $i = 3$, 4 and 5 were also calculated) during a sample of 20,000, at which point marginal cdfs domains show clear convergence patterns for all coefficients. Once the $U_i(y)$ coefficients are estimated, $u_i(y)$ can be computed using equation 3.8. The resulting profiles of the first five $U_i(y)$ and $u_i(y)$ coefficients ($i = 0$, 1, 2, 3, 4) corresponding to the fifth order one-dimensional PC expansion are presented in Figures 3.18 and 3.19 respectively.

The third component in the formulation of the PC expansion is the selection of the polynomial order that best reproduces the marginal empirical cdfs (targets). A first approach is to define a generalized order for the entire spatial domain. A local analysis at the variation of the $m(y)$ field is developed for elaborating this particular assessment. An example of this analysis is presented in Figures 3.20 and 3.21. These figures show the empirical and synthesized K-L cdfs at control points y = 0.22 and y = 0.72 respectively. They also show the synthesized PC cdfs for the second (Figure 3.20) and third (Figure 3.12) order polynomials for one-dimensional PC expansions. From these figures it is observed that the use of the PC expansions fit better the empirical cdfs than the K-L ones,

proving the adequacy of the method for Non-Gaussian random fields. In addition, it is observed that there is a tradeoff when assuming a generalized order for each PC expansion. If the criteria is to 'better fit the empirical cdfs and to allow smooth transitions at their tails', the second order works better for control point $y = 0.72$ (Figure 3.20) and the third order for the control point $y = 0.72$ (Figure 3.21). If the 'best fit' is the only criteria, the previous conclusion should be reversed.

In order to improve the incompatibility in the selection of the polynomial order, and taking advantage of the PC method definition, it is proposed to assign individual polynomial orders for each variable $m(y)$. Considering the marginal cdfs as those presented in Figure 3.20 and 3.21, but for all other y positions, and assuming the first criteria discussed before of 'best fit and smooth transition tails', multi-order expansions are formulated following the order profile shown in Figure 3.22. The updates of the empirical and PC synthesized cdfs at the two control points for the multi-order one-dimensional expansion are presented in Figure 3.23.

The fourth and final component required to ensure the optimal definition of the PC formulation is the selection of the polynomial dimension. As described in the work of Sakamoto and Ghanem (2002a, 2002b), the greater the dimension, the better the approximation to the target correlation structure. To illustrate this effect, Figure 3.24 and 3.25 present the synthesized covariance and correlation functions from the PC expansions as calculated from multi-order one-dimensional polynomials after 20,000 realizations. Both functions show significant deviation from their corresponding targets (Figures 3.4 and 3.5). This problem can be overcome by using the multi-order coefficients $U_i(y)$ and

37

higher order Hermite polynomials. Once the $U_i(y)$ coefficients are updated, estimates of the $u_i(y)$ coefficients are obtained for the second, third and fourth dimensions respectively. Based on these configurations, PC realizations are sampled showing a good agreement with the actual observations as the polynomial dimensions are increased. This change is illustrated in Figures 3.26 and 3.27. These show the synthesized covariance and correlation functions associated with 20,000 PC realizations based on multi-order four-dimensional estimates. These figures prove that for this particular PC design there is good agreement with the target functions (Figures 3.4 and 3.5). A set of typical PC realizations of the field are introduced in Figure 3.28 which fulfill the first order marginal and second order correlation statistics discussed above.

In summary, for this benchmark case demonstrates the PC simulations are significantly better than K-L ones. It also shows that the use of discrete 'raw data' to evaluate the chaos coefficients $U_i(y)$ is not as effective in terms of performance of the synthesized PC marginal cdfs when compared to the case where the empirical cdf was modeled using a continuous function. This case also demonstrates that modeling empirical marginal cdfs with a generalized order did not provide a consistent criterion selection for defining the best PC synthesized marginal cdfs. Instead, a method where the order of the expansion was adjusted for each point over the spatial domain showed better behavior for the different random responses captured by each marginal cdf. Finally, this case corroborated that as the dimension of the expansion increases, the difference between the target correlation and the synthesized PC correlation decreases. In particular,

the multi-order four-dimensional PC expansion showed good results for the simulation of the $m(y)$ field.

3.3. PC Benchmark Case II: Simulation of a 1D-T Process

The second benchmark case illustrates the applicability of the PC method for a 1D-T spatio-temporal process corresponding to the same field m defined in the previous section, but with the addition of the time reference, such that $X = (y,t)$ id defined as a point in the spatio-temporal domain, with y representing the spatial dimension and t representing the time dimension, and where $m(y,t)$ represents the averaged vertical displacement at different stages of deformation (or times t). The field $m(y,t)$ is measured in mm and t in seconds.

To illustrate the nature of the field, one data sample is presented in Figure 3.29, while a data ensemble which includes13 observations from which statistics are retrieved for the simulation of $m(y,t)$ is presented in Figure 3.30. The four set of data showed in Figure 3.30 correspond to stages of deformation at t_1=15 sec, t_2=30 sec, t_3=45 sec and t_4=60 sec. Also, as in the previous case, the data ensemble is interpolated at 20 equally distributed points along the y domain to facilitate the computation of the spatio-temporal statistics.

The process mean and variance estimates are presented in Figures 3.2 and 3.3 respectively. These provide a first evaluation of heterogeneous local variations. Both the vertical displacement means and the variances show global incremental trends and local changes on both the spatial and time domains. These characteristics confirm the non-

stationary condition indicating the adequacy of the simulation method. The variation of the means is smoother than the variation of the variances with respect to time. The mean process shows a monotonic behavior with respect to space and time. The variances on the other hand show a general trend to increase from the bottom to the top of the spatial domain as the progresses in time. They show some periodicity at specific y locations in the form of local maximums and minimums.

In order to capture the correlation structure between data ensembles at different times, it is necessary to establish a spatio-temporal relationship with each variable to create a reference to $m(y,t)$. This allows for the assessment of the covariance and correlation matrices of the process. A simple way to create this association is by assigning to each variable a number that increases monotonically from the bottom to the top of the specimen and that also increases over time. A graphical representation of the variable assignment is depicted in Figure 3.33 (note that other forms can be used without changing the process estimates). In this figure, the first twenty variables represent the displacements of the first data ensemble measured at t_1, where variable number 1 represents data at the bottom of the spatial domain and variable number 20 represents the observations at the top. The following sets of twenty variables are associated with the data ensembles measured at times t_2, t_3 and t_4 respectively.

With the variable arrangement described above, it is possible to evaluate the empirical covariance and correlation matrices considering the four data ensembles. The graphical representation of the empirical covariance matrix is presented in Figure 3.34. A mosaic of 4 x 4 = 16 sub-matrices is illustrated in this figure, including 20 x 20 = 400 covariance

values, for a total of 16 x 400 = 6,400 covariance estimates. The sub-matrices located in the main diagonal are the covariance functions corresponding to times t_1 through t_4 respectively. The sub-matrices out of the main sub-matrix diagonal represent the covariance matrices between data ensembles observed at different times. For instance, the sub-matrix located in the bottom row and the third column (from left to right), compares variables 1 to 20 with variables 41 to 60. It represents the covariance sub-matrix between data observed on the first data ensemble (t_1) and the third data ensemble (t_3). Similarly, Figure 3.35 shows the empirical correlation matrix, which follows the same arrangement as the covariance matrix. As in the previous case, the empirical covariance and the correlation matrices are considered the 'target' values for the PC simulations.

A detailed analysis is developed to define the best polynomial order associated with each variable $m(y,t)$. An arrangement of the polynomial orders is introduced in Figure 3.36. This arrangement is used to calculate the converging $U_i(y,t)$ coefficients following the evaluation of 20,000 samples. Based on the correlation matrix of the process, the eigenvalues and eigenvectors are evaluated and presented in Figures 3.37 and 3.38 respectively.

Once the order of each variable is identified, and the coefficients $U_i(y,t)$ and the eigen-quantities are calculated, the $u_i(y,t)$ coefficients are evaluated. For this purpose, the first four dimensions of the Hermite polynomials are tried at the time to define the optimal polynomial design. This is achieved by simulating 20,000 realizations for each order, and then by comparing the target and PC synthesized statistics. In this case, the

41

multi-order four-dimensional polynomial generates the process estimates that best approximate better to the observations. The order of magnitude and trend of the first five coefficients $u_i(y,t)$ are presented in Figure 3.39.

The recovered synthesized PC marginal cdfs show good fit to the data trends, as can be observed at the control point $y = 0.98$ for the four-time steps included in the process (Figure 3.40). Also, the synthesized PC covariance and correlation matrices coincide with the empirical covariance estimates as illustrated in Figure 3.41 and 3.42 respectively. Finally, Figure 3.43 shows a typical spatio-temporal PC realization generated under the previous assumptions with the actual observations in the background as a reference. This simulation shows the PC capability to generate complex data behavior with the same statistical characteristics than the observations.

In summary, this second benchmark case presents the simulation of a spatio-temporal process $m(y,t)$. As in the 1D simulation presented in the previous section, the 1D-T process generated satisfactory results when continuous empirical cdfs where used for the estimates of the $U_i(y,t)$ coefficients and the corresponding marginal cdfs. Assignment of a variable number was necessary to manage and calculate the empirical covariance and correlation matrices due to the multidimensional nature of the process. A multi-order and four-dimensional expansion allowed for an adequate simulation of the process. This was demonstrated by comparing the target and empirical marginal cdfs and covariance and correlation matrices.

3.4. PC Benchmark Case III: Simulation of a 2D Field

The third benchmark case illustrates the applicability of the PC method for a 2D random field of a synthetic experiment associated with the simulation of spatial varying material properties. This problem represents a key element for the probabilistic calibration, where $X = X(x_{norm}, y_{norm})$ is a point in the vertical cross section domain of a 3D-FEM cylindrical specimen normalized with respect to the specimen diameter, and where $m(X) = \theta(X)$ represents the material field as defined in the FB approach described in the previous chapter (section 2.4.6). In this case, (x_{norm}, y_{norm}) is dimensionless while $m(x_{norm}, y_{norm})$ is associated with the spatial variation of the Young's modulus which is measured in MPa. The particular spatial configuration of the spatial domain X is presented in Figure 3.44. It includes a reference grid that identifies the material random variables considered for the field simulation.

The conditions defined for the PC material simulation include stationary log-normal marginal pdfs with mean 92.33 MPa, standard deviation 45.98 MPa (Figure 3.45), and an isotropic correlation function with correlation parameter $\delta = 0.5$ (Figure 3.46). Based on these assumptions it is possible to compute the covariance and correlation matrices (Figure 3.47 and 3.48 respectively), which along with the log-normal marginal pdfs become the target statistics. The eigen-quantities are estimated from the empirical correlation estimates. These are presented in Figure 3.49 and Figures 3.50 – 3.52 respectively (only the first three eigenfunctions).

After analyzing the effect of the polynomial order and dimensionality, it is assumed that a third order four-dimensional Hermite polynomial is appropriate for the PC simulation. The projection of the first five terms of the chaos coefficients $u(x_{norm}, y_{norm})$ plotted over the normalized vertical cross section is presented in Figure 3.53. In order to establish that the PC simulations approximate the target functions, a series of 20,000 PC samples is generated and the corresponding spatial statistics calculated. Figure 3.54 shows the cdf of the synthesized PC simulations corresponding to control points X(-0.25, 1.10) and X(0.25,, 1.10) along with the target empirical and lognormal models. From this figure it can be observed that the PC simulations show good agreement with the targets. In terms of the covariance and correlation functions, the synthesized matrices are presented in Figures 3.55 and 3.66.   These also show good agreement with the corresponding targets. Finally, a typical PC realization of the material field is presented in Figure 3.57.   This illustrates a process sample like the ones to be included into the probabilistic calibration case study presented in chapter 6.

In summary, the last benchmark case described the simulation of a spatially varying material which is efficiently sampled using the PC method. By providing first order statistics information about the stationary marginal pdf and second order statistics about the correlation function, it was possible to populate the material field using third order four-dimensional PC expansions. Evidence was presented showing that statistics from the synthesized PC samples approached the target models.   This means that the material random field representation is efficiently carried out by the PC method.

4. Soil Experimentation

The previous two chapters introduced the theoretical components of the Functional Bayesian (FB) method for the solution of the inherent inverse problem (chapter 2), and the PC method for the simulation of a spatially varying material field (chapter 3). This chapter discusses an experimental database populated to validate the application of the FB method for the calibration of soil constitutive models. The experimental evidence discussed here is obtained by combining a standard triaxial soil testing method and an advanced non-destructive technique for the measurement of full-field displacements based on 3D imaging. Together these allow for the definition of 3D-T displacement fields captured over the surface of a deforming soil specimen.

The experimental database is used to evaluate the performance of the predictive model (3D-FEM) in reproducing local non-homogeneous responses (chapter 5). It is also used to identify patterns and causes of the soil random responses by generating the empirical spatio-temporal inferences (chapter 6) required for the solution of a probabilistic calibration case study (chapter 7). As mentioned above, although testing included the soil response until after failure, only data contained within a short deformation range predominantly associated to a linear elastic response is considered for further analysis. These are the data that represent the observations, one of the two sources of information required for the integration of the solution of the probabilistic calibration.

4.1. Triaxial Testing

It is common practice to rely on triaxial test results for the calibration of soil constitutive models. Triaxial testing is a standard procedure that aims to capture relationships between global stress, strain and volumetric change of a soil specimen for the assessment of its fundamental mechanical properties. The type of triaxial testing procedure chosen depends on the soil classification and the expected behavior of the sample. The triaxial test consists of loading (also known as shearing) a soil specimen until it fails. In this work, an isotropic compression is applied to the specimen to reproduce prescribed confinement pressure conditions. The soil sample can be either an undisturbed field sample or a reconstituted sample constructed in the lab. The choice depends on the objectives of the investigation and the soil nature.

Previous investigations have studied the influence of control variables related to triaxial soil testing. Though this is not a comprehensive list, studies have been conducted on specimen characteristics, such as specimen grains arrangement and compressibility (Oda, 1972; Mahmood, 1976; Kuo et al., 1996; Wang et al., 2003), grain size distribution (Ghalib and Hryciw, 1999), test repeatability, sample uniformity and homogeneity (Ladd, 1978; Vaid and Negussey, 1988; Al-Shibli et al., 1996; Muhunthan et al., 2000), relative density range of variation (Passalacqua, 1991), maximum density (Lo Presti et al., 1992; Cresswell et al., 1999), and minimum density (Naeini and Baziar, 2000). Building on this previous research, this work attempts to identify and quantify uncertainties associated with triaxial testing focusing on the influence that they have on the calibration of

46

constitutive models. Additionally, numerical modeling details considered as sources of uncertainty to be incorporated into the calibration are discussed in chapter 5.

The series of triaxial experiments presented in this work are based on the standard test for Consolidated Drained (CD) compression conditions (ASTM D 4767) with some modifications. These modifications were implemented to guarantee a controlled testing environment and to facilitate the incorporation of the digital imaging technique. The modifications consisted in removing the Plexiglas cell to avoid light reflection during the capture of the stereo digital images. This required the confinement pressure to be applied using a vacuum pump instead of with the cell fluid (dry test).

The GeoComp automated system (Geocomp Corporation, 2002) was used to perform the experiments. It controls and records loads, displacements, cell and pore water pressures. The system controls the test through a PC connected to the loading frame (LoadTrac II) and to two pressure pumps (FlowTrac II). The test characteristics are configured in the software provided as part of the system (Triaxial) and saved in a file before running the experiment. Some of the test characteristics include the initial sample geometry (height, diameter), physical properties of the sample (weight, density), area correction effect, test type (strain or load controlled, drained, undrained), and other reference information (reading time, units, etc.). The 'LoadTrac II' device loads the specimen from the bottom using a micro-step motor. The top is fixed to the loading frame through a steel rod attached to the top Plexiglas platen at one end and to the load cell at the other. The triaxial system reads the vertical platen displacements using a transducer located underneath the loading base. It reads the loads using a load S-shaped

cell fixed in the upper beam of the loading frame. The only pore pressure readings taken during the test are given by the gauge attached to the vacuum pump which is maintained constant throughout each test. A picture showing the GeoComp system is presented in Figure 4.1, with a) the triaxial base and frame, and b) the automated system, including the 'LoadTrac II' and the two 'FlowTrac II' pumps.

4.2. Properties of Soil Specimens

Sieved construction sand was chosen as the testing material because its individual grains provided an adequate color spectrum suitable for pattern recognition during imaging analysis. Reconstituted dry sand specimens were prepared using uniform sand. Some of the sand characteristics included a specific gravity of G_s = 2.63 with a mean diameter D_{50} = 0.5 mm and coefficients of uniformity and curvature of C_u = 2.34 and C_c = 1.11 respectively. The graphical representation of the sand grain size analysis is presented in Figure 4.2 highlighting the material uniformity.

Specimens were formed using a standard mold of cylindrical shape of 7.11 cm diameter and 15.6 cm height. For ensuring the specimen uniform geometry the mold was conditioned so that the wrapping membrane stayed suctioned to its wall during the grains placement. Samples were formed in layers using dry pluviation and a vibratory compaction method. The surface of each layer was compacted uniformly with no scarification between the layers. Porous stones were included at the ends of the specimens following the triaxial standard. Figure 4.3 illustrates the sample preparation process which includes a) mold assembling, b) membrane collocation, c) top platen

seating d) mold removal (under vacuum pressure) and e) the measurement of sample properties.

4.3. Triaxial Testing Application

An experimental database was populated with the results of thirteen vacuum-consolidated drained triaxial compression tests on dense sand specimens that were prepared in three compacting layers. In addition, one 'layered' sample (120704c) was built, including two compacting layers, the bottom half 'dense' and the top half 'loose'. The 'dense' segment was prepared using the same technique as the other thirteen samples, and the 'loose' segment was prepared placing the sand manually at a zero height.

The experimental control variables included the specimen height, density, and initial geometry. Only specimens with relative density varying between 85% and 95% were considered for testing. In the case of the layered specimen test the relative density was 68.9%. Samples were consolidated to 40 kPa effective stress (using the vacuum pump) and included non-lubricated ends. All specimens were loaded with a controlled deformation rate of 0.2 % of axial strain/min. A summary of the main specimen characteristics is presented in Table 4.1.

A first step for the characterization of the database consists in evaluating some basic statistics from Table 4.1. For instance, after excluding the data of the layered specimen test, it is observed that the average height of the specimens is 157.3 mm with standard deviation of 2 mm; the average density is 1,711 kg/m^3 with a standard deviation of 7.44

kg/m^3; the average relative density is 91.8% with a standard deviation of 2.03%; and the average peak friction angle is 48.13^o with standard deviation 0.69^o.

Global stress-strain curves for all tests carried out are presented in Figure 4.4. From the main body of curves (13 tests) it should be noted that although all thirteen tests results were nominally similar, significant scatter is present in the global soil behavior. The layered specimen test does not produce the typical behavior of a dense specimen (no peak stress). Notice that all tests results including the layered specimen test converged to approximately the same critical state condition, which ranged between 150 and 180 kPa.

As mentioned above, this work concentrates on the linear elastic range to illustrate the applicability of the calibration method. From the strain-stress curves it is possible to identify the linear elastic range, which in this case is defined from 0.0 % to 0.2 % of axial strain. This range was limited after computing the first derivative functions and defining the extension of the plateau sections common to all tests results.

4.4. Digital Image Correlation (DIC)

The Digital Image Correlation (DIC) technique is an innovative approach aimed at capturing local phenomena of deforming specimens. Three seminal papers introduce the use of digital images for the assimilation of displacement fields. Peters and Ranson (1982) were the first to use principles of continuum mechanics to assimilate deformation information from images. Sutton et al. (1983) introduced the Digital Image Correlation (DIC) technique, which is the basis of the imaging method used in this work. Chu et al. (1985) were the first to design experiments to evaluate the accuracy and precision of the

DIC method. A thorough description of the evolution from 2D to 3D DIC analysis can be found in Sutton et al. (2000). More recently, DIC techniques have proven to be reliable and accurate tools for investigating local soil deformation phenomena in sands either in 2D (Rechenmacher and Finno, 2004) or in 3D (Rechenmacher and Medina-Cetina, 2006). These investigations captured hundreds to thousands of displacement vectors obtained from soil deforming specimens in biaxial and triaxial devices respectively.

4.5. 3-D Digital Image Correlation (3D-DIC)

VIC-3D is based on a DIC technique that relies on the correlation coefficient to match pixel subsets between pairs of images located at different stages of deformation. This is possible, since digital images are comprised of a grid of pixels that measure gray intensity values representing the light intensity of the sample's surface. In this case they capture the direct impression of the color variation of the individual sand grains seen through the wrapping membrane.

The correlation kernel embedded in VIC-3D that helps to find the best match of pixel subsets between stereo images is the iterative spatial domain cross-correlation algorithm (Sutton et al., 2000). This algorithm solves for the pixels subsets translation as well as for its rotations and strains. In this way, once the best matches between subsets are found, vectors are traced between the pixels subset centroids defining the 3D displacement fields. A simple representation of this matching is depicted in Figure 4.5.

In this work, 3D-DIC is used to estimate 3D-T spatio-temporal full-field displacement fields ranging from the actual initial specimen geometry to the assessment of kinematic

51

local heterogeneities captured over sample surface at different stages of deformation. In order for 3D-DIC analysis to be performed, a pre-testing calibration procedure is required. This calibration consists in taking twenty or more pictures of a standard grid fixed at different positions so that the system parameters can be evaluated (focal length, lenses distortion, etc.). Figure 4.6 shows the left and right images of the standard grid used for the VIC-3D calibration.

During each triaxial test, pairs of digital images are taken simultaneously every 15 seconds (0.05 % of axial strain) using two 14-bit digital cameras Q-Imaging PMI-4201, with 4.2 Mega pixels of resolution (2024 x 2024 pixels), positioned approximately 25 cm from each other, and mounted on a tripod whose axis was located approximately at 50 cm from the sample. In addition, in order to enhance the pixel gray level variation in the images captured by 3D-DIC, four lamps with equal light intensity were optimally located and oriented toward the specimen. This tended to enhance the individual grain color contrasts in the sand. The overall scheme of the equipment set up is shown in Figure 4.7.

The software used to capture the stereo digital images during the triaxial tests is VIC-SNAP developed by Correlated Solutions (2004). This software allows for the selection of periodicity in which the images are taken and for enhancing some of the image characteristics before the beginning of the test. The computer where the VIC-3D controls the image shooting also serves to store the stereo digital images. No synchronization between the Triax and VIC-3D timers was designed. A click on each mouse served to simultaneously start both processes – the image acquisition and the triaxial shearing.

The software used to measure the 3D full-field displacements is VIC-3D, also developed by Correlated Solutions (2004). For the correlation analysis to be performed, VIC-3D requires the selection of an 'area of interest' in the first set of images (undeformed state), that serves as reference for where in the image the displacements will be quantified. Also, a 'seed' window on both images must be defined, where common pixels are clearly identified, so that the correlation starts at the same point in the spatial reference to help in the correlation convergence. To accommodate the measurements of non-integer pixel displacements, pixel gray levels are interpolated such that continuous intensity distributions are matched. Various forms of interpolation functions may be used. In this work the cubic interpolation was used.

The VIC-3D calibration establishes a 3D spatial reference defined as the orthogonal 3D coordinate system (x, y, z), introducing the depth perception into the analysis that allows for the definition of the sample 3D shape (Triggs et al., 2000). This means that at each deformation stage, it is possible to generate the actual geometry of the specimen using the corresponding stereo digital images. To illustrate this step in the DIC analysis, Figure 4.8 shows a couple of stereo digital images taken before loading, along with a measure of the initial specimen geometry as calculated by VIC-3D. This figure also shows the spatial reference system considered for the 3D-DIC analyses (x, y and z). This helps to estimate one of the specimens' initial boundary conditions.

For the calibration purposes discussed, 3D displacement fields are obtained between the reference stereo images that correspond to the undeformed stage, and the target images that correspond to subsequent deformation stages that lie within the linear elastic

53

range. Once displacement fields are obtained for each deformation stage it is possible to estimate the sample surface deformed configuration.

An average of 40,000 displacement vectors was found over the sample surfaces for each stage of deformation. The center to center distance is approximately 0.4 mm, and covers a digitized area limited by a sector angle of approximately 85$^{\text{o}}$. The area includes measurements from the bottom to top of the porous stones, except a narrow segment on the soil-porous stones interfaces (less than 1 mm on each boundary). This constraint arises because of the limitation in DIC capacity to identify variations in color patterns on uniformly-colored the porous stones.

To illustrate the application of the 3D-DIC technique, Figure 4.9 presents the stress-strain curve of test 100203a including marks at 0.2 % and 2.0 % of axial strain. The corresponding 3D displacement fields u, v and w measured by 3D-DIC (displacements in the x, y and z directions) are shown in Figure 4.10. This figure illustrates the local heterogeneous displacement responses observed on the sample surface. The u displacement field is expected to be symmetric with respect to the center lines traced over the sample surface on the axial and horizontal directions. Instead, a consistent slight deviation is observed towards the right and bottom sides at 0.2 % and 2.0 % of axial strain. The w displacement is expected to show the bulging effect from the initial deformation stages. Instead, a slight displacement inwards is observed at 0.2% of axial strain, which is reversed later when the bulging effect takes place at later deformation stages. This effect is slightly deviated down from the center of the specimens' surface.

54

Deformation on the axial direction seems uniform at all stages of deformation, although some local non-uniformity can be more easily identified at early stages of deformation.

4.6. Top Platen Motion

A review of the 3D-DIC measurements reveals the identification of a vertical top platen motion at early stages of deformation. A typical representation of this effect is portrayed by the v field presented in Figure 4.10 at 0.2 % of axial strain. A more extensive and refined analysis was made on the boundary between the soil and the top porous stone due to the potential impact that this effect could have on the estimates of the constitutive parameters. An example of these measurements made on the same test is presented in Figure 4.11, which shows the 3D projection of the displacement profile of the v field over the specimen vertical cross section at 0.2 % of axial strain.

Results from the top platen motion show a significant vertical displacement probably due to the addition of local deformations, such as the vertical load cell compression, the axial loading rod sliding in the Plexiglas platen, and the soil's bedding effect on the soil-porous stone interface. Similar displacements were consistently found on all other tests results included in the experimental database. These findings show that the 3D-DIC measurements make it possible to adjust the estimates of constitutive parameters dependent on strain measures. As a result, the global axial strain is calculated as the difference between the triaxial device reading (at the bottom of the specimen) and the local displacement measured by VID-3D (at the top of the specimen), yielding better estimates of the constitutive parameters. Figure 4.12 presents the strain-stress curve of the

triaxial measurements observed on test 100203a and its corresponding adjusted curve after introducing the VIC-3D measurements for a deformation range from 0.0 % to 0.2 % of axial strain. This figure shows also the secant estimates of Young's modulus for each curve, with E_{Triax}= 84.97 MPa and E_{Adjusted}= 179.15 MPa for the triaxial and adjusted curves respectively. The difference between these estimates put in evidence the sensibility of the elastic parameter at early stages of deformation, but more importantly, makes clear the necessity of incorporating the imaging measurements for the assessment of more realistic constitutive parameters. Furthermore, as will be seen in chapter 5, numerical estimates based on the adjusted elastic parameters show better agreement with the actual displacement observations, which corroborates the impact of this particular finding. In this work, the sum of all the local vertical deformation effects discussed above will be referred as the compliance effect (C). It is one of the local effects included in the predictive models discussed in chapter 5.

Also, using the 3D vertical displacement information captured on the top platen, a tilt analysis was performed on the top porous stone. This was done to investigate the extent to which the relative displacements observed on the vertical profiles were associated with local displacements due to the seating mechanism of the top Plexiglas platen and the steel rod connected to the load cell. This particular mechanism was fixed prior to the experimentation phase. However, in order to quantify the magnitude and orientation of any of the porous stone apparent tilt, a hyper-plane was fit to the data generated by VIC-3D. This hyper-plane was given by the profile of vertical displacements as the one shown in Figure 4.11. The fitting surface has the form $\partial v(x,z) = ax + cz + d$, where ∂v is the

assumed vertical displacement at the point (x,z), where x is the horizontal coordinate going from left to right, z is the hotizontal coordinate going out of the vertical plane, a and c are the slope coefficients on the x and z directions respectively, and d is the intercept on the y direction.

In order to obtain inferences about the apparent tilt, the same analysis was repeated to all tests. Table 4.2 presents a summary of the coefficients of the equations fit to each one of the vertical profiles of the tests included in the database for an axial strain of 0.2 %. Values of the a coefficient oscillated between -0.0006 and 0.0009, while values of the c coefficient oscillated between -.0017 and 0.0025. The means were 0.0 and 0.0002 and the standard deviations were 0.0004 and 0.0011 respectively.

A graphical representation of the order of magnitude and orientation of the porous stone tilt can be obtained by considering the hyper-plane coefficients a and c as vector components. Figure 4.13 shows the vector representation of all tests included in the database. The results presented in Table 4.2 and Figure 4.13 can be interpreted as small displacements that are considered to have a minimum impact into the overall sample deformation.

4.7. Sample Initial Geometry

As described above, the 3D shape of the specimen is known at the zero deformation stage thanks to the measurements of VIC-3D. From the coordinates of the boundaries between the soil and the porous stones it is possible to estimate the axis of the specimen. It serves as a reference to evaluate the radius over the specimen area of interest where

3D-DIC is applied. In order to capture the radius trends over the surface, the average of the radius estimates located at the same heights are calculated. This yields a profile depicting the radius local variation on the vertical direction. A typical vertical profile of radius local averages corresponding to test 100203b is presented in Figure 4.14. It should be noted that in this Figure the ratio considered between scales is enhanced to improve the perception of radius variability. Similar profiles are obtained for all other tests included in the experimental database, which are later incorporated into their corresponding predictive models. The influence of this effect is studied later during the model performance analysis in chapter 5 where it is referred as the (G) effect.

4.8. VIC-3D Accuracy Analysis

In order to check on the accuracy of VIC-3D, vertical displacements obtained by VIC-3D are compared to global displacements obtained by the triaxial device. Measurements taken from VIC-3D are local displacements at the bottom of the specimen obtained from the images taken during the triaxial tests. Figure 4.15 shows an example of the area of interest on the left image of test 100103d. In general, 3D-DIC analysis presented some difficulties since the process to define the seed point where the correlation starts was more complicated than usual due to the color uniformity found within the porous stone. This made the image correlation more difficult. To minimize this problem, a small portion of the soil area was included to facilitate the identification of the common point of reference on the left and right images.

For the most part, tests considered for the accuracy analyses are the same as those included in the experimental database. Test 100203a was the only exception – the area of interest did not allow for the generation of results. On the other hand test 120704a, which was not included into the database due to a non-uniform local deformation identified at the top of the specimen was included, as well as the layered specimen test 120704c.

Data points included in the accuracy analysis lie within the assumed linear elastic range (0.0 % to 0.2 % of axial strain). The correlation analyses were performed by comparing the undeformed state of the specimen (at time zero) with stereo images at the deformed states corresponding to 15, 30, 45 and 60 seconds. The analysis of the local displacements by VIC-3D gives a small displacement field that primarily covers the porous stone. An average of such field along the horizontal direction gives a vertical displacement profile of the bottom of the specimen. For instance, Figure 4.16 presents a set of averaged local vertical displacements corresponding to test 100103d.

The mean value of this particular profile helps to establish a comparison between the global and the averaged local vertical displacements as measured by Triax and by VIC-3D. The comparative measures corresponding to test 100103d are shown in Figure 4.17, which follows the linear trend imposed automatically by the triaxial system for a prescribed strain rate of 0.2 % of axial strain per minute. This is true for all tests in the database.

Triaxial measurements were considered the reference when compared with those of VIC-3D. The correlation between both datasets can be observed by plotting the

corresponding displacements measured at 15, 30, 45 and 60 seconds respectively. Figure 4.18 shows a total of sixty data points, representing 4 displacements stages for 15 tests, where each data comparison is independent of each other. The value of the correlation coefficient between both measurements is $\rho = 0.98$, indicating a very strong correlation between the instruments. The linear regression associated with the same points is $y = 0.97x + 0.0089$ (mm), where x represents the information given by VIC-3D and y represents the information given by Triax. The linear regression coefficient confirms the evidence given by the correlation coefficient, and shows no bias on the error measurements.

The second measure of accuracy is given by the absolute error of VIC-3D defined as the difference between the vertical displacement obtained by VIC-3D and the reference displacement measured by Triax. The histogram of the relative frequency of the absolute error is presented in Figure 4.19. It shows a distribution that approaches to a normal distribution. The mean of the absolute error was 0.00 mm, with a standard deviation of 0.02mm. These statistics indicate that the measurement accuracy of VIC-3D is of the order of ± 0.02 mm.

Previous research suggests that the accuracy of the horizontal in-plane and out-of-plane displacements should be of the same order as the vertical displacements (Sutton et al., 2000). This observation confirms that although some horizontal deformations were observed on the boundary with the porous stone for deformations within the linear elastic domain, they all lay within the order of accuracy. This is the reason why they are not incorporated into the predictive models.

60

5. Soil Modeling

The previous chapter introduced the experimental methods implemented to generate the observations. 3D full-field displacements were captured over the surface of a set of deforming specimens allowing for the integration of a spatio-temporal database that included specimen local deformation effects. This chapter introduces four predictive models (3D-FEMs) and a parametric analysis to measure the ability of the models to reproduce the local heterogeneous responses captured on the experimental observations.

The parametric analysis is based on an optimization approach implemented to minimize the difference between the experimental observations and the numerical predictions as for different modeling configurations that include the sample geometry (G), the compliance effect (C) and the material spatial variability (S). By repeating the same procedure in all tests, it is possible to measure the sensitivity of the models. This is done by evaluating the prediction error that produces a probabilistic measure that gives fundamental information for the definition of the likelihood function, one of the two components required for the Bayesian formulation for the solution of the inverse problem.

5.1. Modeling of Soil Heterogeneous Local Responses

A rational approach for measuring the performance of the predictive model $g(\mathbf{\theta})$ is to pair the full-field displacements synthesized from experimental observations and those synthesized from numerical predictions. One possibility is to define an objective function

of the form $L\left(d_{pred}, d_{obs}\right) = L\left(\left\|\mathbf{d}_{pred} - \mathbf{d}_{obs}\right\|\right)$. This function can be minimized by a set of estimates $\hat{\boldsymbol{\theta}}$ of the constitutive parameters using the LSE optimal solution (section 2.3.1.). In fact, the optimal estimates $\hat{\boldsymbol{\theta}}$ represent the deterministic solution to the inverse problem. This particular solution offers a set of constitutive parameters that can subsequently be used to predict the performance of various designs beyond the experimental conditions.

Standard characterization of soil constitutive parameters based on triaxial testing relies on measurements of global responses due to the testing device configuration. This enables characterization of soil behavior only in a volume-averaged sense, implying that the material is homogeneous. This assumption can be acceptable only under ideal material configurations such as situations with perfectly arranged granular media with statistical stationary conditions.

There have been numerous studies carried out to understand the non-homogeneous global responses observed on triaxial tests results. Studies have been done on the effect of the specimen's frictional ends (Carter, 1982; Drescher and Vardoulakis, 1982; Airey, 1991; Fourie,1991; Shanz and Gussmann, 1994; Sheng et al., 1997; Sidarta and Ghaboussi, 1998; Jeremić et al., 2004). Studies have also been done on the strain rate effect (Carter J.P, 1982; Airey, 1991; Sheng et al., 1997). All of these studies assumed spatial homogeneity in specimen material.

With the advent of imaging technology coupled with soil testing, it has been possible to measure local kinematic phenomena in addition to global characteristics (Desrues et

al., 1996; Finno et al., 1997; Rechenmacher and Finno, 2004; Desrues and Viggiani, 2004; Rechenmacher, 2006). These studies have found heterogeneous responses in apparently homogeneous specimens. Some recent efforts have successfully reproduced successfully local effects by incorporating random material parameters into soil simulations as a way to consider the inherent material variability (Andrade and Borja, 2006; Gudehus and Nubel, 2004). However, these investigations included simulation results that solved the 'forward problem' only. They did not incorporate local observations.

This chapter presents a set of analysis that includes the effect of material heterogeneity into the actual performance of the specimen by formulating four different numerical models (3D-FEMs), having special reference to the extent to which they are capable of reducing the predictive error. These four models involve 3D finite element representations including an increasing number of 'materials' containing particular groups or elements, allowing for more freedom in fitting the experimental data. This particular effect is referred as the (S) effect. Minimization results are presented by making vertical cross sections on each of the FEMs to visualize the optimal distributions of the 'material' parameters.

Once these models are built, the next step is to verify through a 'proof of concept' case that the 3D-FEM is actually capable of reproducing an elemental material composition given by the layered specimen test (120704c), comprised of a 'half loose' and 'half dense' segments (section 5.4). Once this is shown, the next step is to investigate the sensibility of the predictive model to assess the influence of information captured by the

use of 3D-DIC on each of the four FEMs by conducting a parametric analysis (section 5.5) on one particular test (100103b), where the control parameters are the initial 3D sample geometry (G), the compliance effect (C), and the material spatial variability (S). As mentioned above, initially, the parametric study focuses only on the linear elastic range to illustrate the applicability of the calibration methodology. Subsequently, the same calibration procedure is applied to each of the remaining tests included in the experimental database (section 5.6). This means that for each of these tests, initial and boundary conditions are adjusted in the corresponding FEMs according to the observations captured by 3D-DIC. After the same calibration process is applied for each test, results are analyzed so that the spatial statistics of the constitutive parameters can be obtained from the parameter vertical cross sections. This provides the uncertainty measures about the materials local spatial variability and a measure of the global correlation structure. Most importantly, it also provides a measure of the predictive model performance given by the independently optimized solutions. These statistical inferences set the basis for the understanding of the local variability of the materials and the influence it has on the model performance. In this way, a rational approach is developed for the definition of the assumptions required for both the prior and likelihood respectively (see chapter 2).

5.2. Predictive Model: 3D-Finite Element Modeling

Four 3D-FEMs with spatially varying parameters are developed to simulate the triaxial testing conditions defined in the experimental database. The first is the homogeneous model (Hom) with only one 'material' uniformly distributed within the specimen (Figure

5.1). The second is the Axisymmetric model (Axi) with five vertical layers and three horizontal concentric layers including as many as 15 materials (Figure 5.2). The third is the Heterogeneous model I (Het-I) with five vertical layers and three concentric layers split vertically in two sections allowing for up to 25 materials (Figure 5.3). The fourth is the Heterogeneous model II (Het-II) including 50 materials allowing for material variations in all three spatial directions, with five vertical layers and three concentric layers comprised of one circular segment (core), three 120-degree segments (middle radial layer), and six 60-degree segments (outer radial layer) (Figure 5.4). Each of the four 3D-FEMs included 1296 eight-node solid iso-parametric elements integrated implicitly with respect to time. The solver used for the triaxial testing simulations was LS-DYNA (Hallquist, 1998).

The three factors considered in the parametric study are the compliance effect (C), the initial geometry (G), and the level of permitted material spatial variability (S). For consistency and computational manageability, the same FEM configuration was used throughout the parametric analysis.

As mentioned above, the initial geometry (Section 4.6) and the compliance effect (Section 4.7) are obtained from the imaging analyses. The initial geometry (G) is introduced into the models by accommodating the shape of the model to the vertical profile of the radius. The compliance effect (C) is introduced into the models as a prescribed vertical motion induced by the top porous stone. The level of heterogeneity (S) is introduced into the model according to the prescribed 'material' variability. In addition, two types of solicitations are included in the models. The first is the isotropic

compression (I), which is introduced into the model as a uniform normal pressure applied all around the soil specimen. The second is the shearing loading (L), which is applied as a uniformly distributed upward pressure underneath the bottom porous stone according to the data recovered from the actual test. The top and bottom porous stones are modeled as rigid bodies. They are restrained for any motion on the horizontal direction (x - z plane), and fixed to the soil through contiguous elements showing the same nodes. This is done in order to reproduce the effect of frictional ends.

5.3. Deterministic Solution to the Inverse Problem

Experimental displacement fields $u(x,y,z,t)$, $v(x,y,z,t)$ and $w(x,y,z,t)$, where t is the time at which images were taken, are all assimilated into the deterministic inverse problem solution. While the DIC-measured fields have tens of thousands displacement data points, the finite element model can typically only predict nodal displacements at a few dozen locations. To address this disparity, it is necessary to take local averages of each displacement field over net areas centered at the n finite element nodes that lie within the area of interest over the specimen surface captured by the 3D-DIC. The averaging allows for matching observations and predictions, by including fields $u_{avg}(x,y,z,t)$, $v_{avg}(x,y,z,t)$ and $w_{avg}(x,y,z,t)$ into the vector of observations $\mathbf{d}_{obs}$ for each time t. These are then compared with the vectors of predictions $\mathbf{d}_{pred}$ given by the 3D-FEMs.

To illustrate the averaging pre-processing step, Figure 5.5 shows field v at 0.2 % of axial strain (t = 60 sec) as captured by 3D-DIC, and traced over the deformed specimen,

66

with the corresponding averaged displacements v_{avg}. The same process is applied for all three fields at times $t = 15, 30, 45$ and 60 sec.

The deterministic solution to the inverse problem described above is implemented based on the LSE approach (section 2.3.1.), with weighting factors $\Gamma_k=1$ and $W_k=1$. This approach estimates a vector of constitutive parameters $\hat{\boldsymbol{\theta}} = \{\theta_i(x,y,z)\}$, with i number of spatially distributed materials so that it can minimize an objective function of the form:

$$h(\boldsymbol{\theta}) = h(L) = \sqrt{\sum_{k=1}^{K} \left\{ (L)^T (L) \right\}_k} =$$
$$\sqrt{\sum_{k=1}^{K} \left\{ (\mathbf{d}_{pred} - \mathbf{d}_{obs})^T (\mathbf{d}_{pred} - \mathbf{d}_{obs}) \right\}_k} = \sqrt{\sum_{k=1}^{K} \left\{ (g(\hat{\boldsymbol{\theta}}) - \mathbf{d}_{obs})^T (g(\hat{\boldsymbol{\theta}}) - \mathbf{d}_{obs}) \right\}_k}$$

(5.1)

where $L(d_{pred}, d_{obs}) = |\mathbf{d}_{pred} - \mathbf{d}_{obs}|$ is a loss function, $\mathbf{d}_{pred} = g(\hat{\boldsymbol{\theta}})$ is one realization of the forward problem in the form of a vector of displacement predictions that are calculated at the same points in space and time as the observations $\mathbf{d}_{obs}$, and K is the number of stages of deformation where the images are taken.

The optimization tool used to minimize $h(L)$ is LS-OPT (Stander et al., 2003). This tool is based on the response surface methodology (Myers and Montgomery, 2002) and on the leap-frog algorithm (Snyman, 2000). A linear Koshal experimental design and a linear hyper-surface are chosen as design and fitting surfaces respectively for each one of the optimizations performed on the tests included in the experimental database.

5.4. Proof of Concept: Layered Specimen (120704c)

Before turning to a discussion of model performance, this section looks at the capability of the predictive models to reproduce a prescribed elemental heterogeneous condition. This section discusses the case where observations corresponding to the layered specimen test 120704c are incorporated into the deterministic solution to the inverse problem through the optimal solution.

Two different densities were introduced on the sample as a way to investigate the predictive model sensitivity to capture materials differences. The expected responses associated to different compacted materials are higher deformations for loose materials and lower deformations for stiffer materials. The lower segment was compacted with a relative density of 98.87 % and the upper segment reached a relative density of 30.54 % just by placing the sand grains manually into the mold at zero height. The boundary between both segments was located approximately at the mid height of the specimen (78 mm).

The density clearly showed an impact on the material response. For instance, when the layered specimen test is compared with a typical test considered for the probabilistic calibration (test 100103b) two different responses are retrieved. This difference can be observed in Figure 5.6, which shows the averaged vertical full-field displacement v_{avg} with respect to the specimen normalized height y_{norm} for both tests. Results from the layered specimen test shows a significantly higher deformation rate on the upper segment

and a stiffer response on the lower one. Test 100103b shows clear evidence of the layers transition approximately at the thirds of the specimen height.

Predictive model Het-I along with the linear elastic constitutive model provided the optimal solution for the deterministic calibration of the layered specimen case. The parameters allowed to vary during the minimization process were Young's modulus and the density. The initial guess of the $\boldsymbol{\theta}$ components were obtained from the secant estimate of Young's modulus computed from the global stress-strain curves and adjusted to account for the top platen vertical displacement measured by 3D-DIC (E = 31.88 MPa). The initial guess of the $\boldsymbol{\rho}$ components were obtained during the sample preparation and were pre-assigned to the bottom and top sections of the 3D-FEM as the actual test (ρ_{bottom} = 1,734.17 kg/m^3 and ρ_{top} = 1,549.61 kg/m^3), with the mid 'materials' row taking on the average of both segments. The Poisson ratio was held constant and considered to be equal to 0.2.

Results of the deterministic calibration are presented in Figures 5.7 and 5.8. These figures show the optimal spatial distribution of the density and the Young's modulus respectively. The density values were consistent with the experimental measurements with some local variation. The Young's moduli on the other hand showed a clear uniform behavior at the bottom of the specimen where the highest E values are located, while the lowest E values were found in the upper segment with significant higher variability. It should be noted that the average of the upper segment $E = 29$ MPa is close to the overall Young's modulus of the specimen ($E = 32$ MPa).

In summary, results from this layered specimen case indicate the following. First, two distinctive 'materials' appear to be present. Second, the proximity of the parameter estimates on the upper sections to the overall response of the specimen supports the relevance of studying the impact of material heterogeneity in order to improve the calibration of constitutive models. It can be concluded from these results, that this model is able to capture the order of magnitude of the experimental evidence. And it is also able to provide new insight into the influence of material heterogeneity. Based on these conclusions, the next section introduces a parametric analysis that further investigates the influence of some of the factors that are considered most relevant in the predictive models.

5.5. Parametric Analysis

Test 100103b is chosen as the benchmark case to study the influence of control parameters (C), (G), and (S) on the modeling of the triaxial test as an attempt to select the most adequate predictive model for the probabilistic calibration. For the parametric study on (S), only the Young's modulus is allowed to vary during the optimization process. Therefore, θ is defined as a vector of Young's moduli with 1, 15, 25 and 50 'materials' corresponding to models Hom, Axi, Het-I and Het-II respectively. As in the case of the layered specimen test, the initial values of θ are the secant values of Young's modulus obtained from the global stress-strain curves and adjusted to account for the top platen vertical displacement measured by 3D-DIC. For test 100103b the initial guess is 66.8 MPa. To simplify the computational burden during the minimization process due to the increasing number of parameters included in the different models, the Poisson ratio and

70

the density are taken as constants. The value of Poisson ratio was assumed to be equal to

0.2 and the density equal to 1,717.13 kg/m^3 as calculated during the sample preparation

(see Table 4.1).

Figure 5.9 summarizes the results of the parametric study for six different

configurations on the triaxial modeling simulation used for the solution of the

deterministic inverse problem. This figure shows the value of the objective function

versus the iteration count of the optimization process. Three groups of curves can be

identified. The first group, consisting of the two curves labeled (Hom,G,NC) and

(Hom,G,C) represents a comparative analysis where the compliance effect is (C) and is

not (NC) included in the Homogeneous model Hom. These results suggest a much lower

objective function and thus better model performance when the compliance effect is

included. This highlights the need to properly account for apparatus compliance and/or

bedding error in modeling the triaxial test. The second set represents a comparative

analysis between two axisymmetric models. One includes the sample's geometry (G)

and the other assumes the initial specimen shape to be a straight cylinder (NG). The two

curves associated with this case are labeled (Axi,G,C) and (Axi,NG,C). As in the

previous case, the initial configurations are different and the objective functions start at

different residual levels. Although the final value of the objective function is nearly the

same in both cases, in the case where (G) is included, it is achieved with significantly

fewer iterations in the optimization loop. This gain in computational efficiency is likely

to be critical for the calibration of more robust soil material models that feature either a

finer finite element mesh or more complex constitutive laws. The third set of curves

71

compares the effect of the spatial variability of the materials (S) by looking at the performance of all four 3D-FEM models when both the geometry (G) and the compliance effect (C) are included. The corresponding curves are labeled (Hom,G,C), (Axi,G,C), (Het-I,G,C) and (Het-II,G,C). While enabling axisymmetric material variation does not substantially improve the performance over that of a homogeneous model, a measurable gain in performance is observed when heterogeneity is enabled in Het-I and Het-II. It should be noted that while the computational effort to calibrate model Het-II with 50 materials was approximately 20 times more than for Het-I, the corresponding gain in overall performance was minimal. Breaking the symmetry (from model Axi to Het-I) seemed to have the most significant impact on response prediction, as measured by the highest change in magnitude of the objective function. This suggests that the greater the freedom of the model in terms of material variability, the better performance with respect to the actual observations.

Figure 5.10 shows the full-field displacements u, v and w corresponding to test 100103b at 0.2 % of axial strain, while Figures 5.11, 5.12, 5.13 and 5.14, show the corresponding predicted displacement obtained from each of the four 3D-FEM models described above. By comparing these figures with the actual observations (Figure 5.10), qualitative agreement is observed for the vertical displacements v for all cases, but not for the horizontal displacements u and w. The compliance effect is clearly reproduced since the vertical displacements observed at the top depart from zero as observed in the actual measurements. Qualitative improvement on the u displacement performance is observed with the Het-I model. A slight gain in model performance is observed for the w

displacement using the Het-II model, as can be verified by calculating the net error between both displacement fields.

The deterministic solution to the inverse problem for models Hom, Axi and Het-I is presented in Figure 5.15 in the form of vertical cross-sections of optimized Young's moduli E. The Hom model shows an expected flat distribution with a uniform value of 73.28 MPa. The Axi and Het-I models show a trend in the spatial material distribution with higher spatial variability on the latter. In the case of model Axi, Young's modulus varies from 48 to 88 MPa (mean 71.85 MPa, standard deviation 13 MPa), while model Het-I varies from 25 to 108 MPa (mean 77.4 MPa, standard deviation 27.2 MPa). In both models, higher values of Young's modulus are concentrated in the middle lower section while lower values are concentrated at the boundaries.

One possible explanation for the overall optimal response observed on the vertical cross sections of Young's moduli, is the linear association between stress and strains within the body of the specimen. With higher strained elements close to the specimen boundaries and lower strained elements at its center, it is expected that lower values of Young's modulus would be concentrated at the boundaries and higher values at the center. The increased variability around the edges could also be associated with the difficulty in controlling compaction in those areas during sample preparation.

In addition, optimal distributions show local variability particularly when the horizontal symmetry is broken as is the case of models Het-I and Het-II. This may be an indicator of material heterogeneity. The non-symmetries observed between the optimal

73

responses at the top and bottom rows can be associated with different deformation processes. For instance, the local deformation at the top is significantly influenced by the deformation rate of the compliance effect (non-linear), while the local deformation at the bottom is practically controlled by the load application rate (linear). But even in these particular regions, local variations are observed that might also be associated with material heterogeneities.

A 3D smooth description of the optimal calibration corresponding to model Het-II is presented in Figure 5.16. This is obtained by linearly interpolating Young's moduli values contained on the two vertical cross sections indicated in Figure 5.4. Interpolation is performed to improve the understanding of the variability and continuity of the 'materials' distribution within the specimen body. Figure 5.16 shows vertical cross sections showing four different angles according to quadrants I through IV as indicated in Figure 5.4. Optimal values of E range between 17 MPa and 117 MPa (mean 77.58, standard deviation 25 MPa), showing statistics similar to the material distribution of model Het-I. A consistent general behavior is observed regarding the concentration of higher and lower E values compared to the Axi and Het-I models, showing a tendency for higher values to concentrate at the core of the specimen, and lower values at its boundaries. However, these observations also presented significant local material variability. This can be associated with the heterogeneous composition of the specimen.

Global strain-stress relationships also show good correspondence between observations and predictions as presented in Figure 5.17 for the assumed linear elastic range (0.0 % to 0.2 % of axial strain). This figure shows predictions generated by model

'Het II' based on the optimal distribution of Young's modulus shown in Figure 5.16 only for the linear elastic domain.

5.6. Performance of the Predictive Model

In order to measure the performance of the predictive models the same procedure used for the solution of the deterministic inverse problem is repeated on all specimens included in the database. In this way, spatial statistics can be computed by assembling the optimal solutions (vertical cross sections of Young's moduli), so that inferences about the influence of material heterogeneity can be formulated and a measure of the model performance can be estimated. For this purpose, the compliance effect (C), the actual initial specimen geometry (G) and the models Hom, Axi and Het-I representing different degrees of 'material' spatial variability (S) are considered in this section. Given the small improvement in performance and the significant computational burden associated with model Het-II, it is dropped from this analysis.

After obtaining the optimal distributions of Young's moduli for each of the thirteen tests, it is observed that the objective functions follow a consistent behavior as the one discussed for the third set of curves presented in Figure 5.9. This particular observation makes Model Het-I the best candidate for the soil modeling from the four models available. This is true both in terms of model performance and computational efficiency.

By normalizing the vertical cross sections of optimal Young's moduli with respect to the specimen radius, it is possible to investigate the materials spatial variability as prescribed in each FEM. Figures 5.18, 5.19 and 5.20 show the mean and standard

deviations corresponding to all optimal solutions for the predictive models Hom, Axi and Het-I respectively. From these figures, the following is observed. The Hom model has a constant value of 88.22 MPa. The mean of the Axi model ranges from 73 to 95 MPa, showing higher values on the middle lower section of the specimen and lower values at the boundaries. The Het-I model shows a similar behavior as the Axi model, with the mean ranging from 72 to 112 MPa, and with higher values on the middle lower section of the specimen, and lower values at the boundaries. This means that for each condition of spatial variability (S), consistent results were obtained with respect to the benchmark analysis discussed in the previous section.

Based on the same data ensemble of optimal E distributions, the same figures show the corresponding spatial distribution of the standard deviations for the three models. As expected, model Hom shows a constant standard deviation of 43.86 MPa; model Axi shows a variation from 29 to 50 MPa, with higher values of the specimen's boundaries (the highest is located at the bottom), and with lower values concentrated in the middle lower section; and model Het-I, shows a similar behavior as model Axi, with values ranging from 35 to 56 MPa, also with higher values at the specimen's boundaries (with the highest at the bottom), and with lower values in the middle lower section. The statistical consistency between models Axi and Het-I suggests that this material variability is an intrinsic property of the specimen and not an artifact of the selected model.

An additional investigation is performed to evaluate the spatial correlation structure of the material variability. This is done by evaluating the empirical correlation coefficient

76

between vectors of data located at the different cells identified on normalized vertical cross sections of the optimal solutions. Results show that the overall correlation values decrease as the number of materials increases. It ranges from values of 1.0 for the Hom model; to values between 0.7 and 1.0 for the Axi model; and to values between 0.4 and 1.0 for the Het-I model. The clouds of correlation coefficient points as traced over the lag distances of the normalized vertical cross section showed no trend as to fit a function, which limit the possibility of representing the material distribution as a stationary field.

A complementary consistency test is carried out by comparing the correlation between the spatial averages of the optimal Young's moduli, E_{inv} (average of optimal E values for each vertical cross section), to the globally estimated Young's moduli, E_{global} (adjusted secant value from global stress-strain curves), for the same optimal solutions discussed above. Figures 5.21, 5.22 and 5.23 show the corresponding plots of E_{inv} versus E_{glob} for the three selected models. The correlation coefficient for all three cases was 0.99, which denotes a strong linear relation between both variables. This can be interpreted as a good sign, since the overall estimate of the observations are consistent with the overall estimates of the predictions. Additionally, from comparing results from the three models, it can be deduced that E predictions across the three models are also consistent with the corresponding observations, which makes the predicting model independent from the global optimal solution.

It is worth noting that other factors may play a key role in the improvement of the triaxial modeling (and consequently in the constitutive model calibrations). Future analysis should consider the refinement of the mesh accordingly to the correlation length

77

of the constitutive parameters and to the concentration areas of stresses and strains; the incorporation of relative settlements of the platens during shearing, the effect of the membrane (compressive stress and restraining motion at failure), the adequate selection of the mesh size for the finite element model, the drainage and pore water pressure in the saturated case, and the implementation of more complex constitutive parameters.

Once Het-I is selected as the predictive model for the probabilistic calibration, the optimal solutions associated with it obtained from all tests included in the database, represent the basis for evaluating the predictive error given by the difference between its predictions and the corresponding observations. This error is a measure of the predictive model performance and a key step in the definition of the shape of the likelihood function since it allows for the evaluation of its random behavior. Figure 5.24 introduces the relative frequency histogram of the norm computed from the difference between observations and predictions of the three displacement fields at the four stages of deformations for all tests included in the database. The major assumption for the construction of this figure is to consider that the error estimates between observations and predictions are independent from each other, which is corroborated by the model construction and the nature of the experimental measurements. Following the trend of the error results it is proposed to use initially a Gaussian-type model for the likelihood function for the case study discussed on chapter 7. Further analysis regarding the predictive error is suggested particularly when confronted with the convergence of the posterior sampling during the application of the MCMC method.

6. Elements for the Bayesian Formulation

The probabilistic calibration is performed by incorporating physical evidence obtained from the coupling of triaxial testing and 3D imaging technology (chapter 4) into the solution of the inverse problem solved by the Bayesian paradigm (chapter 2). This includes the spatial representation of material properties using the PC method (chapter 3) as a generalized approach for the sampling of spatial non-Gaussian and non-stationary fields. Also, for the probabilistic calibration to be performed it is necessary to estimate specific statistics defined by the Functional Bayesian (FB) solution to the inverse problem. This chapter introduces the elements required for the Bayesian formulation, including the methods for their computation and a comprehensive analysis of their relation to the experimental observations and numerical predictions. In particular, these elements consist of the statistical inferences generated for the formulation of the likelihood and the prior, and for the algorithm for the integration of the posterior.

The elements for the Bayesian formulation are defined considering that the validation of the FB method is circumscribed to the linear elastic domain. Inferences about material properties and responses discussed in this chapter refer only to the Young's moduli, to the experimental observations included in the database and to the predictions generated by model Het-I. The spatial domain selected for the representation of the constitutive parameters and material displacements is the specimen normalized cross section presented in Figure 3.44. Furthermore, in view of the case study presented in the next chapter, where test 092903b is selected to illustrate the applicability of the calibration

method, some statistical inferences discussed in the following sections make specific reference to it.

6.1 Statistical Inferences from Observations and Predictions

The integration of the posterior via MCMC and M-H requires the assessment of the prior and the likelihood (section 2.4.). At the beginning of the MCMC iterations, some of their components need to be initialized based on different a-priori information sources, such as knowledge about the constitutive parameters (i.e. E cannot take negative values), and knowledge about the observations and predictions. Specifically, it is expected that the following will be estimated for the prior, the marginal pdfs $f(\theta(X)) = f(\theta(x_{norm}, y_{norm}))$, the covariance matrix of the parameters $\mathbf{C}_{\theta_{prior}(\mathbf{x})}$, and the corresponding chaos coefficients $\mathbf{u}(\mathbf{X})$. For the likelihood function, the covariance matrices of the observations $C_{\mathbf{d}_{obs}}$, and the covariance matrix of predictions $C_{\mathbf{d}_{pred}}$ will be estimated.

The better the estimates for each of these components the faster the convergence to the MCMC sampling stationary condition. As long as the predictive model (3D-FEM) produces accurate simulations with an error consistent with the prescribed shape of the likelihood, there is still convergence to the sampling stationary condition. This is the case even if the initial guesses for each component are poorly assessed.

6.1.1. Marginal Probability Density Function of the Constitutive Parameters

The global Young's modulus E is computed for the prescribed domain of analysis using a linear regression fit (secant) to the global adjusted stress-strain data. The cdf of

the resulting E estimates is shown in Figure 6.1. This figure shows that although all thirteen tests were nominally similar, significant scatter is present in the stress-strain behavior. This is true even at early stages of deformation, which implies the presence of random responses in the observations at the global level. The mean and standard deviation of the E estimates are 82.55 MPa and 44.15 MPa respectively.

The first statistical inference used for the prior definition arises from the empirical cdf estimate of the Young's moduli. By fitting a Gaussian and a log-normal model to the cdf of the E estimates, the model that shows better agreement with the global observations is the latter (Figure 6.1). This means that the log-normal model is an adequate representation of what is known a-priori about the global variability of the constitutive parameter E.

Based on this finding, the log-normal model is used to sample the marginal pdfs of the 'materials' $\boldsymbol{\theta}(\mathbf{X})$ associated with test 092903b, using a mean equal to the test E global estimate 92.33 MPa, and with standard deviation computed from the E estimates of the experimental database but without including the estimate of test 092903b (to avoid spurious inferences). The standard deviation of the twelve remaining tests has a value of 45.98 MPa. Both the log-normal pdfs of the experimental series and of the test 092903b are presented in Figure 6.2. The prior is defined by assuming that the field $\boldsymbol{\theta}(\mathbf{X})$ is stationary, with vector elements of $\boldsymbol{\theta}_{prior}(\mathbf{X})$ having a constant value of 92.33 MPa for each 'material', corresponding to the actual E value of test 0929093b. The marginal pdfs $f(\theta(X))$ are all the same at the beginning of the MCMC sampling. These assumptions

mean that the vector of random chaos coefficients $\mathbf{u}_j$ used to fit the log-normal marginal pdfs should also all be the same at step $s = 0$ of the MCMC sampling. A change of the shapes and positions of the initial marginal pdfs are expected as the MCMC sampling progresses.

6.1.2. Covariance Matrix of the Constitutive Parameters

The a-priori knowledge about the correlation structure of the 'materials' is limited since there is no evidence regarding the spatial variability of the constitutive parameters. However, by the definition of the covariance, one approach for estimating $\mathbf{C}_{\boldsymbol{\theta}_{prior}(\mathbf{X})}$ is by multiplying the corresponding local variances times the proper correlation function value, defined as a function of the lag distances between the spatial references of the 'material' parameters. From the assumption made about the $\boldsymbol{\theta}(\mathbf{X})$ marginal pdfs at step $s = 0$ of the MCMC sampling, the E local variance is assumed to be the same for all 'materials'. The correlation function on the other hand is assumed to follow a simple form as a starting point, such as the isotropic correlation function $\rho_{\boldsymbol{\theta}(\mathbf{X})} = e^{-\frac{1}{\delta}\tau_{\mathbf{X}}}$, where δ is the correlation length parameter and $\tau_{\mathbf{X}}$ represents the lag distance between the positions of any two 'materials' located over the normalized vertical cross section.

In order to explore possible correlation configurations, Figure 6.3 presents the behavior of the isotropic correlation function for four possible values of δ. The findings on this figure indicate that the correlation parameter should be around $\delta = 0.5$ based on the extents of variability within the normalized domain (from -1 to 1 on the x_{norm}

82

direction, and from -2.25 to 2.25 on the y_{norm} direction). The graphical representation of the synthesized covariance matrix $\mathbf{C}_{\boldsymbol{\theta}_{prior}(\mathbf{X})}$ is presented in Figure 3.47 as part of the benchmark case III (section 3.4.).

The full description of the random field $\boldsymbol{\theta}(\mathbf{X})$ is defined by the chaos expansion introduced by $\theta(u(X),\xi)$ as defined in equation 3.7. Hence, by evaluating the chaos coefficients $u_n(x_{norm}, y_{norm})$ and sampling the standard Gaussian variables $\{\xi\}$, realizations of $\boldsymbol{\theta}(\mathbf{X})$ are retrieved one at a time. The computation of the chaos coefficients requires the evaluation of the eigen-quantities λ_k and f_k obtained from the correlation function $\rho_{\boldsymbol{\theta}(\mathbf{X})}$. It also requires the evaluation of the coefficients $U_p(x_{norm}, y_{norm})$ obtained from the marginal pdfs $f(\theta(X))$ as indicated by equation 3.2.

Considering the assumptions for the prior definition discussed in the previous section (stationary log-normal marginal pdfs with mean 92.33 MPa, standard deviation 45.98 MPa, and isotropic correlation function with correlation parameter $\delta = 0.5$), it is possible to compute the eigenvalues and the corresponding eigenfunctions, as well as the Fourier type coefficients $\mathbf{U}(\mathbf{X})$ required for the assessment of the chaos coefficients $\mathbf{u}(\mathbf{X})$, as indicated by equation 3.8. Convergence for the assessment of the $\mathbf{U}(\mathbf{X})$ coefficients was achieved after taking 20,000 samples, as in the benchmark cases introduced in chapter 3. For the PC representation of the parameter field $\boldsymbol{\theta}(\mathbf{X})$, it is assumed that a third order four- dimensional Hermite polynomial is adequate for reproducing the field's prior conditions (section 3.4). Results of the eigenvalues were presented in Figure 3.49, while

Figures 3.50, 3.51 and 3.52 presented only the first three eigenfunctions as a way to illustrate their order of magnitude and general trends.

With the assessment of the eigen-quantities and the $\mathbf{U(X)}$ coefficients, the chaos coefficients $\mathbf{u(X)}$ can then be calculated. A projection of their first five terms over the normalized vertical cross section was shown in Figure 3.53. This figure corroborates that the first coefficient (top surface) is associated with the mean values of the $\mathbf{\theta(X)}$ field. It shows that influence on the other expansion terms is significant. This is observed on a typical realization of $\mathbf{\theta(X)}$ presented in Figure 3.57.

In order to assess random measures of the estimates of the chaos coefficients to be included as part of the MCMC sampling, the correlation length parameter δ is considered a random variable. This means that the estimate of the specimen correlation structure is also random, enhancing the sampling of $\mathbf{\theta(X)}$ by allowing for more spatial correlation patterns. Based on the exploratory analysis made in Figure 6.3, δ is assumed to follow a log-normal behavior with mean 0.5 and standard deviation of 2.0, as shown in the pdf model presented in Figure 6.4. The assessment of the chaos coefficients follows the same procedure described above for different sampling values of δ until their numerical convergence is achieved. The resulting distributions of the mean $\mathbf{\bar{u}} = E[\mathbf{u(X,}\delta)]$ and standard deviation $\mathbf{\sigma_u} = \sqrt{Var[\mathbf{u(X,}\delta)]}$ are presented in Figures 6.5 and 6.6.

6.1.3. Covariance Matrix of the Observations

The covariance matrix of the observations $C_{\mathbf{d}_{obs}}$ reflects the uncertainty associated with the actual response of the specimen, which might be related with different sources, such as the inherent variability of the material, the variability of the measuring devices, the variability induced by the operator, or by a combination of these. $C_{\mathbf{d}_{obs}}$ is estimated based on the spatio-temporal data contained within the linear elastic domain. This means that four displacement fields are included into the calibration that corresponds to the stereo digital images taken at $\varepsilon_a = 0.05$ %, $\varepsilon_a = 0.10$ %, $\varepsilon_a = 0.15$ % and $\varepsilon_a = 0.20$ %. As discussed above (section 5.3), experimental displacement fields $u(x,y,z,t)$, $v(x,y,z,t)$ and $w(x,y,z,t)$, measured by 3D- DIC are synthesized into local averages $u_{avg}(x,y,z,t)$, $v_{avg}(x,y,z,t)$ and $w_{avg}(x,y,z,t)$ (Figure 5.5), so that they can be included in the vector of observations $\mathbf{d}_{obs}$.

6.1.3.1. Spatio-Temporal Data Assembling

After carrying out the averaging process, the spatio-temporal data is pre-assembled and projected over the normalized vertical cross section to facilitate the computation of statistical inferences. To illustrate the variability of the observations and the presence of local non-homogeneous effects, Figures 6.7, 6.8 and 6.9 present displacement fields of all tests captured at each stage of deformation for the u, v and w fields respectively. From the data ensembles, the following is observed. The u_{avg} displacement process oscillates between -0.0630 mm and 0.0487 mm. The v_{avg} displacement process oscillates between 0 mm and 0.3148 mm. And the w_{avg} displacement process oscillates between -0.1496

mm and 0.0545 mm. From these figures, it is also observed that the local variability of all displacement processes increases as the tests evolve, identifying qualitatively significant variability increases for the three displacement process, particularly on the upper segment of the samples for the u_{avg} and v_{avg} processes. Since the testing configurations were the same for all tests, it is thought that material heterogeneity is one of the main sources of the local variability. However, in order to reach some conclusions about the patterns of deformation, it is necessary to perform the data 4D statistical computations as discussed below.

The next step in the data assimilation is to assemble the data points making them coincide in the averaged coordinates of the clustered data defined as the spatio-temporal grid (x_{norm}, y_{norm}, t). In fact, measured data points coincide in their time coordinate since images from different tests were taken at the same times, but they do not coincide in their spatial coordinates due to differences in sample geometry. This mismatch can be seen in Figure 6.10a. This figure presents a projection of the data coordinates over the normalized vertical cross section. A zoom into a random selection of these points shows the disparity of the data spatial positions. This figure also shows that the observations are not the same for all tests. Some experiments have more data than others, showing that the area covered by each test is different due to slight differences in the positions of the cameras every time a test was performed. The resulting area of observations common to all tests is a reduced segment over the sample's spatial domain. The final overlapping segment in terms of number of observations can be assessed by constructing a spatial histogram projected over the sample surface as shown in Figure 6.10b. Based on this

86

layout and trying to incorporate as much information as possible into the statistical analysis, it is proposed to increase the domain of observations on those tests which points did not exceed six counts (approximately half of the maximum observations) by doing data extrapolation, which is performed using third order linear interpolation. Once data extrapolation is performed, data clusters must be interpolated at the mean coordinate positions only for those containing the maximum counts of data. Interpolation is performed using the 'griddata' function of Matlab (Mathworks, 2003). A typical case of extrapolation and interpolation is illustrated in Figure 6.11, corresponding to the $\mathbf{v}_{avg}$ field at 0.20 % of axial strain for test 100103b.This figure demonstrates that extrapolated data points are in good agreement with the local and global trend of the measured data. Similar behavior is observed for the other displacement process. Figure 6.11 also shows that interpolated data points practically overlap with actual observations (a zoom into these points would show the exact location of each point). Finally, the spatio-temporal data ensemble of each displacement field is integrated by coupling the extrapolated and interpolated data points in the same spatio-temporal coordinates (x_{norm}, y_{norm}, t).

Once the observations are properly assembled, empirical spatio-temporal statistics including the mean, standard deviation and the structural correlation analyses required for the assessment of the $C_{\mathbf{d}_{obs}}$ matrices can be estimated. The mean and standard deviations at each stage of deformation for displacement fields $\boldsymbol{u}$, $\boldsymbol{v}$ and $\boldsymbol{w}$ are presented in Figures 6.12, 6.13 and 6.14 respectively; while their corresponding correlations are introduced in

Figures 6.15, 6.16, 6.17 (see table 6.1). A brief description of each follows in the next two sections.

6.1.3.2. First Order Marginal Statistics

The $u_{avg}(x_{norm}, y_{norm}, t)$ mean surface (Figure 6.12, left column) shows a good approximation of the expected pattern of deformation (as if it was a uniform sample), with a simultaneous gradual increase in the positive and in the negative values, which means the presence of uniform deformations on the right and left sides of the specimen respectively.

The mean surface shows values ranging between $\pm$ 0.01 mm at 0.2 % of axial strain. Its corresponding standard deviation (Figure 6.12, right column) shows a monotonic increase, uniformly distributed on the horizontal direction starting at the samples vertical center line, for all deformation stages, and initially uniform at the bottom of the specimen on the vertical direction, having a significant increase on the upper segment of the specimen after the 0.15 % of axial strain. The maximum standard deviation value observed was 0.03 mm at 0.2 % of axial strain.

The $v_{avg}(x_{norm}, y_{norm}, t)$ mean surface (Figure 6.13, left column) shows a uniform monotonic increase for all data points, with uniform deformation in the horizontal direction, and an approximate linear increase in the vertical direction, with higher values at the bottom, and lower values at the top. The maximum mean values are 0.29 mm at the bottom and 0.12 mm at the top. Its standard deviation (Figure 6.13, right columns) shows a clear increment from the bottom to the top of the specimen at all stages of deformation,

with approximately uniform values on the horizontal direction. Local maximums are observed at the thirds of the vertical domain at 0.20 % of axial strain. The maximum standard deviation value observed was 0.029 mm.

The $w_{avg}(x_{norm}, y_{norm}, t)$ mean surface (Figure 6.14, left column) shows a particular 'rigid body' type deformation pattern for all stages of deformation, representing a slight uniform displacement inwards the specimens. A significant deformation increment of approximately -0.02 mm is observed only from the undeformed state to 0.05 % of axial strain. Later stages of deformation show lower deformation increments, of approximately -0.028 mm, -0.032 mm and -0.035 mm for 0.10%, 0.15% and 0.20% of axial strain respectively. The standard deviation (Figure 6.13 right column) shows a relatively uniform distribution at 0.05% of axial strain.   The standard deviation also shows a gradual increment on the upper segment of the specimen for later deformation stages, reaching a maximum value of 0.06 mm.

Based on the means and standard deviations of the three displacement processes, it can be inferred that observations are more uniform from the bottom to the top of the specimen.   This suggests some possible dependence on the compaction variability, the compliance effect (C) absorbed at the top of the specimen, and other local displacements like the seating effect of the top porous stone. An important observation regarding the samples compaction is that the local variability observed on the vertical displacement process $v_{avg}(x_{norm}, y_{norm}, t)$ also seems to be an indicator of the effect of the layering. This indicates local changes in the standard deviation at the thirds of the specimen's height, corresponding to the positions of the layers' boundaries. The $w_{avg}(x_{norm}, y_{norm}, t)$

deformation process shows the highest global and relative standard deviations with respect to the other two processes. And the pattern of deformation may represent a compensation effect of horizontal rigid-type displacement on the z direction. Also, a comparison between the horizontal maximum displacements (absolute) with respect to the vertical displacement shows ratios of the order of 3 % and 9 % for the $\boldsymbol{u_{avg}}(x_{norm}, y_{norm,} t)$ and $\boldsymbol{w_{avg}}(x_{norm}, y_{norm,} t)$ processes respectively. This corroborates the idea of major displacements in the z direction.

6.1.3.3. Second Order Correlation Statistics

A simple approach for the interpretation of the empirical evaluation of the correlation structure of each of the displacement processes is to assume that they represent random variables at the ith fixed point $(x_{norm,i}, y_{norm,i}, t_i)$. Therefore, it is proposed to estimate the correlation coefficient for each possible combination of random variables, with the addition of the tracking of their spatio-temporal references between data contained in any two points p_2 and p_1 reference in space-time. Hence, the empirical covariance computed for displacement process $\boldsymbol{u_{avg}}(x_{norm}, y_{norm,} t)$ is defined as:

$$C_u(p_2, p_1) = E\left[\left\{u_{avg}(p_2) - \bar{u}_{avg}(p_2)\right\}\left\{u_{avg}(p_1) - \bar{u}_{avg}(p_1)\right\}\right] =$$
$$\frac{\sum_{i=1}^{n}\left\{u_{avg\,i}(p_2) - \bar{u}_{avg}(p_2)\right\}\left\{u_{avg\,i}(p_1) - \bar{u}_{avg}(p_1)\right\}}{n-1} \qquad (6.1)$$

where,

n   represents the amount of data

u_{avg} represents the sample of the random field at point p_i

$$p_2 = \left(x_{norm,2}, y_{norm,2}, t_2\right)$$

$$p_1 = \left(x_{norm,1}, y_{norm,1}, t_1\right)$$

$\overline{u}_{avg}$ represents the sample mean at point p_i

and the empirical correlation coefficient is calculated as:

$$\rho_u\left(p_2, p_1\right) = \frac{C_u\left(p_2, p_1\right)}{\sigma_u\left(p_2\right)\sigma_u\left(p_1\right)} \qquad (6.2)$$

where $\sigma_u\left(p_i\right)$ represents the standard deviation of the sample taken at point i.

An ideal situation for the spatio-temporal representation of the covariance or the correlation coefficient, would be if a clear pattern can be identified when they are plotted with respect to the spatio-temporal lag distances $\tau_x = x_{norm,2} - x_{norm,1}$, $\tau_y = y_{norm,2} - y_{norm,1}$ and $\tau_t = t_2 - t_1$, so that a stationary function can be fitted with the capability to represent the covariance as $C_u\left(|p_2 - p_1|\right) = C_u\left(\tau_x, \tau_y, \tau_z\right)$, and the correlation coefficient as $\rho_u\left(|p_2 - p_1|\right) = \rho_u\left(\tau_x, \tau_y, \tau_z\right)$. If that is the case, significant simplifications are expected for the numerical simulation of the displacement process. Similar definitions are applied for the computation of the statistics of the v and w processes.

A simple way to represent all possible correlation combinations between same variables (same displacement fields) referenced at different points in space-time p_1 and p_2 is presented in Table 6.1. In this scheme, correlation combinations lying on the diagonal, represent the process autocorrelation with respect to time, such that $\tau_t = 0$, and $\tau_x \neq 0$

and $\tau_y \neq 0$. Cases off the diagonal are full cross correlations, since all lags are non-zero. For simplification only graphics showing the correlation coefficients projected on the spatial lags domain are discussed here.

A first representation of the empirical correlation structure is the plot of correlation coefficients for all possible spatial combinations where $\tau_x \neq 0$ and $\tau_y \neq 0$, for different time lags τ_t. This particular representation shows clouds of points of correlation coefficient values traced over the spatial lag domain. Figures 6.15, 6.16 and 6.17 introduce the empirical correlation structure of the $u_{avg}(x_{norm}, y_{norm}, t)$, $v_{avg}(x_{norm}, y_{norm}, t)$ and $w_{avg}(x_{norm}, y_{norm}, t)$ processes respectively. As an attempt to capture the spatio-temporal correlation structure of each displacement process in a 3D plot, a 4D curve fitting all correlation combinations is prepared using a multivariate third order linear regression model. Figures 6.18, 6.19 and 6.20 show these particular smooth representations corresponding to each of the displacement process.

The representations of the empirical correlations for the three displacement processes (Figures 6.15-5.17) show that in general, it is possible to fit a smooth curve through the clouds of correlation points of each correlation combination. The shapes and the order of magnitude of the correlation clouds vary across displacement processes but they follow a characteristic pattern. For the $u_{avg}(x_{norm}, y_{norm}, t)$ and $w_{avg}(x_{norm}, y_{norm}, t)$ processes, the clouds of correlation points follow an inverted hyperbolic shape with order of magnitude varying between 0.65 and 1.0 and 0.2 to 1.0 respectively. For the $v_{avg}(x_{norm}, y_{norm}, t)$ process, it follows an inverted 'v' shape with order of magnitude varying between -0.2

92

and 1.0. These orders of magnitude imply that the relative degree of predictability between any two variables included in $v_{avg}(x_{norm}, y_{norm}, t)$ is significantly lower than that in the other two processes.

In terms of the local variability observed in the clouds of correlation coefficients, processes $u_{avg}(x_{norm}, y_{norm}, t)$ and $w_{avg}(x_{norm}, y_{norm}, t)$ present significantly less variability than the $v_{avg}(x_{norm}, y_{norm}, t)$ process. They also show an approximately constant behavior along the τ_x direction, whereas the $v_{avg}(x_{norm}, y_{norm}, t)$ process shows a slightly curved trend. The constant trend in the horizontal direction can be interpreted as the data degree of variability associated with relative changes of lag positions in the τ_x direction.

One feature common to all correlation representations is the symmetry in the shape of the clouds of correlation points for the time lags $\tau_t = 0$ (which follows the autocorrelation definition on the space domain). This effect can be observed in the figures located on the diagonal of the graphics matrix of each displacement process (Figures 6.15, 6.16 and 6.17). For different deformation stages, though, when $\tau_t = 0$, the clouds of correlation coefficients are slightly different, tending to show an overall decrement associated with the effect of non-homogeneity as the specimens experience some distortion from one deformation stage to another.

An interesting feature observed off the diagonal of the graphic matrices for the $u_{avg}(x_{norm}, y_{norm}, t)$ and $w_{avg}(x_{norm}, y_{norm}, t)$ processes, is the non-symmetric behavior of the correlation trends when comparing data at different stages of deformation. This effect

93

suggests that it is not the same to compare data sets from $(x_{norm,1}, y_{norm,1}, t_1)$ to $(x_{norm,2}, y_{norm,2}, t_2)$ and from $(x_{norm,1}, y_{norm,1}, t_2)$ to $(x_{norm,2}, y_{norm,2}, t_1)$.

Finally Figures 6.18, 6.19 and 6.20 show smooth approximations that fit the correlation structures of each displacement process based on multivariate third order linear regressions. By confronting the observations made previously for each displacement process, it can be concluded that they show good agreement with each of the correlation structures. This means that they can be used to estimate the spatio-temporal correlation value for those points not included in the empirical estimates.

6.1.3.4. Computation of the Covariance Matrix of the Observations

The estimate of the covariance matrix of the observations $C_{\mathbf{d}_{obs}}$ is based on the definition of the correlation coefficient. Couples of local variances and the corresponding correlation values are multiplied for all possible combinations of spatio-temporal data points. In this case, the value of the local variances is taken from the first order statistics calculated from the data ensembles (section 6.1.3.2). The correlation value is estimated from the smooth representations of the correlation functions presented in Figures 6.18 – 6.20.

Estimates of the covariance matrix $C_{\mathbf{d}_{obs}}$ for displacement fields $\mathbf{u}_{avg}$, $\mathbf{v}_{avg}$ and $\mathbf{w}_{avg}$ are shown in Figures 6.21, 6.22 and 6.23 respectively. From these figures it is possible to identify the arrangement of 4 x 4 combinations of covariance blocks corresponding to the four stages of deformation included in the analysis. The covariance matrix is constructed

94

estimating the covariance between two displacement variables d_{obs} located at different points in space and time. According to the data ensemble, there are 46 data points at each stage of deformation x 4 stages of deformation = 184 spatio-temporal data points (or number of d_{obs} variables). This means that a total combination of 33,856 covariance estimates is included in each covariance matrix. The arrangement of variables d_{obs} in the covariance matrices follow the coordinates of the data ensemble as projected on the normalized vertical cross section, counted row by row from the bottom left to the top right data points.

6.1.3.5. Computation of the Covariance Matrix of the Predictions

The covariance matrix of the predictions $C_{\mathbf{d}_{pred}}$ reflects the uncertainty associated with the response of the mechanistic model. This can be interpreted as the sensitivity of the model to changes induced by the uncertainty introduced by the constitutive parameters. The covariance matrix of the predictions is computed by sampling realizations $\theta(\mathbf{X})$ of the constitutive parameter E from the prior. These are then plugged into the predictive model $g(\theta(\mathbf{X}))$ to obtain the estimates of the predictions $\mathbf{d}_{pred}$. And finally the synthesized covariance for the spatio-temporal data is captured on the same set of points used to estimate the covariance matrix of the observations. It is worth noting that the sampling of $\theta(\mathbf{X})$ is performed by the PC technique under the assumptions of the prior discussed above, where the correlation length parameter was considered to be random. Figures 6.24, 6.25 and 6.26, present the estimates of the covariance matrices of the predictions corresponding to displacement fields u_{avg}, v_{avg} and w_{avg}. These figures show a

95

more uniform distribution of the covariance matrix for the horizontal displacements $\boldsymbol{u}_{\mathrm{avg}}$ and $\boldsymbol{w}_{\mathrm{avg}}$ compared to the covariance matrix of the observations. This is probably due to the non-random nature of the compliance effect (C). The order of magnitude for the covariance matrix of the vertical displacements $\boldsymbol{v}$ is higher than in the case of the covariance matrix of the observations. This means that it will be dominant when it is added up with the covariance matrix of the predictions for the formulation of the covariance matrix of the likelihood $\mathbf{C}_{\Delta\mathbf{d}}$ as defined in equation 2.16.

6.2. Probabilistic Calibration Algorithm

The following algorithm is applied to the solution of the probabilistic calibration of one test at a time, based on the uncertainty quantification of the observations (specimen responses) captured on the series of experiments included in the database, and the predictions computed from the prior conditions. Once it is assumed that the initial prior configuration follows a log-normal behavior (section 6.1.1) and that the likelihood function follows a Gaussian behavior (section 5.6), the specific posterior definition is that introduced in equation 2.26. This means that the mean values for $\boldsymbol{\theta}^{*}_{prior}(\mathbf{X})$ correspond to the logarithm of the global estimate of the test constitutive parameter E. The mean values in the likelihood correspond to the vector of observations $\mathbf{d}_{obs}$ (averaged displacement fields). And the uncertainty components are those defined previously for the prior $\{ f(\theta(X_{j})),\ \rho_{\boldsymbol{\theta}(\mathbf{X})} \}$, and for the likelihood $\{ C_{\mathbf{d}_{obs}}, C_{\mathbf{d}_{pred}} \}$.

As discussed in section 2.4.7, the MCMC and M-H sampling techniques form the basis for the development of this particular algorithm. The objective of the proposed

96

algorithm is to sample a set of chaos coefficients $\mathbf{u}(\mathbf{X})$ at each step of the MCMC chain. The goal is to generate a full description of the material random field $\mathbf{\theta}(\mathbf{X})$, so that by evaluating their statistics the prior can be sampled, the 'materials' values can be introduced into the likelihood function, and a sample 'point' of the posterior can be estimated. The same process is repeated until the MCMC's sampling stationary condition is achieved. Achieving this condition means that the random mechanistic predictions are as close as possible to the actual observations within a rational probability measure.

The details of the proposed algorithm are given below:

i). Initialize the chain with $\mathbf{\theta}_0(\mathbf{X})$ at $s = 0$

    a. Define the marginal density functions of the materials

    b. Define the correlation structure of the materials

    c. Evaluate the eigen-quantities

    d. Define the appropriate order and dimension of the polynomial chaos approximation

    e. Evaluate the chaos coefficients $\{\mathbf{U}(\mathbf{X})\}_{s=0}$ of the one-dimensional polynomials

    f. Evaluate the chaos coefficients $\{\mathbf{u}(\mathbf{X})\}_{s=0}$ of the multidimensional polynomials

    g. Sample realizations of the material properties $\mathbf{\theta}_{s=0}$ according to the prior assumptions using the PC approximation

    h. Evaluate the covariance matrix of observations $C_{\mathbf{d}_{obs}}$

    i. Evaluate the covariance matrix of predictions $C_{\mathbf{d}_{pred}}$ assuming the correlation length parameter as random

97

j. Evaluate the covariance matrix of the error between observations and predictions $\mathbf{C}_{\Delta \mathbf{d}} = C_{\mathbf{d}_{pred}} + C_{\mathbf{d}_{obs}}$

k. Define the seed sample as $\hat{\boldsymbol{\theta}}_{s=0}(\mathbf{X}) = \boldsymbol{\theta}_{prior}(\mathbf{X})$

ii). Generate a candidate point $\mathbf{Y}$ from $q\left(\cdot \mid \boldsymbol{\theta}_s\left(\mathbf{u}_s(\mathbf{X}),\xi\right)\right)$

a. Assume that the pdfs of the chaos coefficients are Gaussian with mean $\mathbf{u}_s\left(x_{norm}, y_{norm}\right) = \mathbf{u}_{s-1}\left(x_{norm}, y_{norm}\right)$ and standard deviation $\sigma_{\mathbf{u}}$ as computed before when the correlation parameter δ was assumed to be random (Figure 6.6).

b. Sample the candidate point by defining a new field of chaos coefficients and populate the materials random field $\boldsymbol{\theta}_s\left(\mathbf{u}_s(\mathbf{X}),\xi\right)$.

c. Check that the populated random field of the materials satisfy their natural constrains (i.e. some parameters cannot assume negative values)

d. Compute the expected values of the populated random field of the 'materials', such that $\hat{\boldsymbol{\theta}}_s(\mathbf{X}) = E\left[\boldsymbol{\theta}_s\left(\mathbf{u}_s(\mathbf{X}),\xi\right)\right]$

iii). Generate U from a uniform (0,1) distribution

iv). If $U \le \alpha\left(\hat{\boldsymbol{\theta}}_s(\mathbf{X}),\mathbf{Y}\right)$ then set $\hat{\boldsymbol{\theta}}_{s+1}(\mathbf{X}) = \mathbf{Y}$, else set $\hat{\boldsymbol{\theta}}_{s+1}(\mathbf{X}) = \hat{\boldsymbol{\theta}}_s(\mathbf{X})$. This step implies that the forward problem should be solved for the candidate point $\mathbf{Y}$ and for the previous point $\hat{\boldsymbol{\theta}}_s$ as part of the likelihood functions embedded in the posteriors $f\left(\cdot \mid \mathbf{d}_{obs}\right)$.

a. Evaluate $q\left(\hat{\boldsymbol{\theta}}_s(\mathbf{X}) \mid \mathbf{Y}\right)$ and $q\left(\mathbf{Y} \mid \hat{\boldsymbol{\theta}}_s(\mathbf{X})\right)$. In this step it is necessary to accommodate the proposed arrangement of $\boldsymbol{\theta}(\mathbf{X})$ which include 30 materials to

the particular arrangement of the 3D-FEM which include 25 materials. This

adjustment is solved by calculating the average of the couples of 'material'

values comprised of the central segment of the parameters domain

b. Evaluate the likelihood functions $f(\mathbf{Y}|\mathbf{d}_{obs})$ and $f(\mathbf{d}_{obs}|\mathbf{Y})$

c. Evaluate $U \leq \alpha\left(\hat{\mathbf{\theta}}_s(\mathbf{X}), \mathbf{Y}\right)$

v). Set $s = s + 1$ and repeat steps 2 through 5.

The previous algorithm introduces a hierarchy in the inferences of the constitutive

parameters as part of the MCMC M-H sampling. The inferences now span from the

behavior of the random field - $\hat{\mathbf{\theta}}(\mathbf{X})$, to the parameters that control it - $\mathbf{u}(\mathbf{X})$. This feature

is what makes this approach unique. Inferences about the solution of the inverse problem

rely not only on the understanding of the uncertainty associated with 'material'

properties, but also on the parameters that simulate them.

Perturbing the chaos coefficients $\mathbf{u}(\mathbf{X})$ to evaluate the prior at the sth step of the chain,

impacts both the shape of the marginal $f(\theta(X))$ and the correlation structure of the

'materials' - $\rho_{\theta(\mathbf{X})}$. This means that the influence that the chaos coefficients have on the

sampling of the posterior is given by the expansions $\mathbf{\theta}_s(\mathbf{u}_s(\mathbf{X}), \xi)$. A key step during the

posterior integration is to take the expected value of the 'materials' properties

$\hat{\mathbf{\theta}}_s = E[\mathbf{\theta}_s(\mathbf{u}_s, \xi)]$ as the decision element used to accept or reject the material's

realization at each step of the chain.

7. Case Study

This chapter illustrates the applicability of the probabilistic calibration approach to one soil specimen. Previous chapters prepared the elements for this case. The theoretical background was presented in chapters 2 and 3. The generation of experimental data for the validation of the method was discussed in chapter 4. The selection of the predictive model to sample estimates of the actual soil responses was discussed in chapter 5. And the corresponding statistical inferences required for the Bayesian formulation were presented in chapter 6. It is important to note that although the case study is limited to the linear elastic domain, the calibration method can be implemented for a wider spectrum of deformations and consequently to more complex constitutive models. The following sections introduce the problem statement, the implementation of the posterior integration and finally the case calibration results.

7.1. Problem Statement

This case presents the probabilistic calibration associated with test 092903b. The constitutive parameter discussed herein is the Young's Modulus E that follows the prescribed spatial arrangement given by the Het-I model (Figure 5.3) with a maximum of 30 'materials', which can be projected on the vertical cross section of the specimen as shown in Figure 3.44. The total amount of observations includes 184 spatio-temporal data points for each displacement field, allowing for up to 552 local measurements that are incorporated into the calibration. The components for the formulation of the posterior as defined by equation 2.26 are the same as those discussed in chapter 6. They include a

Gaussian-type likelihood, a log-normal-type prior, log-normal marginal pdfs $f(\theta(X))$, an isotropic correlation structure $\rho_{\theta(\mathbf{X})}$ with random correlation length parameter δ, and the PC definition of the random field $\theta(u(X),\xi)$ embedded into the prior, with Gaussian-type chaos coefficients $u(X)$. The integration of the posterior is performed via MCMC and the M-H algorithms (section 6.2).

7.2. Implementation of the Posterior Integration

Following the method algorithm presented in the previous chapter (section 6.2), the MCMC integration is initiated with the condition $\hat{\boldsymbol{\theta}}_{s=0}(\mathbf{X}) = \boldsymbol{\theta}_{prior}(\mathbf{X})$ at $s = 0$. This means that each one of the constitutive parameters assumes the global estimate of the specimen experimental value of Young's modulus $E = 93.22$ MPa. The acceptance and rejection of the vector of Young's moduli estimates is defined by the probability of $\mathbf{d}_{pred}$ to converge towards the actual (mean) values included in $\mathbf{d}_{obs}$. Typical samples of $\hat{\boldsymbol{\theta}}_s(\mathbf{X})$ at s, $s + 1$ and $s + 2$ are presented in Figure 7.1 where two consecutive 'candidate' points are evaluated during the burn in period ($s = 3,000$). As can be observed in this figure, the selection sensitivity is high.

The 'accepted' estimates are divided in the burn in and the stationary phases. Convergence to the stationary condition is continuously checked by evaluating the trend of the mean of the samples and the 'mixing' through the distribution of the decision parameter α.

The stationarity condition is assessed by computing the running average for each vector of estimates $\hat{\boldsymbol{\theta}}_s(\mathbf{X})$, and by computing thereafter the first derivative function, which indicates the inflection point between the burn in and the stationary phase. A typical first derivative function of the 'accepted' samples computed over a running average window of 1,000 samples is presented in Figure 7.2. This figure shows that the stationary condition starts approximately at the $4,000^{th}$ sample, delimiting the domain from which statistical inferences can be made. The stationary domain includes 3,500 samples and five full periods of data, which are considered adequate for generating statistical inferences due to the convergence of their mean values.

The assessment of the sampling 'mixing' is given by the parameter α, which measures the probability of success in 'accepting' a sample when applying the M-H decision rule (with 0 failure and 1 success). The relative frequency distributions of the parameter α for the burn in and the stationary phases are presented in Figures 7.3 and 7.4 respectively. A comparison of these figures indicates that during the burn in period the rate of success for proposing a candidate sample was significantly higher than during the stationary phase. This indicates convergence to the stationary condition.

7.3. Calibration Results

The sequence of sample estimates $\hat{\boldsymbol{\theta}}_s(\mathbf{X})$ corresponding to the burn in and the stationary phases are presented in Figures 7.5 and 7.6 respectively. Estimates from the burn in phase show a tendency of the calibration method to move away from the

'homogeneous' condition known a-priori ($s = 0$), while estimates included in the stationary phase are more likely to achieve the target performance of the actual test.

Two levels of inference are expected from the sampled estimates of $\hat{\boldsymbol{\theta}}_s(\mathbf{X})$ and $\mathbf{u}_s(\mathbf{X})$ during the stationary phase. Beginning with the 'material' parameters, Figures 7.7 and 7.8 show the mean and standard deviation of the Young's moduli estimates. Figure 7.7 shows the highest values of Young's moduli for the mean distribution are found in the upper segment of the specimen slightly deviated to the right, while the lowest values are concentrated almost uniformly at the bottom. Also, relatively lower values are observed along the boundaries of the specimen. Figure 7.8 shows a very similar trend. The highest standard deviation values are concentrated in the upper segment slightly deviated to the right, and the lowest values are concentrated in the lower segment.

It is also possible to depict the marginal pdfs of each constitutive parameter and their corresponding correlation structure. Three typical relative density distributions of $\hat{\boldsymbol{\theta}}_s(\mathbf{X})$ evaluated at control points $X(-0.25, 0.22)$, $X(-0.25, 1.10)$ and $X(-0.25, 1.99)$ are presented in Figure 7.9. This figure shows the increase in the uncertainty from the bottom to the top of the specimen as highlighted in the discussion regarding Figure 7.8 above. It also shows similar findings to those in Figure 7.7 in terms of the order of magnitude of the mean values. Figure 7.10 presents the corresponding graphical representation of the empirical correlation matrix of the mean estimates of $\hat{\boldsymbol{\theta}}_s(\mathbf{X})$. Figure 7.11 shows the same empirical correlation and its trend projected on the domain of the lag distances between data points of the normalized vertical cross section. Information provided from

these two figures is not conclusive regarding the definition of the specimen correlation structure, meaning that it may not follow a stationary behavior.

At the level of the chaos coefficients, similar statistics can be obtained from the samples taken within the stationary phase. The distributions of the mean and standard deviation of the estimates of $u(X)$ for each 'material' are presented in Figures 7.12 and 7.13 respectively. The first chaos coefficient ($i = 0$) shown in Figure 7.12 depicts the mean estimates of $\hat{\theta}(\mathbf{X})$, showing the same trend as the mean corresponding to random field of Young's modulus presented in Figure 7.7. The surfaces of standard deviations on the other hand, show higher values between orders $i = 3$ and $i = 7$, with a general trend to decrease for higher i^{th} values. Typical variation in the first three coefficients of the chaos expansions are presented in Figures 7.14, 7.15 and 7.16. These correspond to the 'material' points $X(0.25, 0.22)$, $X(0.25, 1.10)$ and $X(0.25, 1.99)$ respectively. These distributions provide relevant information about the probability distribution of the chaos coefficients that control the definition of the random field $\theta(\mathbf{X})$. Another enhancement provided by the method, is that uncertainty can be traced back at this level of inference based on the update of information provided by observations.

Finally, to complement the inferences associated with the probabilistic description of the random parameters, a simple comparison between full-field displacements between observation and predictions validate the method applicability. For this purpose, predictions are assessed solving the forward problem based on the estimates of $E\left[\hat{\theta}(\mathbf{X})\right]$. This comparison is presented in Figure 7.17, which presents displacement fields u, v and

w obtained at 0.2 % of axial strain. This figure shows that there is very good agreement between vertical displacements (including local effects). It also shows that the predicted horizontal displacements get to reproduce the general trend captured by the observations. Nevertheless, when *u* and *w* fields are compared to the *v* field, horizontal predictions look limited. This problem may be that the order of magnitude of the differences between predictions and observations are still within the order of accuracy estimated for the 3D-DIC measurements. It could also be that there are other particular limitations associated with the predictive model.

8. Concluding Remarks

· This work introduced the Functional Bayesian FB method as an innovative approach for the calibration of soil constitutive models.

· An appealing characteristic of the FB method is its ability to sample multidimensional non-stationary non-Gaussian constitutive parameters. The Polynomial Chaos PC method proved to be an efficient formulation for sampling this particular 'material' field.

· An innovative technique consisting in the coupling of triaxial testing and 3-dimensional digital imaging allowed for the population of the experimental database used for the validation of the FB method. A unique characteristic of these methods was the capturing of global and local deformation effects on soil deforming specimens.

· A parametric study was developed for the selection of a predictive model capable of reproducing to the extent possible the experimental responses. It consisted in solving the deterministic inverse problem of each test included in the experimental database. The selected model for validating the probabilistic calibration was a 3-dimensional finite element model 3D-FEM including a field of spatially varying parameters, the compliance effect, and a measure of the actual geometry of the specimen.

· Spatio-temporal statistical inferences were generated from the experimental observations and the numerical predictions, including each of the elements required for the computation of the FB solution to the inverse problem.

· A case study was introduced to illustrate the applicability of the probabilistic calibration approach. The most relevant of the method application is the gain of inferences obtained from sampling not only the constitutive parameters but the hyper-parameters that define its 'material' field.

· The goal of developing a probabilistic methodology for the calibration of constitutive models was reached and validated when applied for the elastic model. A robust computational algorithm was outlined and described when applied for the case study facilitating the understanding of the elements required for the probabilistic calibration.

· Regarding soil behavior, significant deformation patterns were identified, characterized and even simulated. In particular those related with the compaction layers and the local effects such as (G), (C), and (S).

· The complexity of the integration of different disciplines was evident when formulating the solution to the inverse problem by the Functional Bayesian method. Engineering applications traditionally solved using optimal solutions now can be benefited from a robust approach that enhances the understanding about local heterogeneous responses and the material variability associated to them.

Tables

<div align="center">

Chapter 4

</div>

Table 4.1 Experimental database

Test number	Test name	Height/Diameter ratio	Volume cm^3	Initial density kg/m^3	Relative density %	Peak σ_1'/σ_3'	Friction angle
1	**092903b**	2.18	621.36	1,710.95	91.09	7.35	49.51
2	**093003b**	2.19	627.46	1,696.00	85.96	6.78	47.98
3	**100103a**	2.21	629.31	1,702.22	88.10	7.03	48.66
4	**100103b**	2.19	621.12	1,717.13	93.18	6.77	47.96
5	**100103d**	2.18	608.56	1,702.41	88.17	6.57	47.37
6	**100203a**	2.20	631.50	1,715.32	92.57	7.12	48.90
7	**100203b**	2.17	622.04	1,711.91	91.41	6.77	47.96
8	**100303b**	2.22	631.38	1,718.70	93.71	6.98	48.52
9	**120904a**	2.23	630.81	1,707.72	89.99	5.89	48.28
10	**120904b**	2.25	633.12	1,720.40	94.28	5.86	48.20
11	**120904c**	2.25	634.07	1,713.13	91.83	5.86	48.21
12	**120904d**	2.24	631.86	1,707.88	90.04	5.44	46.98
13	**120904e**	2.25	633.27	1,718.69	93.71	5.51	47.19
14	**Half dense-Half loose**	2.22	622.12	1,648.06	68.90	4.27	42.91
	Bottom			1,734.17	98.87		
	Top			1,549.61	30.54		

Table 4.2 Tilt Analysis

Test Name	Hyperplane coefficients		
	d	*a*	*c*
Z40C_092903b	0.1787	0.0004	-0.0005
Z40C_093003b	0.1105	0.0000	-0.0007
Z40C_100103a	0.0960	-0.0001	0.0007
Z40C_100103b	0.1082	-0.0006	-0.0004
Z40C_100103d	0.1132	-0.0002	-0.0003
Z40C_100203a	0.1497	-0.0001	0.0000
Z40C_100203b	0.1150	0.0002	0.0000
Z40C_100303b	0.1796	0.0001	-0.0012
Z40C_120704c	0.0529	-0.0006	-0.0003
Z40C_120904a	0.0490	-0.0005	0.0012
Z40C_120904b	-0.0163	0.0000	0.0022
Z40C_120904c	0.0571	-0.0003	0.0015
Z40C_120904d	0.0367	0.0009	0.0025
Z40C_120904e	0.1607	0.0000	-0.0017

Table 6.1 Spatio-Temporal Correlation

Observations taken at	I t=15 sec $\varepsilon_a = 0.05\ \%$	II t=30 sec $\varepsilon_a = 0.10\ \%$	III t=45 sec $\varepsilon_a = 0.15\ \%$	IV t=60 sec $\varepsilon_a = 0.20\ \%$
I t=15 sec $\varepsilon_a = 0.05\ \%$	$\tau_t = 0$ sec ●	$\tau_t = 15$ sec *	$\tau_t = 30$ sec +	$\tau_t = 45$ sec -
II t=30 sec $\varepsilon_a = 0.10\ \%$		$\tau_t = 0$ sec ●	$\tau_t = 15$ sec *	$\tau_t = 30$ sec +
III t=45 sec $\varepsilon_a = 0.15\ \%$			$\tau_t = 0$ sec ●	$\tau_t = 15$ sec *
IV t=60 sec $\varepsilon_a = 0.20\ \%$				$\tau_t = 0$ sec ●

Figures
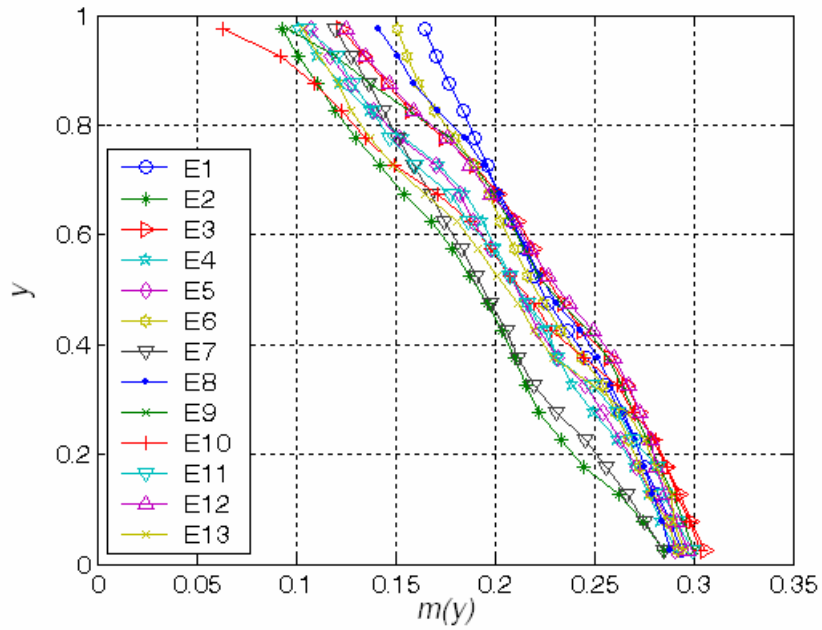
Figure 3.1 Data sample of benchmark case I.
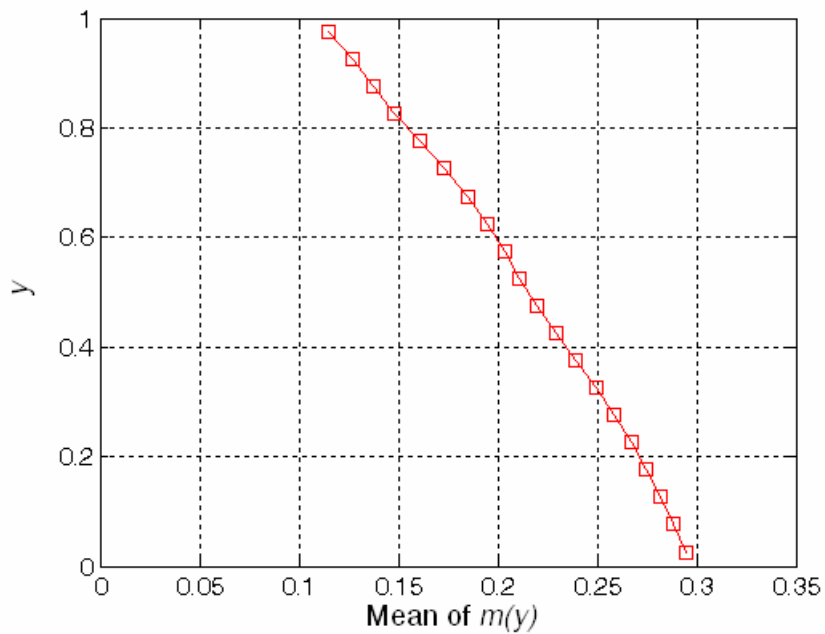
Figure 3.2 Mean profile.
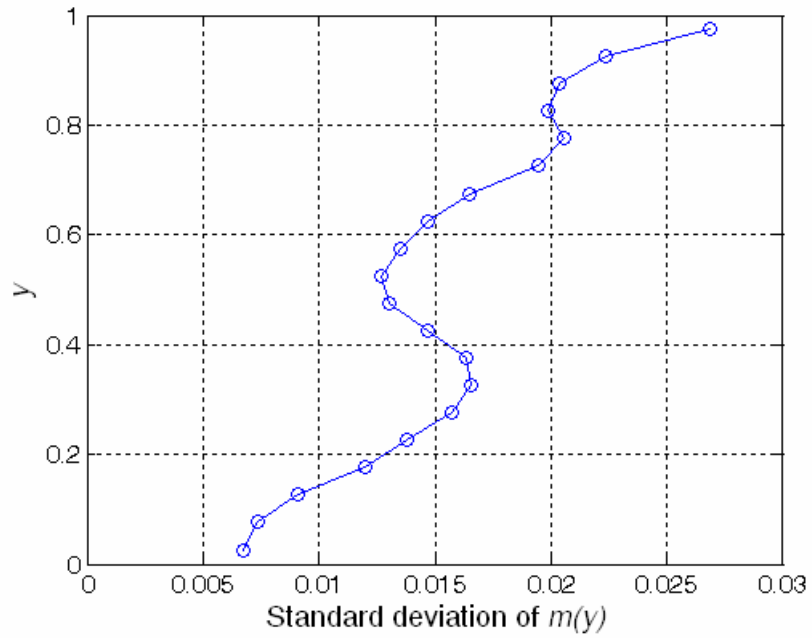
Figure 3.3 Standard deviation profile.
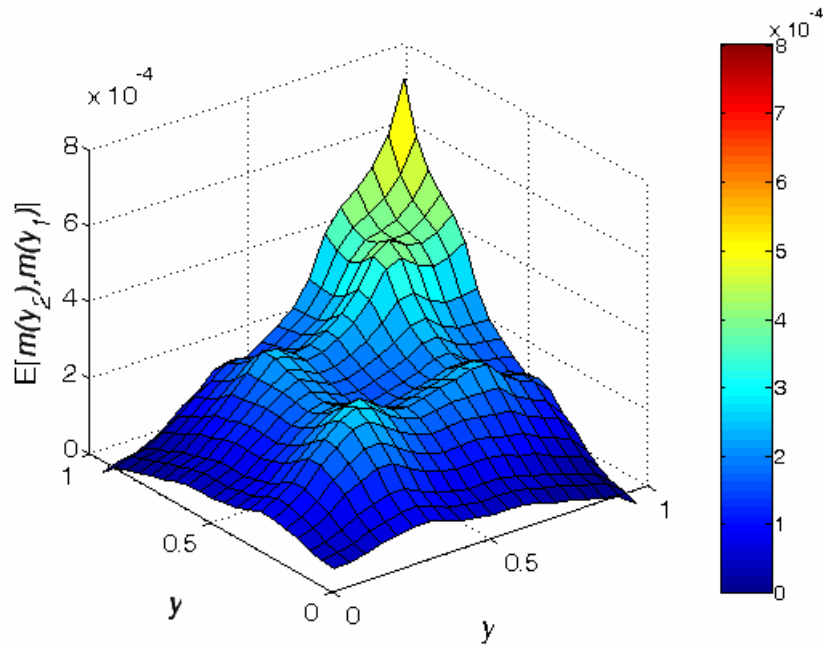
Figure 3.4 Empirical covariance function.

111
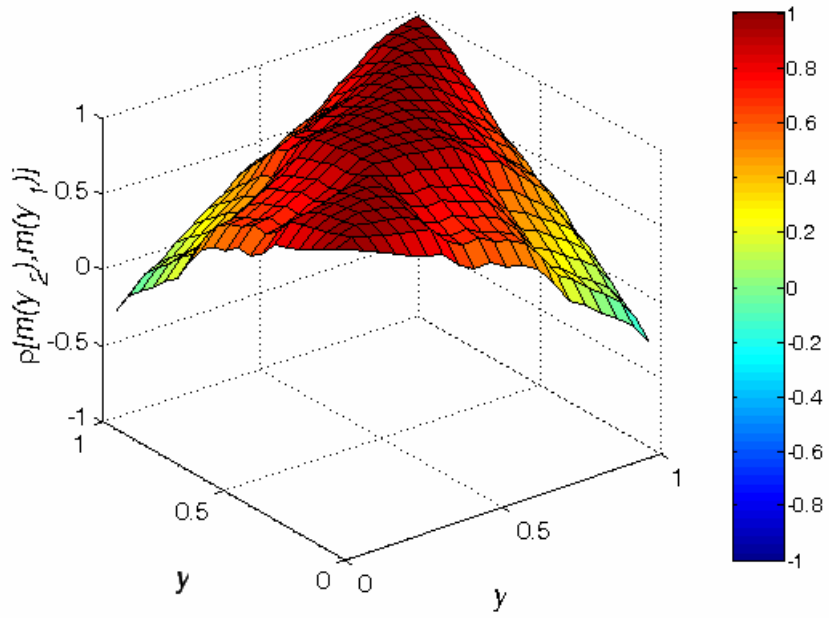
Figure 3.5 Empirical correlation function.
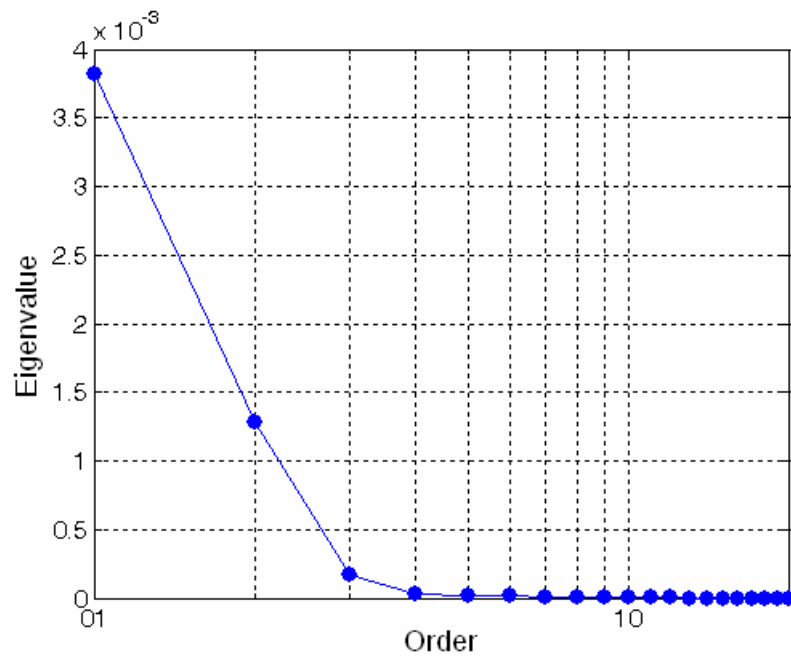
Figure 3.6 Eigenvalues from covariance function.

112
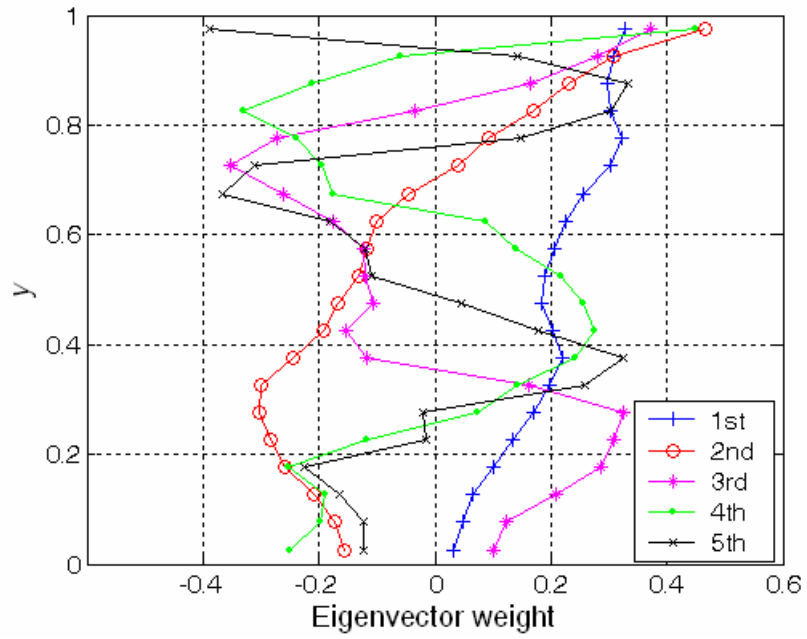
Figure 3.7 Eigenfunctions from covariance function.
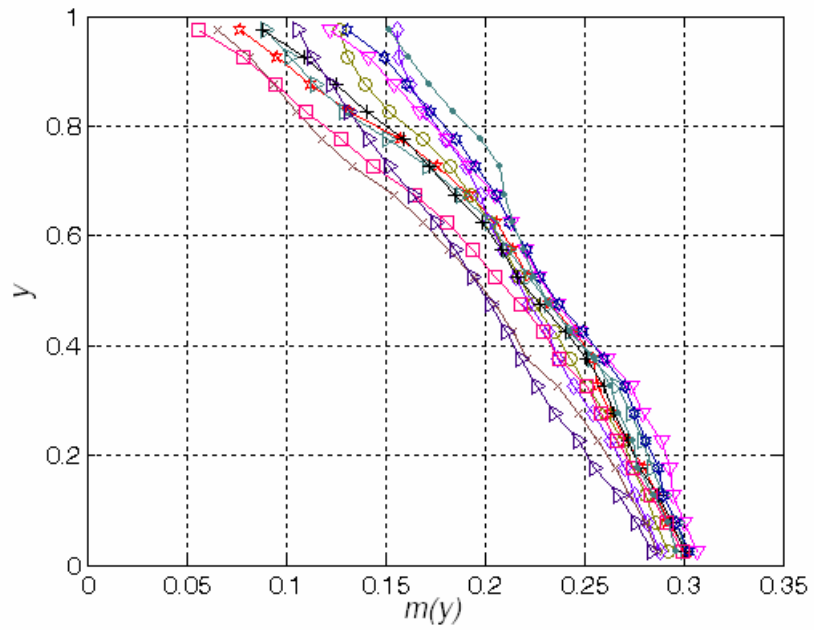
Figure 3.8 Typical K-L simulations.

113
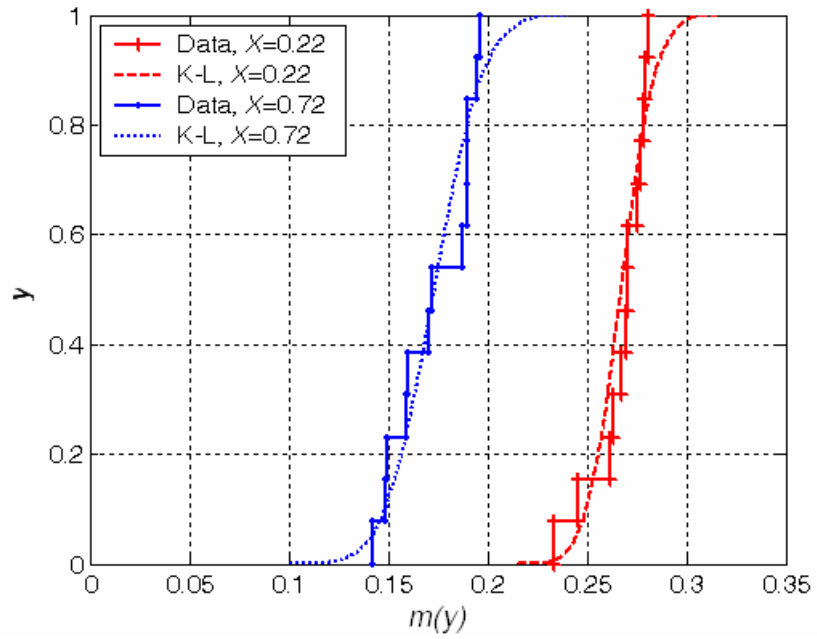
Figure 3.9 Comparison between cdf of Data and synthesized K-L simulations.
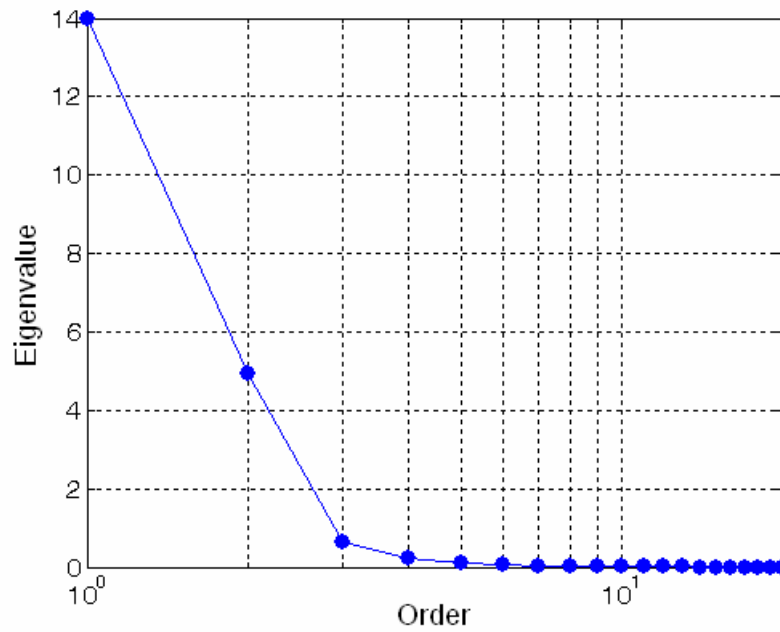
Figure 3.10 Eigenvalues from correlation function.
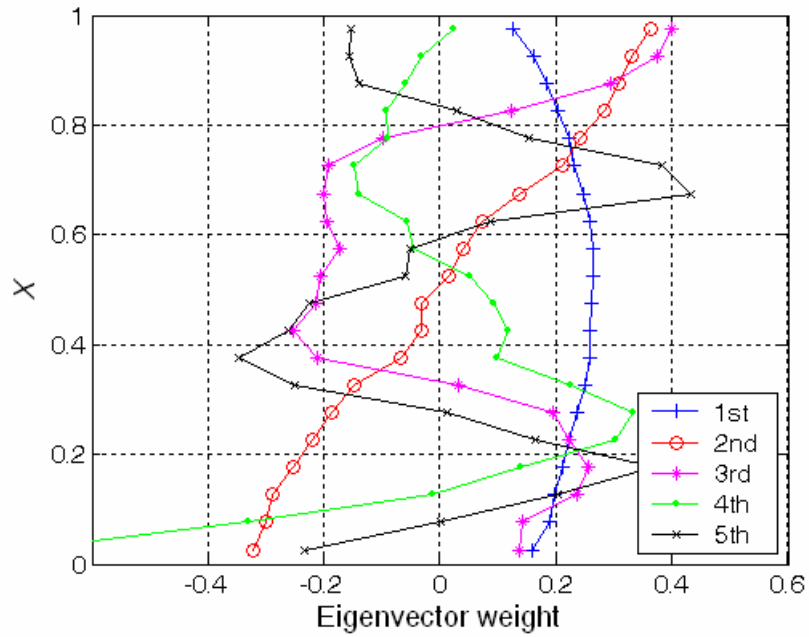
Figure 3.11 Eigenfunctions from correlation function.
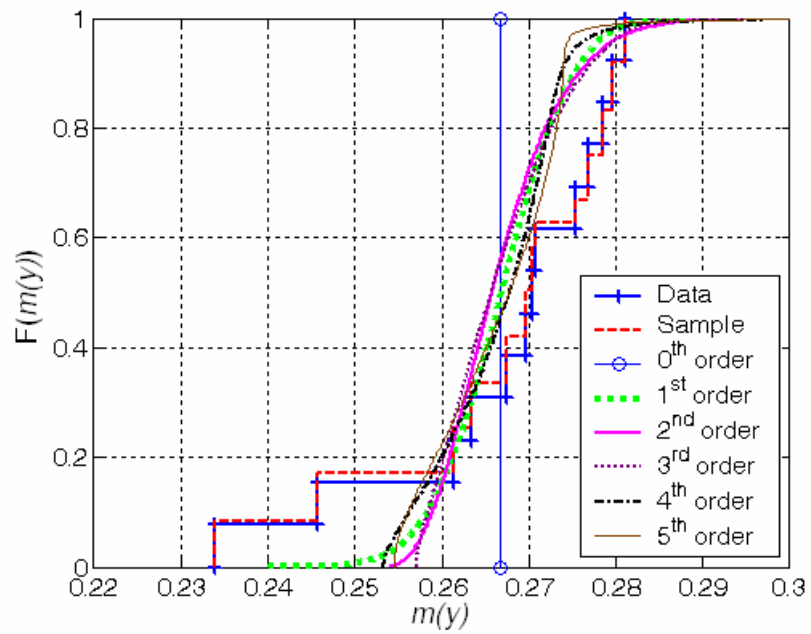
Figure 3.12 Synthesized cdf from raw data at *y* = 0.22.
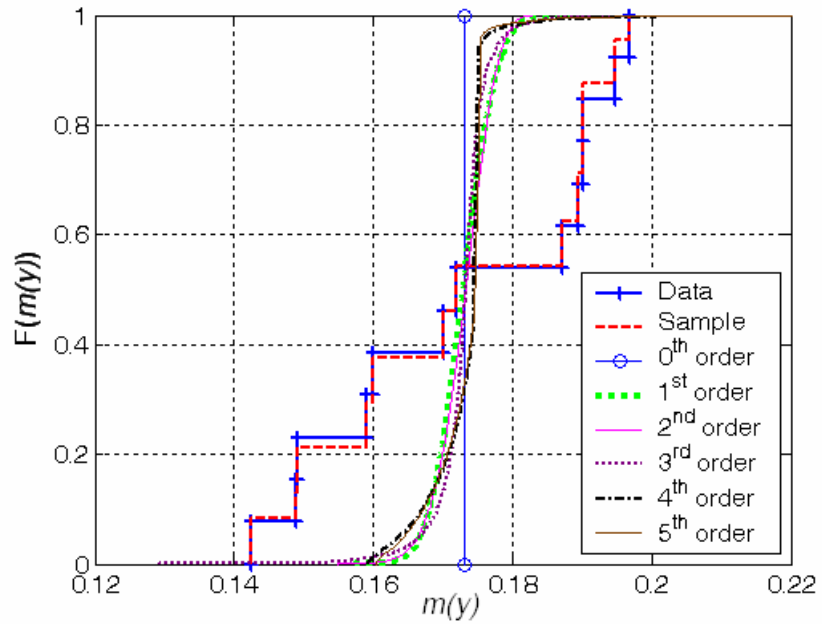
Figure 3.13 Synthesized cdfs from raw data at *y* = 0.72.
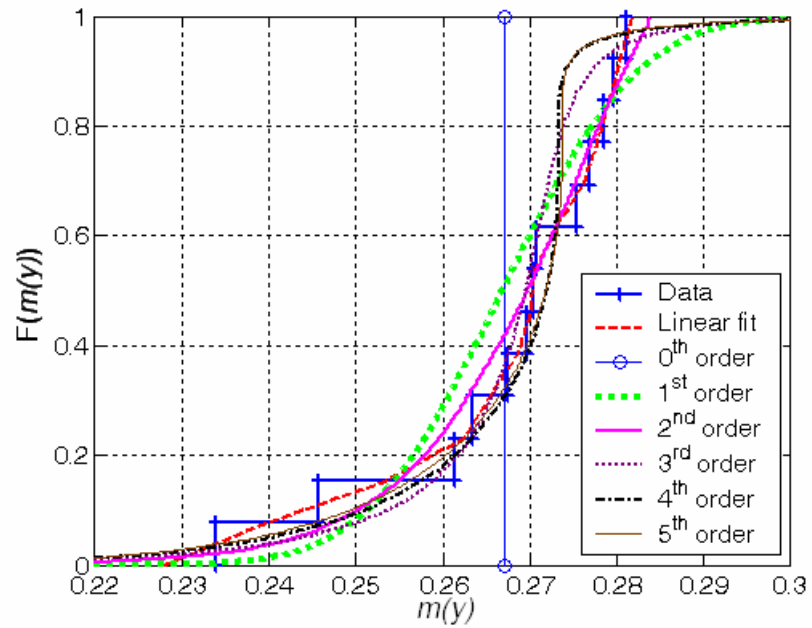
Figure 3.14 Synthesized cdfs from smoothed data at *y* = 0.22.

116
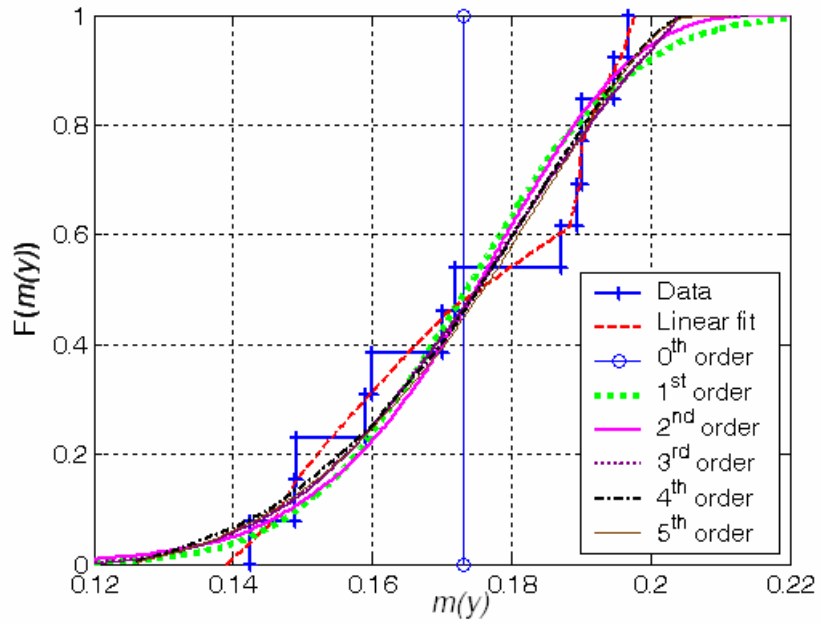
Figure 3.15 Synthesized cdfs from smoothed data at *y* = 0.72.
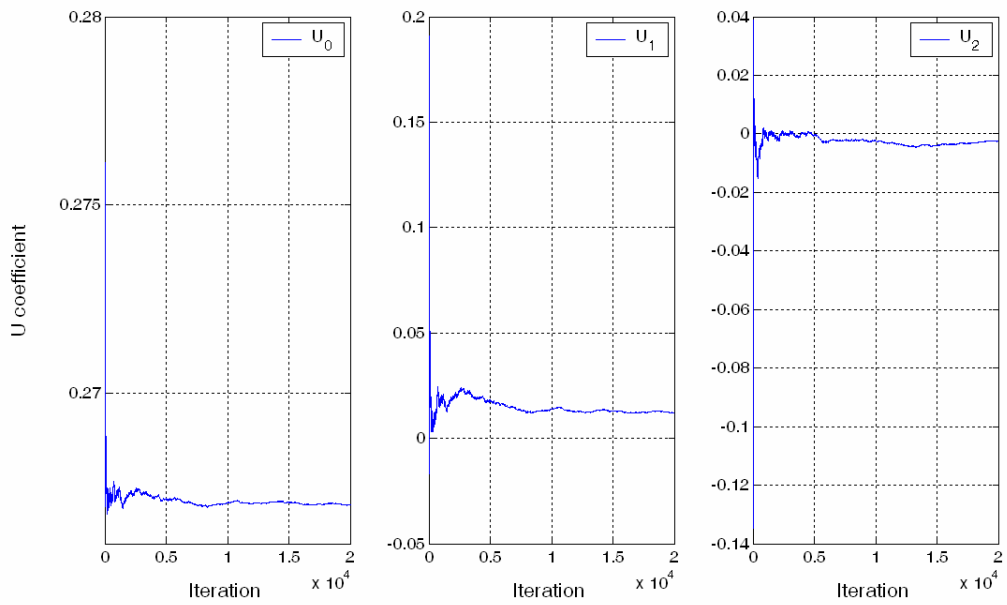
Figure 3.16 Converge analysis of $U_i(y)$ at *y* = 0.22.
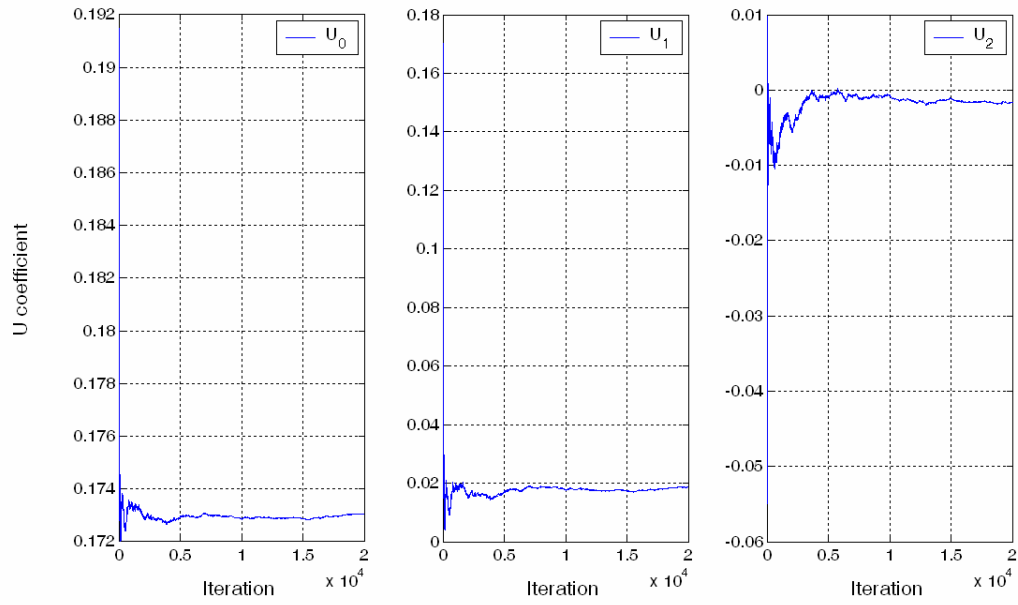
Figure 3.17 Converge analysis of $U_i(y)$ **at y = 0.72.**
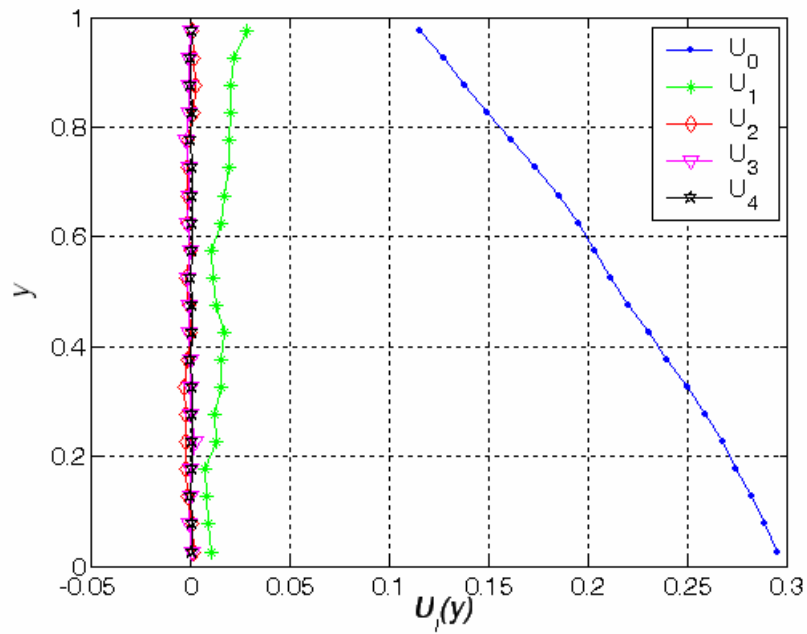
Figure 3.18 $U_i(y)$ **profiles.**

118
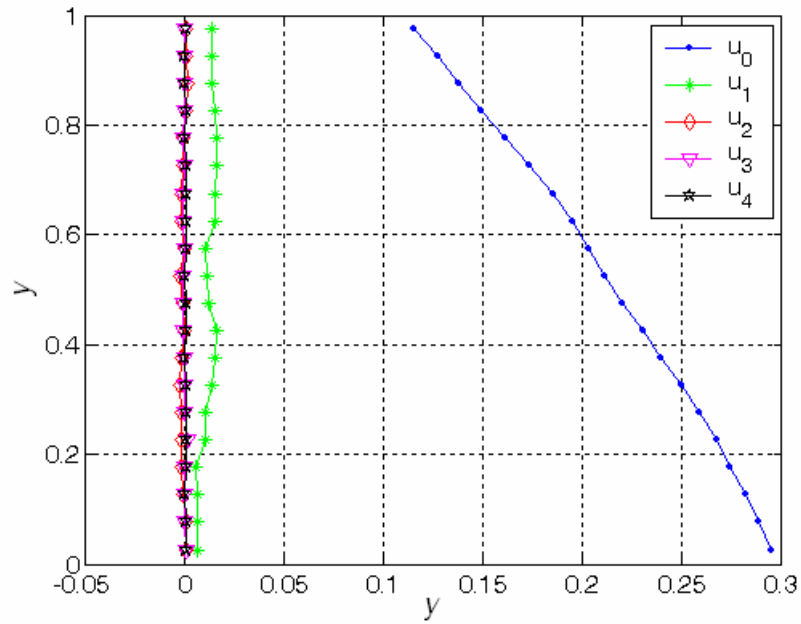
Figure 3.19 $u_i(y)$ **profiles.**
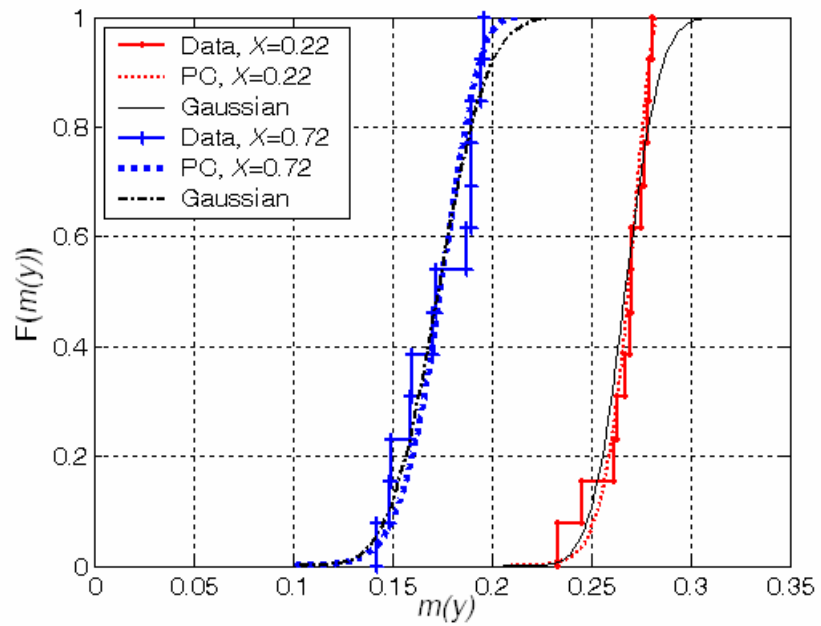
Figure 3.20 Comparison between empirical cdfs and second order one-dimensional PC cdfs.
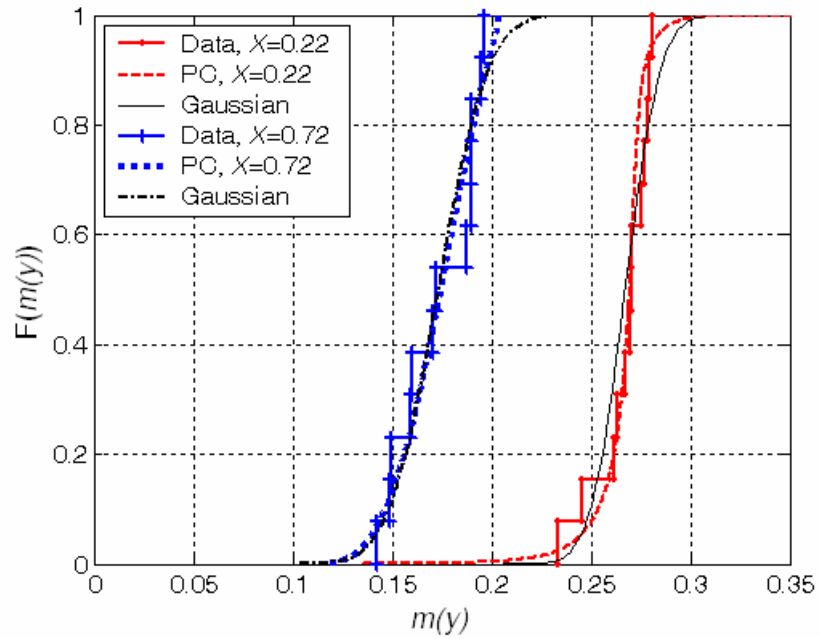
Figure 3.21 Comparison between empirical cdfs and third order one-dimensional PC cdfs.
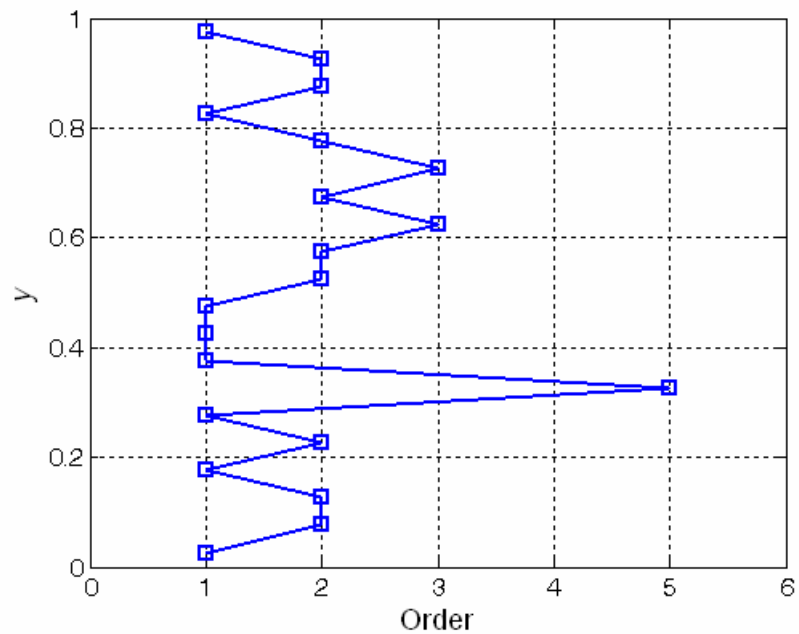
Figure 3.22 Optimal polynomial order distribution.

120
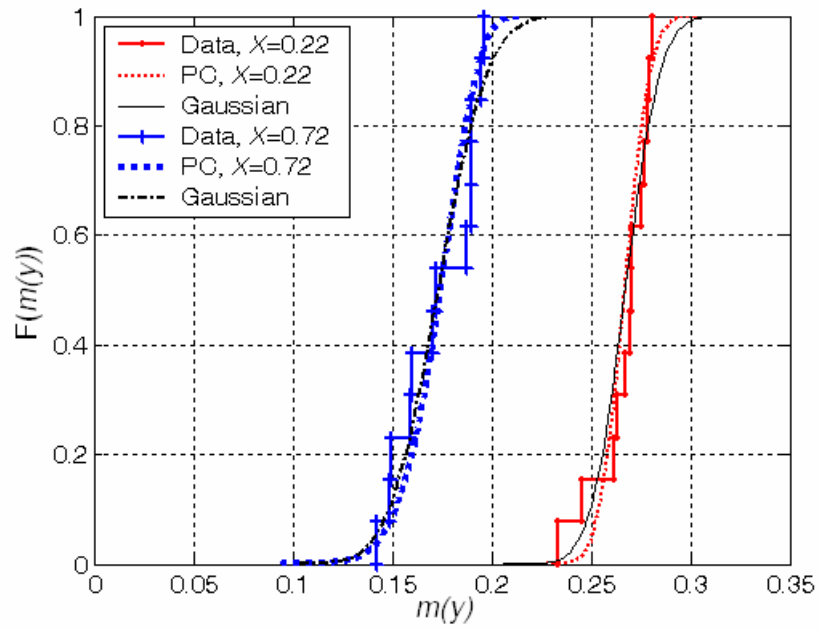
Figure 3.23 Comparison between empirical cdfs and third order one-dimensional PC cdfs.
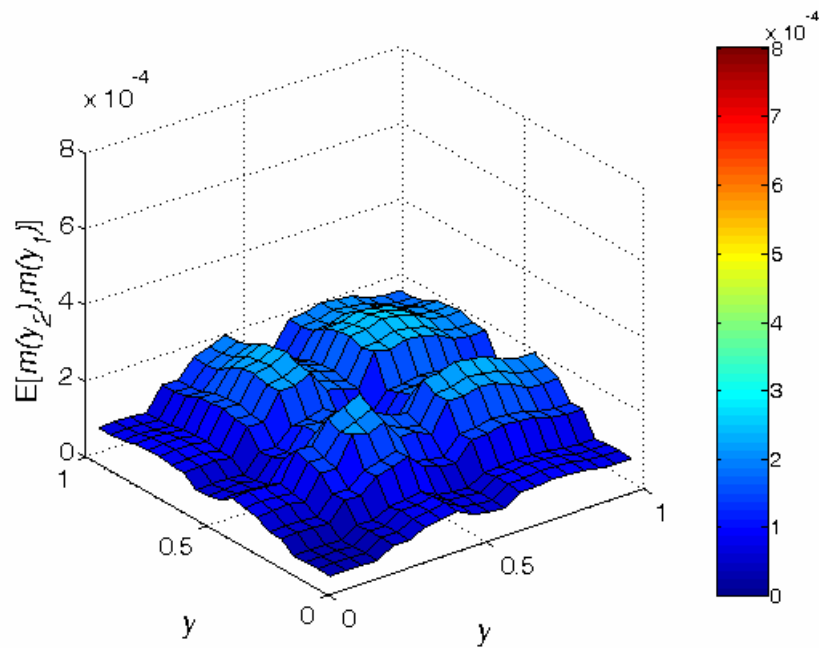
Figure 3.24 Synthesized covariance function from multi-order one-dimensional PC simulations.
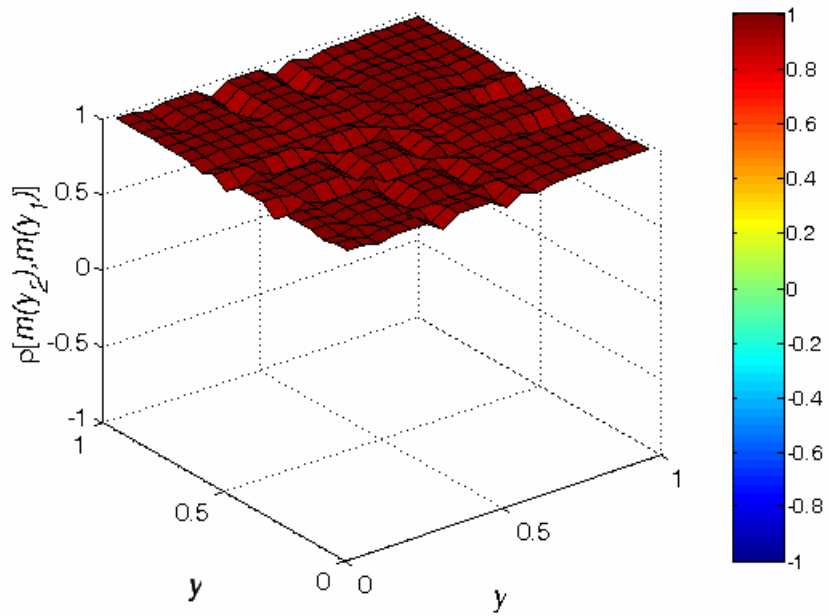
Figure 3.25 Synthesized correlation function from multi-order one-dimensional PC simulations.
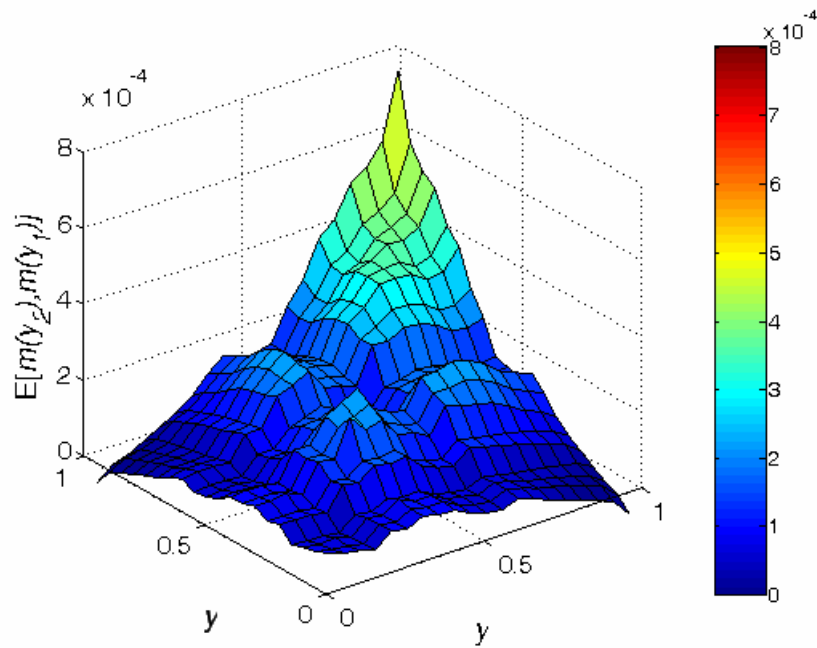
Figure 3.26 Synthesized covariance function from multi-order three-dimensional PC simulations.

122
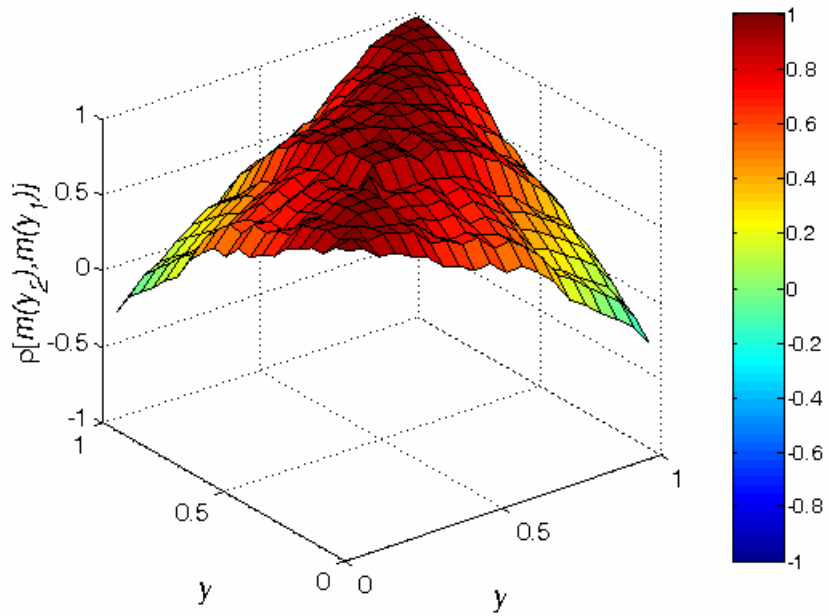
Figure 3.27 Synthesized correlation function from multi-order four-dimensional PC simulations.
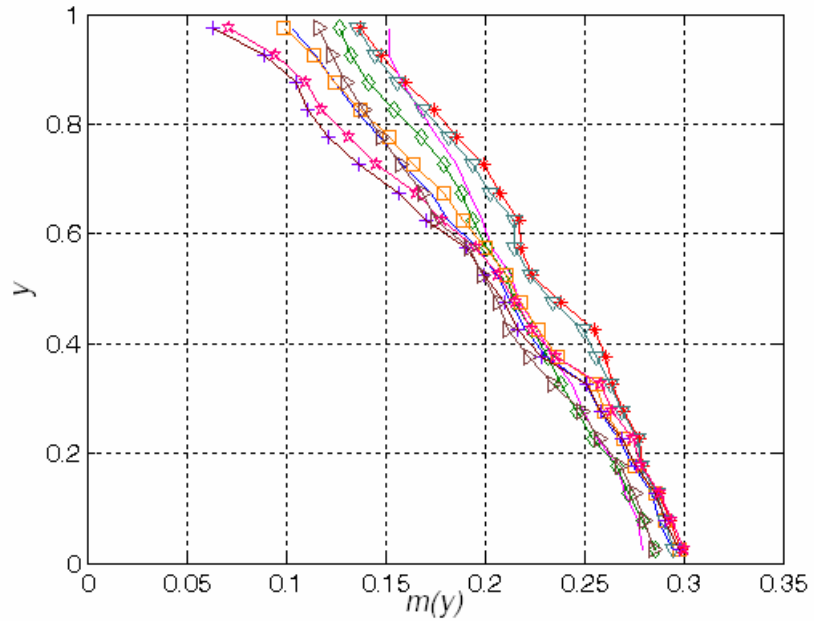
Figure 3.28 Typical multi-order four-dimensional PC simulations.
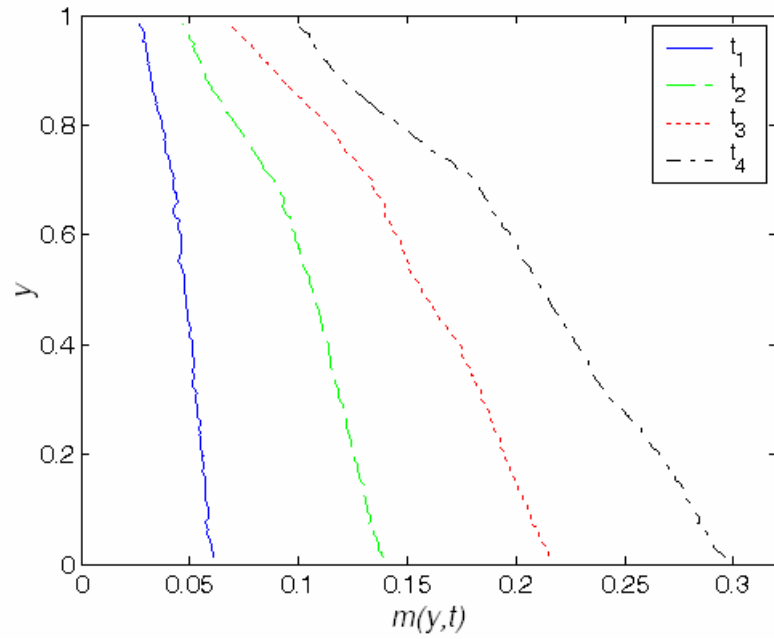
Figure 3.29 Typical data sample of benchmark case II.
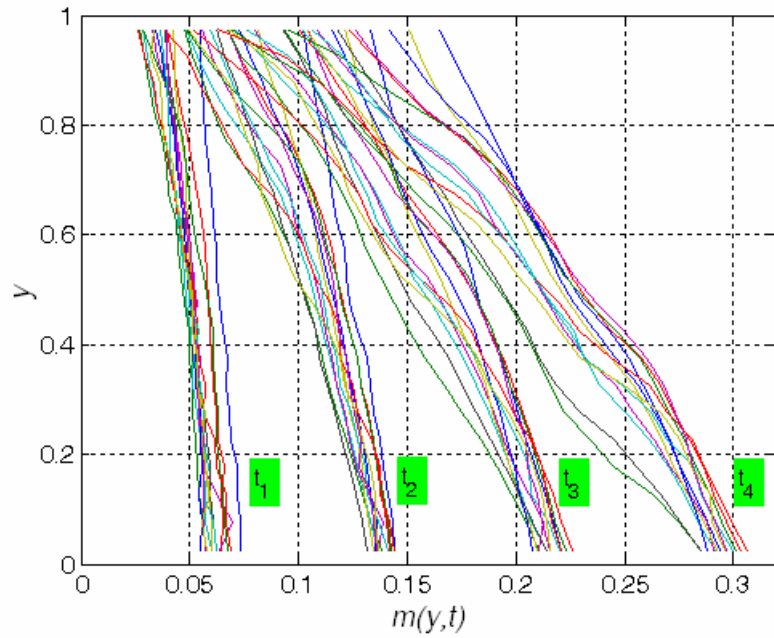
Figure 3.30 Data sample of benchmark case II.

124
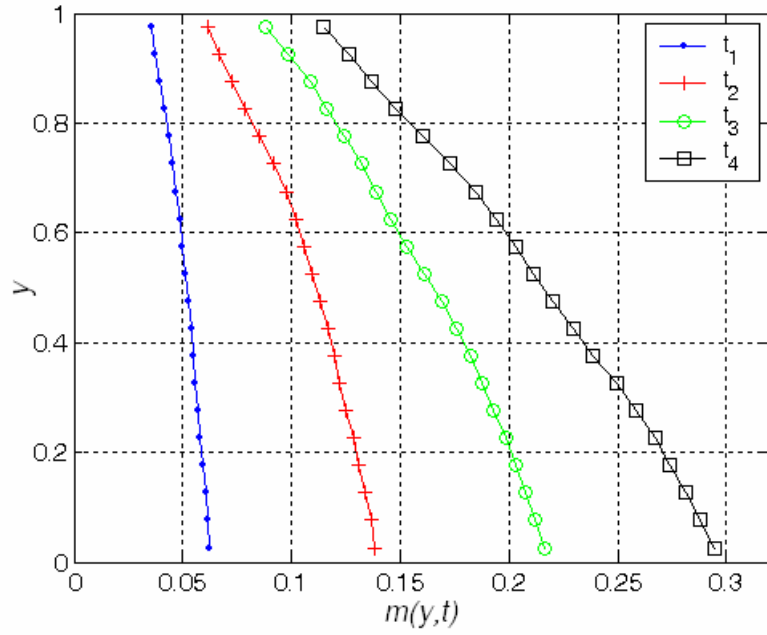
Figure 3.31 Mean profiles.
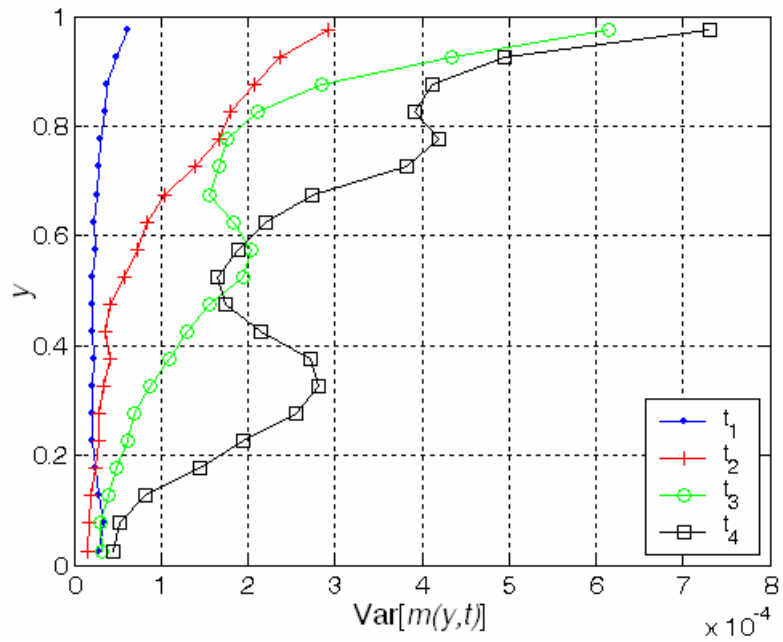
Figure 3.32 Variance profiles.

125
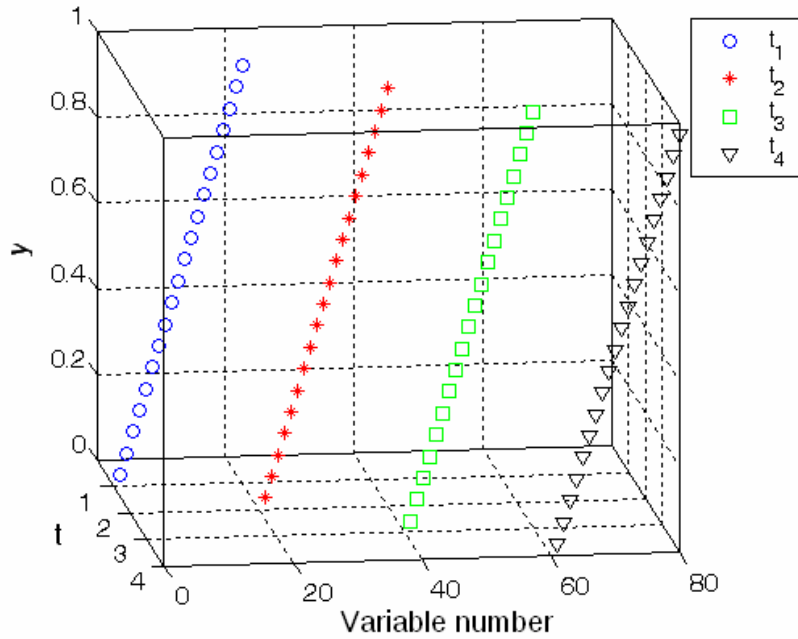
Figure 3.33 Allocation of random variables.
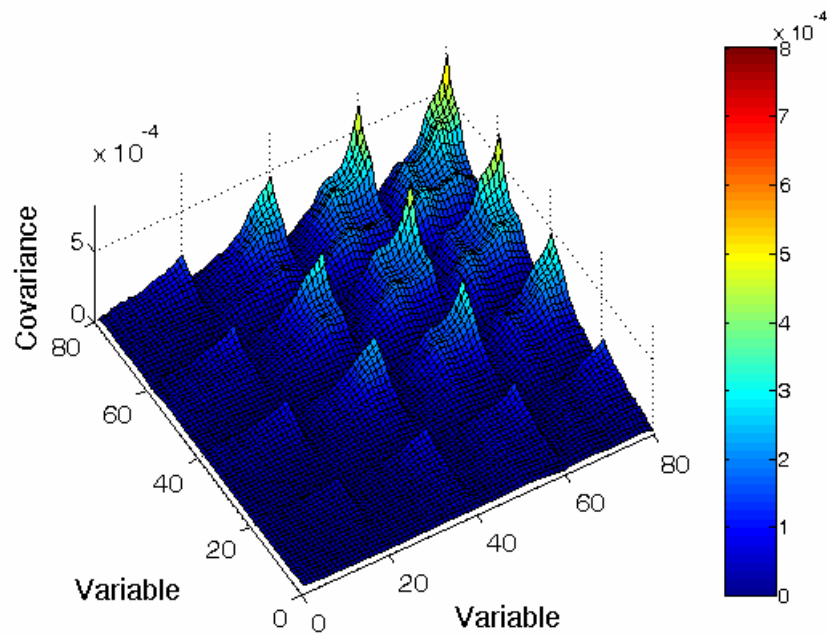
Figure 3.34 Graphical representation of the empirical covariance matrix.
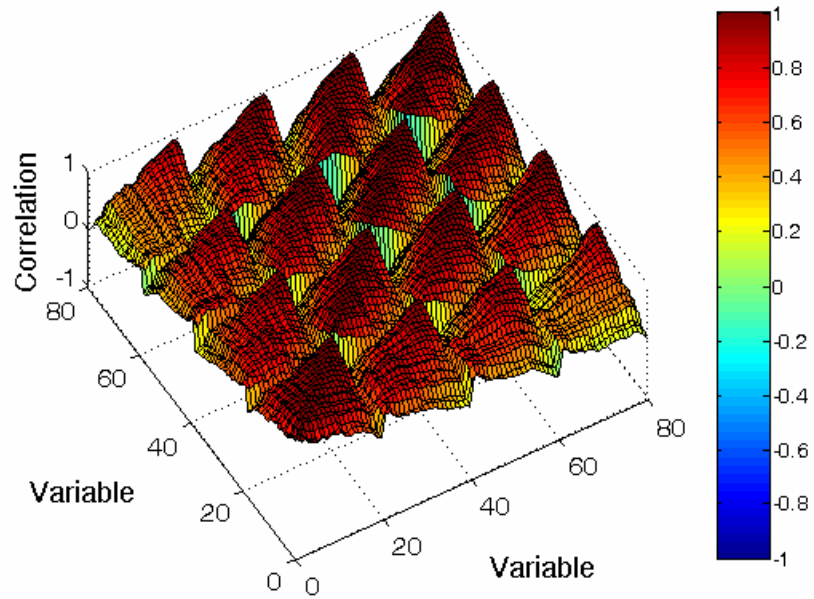
Figure 3.35 Graphical representation of the empirical correlation matrix.
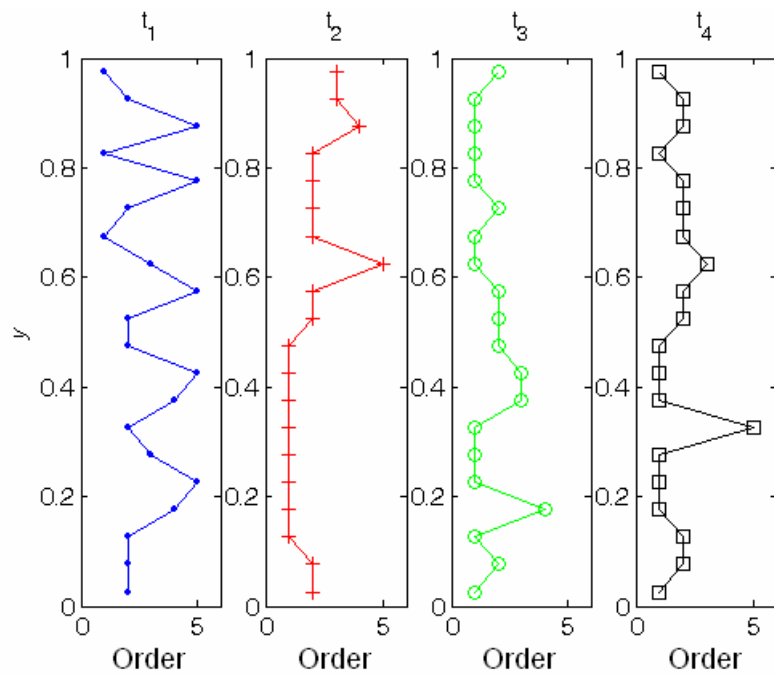
Figure 3.36 Optimal polynomial order distribution.
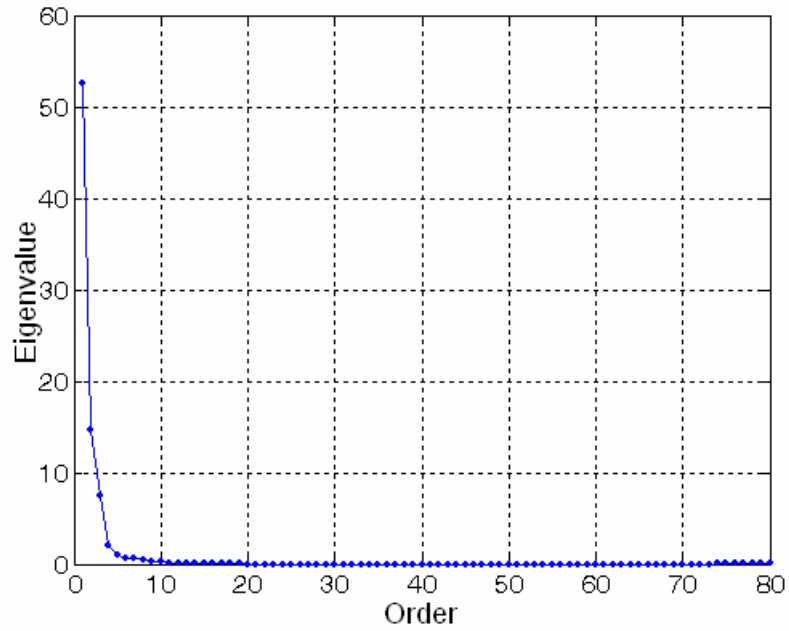
Figure 3.37 Eigenvalues from correlation function.
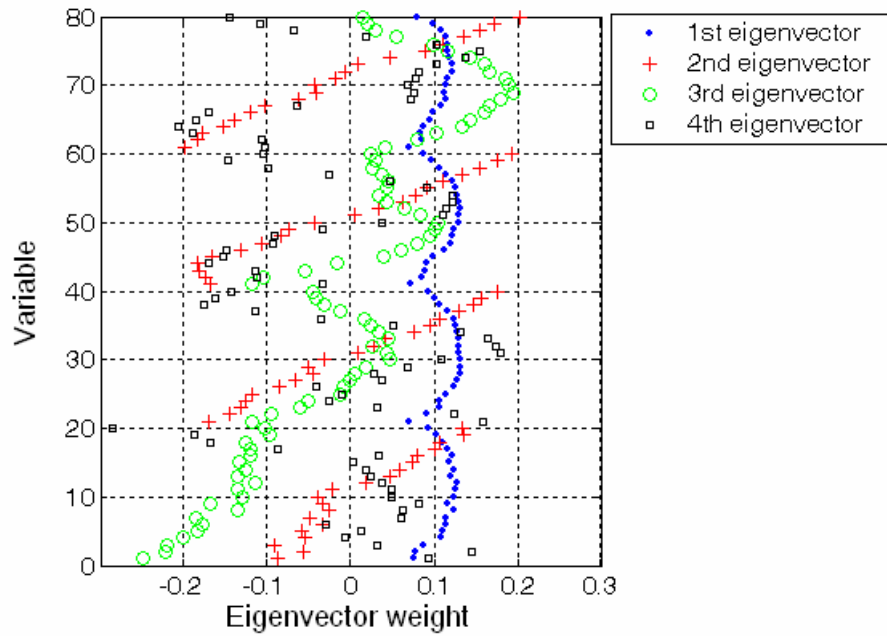
Figure 3.38 Eigenfunctions from correlation function.

128
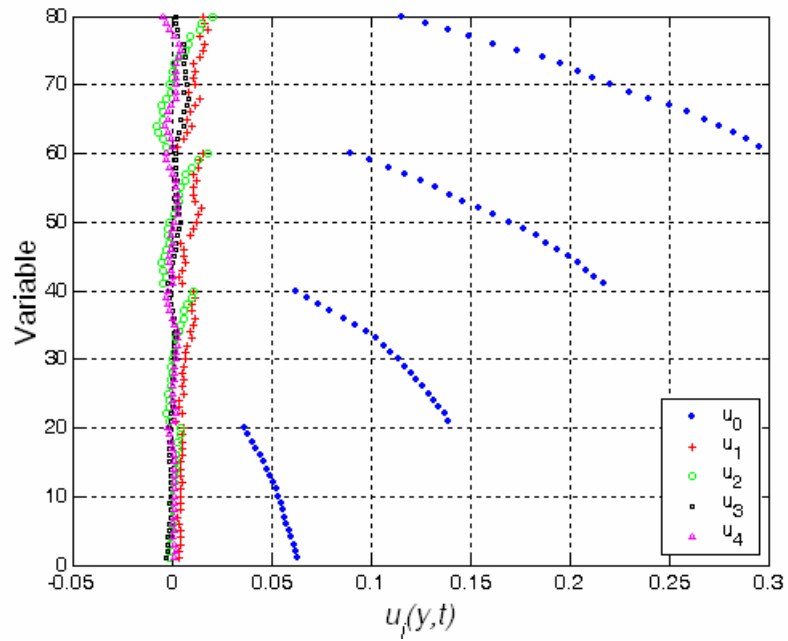
Figure 3.39 $u_i(y)$ **profiles.**
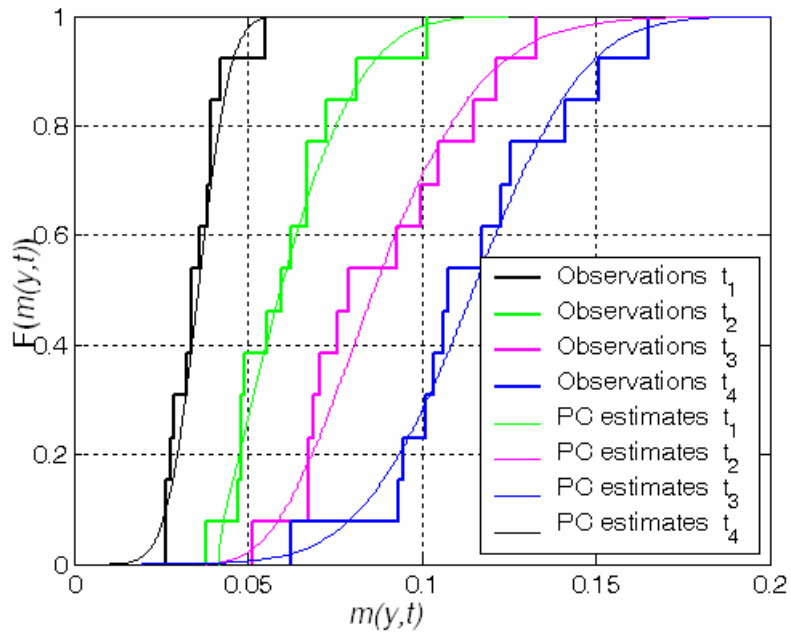
Figure 3.40 Comparison between empirical cdfs and multi-order four-dimensional PC cdfs.
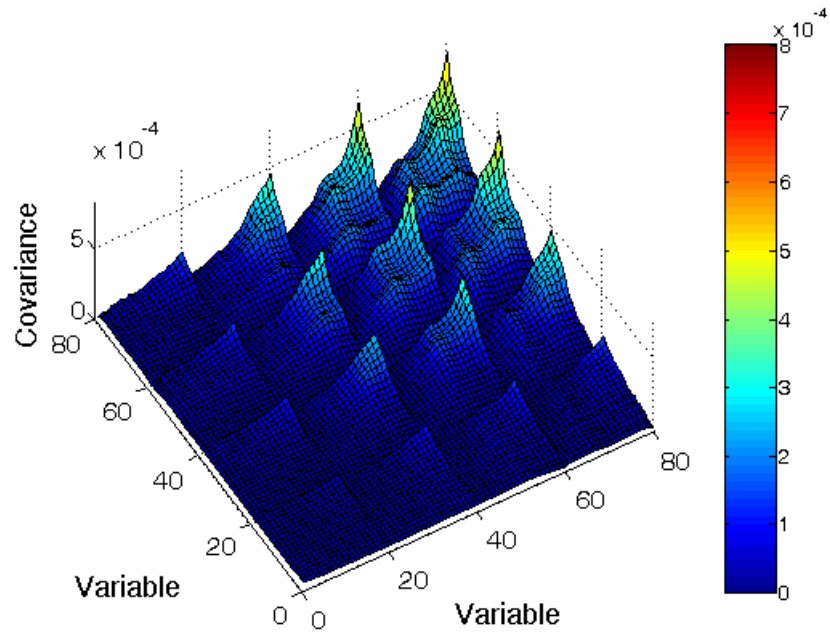
Figure 3.41 Graphical representation of the synthesized covariance matrix from multi-order four-dimensional PC simulations.
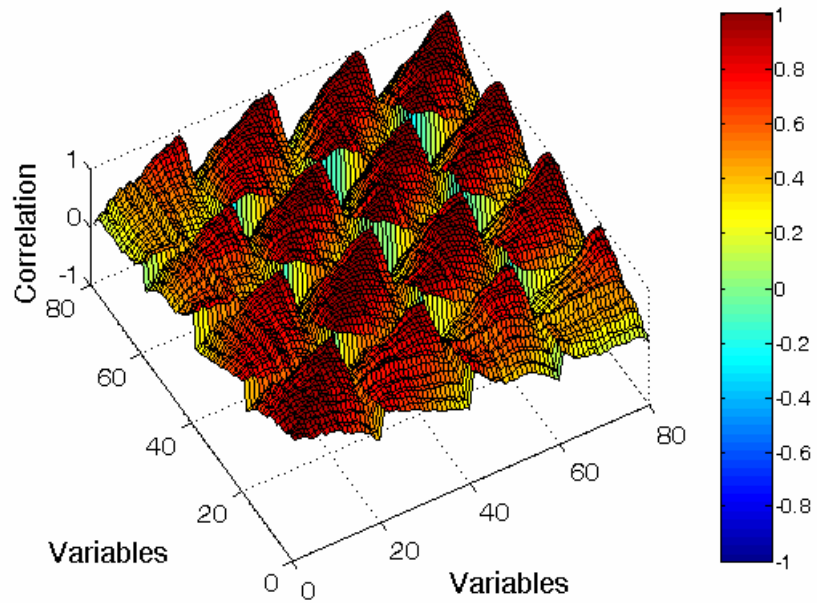
Figure 3.42 Graphical representation of the synthesized correlation matrix from multi-order four-dimensional PC simulations.
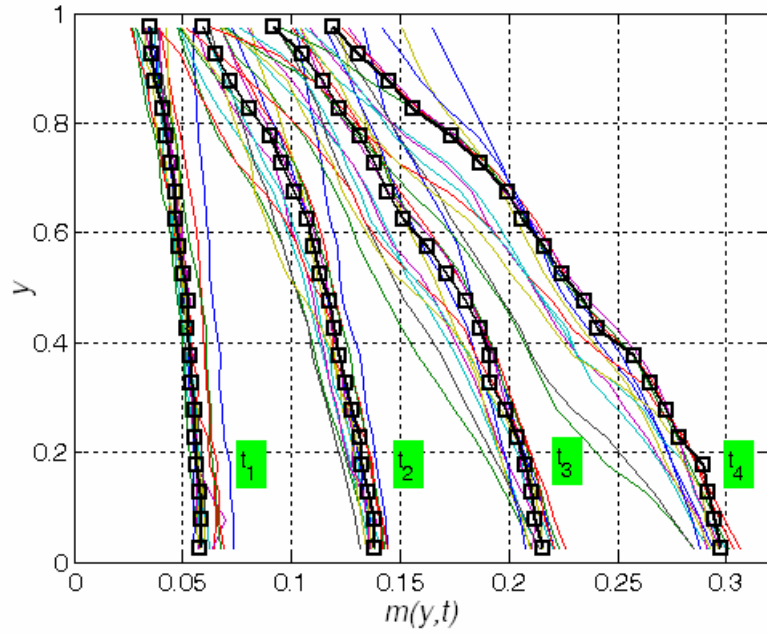
Figure 3.43 Typical multi-order four-dimensional PC simulations.
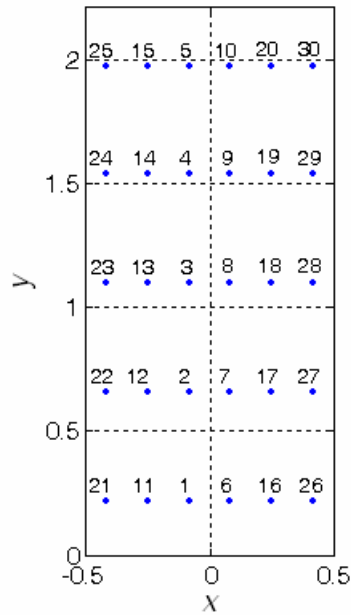
Figure 3.44 Allocation of random variables.

131
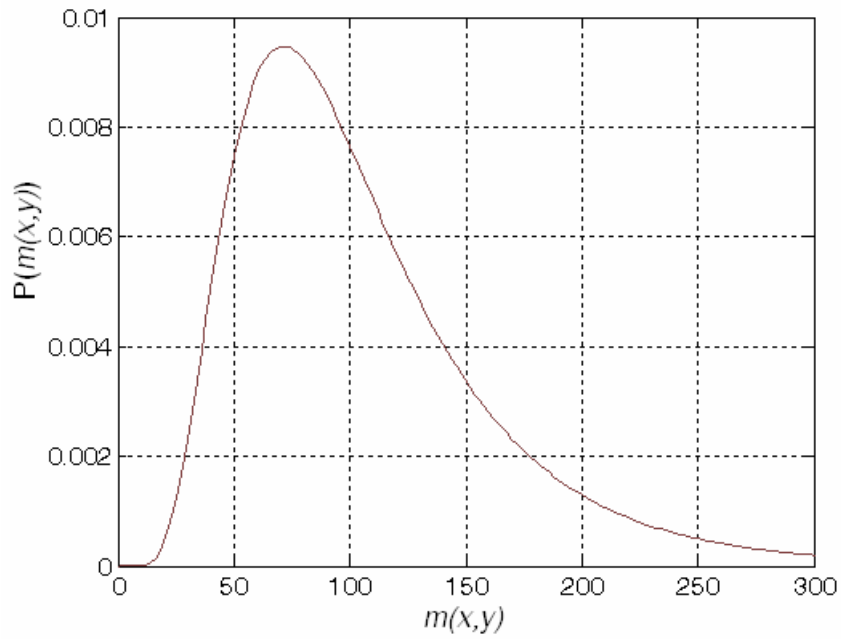
Figure 3.45 Pdf of the marginal log-normal model.
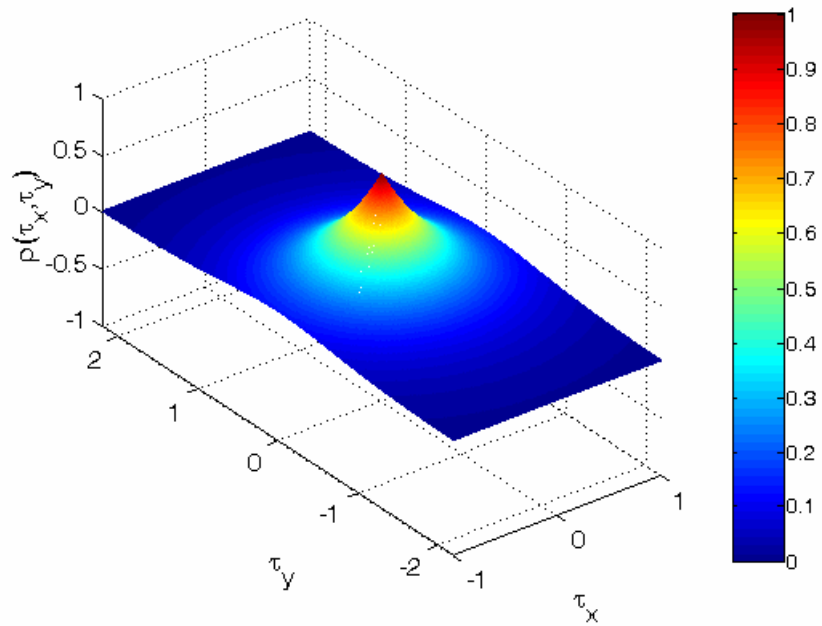
Figure 3.46 Isotropic correlation function with correlation parameter $\delta = 0.5$.
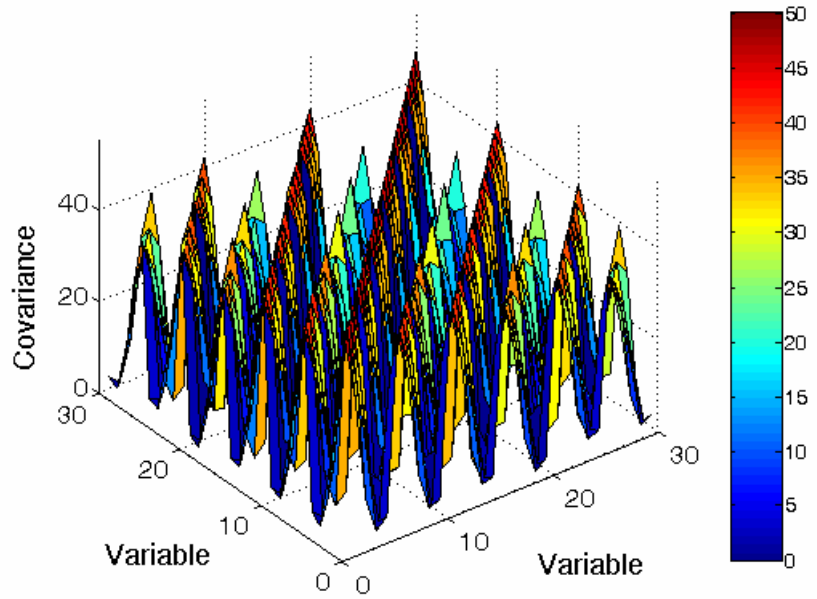
Figure 3.47 Graphical representation of the target covariance matrix.
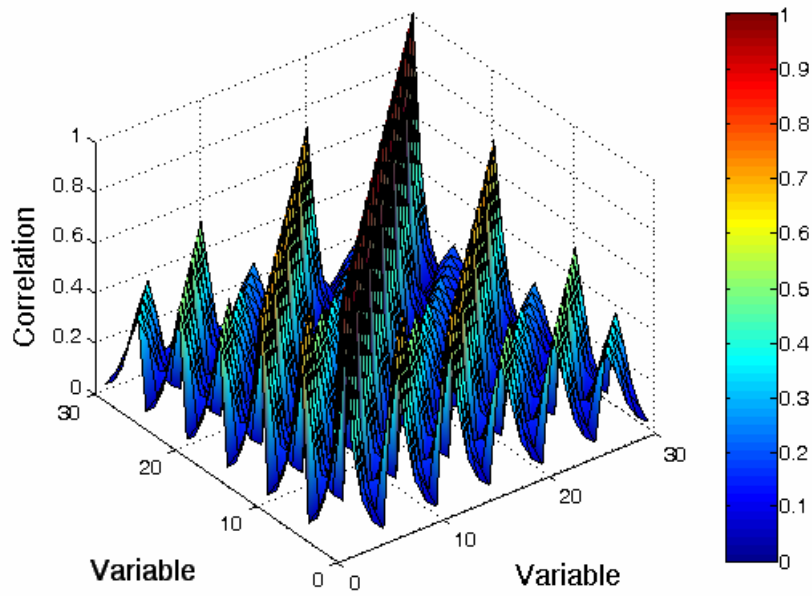
Figure 3.48 Graphical representation of the target correlation matrix.
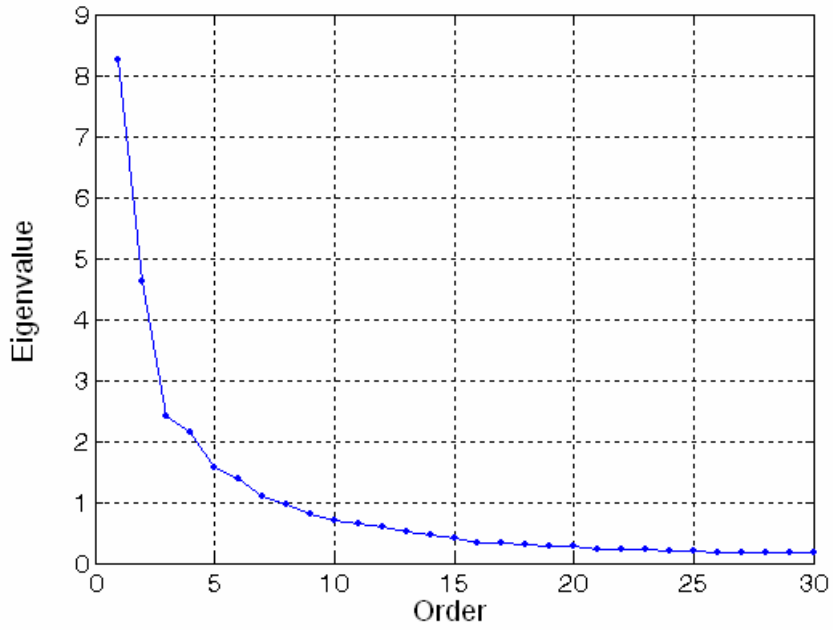
Figure 3.49 Eigenvalues from correlation function.
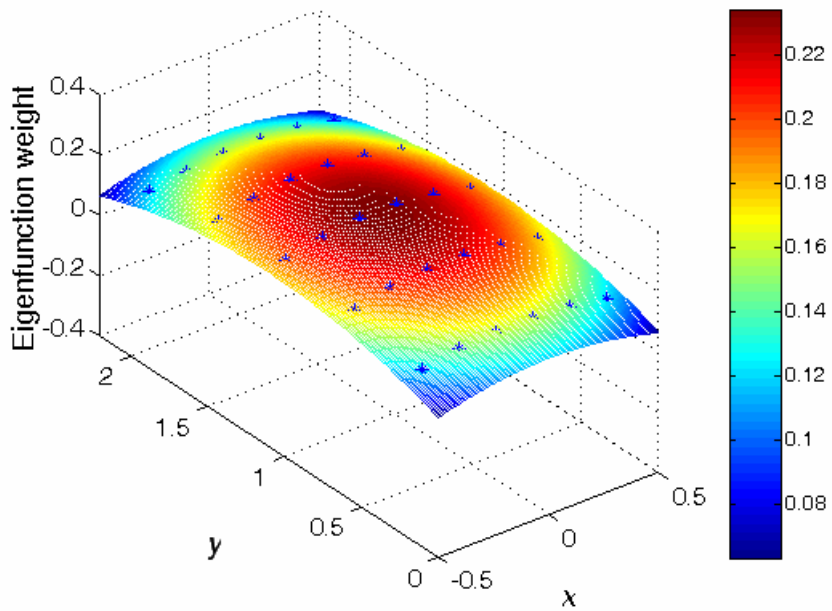
Figure 3.50 First eigenfunction from correlation function.

134
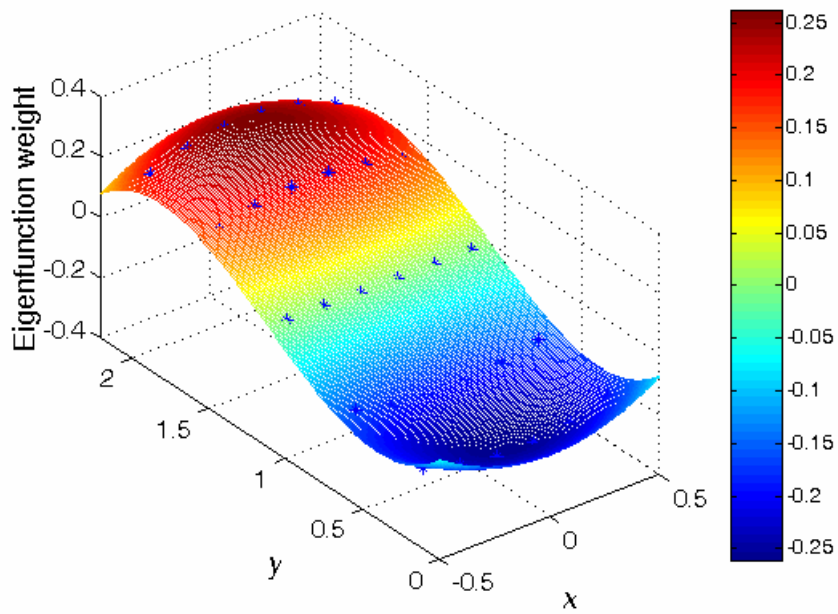
Figure 3.51 Second eigenfunction from correlation function.
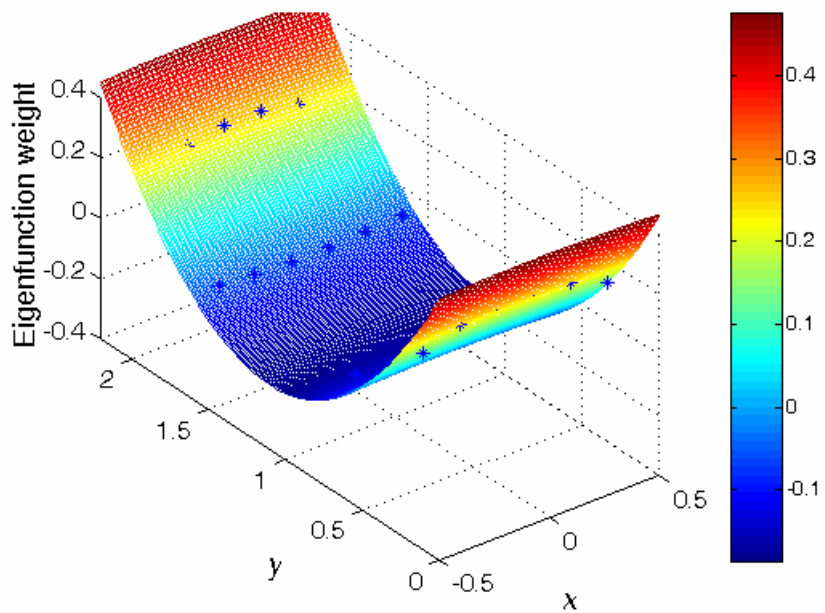
Figure 3.52 Third eigenfunction from correlation function.

135
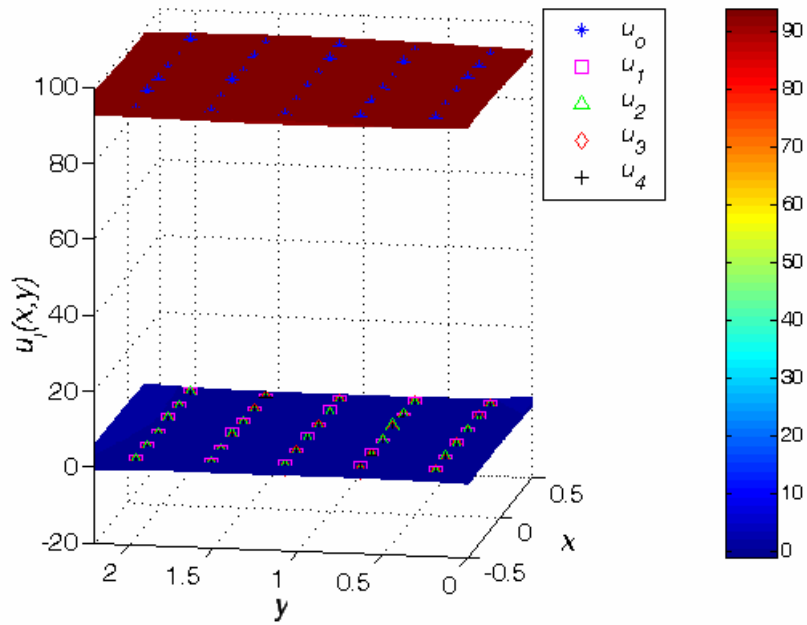
Figure 3.53 $u_i(y)$ **distribution.**
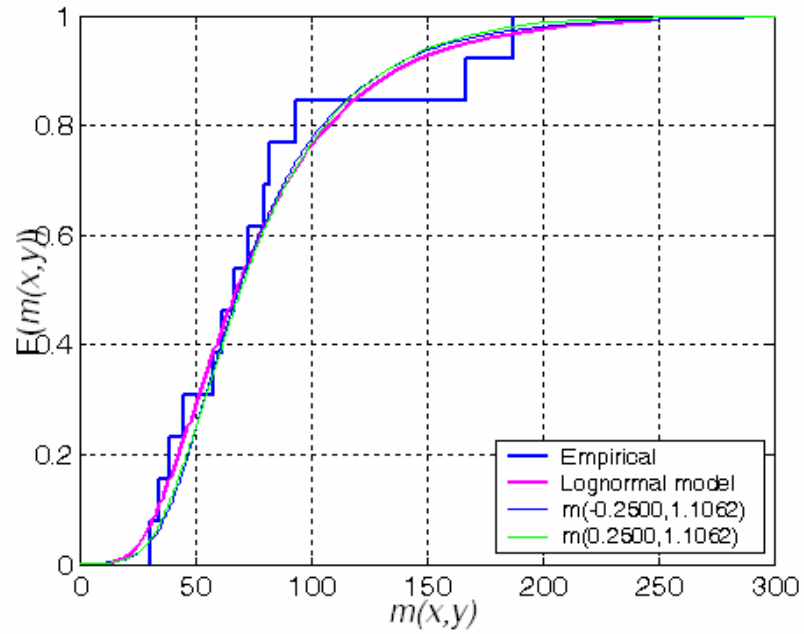
Figure 3.54 Comparison between empirical cdfs and multi-order four-dimensional PC cdfs at control points $X(-0.25, 1.10)$ and $X(0.25, 1.10)$.
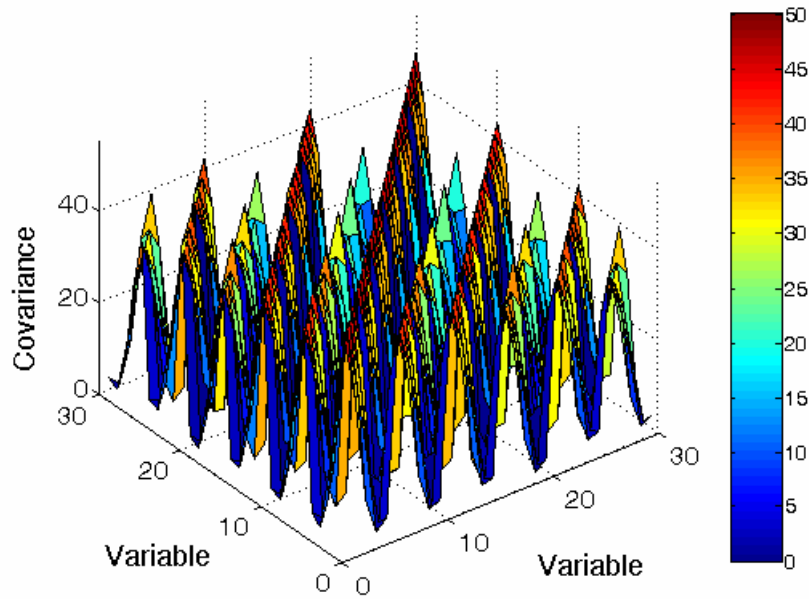
Figure 3.55 Graphical representation of the synthesized covariance matrix from multi-order four-dimensional PC simulations.
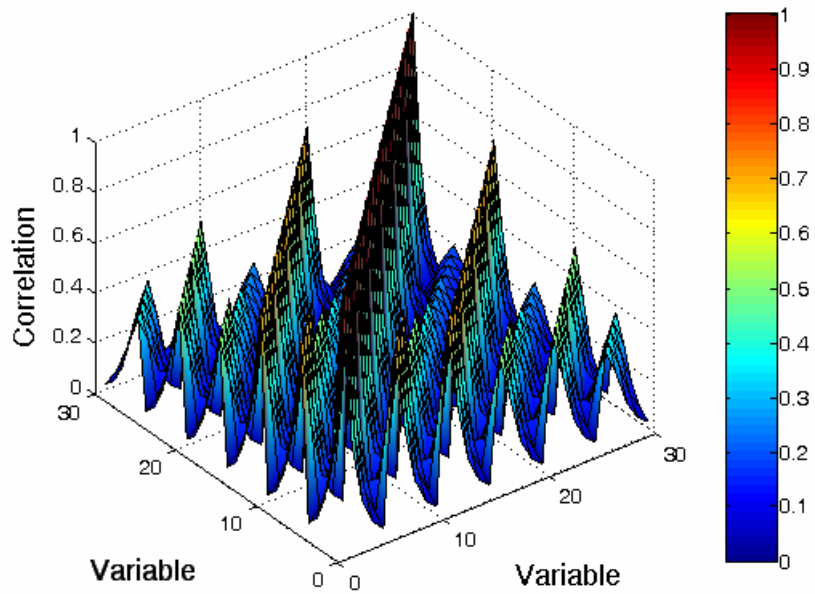
Figure 3.56 Graphical representation of the synthesized correlation matrix from multi-order four-dimensional PC simulations.

137
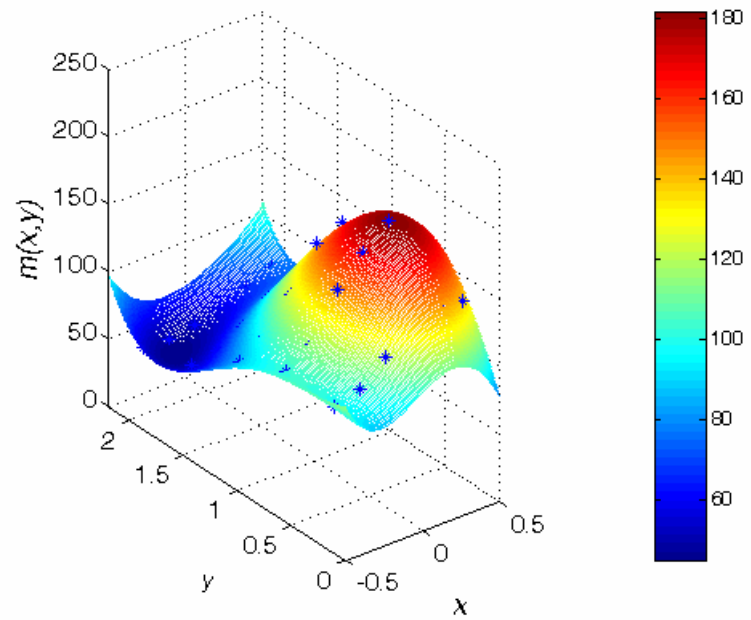
Figure 3.57 Typical multi-order four-dimensional PC simulations.

a)   b)
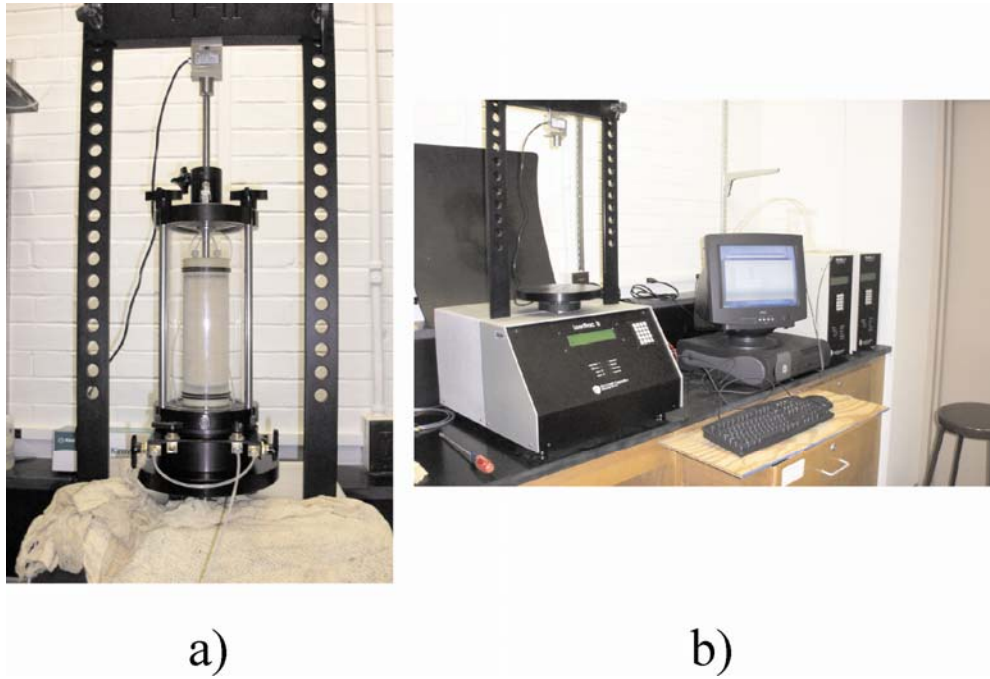
Figure 4.1 Triaxial GeoComp system.
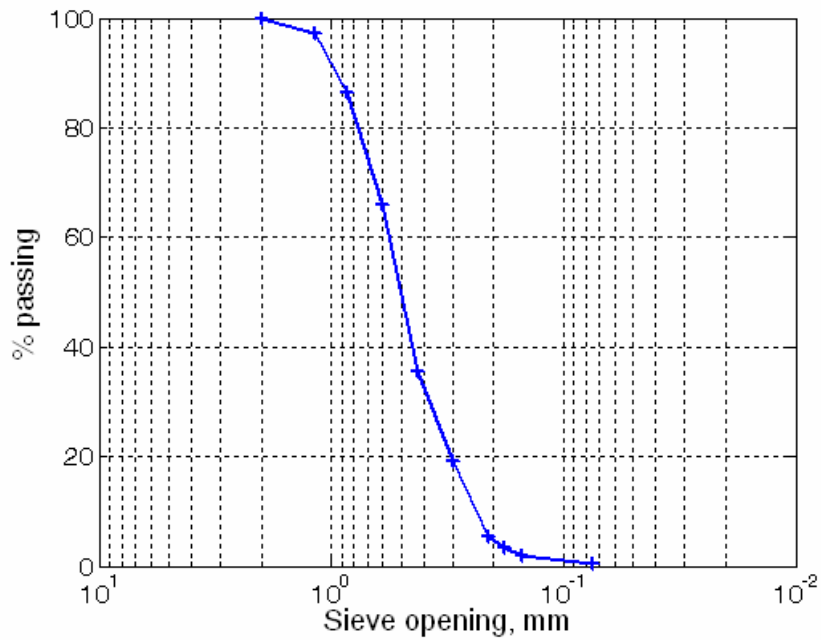
Figure 4.2 Grain size distribution.

a)   b)   c)

d)   e)
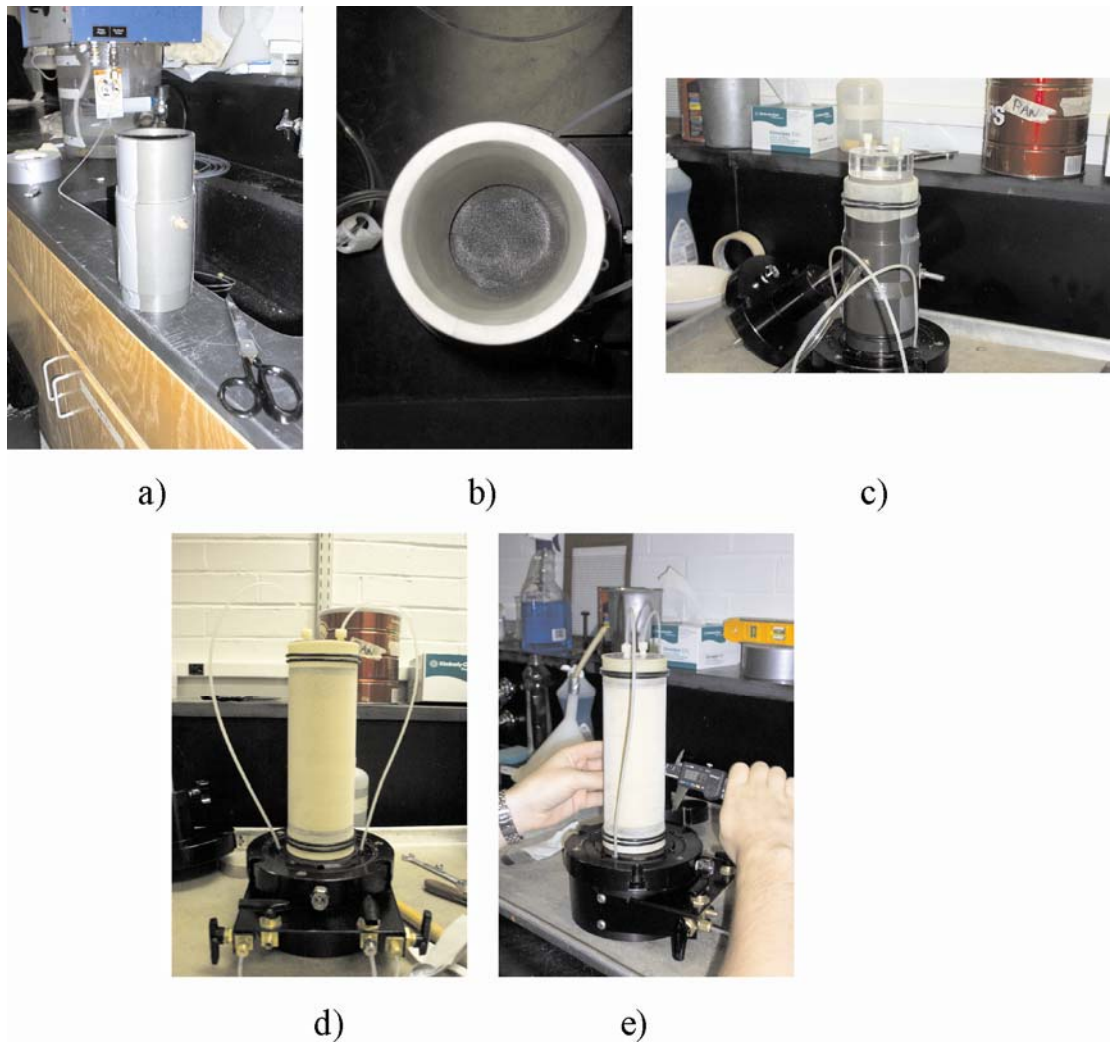
Figure 4.3 Sequence of sampling preparation.
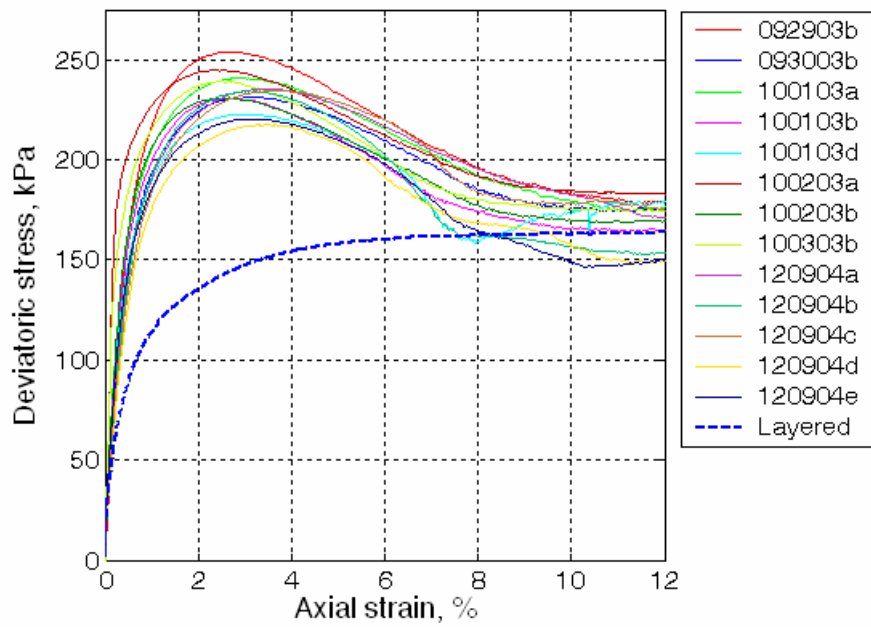
Figure 4.4 Triaxial strain-stress curves.

Reference Surface

Target Surface

Displacement Vector
(best match)

Searching
Area

Time=t_0

Time=t_i
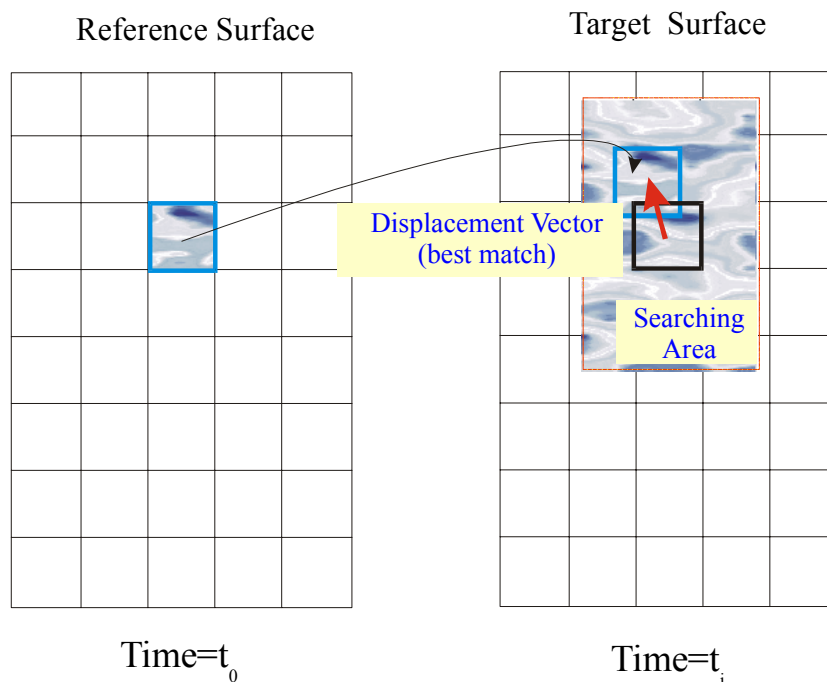
Figure 4.5 Principle of digital image correlation.
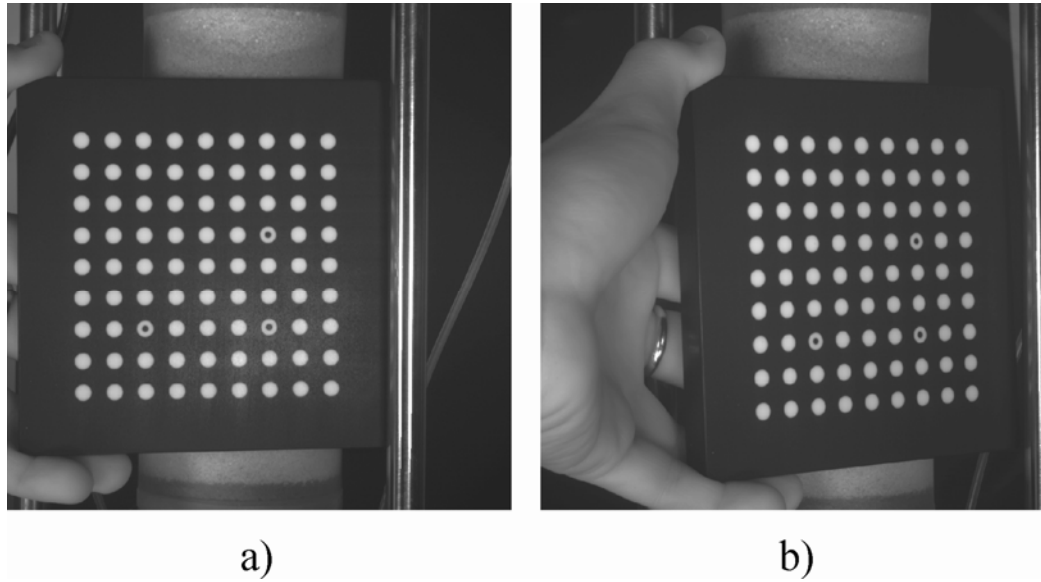
Figure 4.6 Cameras calibration.

Figure 4.7 Triaxial test with 3D imaging system.
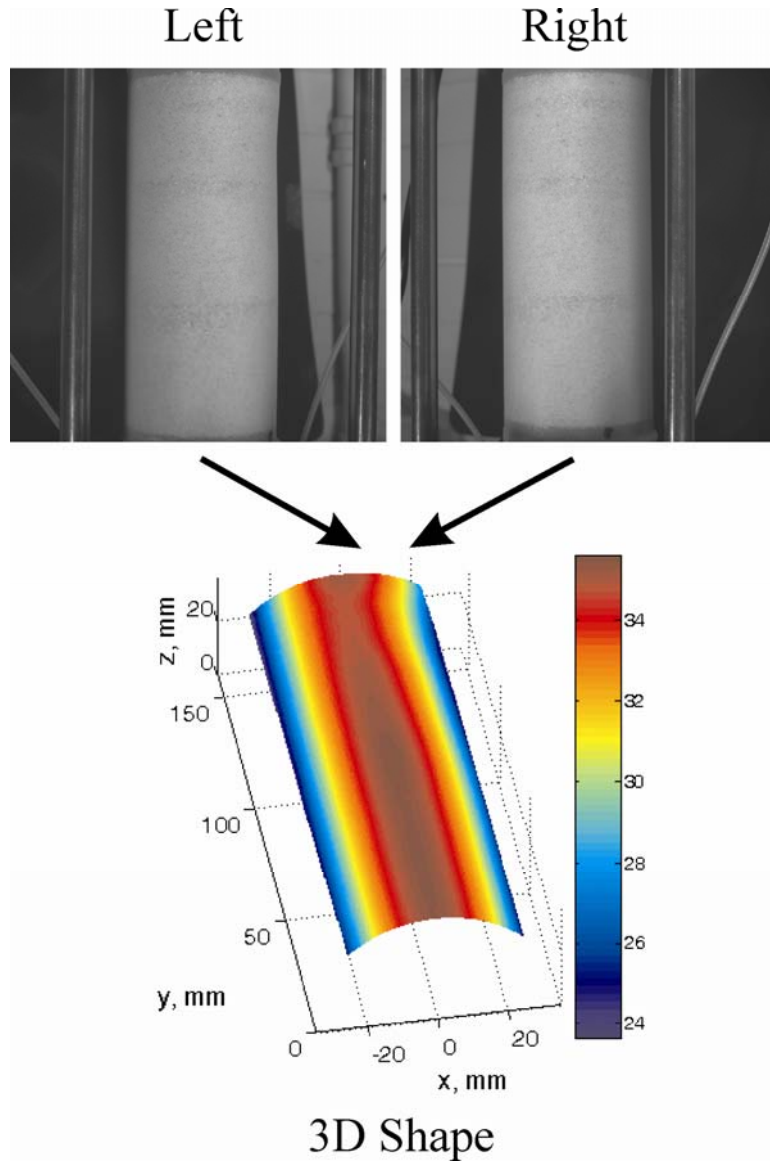
Figure 4.8 Specimen spatial reference and shape estimation.
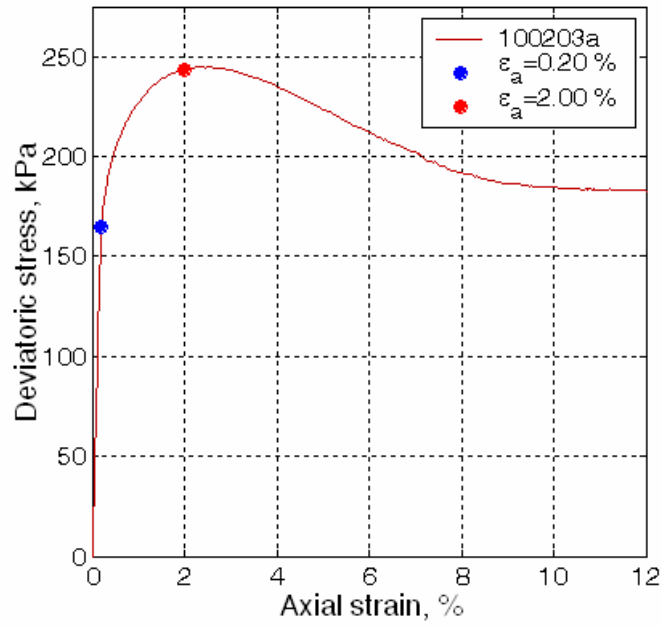
Figure 4.9 Strain-stress curve. Test 100203a.
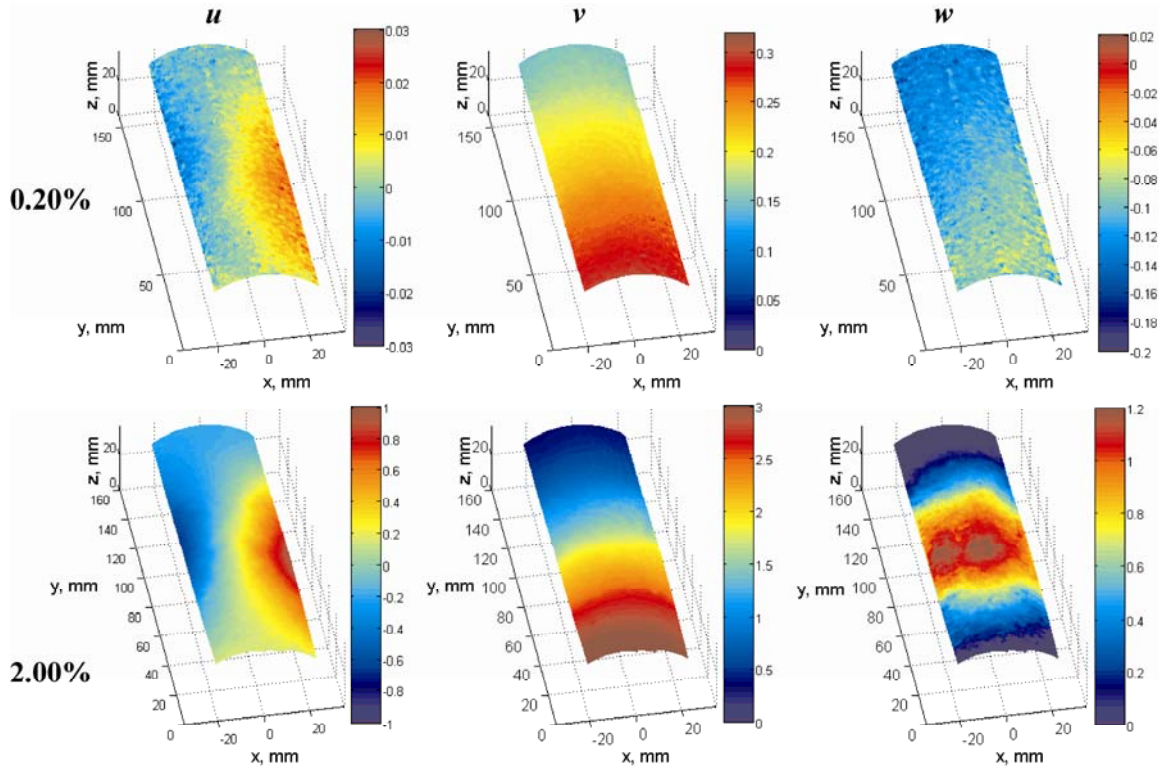
Figure 4.10 *u*, *v* and *w* full-field displacements. Test 100203a.

144
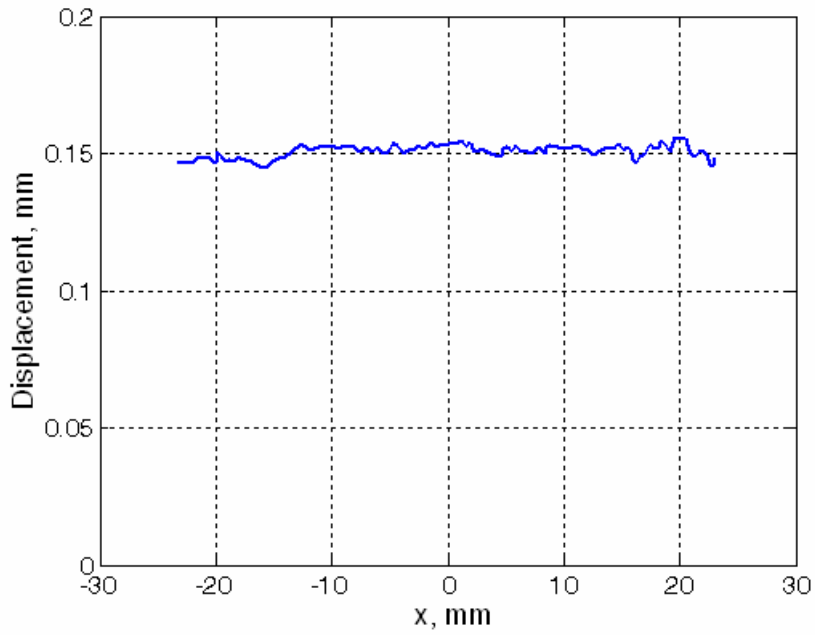
Figure 4.11 Typical profile of averaged vertical displacements on the boundary between soil and top porous stone. Test 100203a.
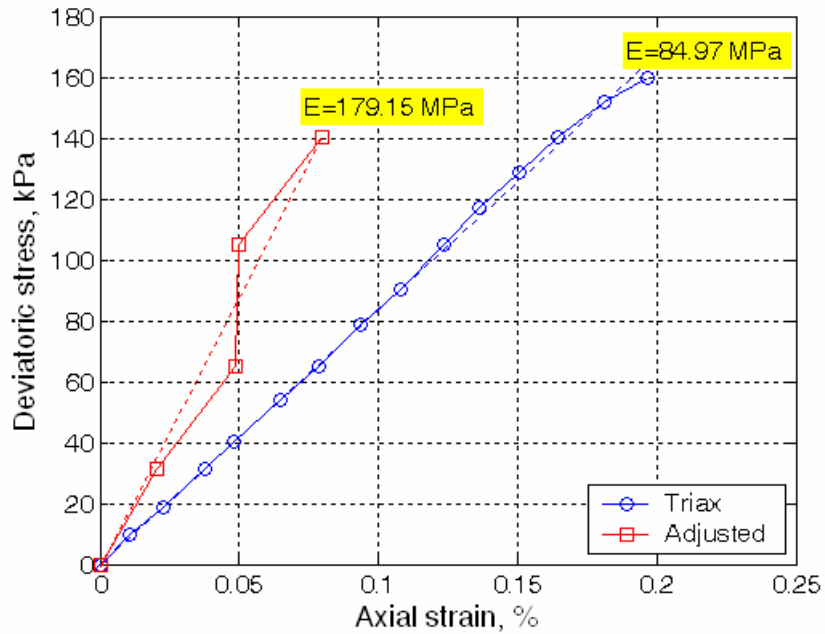
Figure 4.12 Measured and adjusted Young's modulus from stress-strain curves. Test 100203a.

145
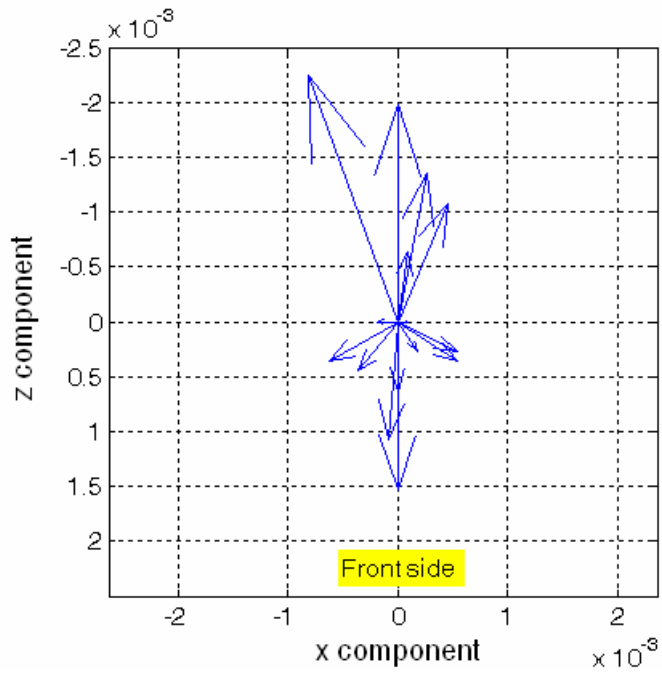
Figure 4.13 Vector representation of top porous stone apparent tilt.
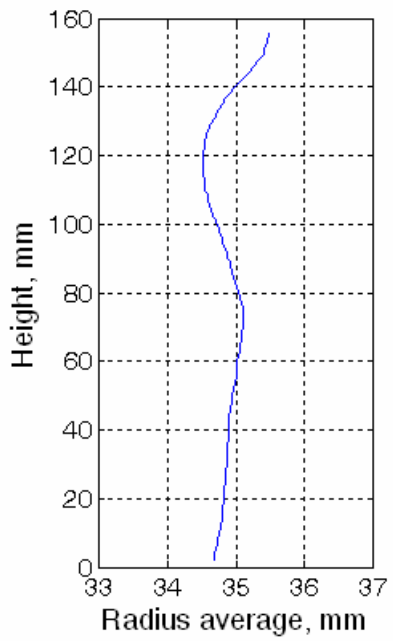
Figure 4.14 Vertical profile of radius local averages of test 100203b.

146

Typical area of analysis

Figure 4.15 Typical area of interests for VIC-3D accuracy analysis.
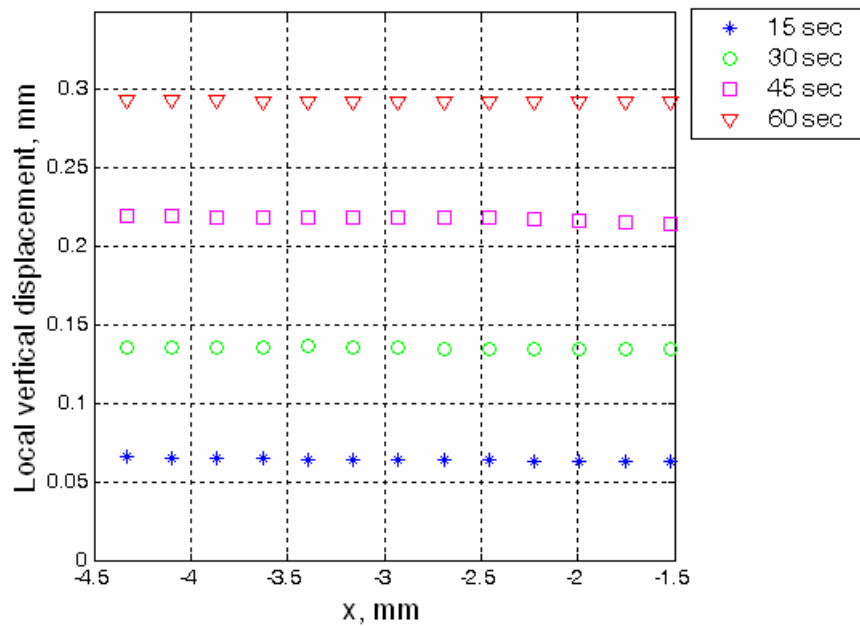
Figure 4.16 Averaged vertical displacements on the boundary between soil and top porous stone at different deformation stages. Test 100103d.
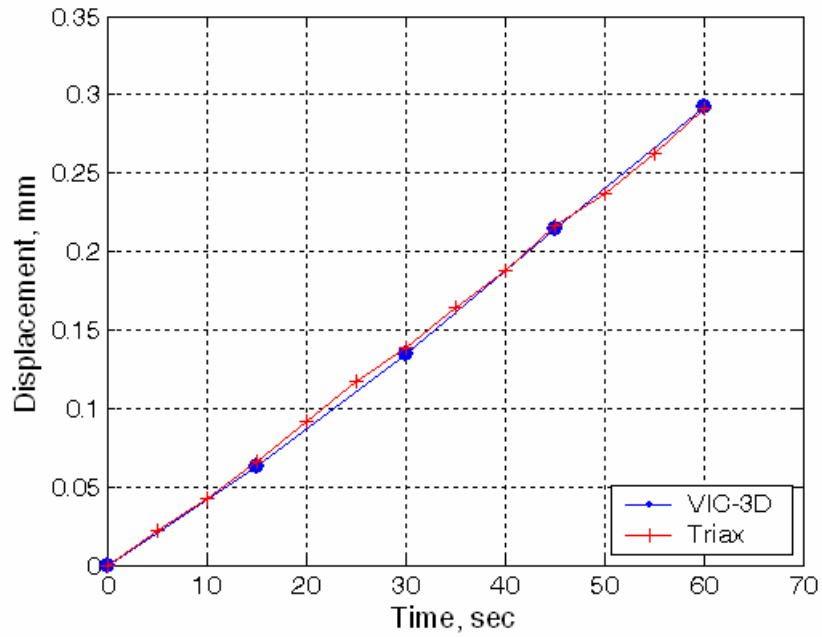
Figure 4.17 Comparison of displacement measurements between Triax and VIC-3D. Test 100103d.
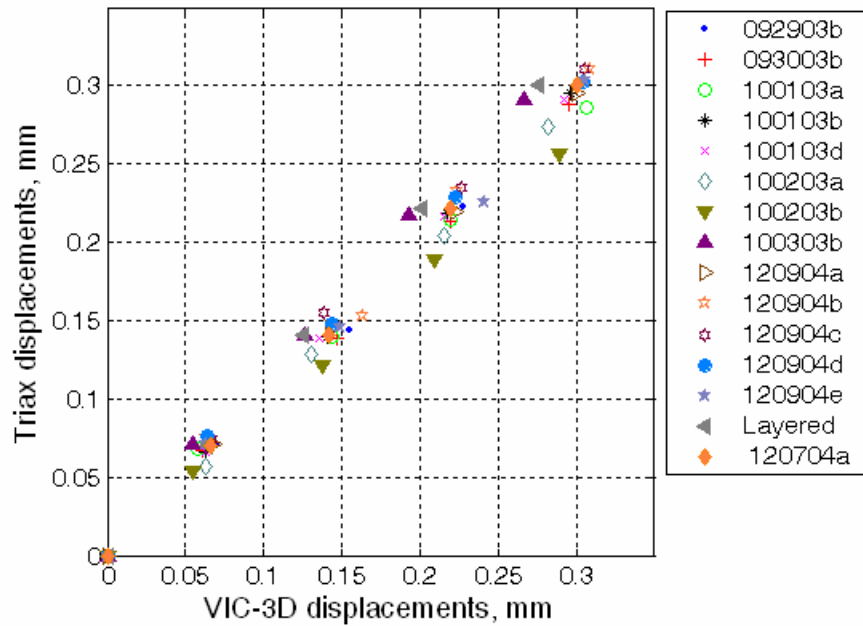
Figure 4.18 Comparison of displacement measurements between Triax and VIC-3D. All tests.

148
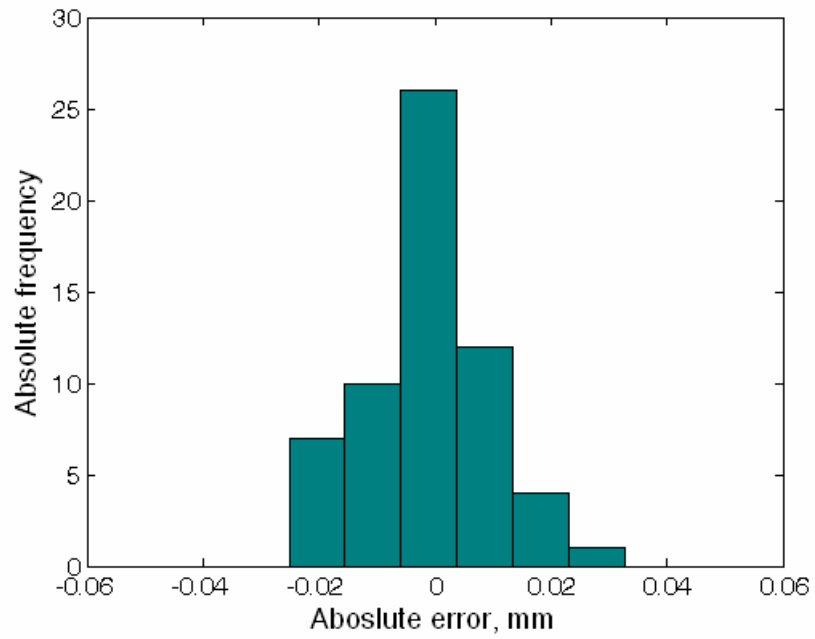
Figure 4.19 Absolute frequency histogram of absolute error of displacement measurements between Triax and VIC-3D. All tests.
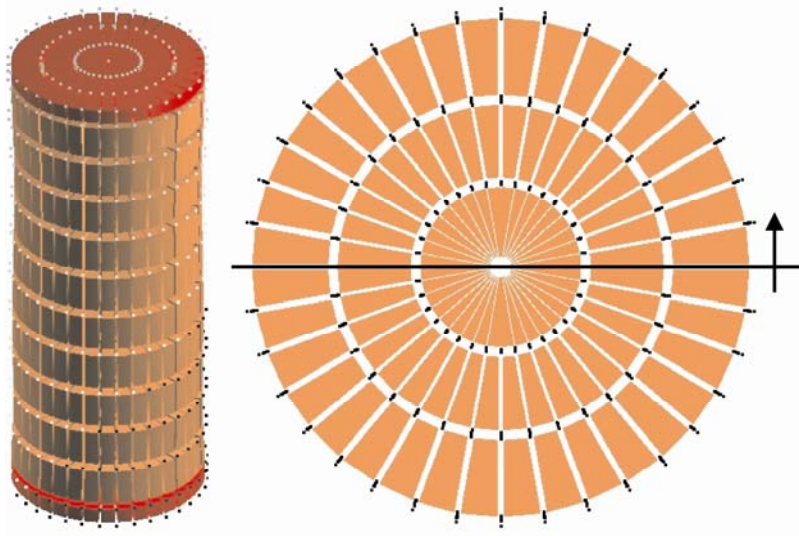
Figure 5.1 3D-FEM 'Hom' model.
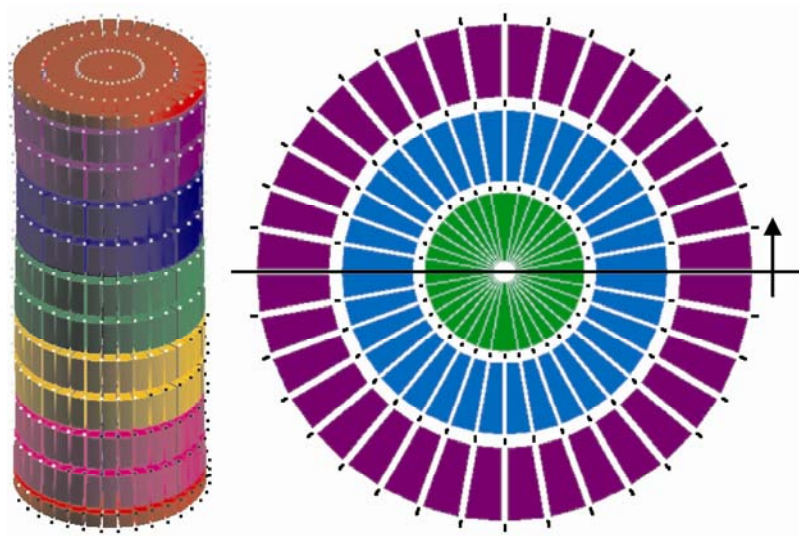
Figure 5.2 3D-FEM 'Axi' model.
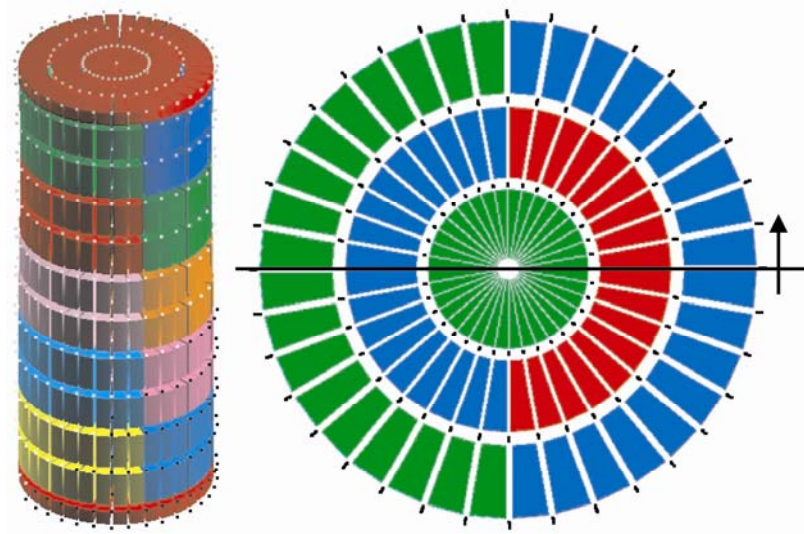
Figure 5.3 3D-FEM 'Het-I' model.
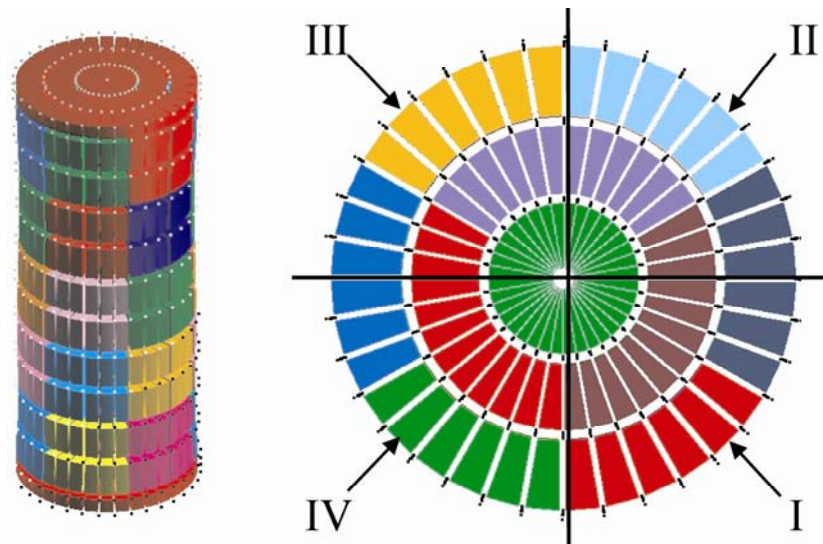
Figure 5.4 3D-FEM 'Het-II' model.
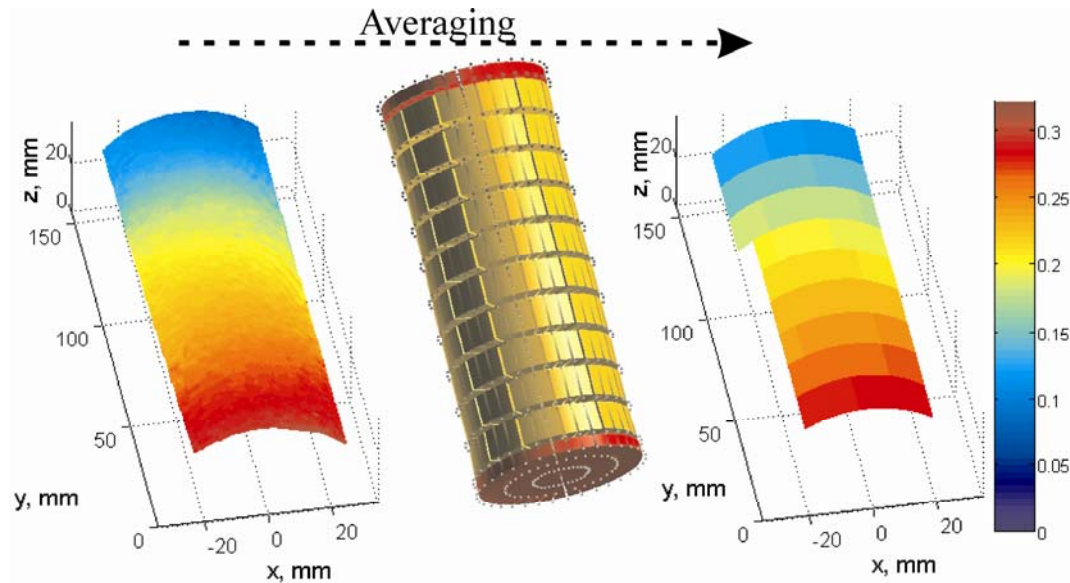
Figure 5.5 Typical averaging transformation.
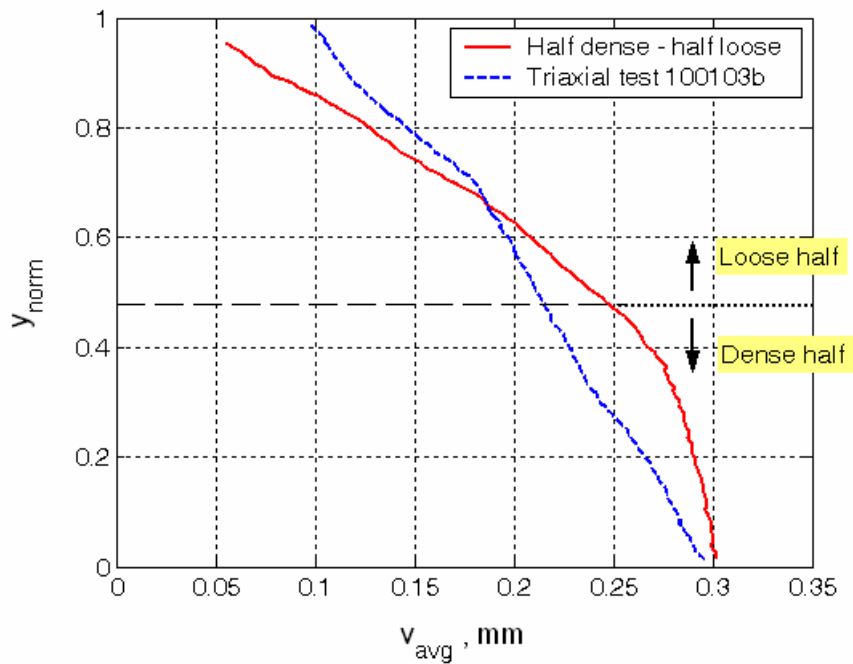
Figure 5.6 Comparison of averaged vertical displacements between tests 120704c (special) and 100103b.

152
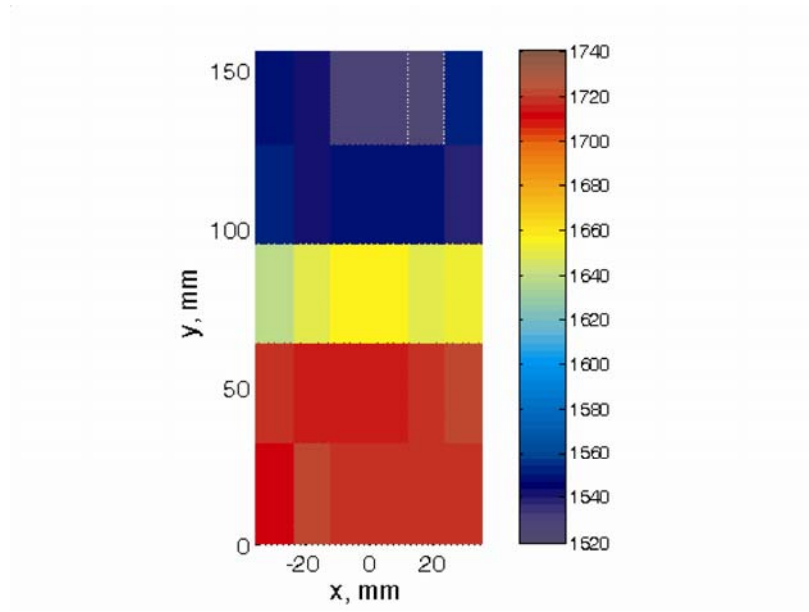
Figure 5.7 Density optimal distribution (kg/m³). Layered specimen.
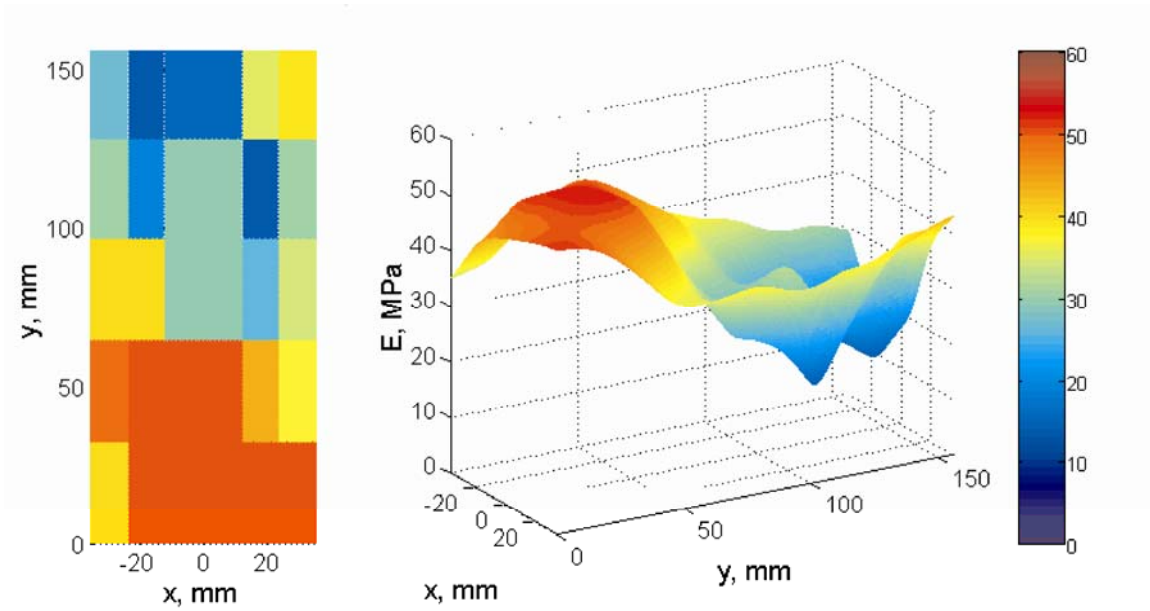
Figure 5.8 Young's moduli optimal distribution. Layered specimen.

153
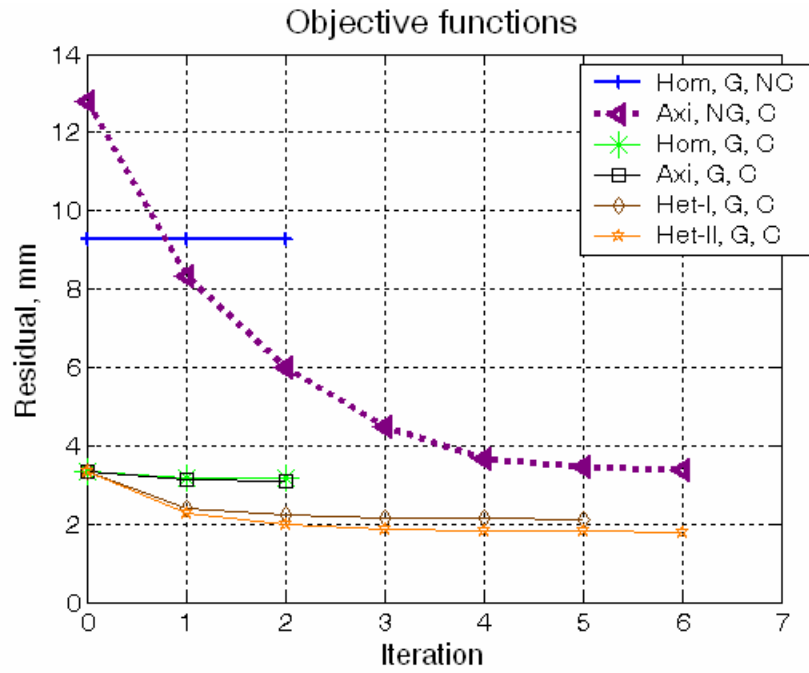
Figure 5.9 Objective functions from parametric analysis. Test 100103b.
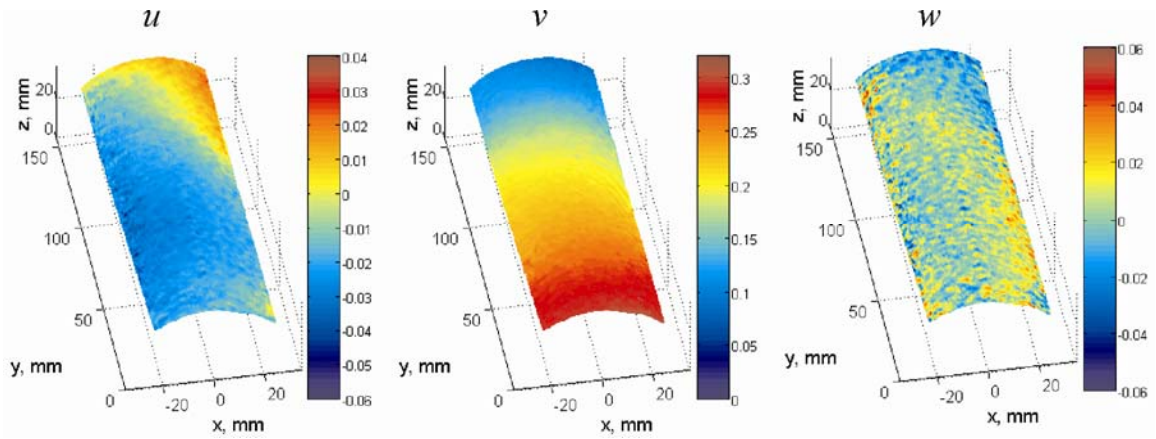
Figure 5.10 *Observations*: Full-field displacements at 0.2 % of axial strain. Test 100103b.
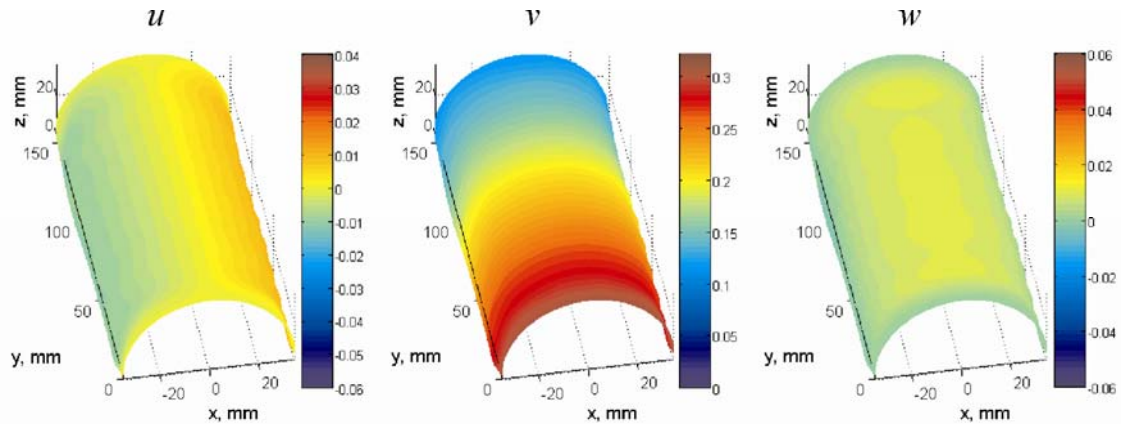
Figure 5.11 *Predictions*: Full-field displacements at 0.2 % of axial strain. Test 100103b, 'Hom' model.
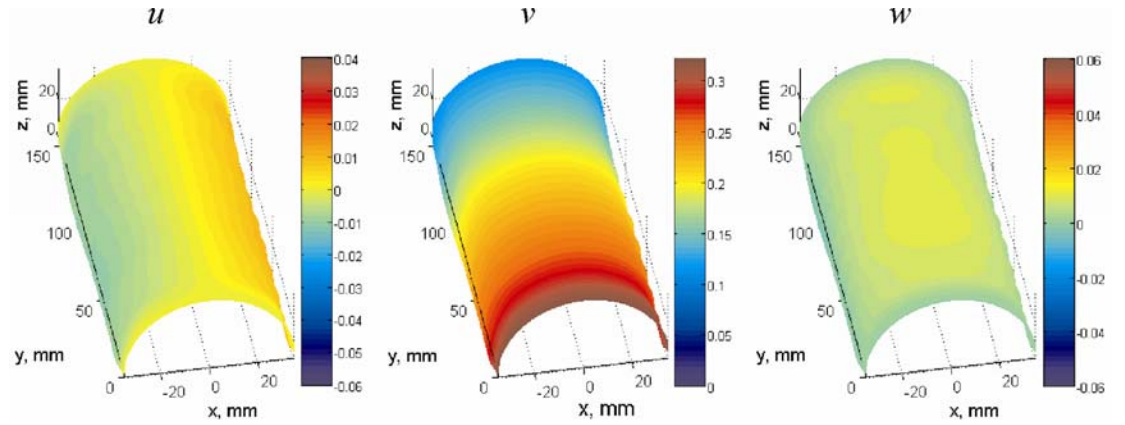
Figure 5.12 *Predictions*: Full-field displacements at 0.2 % of axial strain. Test 100103b, 'Axi' model.
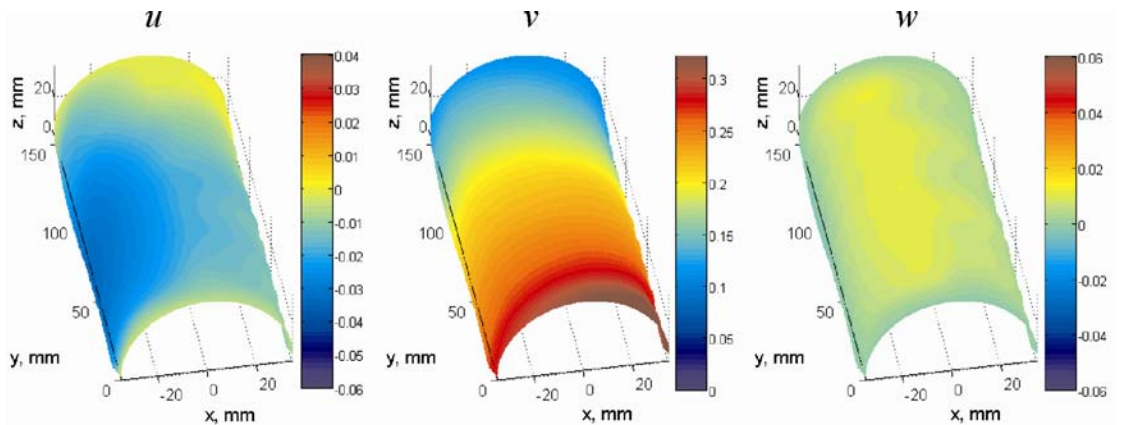
Figure 5.13 *Predictions*: Full-field displacements at 0.2 % of axial strain. Test 100103b, 'Het-I' model.
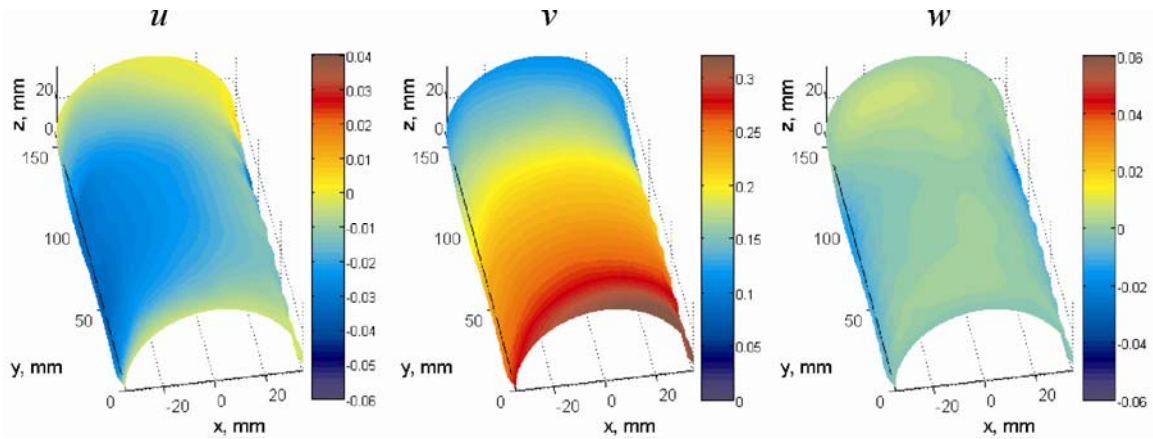
Figure 5.14 *Predictions*: **Full-field displacements at 0.2 % of axial strain. Test 100103b, 'Het-II' model.**

a)   b)   c)
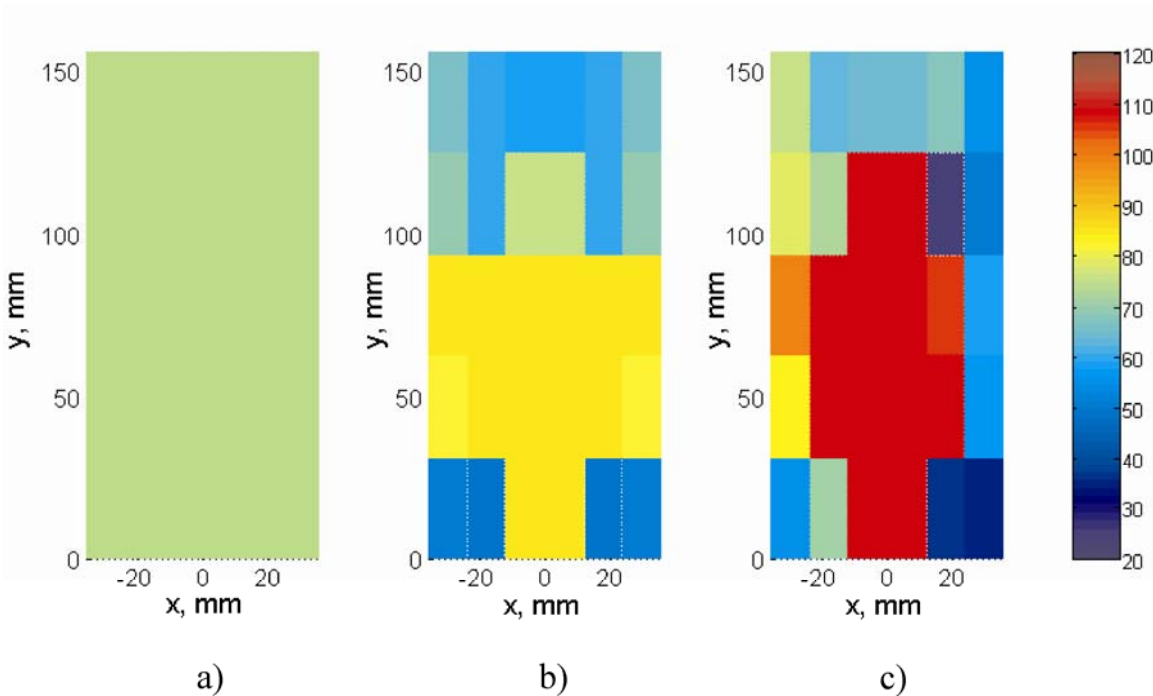
Figure 5.15 Young's moduli optimal distributions for models a) 'Hom', b) 'Axi' and c) 'Het-I'. Test 100103b.
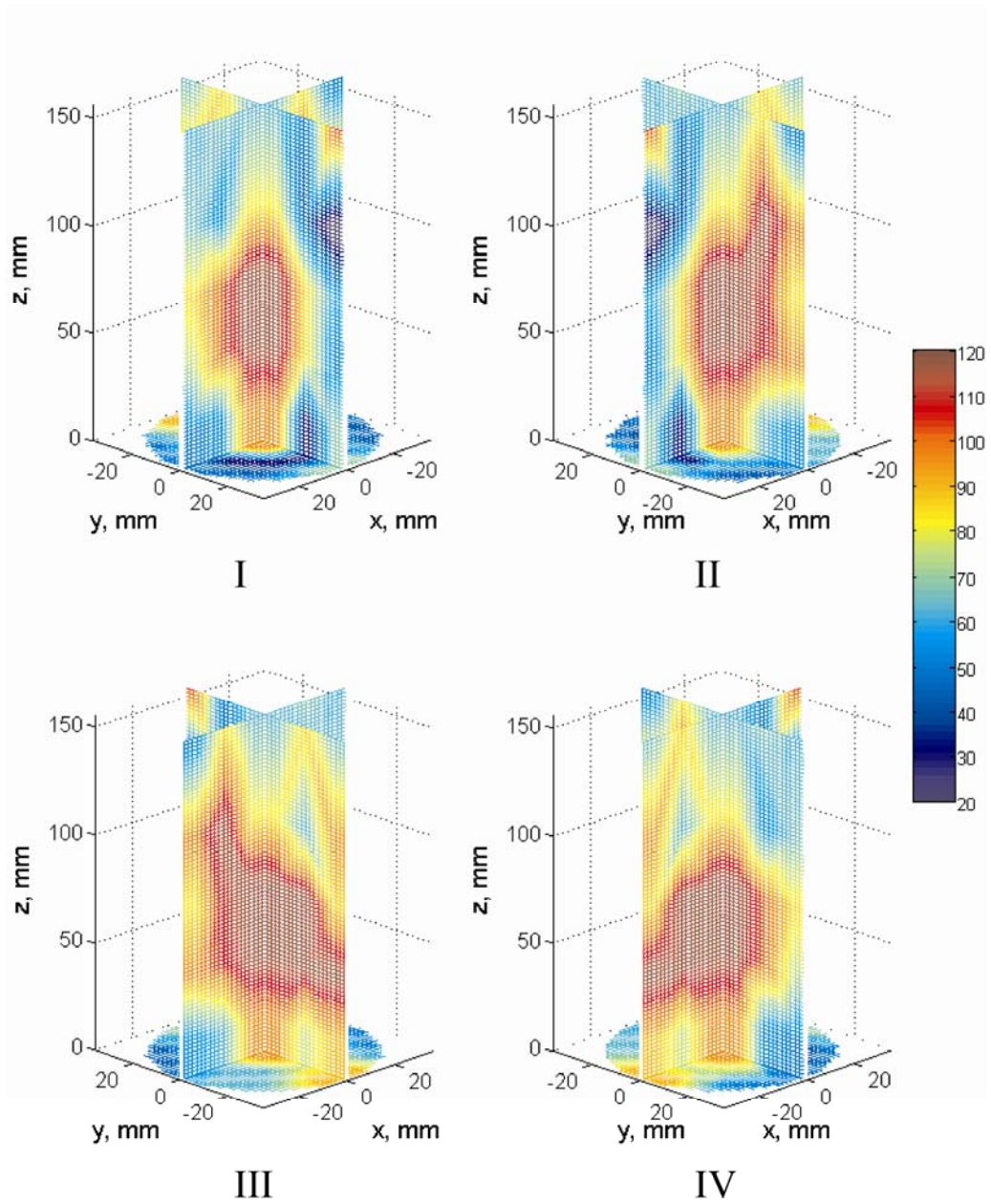
Figure 5.16 Young's moduli optimal distributions for model 'Het-I'. Test 100103b.
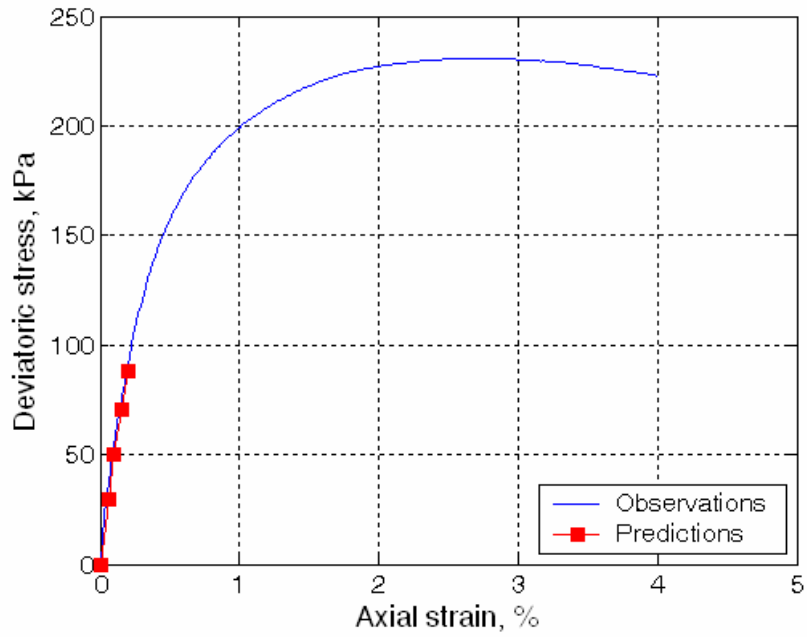
Figure 5.17 Comparison of strain-stress responses between observations (triaxial readings) and predictions ('Het-II model'). Test 100103b.
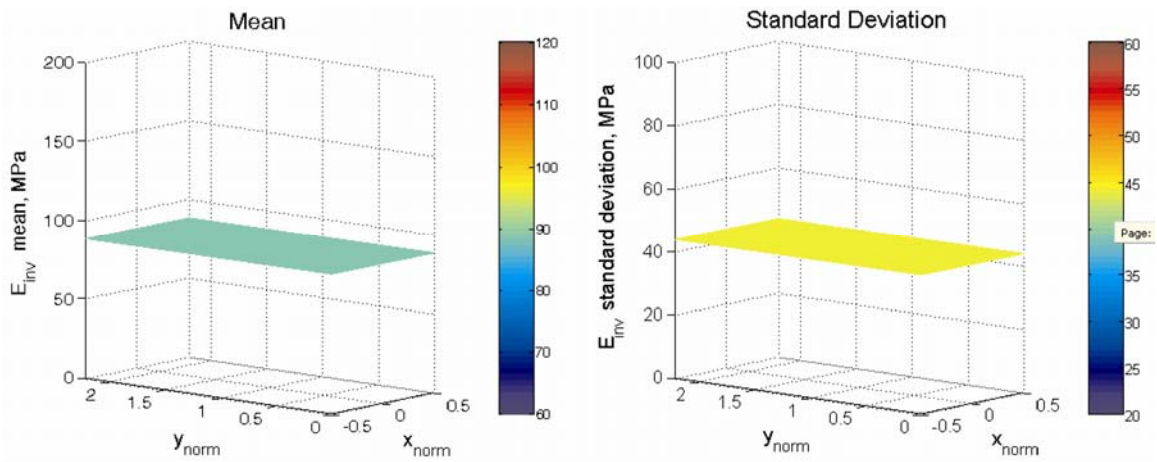
Figure 5.18 Mean and standard deviation distributions of Young's moduli. All tests, 'Hom' model.
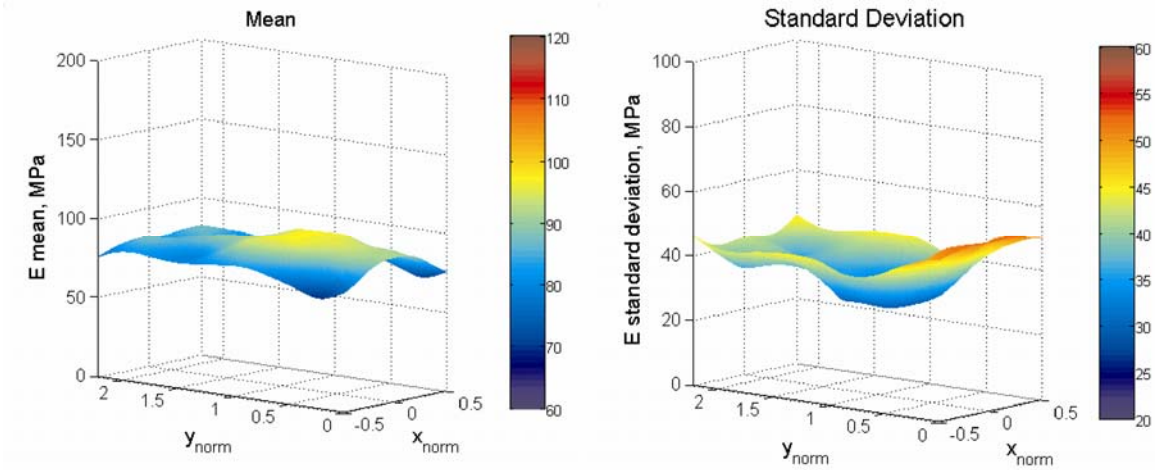
Figure 5.19 Mean and standard deviation distributions of Young's moduli. All tests, 'Axi' model.
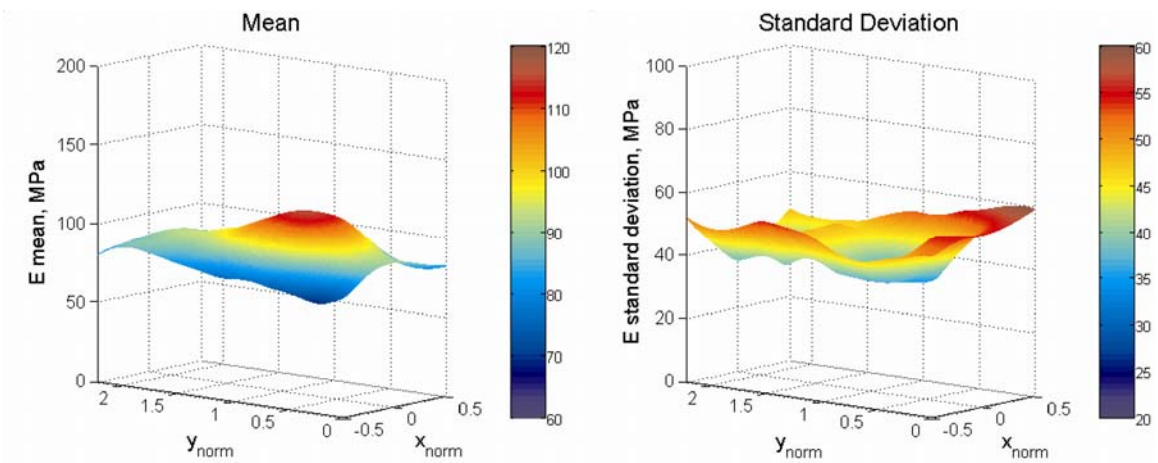
Figure 5.20 Mean and standard deviation distributions of Young's moduli. All tests, 'Het-I' model.

159
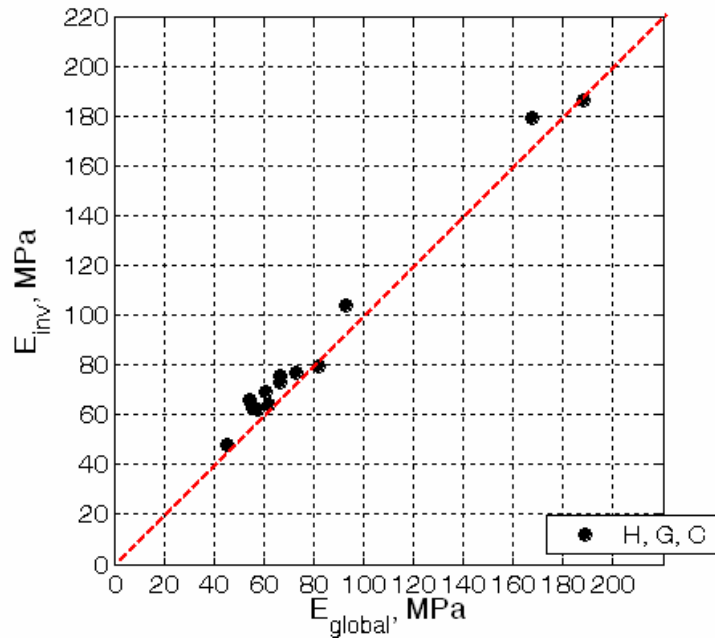
Figure 5.21 Linear correlation between Young's moduli global *observations* and *predictions*. All tests, 'Hom' model.
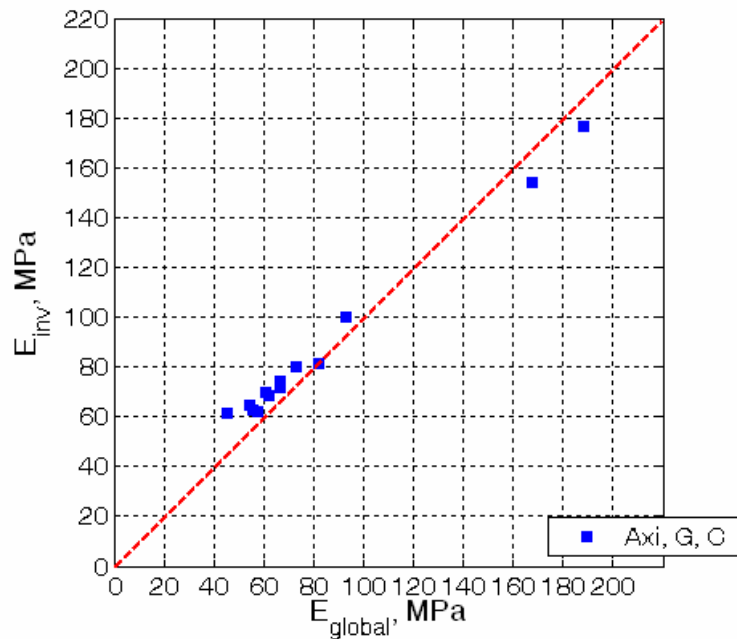
Figure 5.22 Linear correlation between Young's moduli global *observations* and *predictions*. All tests, 'Axi' model.
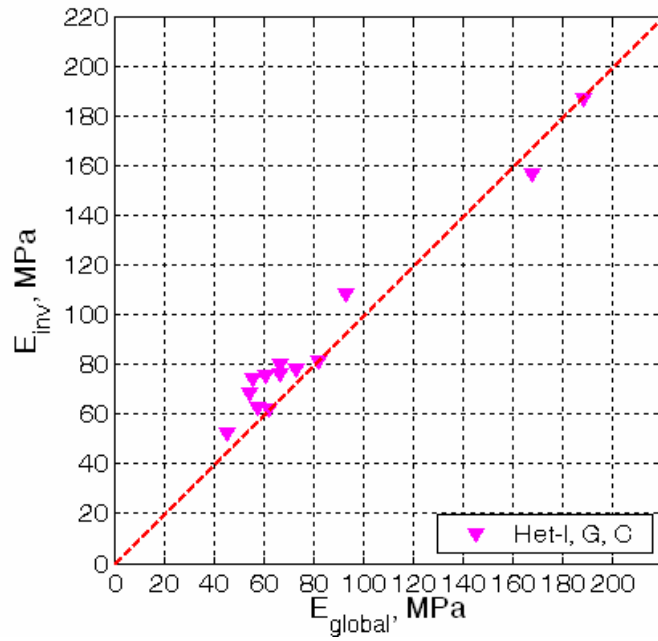
Figure 5.23 Linear correlation between Young's moduli global *observations* and *predictions*. All tests, 'Het-I' model.
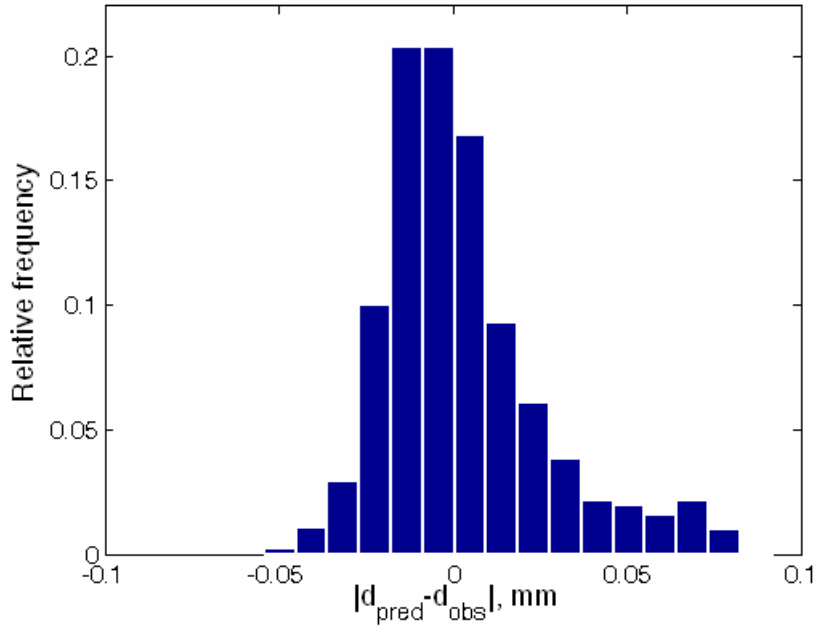
Figure 5.24 Relative frequency histogram of the norm of error estimates.

161
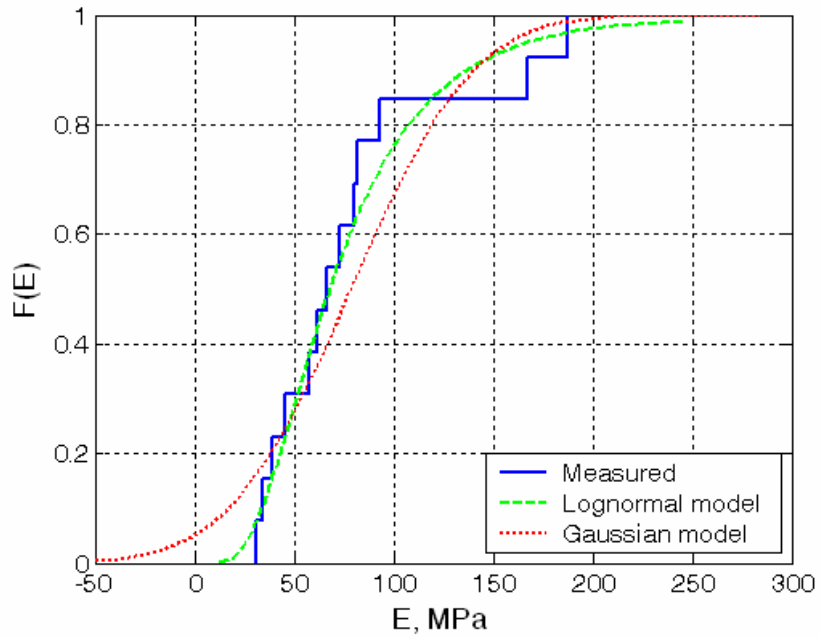
Figure 6.1 Comparison of Young's modulus cdfs between empirical, Gaussian and log-normal distributions.
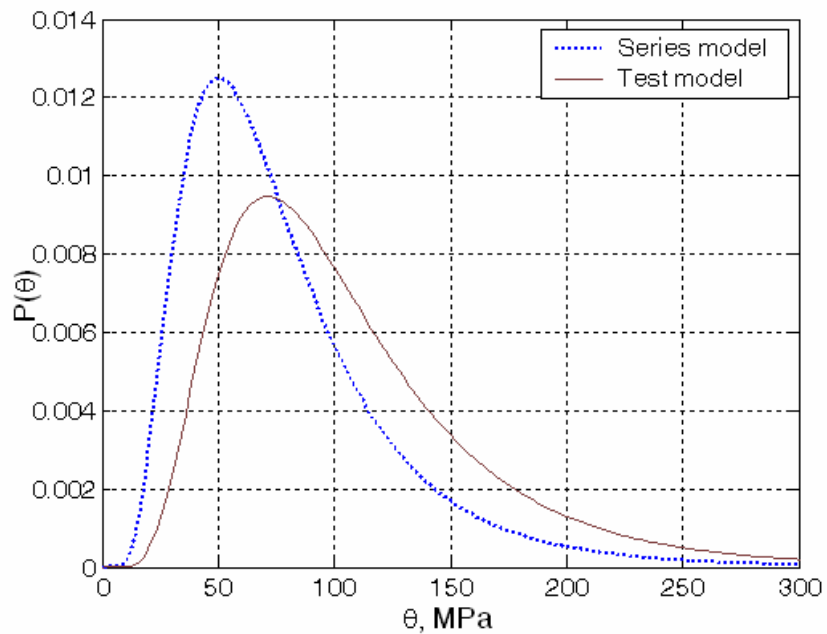
Figure 6.2 Log-normal pdfs of Young's moduli for modeling data and test 092903b.
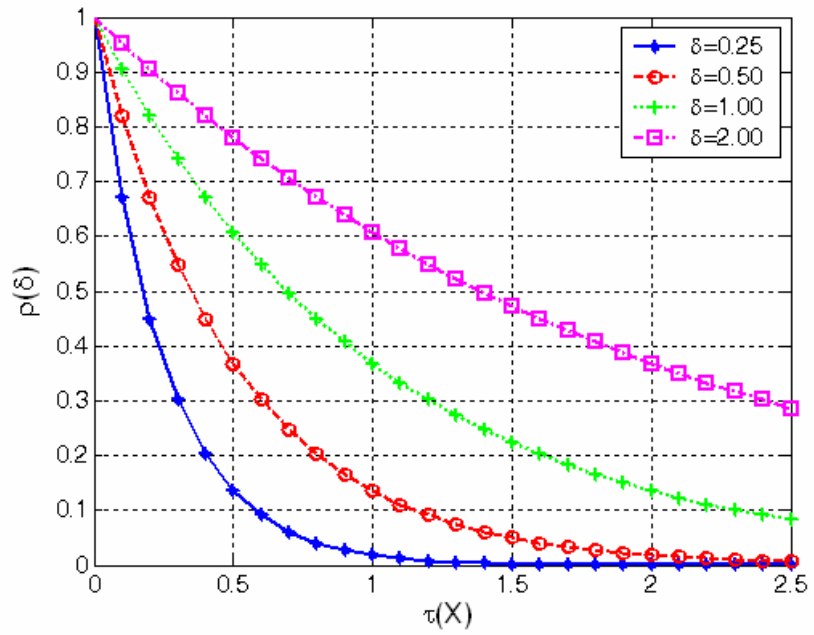
Figure 6.3 Isotropic correlation functions.
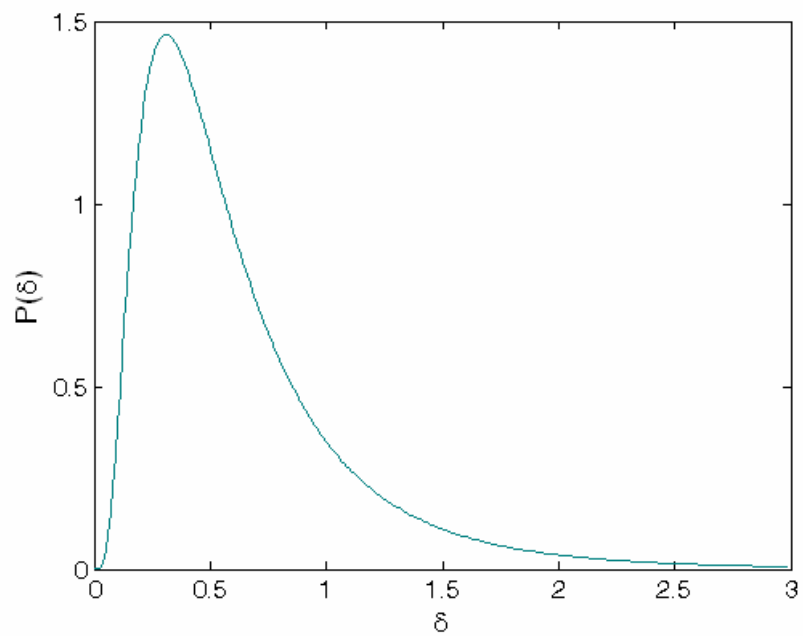
Figure 6.4 Log-normal model of the correlation parameter δ.

163
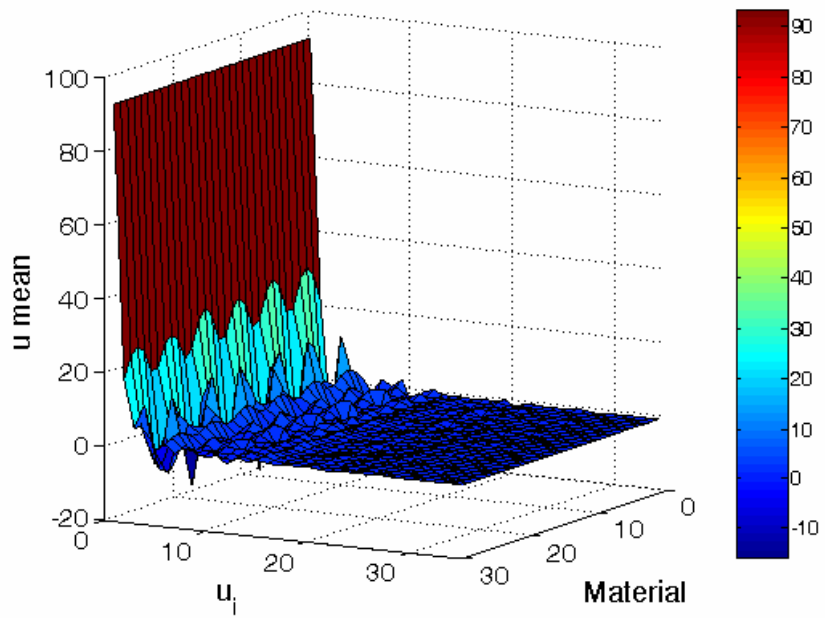
Figure 6.5 A-priori mean of the $u_i(X)$ field.
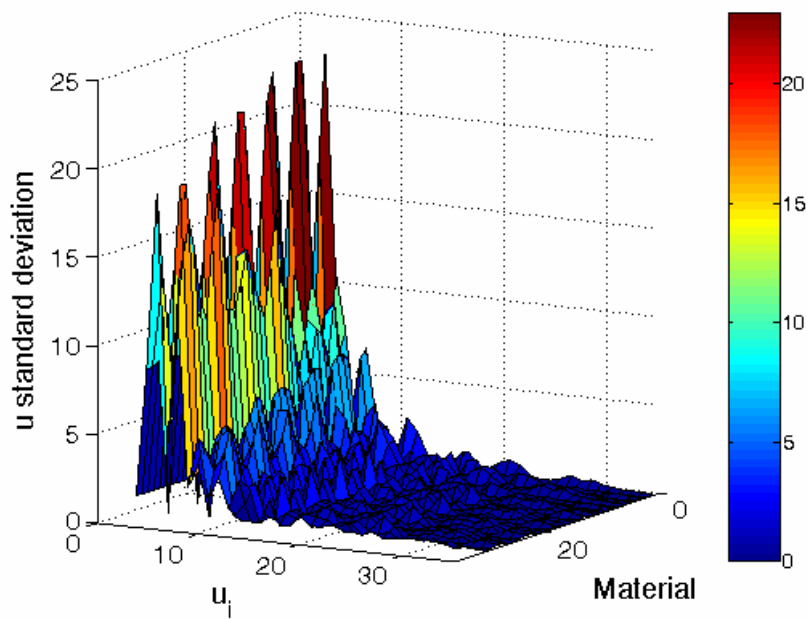
Figure 6.6 A-priori standard deviation of the $u_i(X)$ field.

164
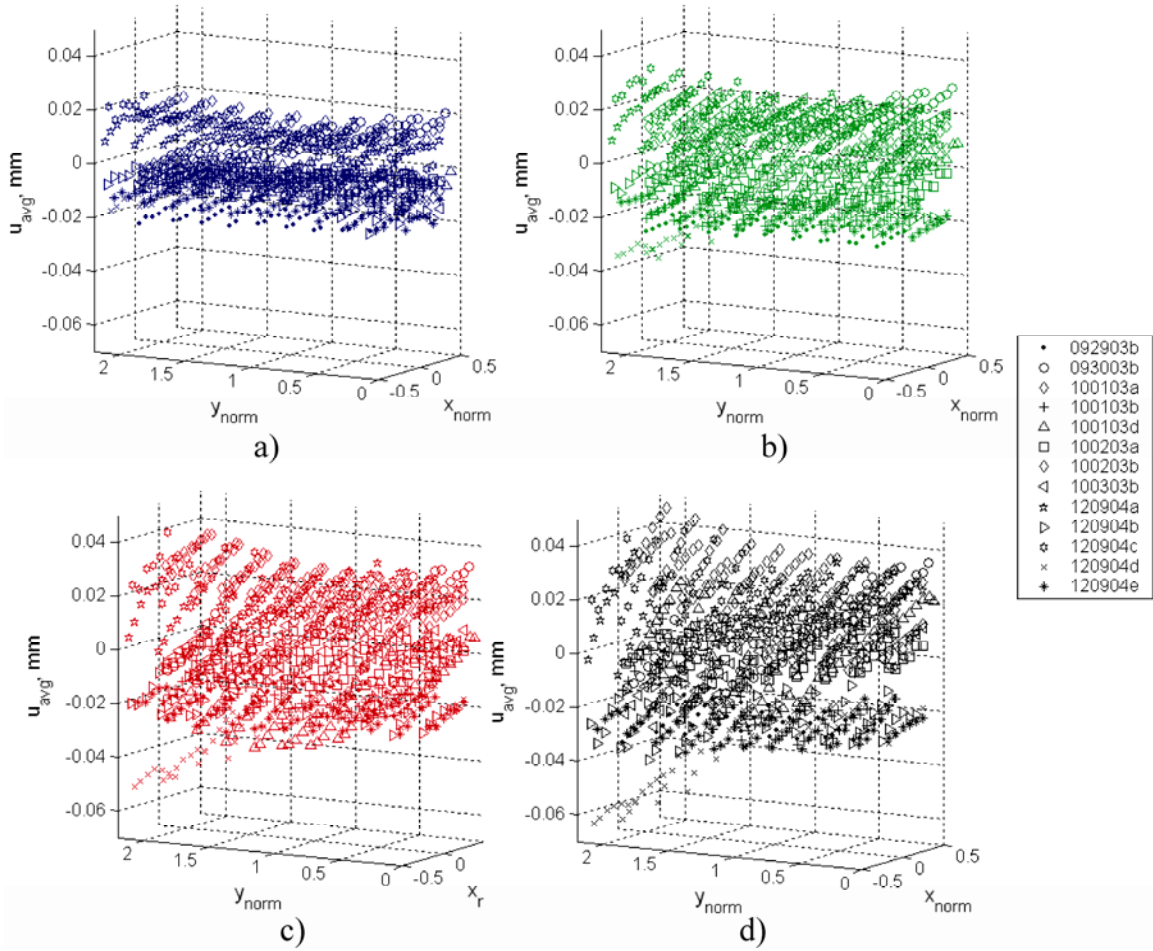
Figure 6.7 Data ensemble of $u(x_{norm}, y_{norm}, t)$ field.
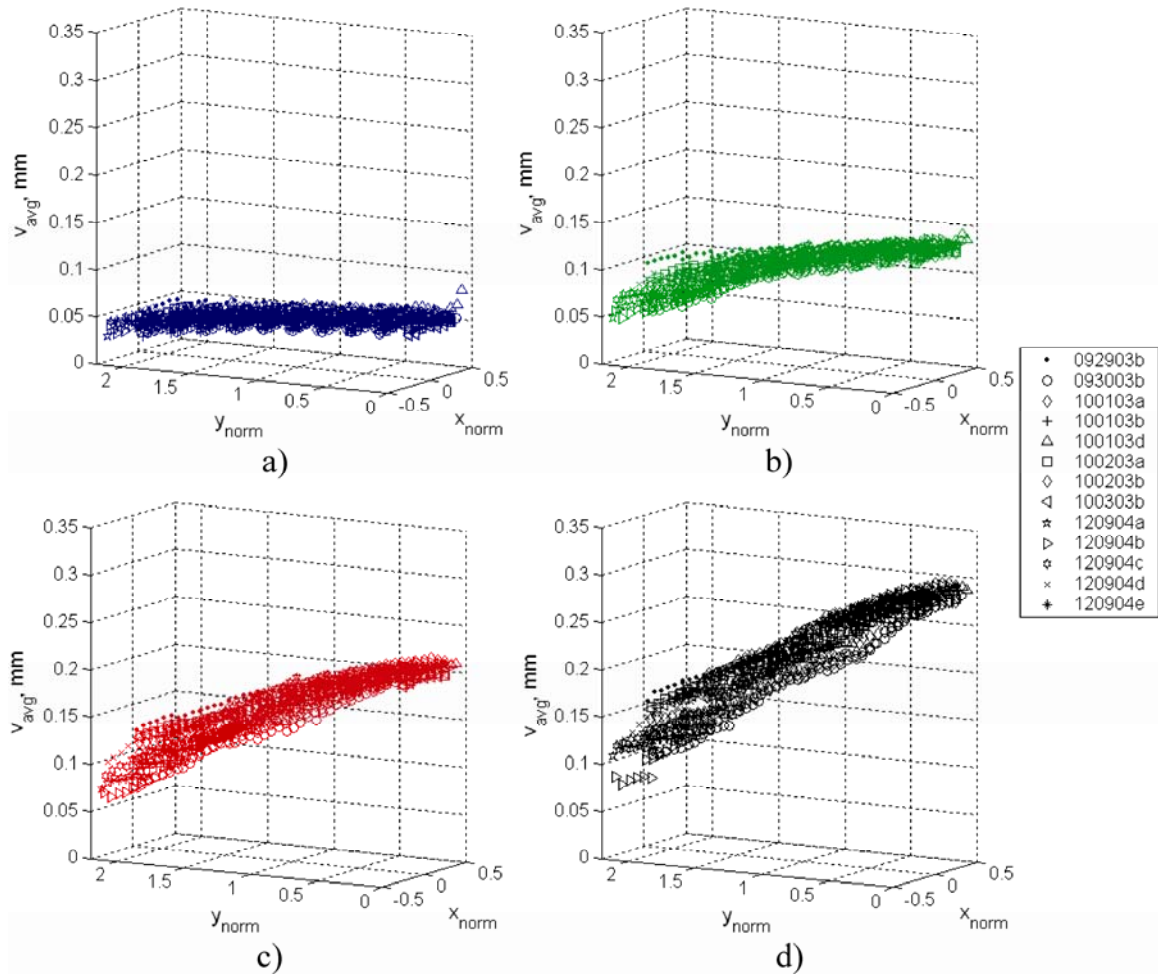
Figure 6.8 Data ensemble of $v(x_{norm}, y_{norm}, t)$ **field.**
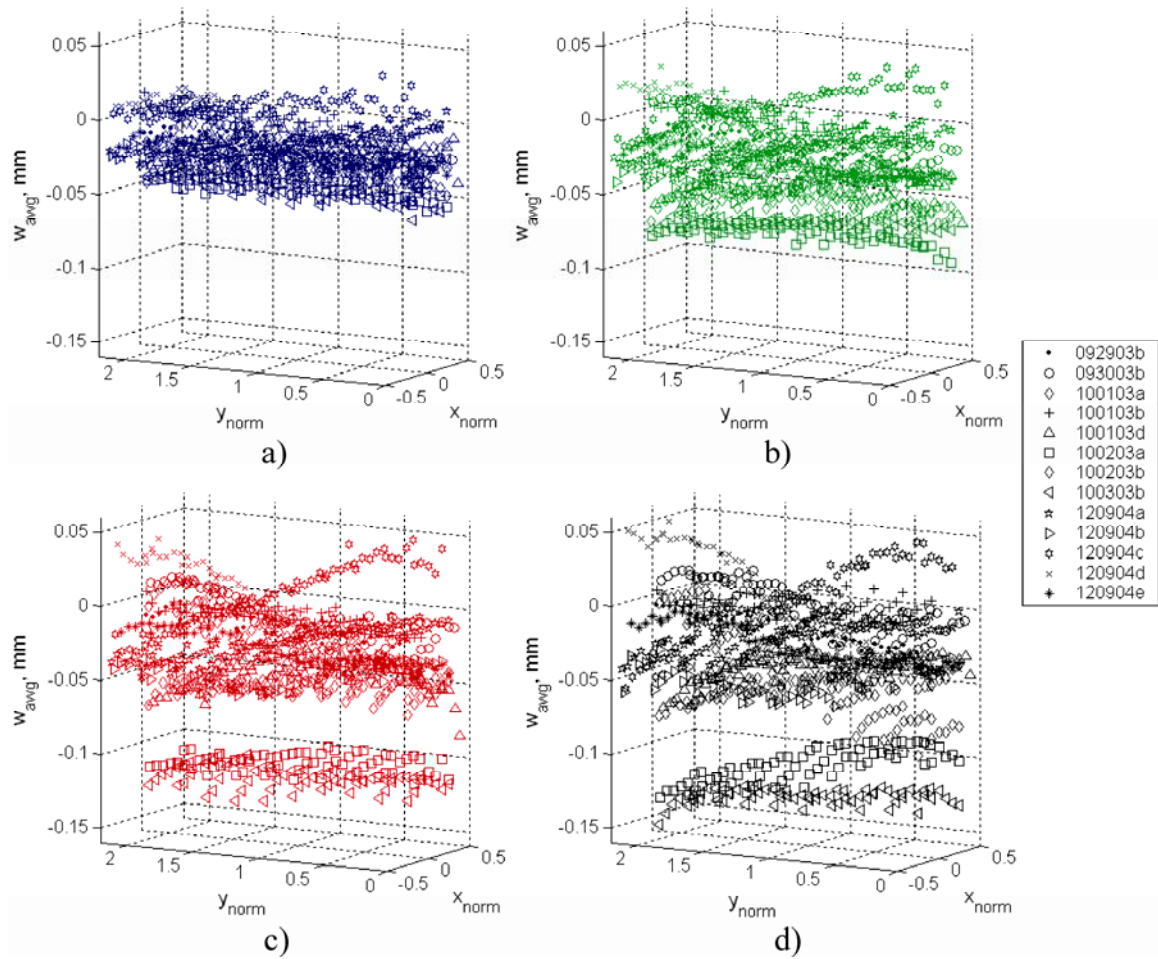
Figure 6.9 Data ensemble of $w(x_{norm}, y_{norm}, t)$ **field.**
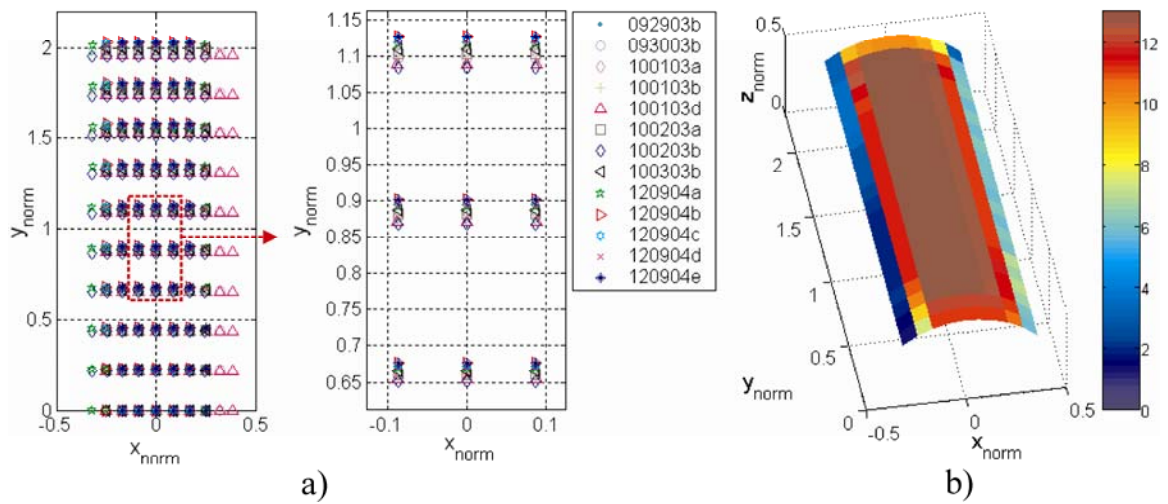
Figure 6.10 Data ensemble : a) Projection over the normalized vertical cross section, and b) spatial histogram of data counts.
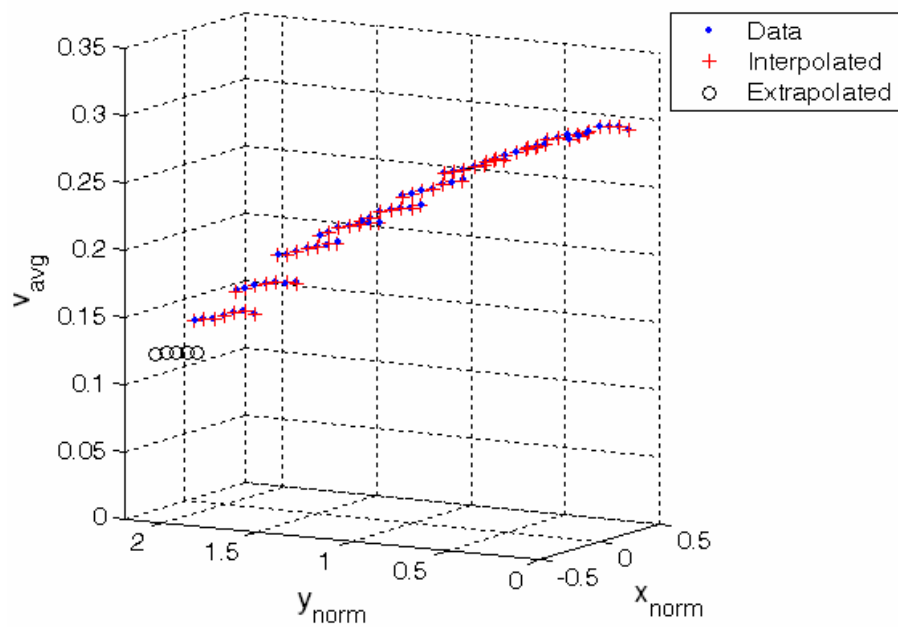
Figure 6.11 Typical data interpolation and extrapolation.

168
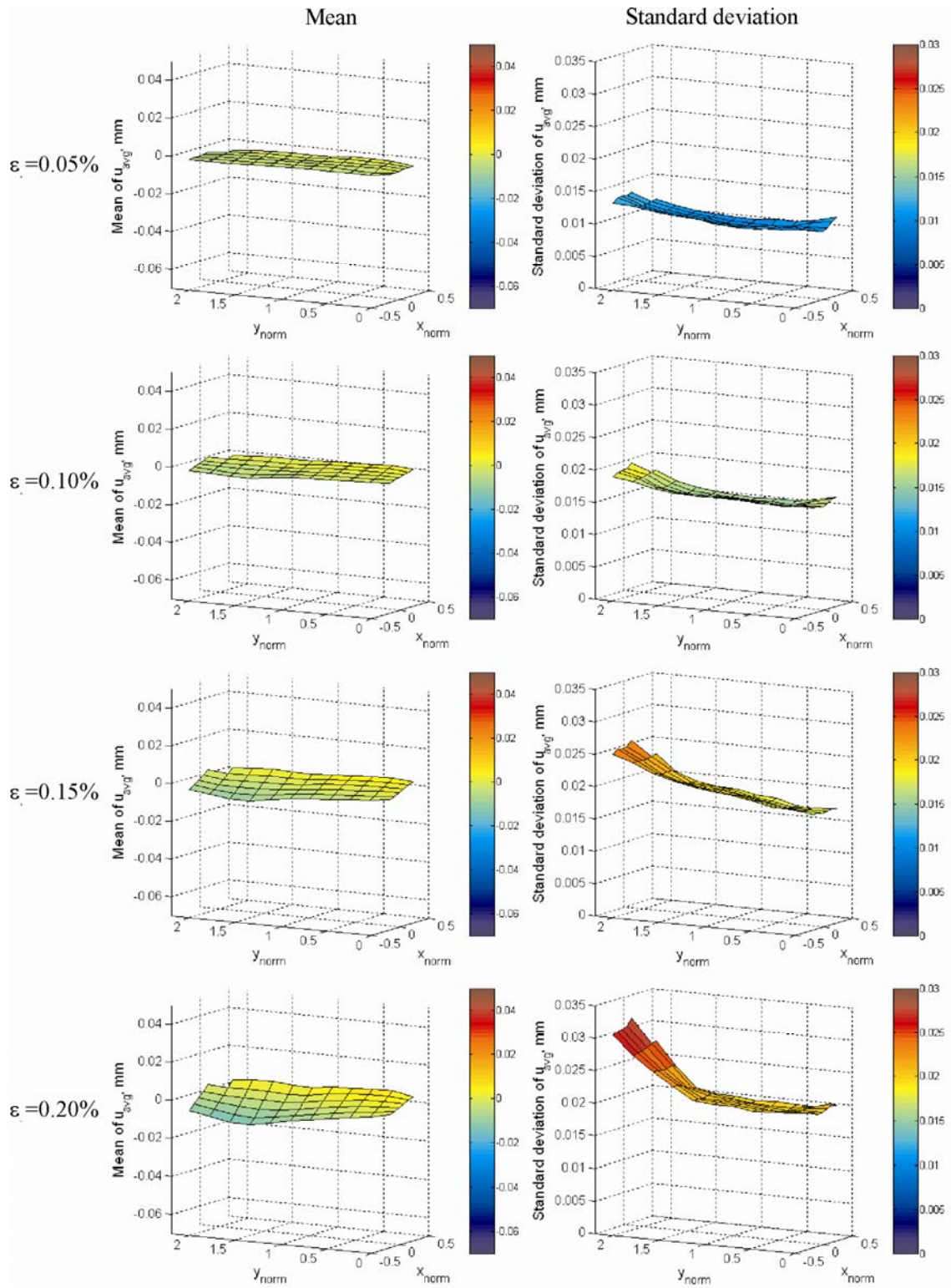
Figure 6.12 Mean and standard deviation distributions of data ensemble
$u(x_{norm}, y_{norm}, t)$.
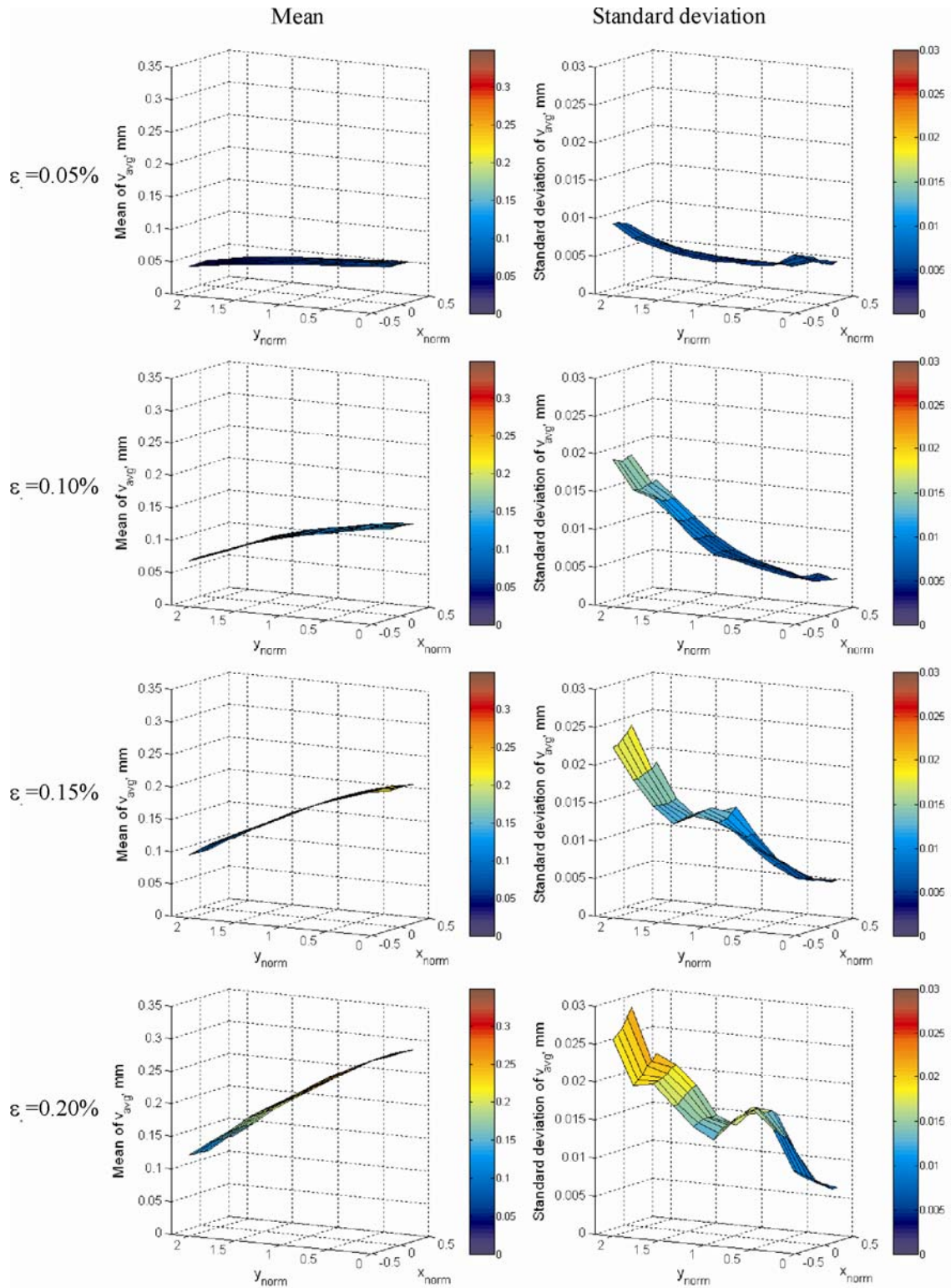
Figure 6.13 Mean and standard deviation distributions of data ensemble
$v(x_{norm}, y_{norm}, t).$

170
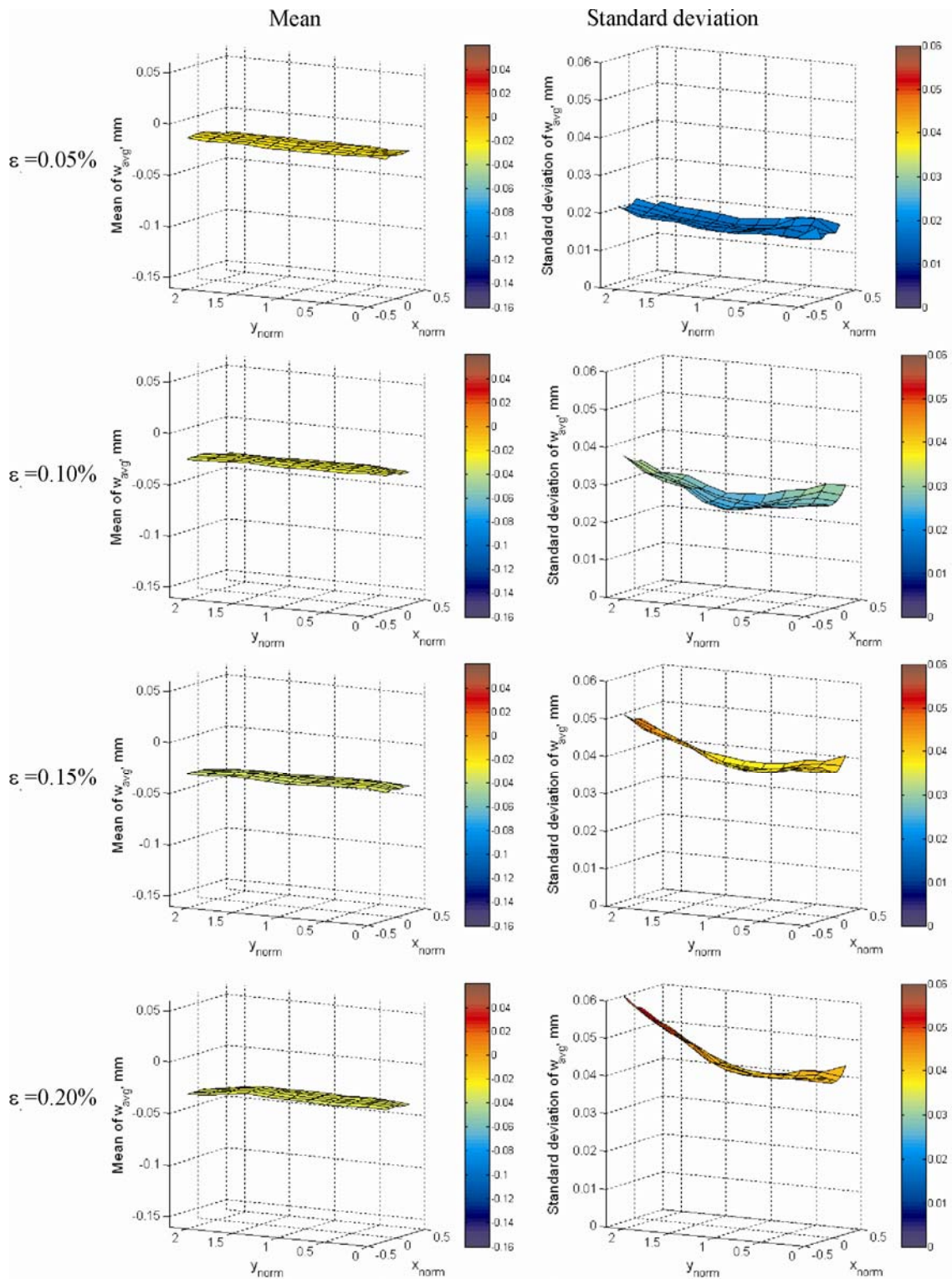
Figure 6.14 Mean and standard deviation distributions of data ensemble
$w(x_{norm}, y_{norm}, t)$**.**

171
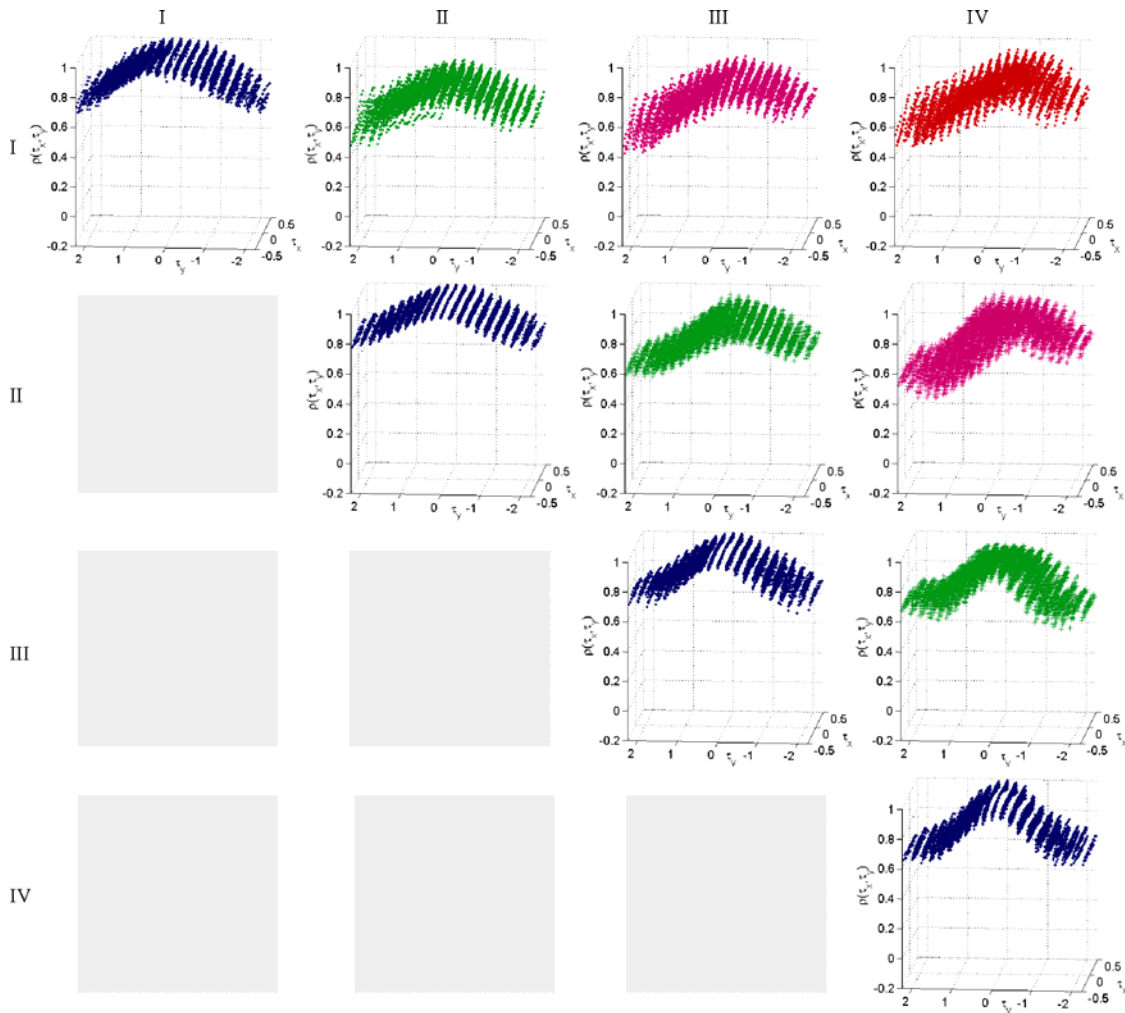
Figure 6.15 Spatio-temporal empirical correlation of data ensemble
$u(x_{norm}, y_{norm}, t)$.
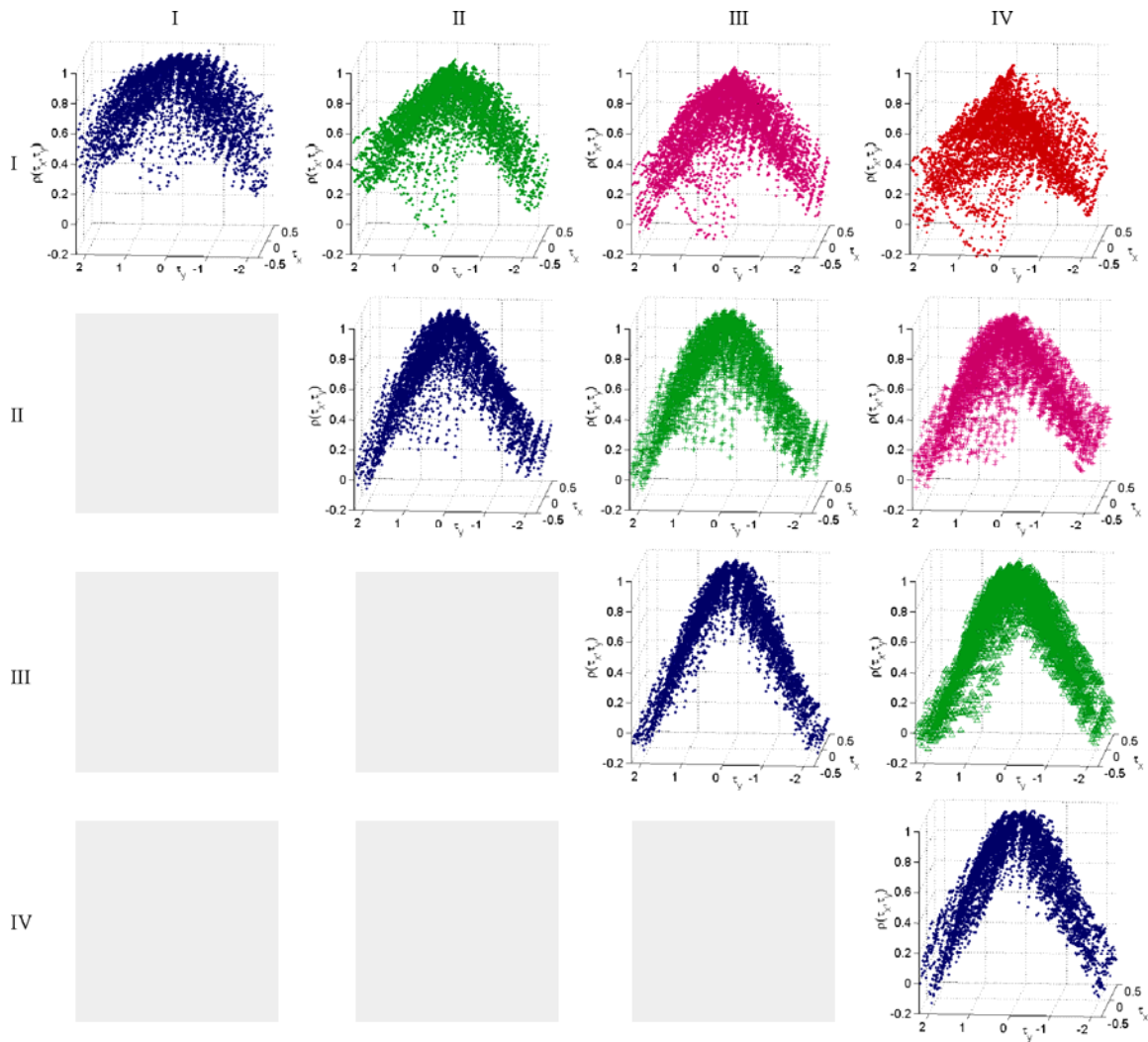
Figure 6.16 Spatio-temporal empirical correlation of data ensemble
$v(x_{norm}, y_{norm}, t)$.
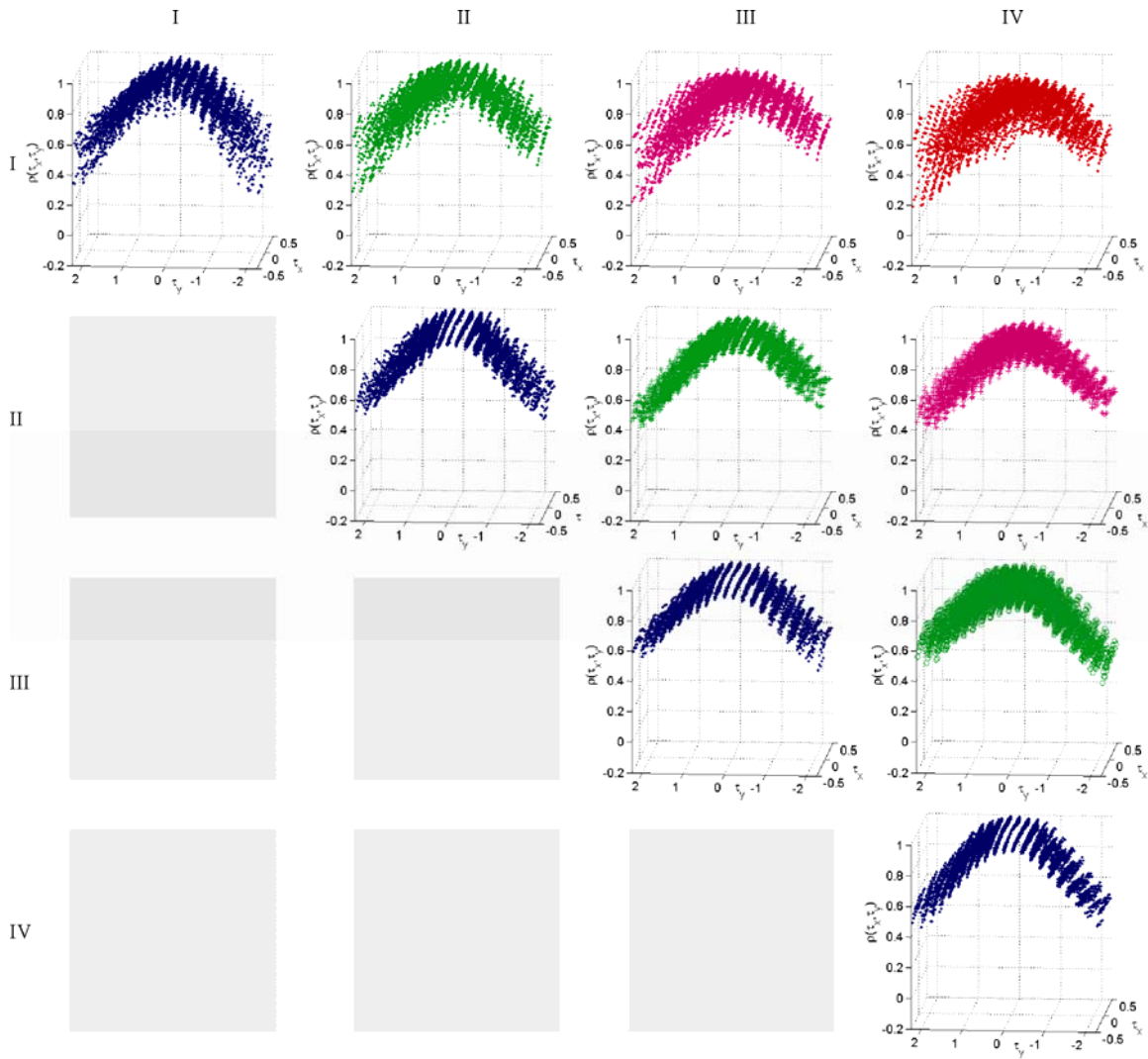
Figure 6.17 Spatio-temporal empirical correlation of data ensemble
$w(x_{\text{norm}}, y_{\text{norm}}, t).$
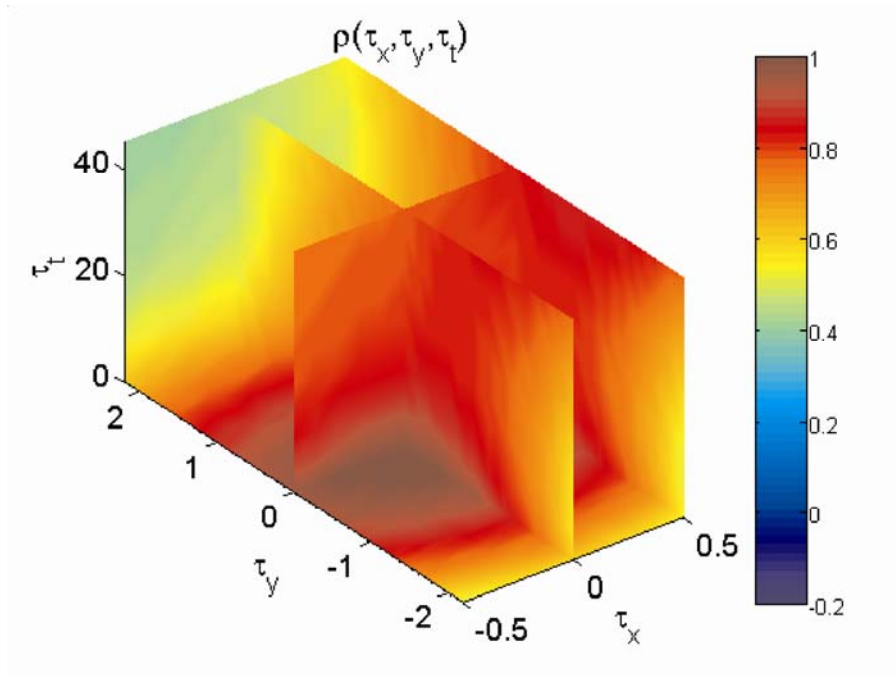
Figure 6.18 Smooth representation of spatio-temporal empirical correlation of data ensemble $u(x_{norm}, y_{norm}, t)$.
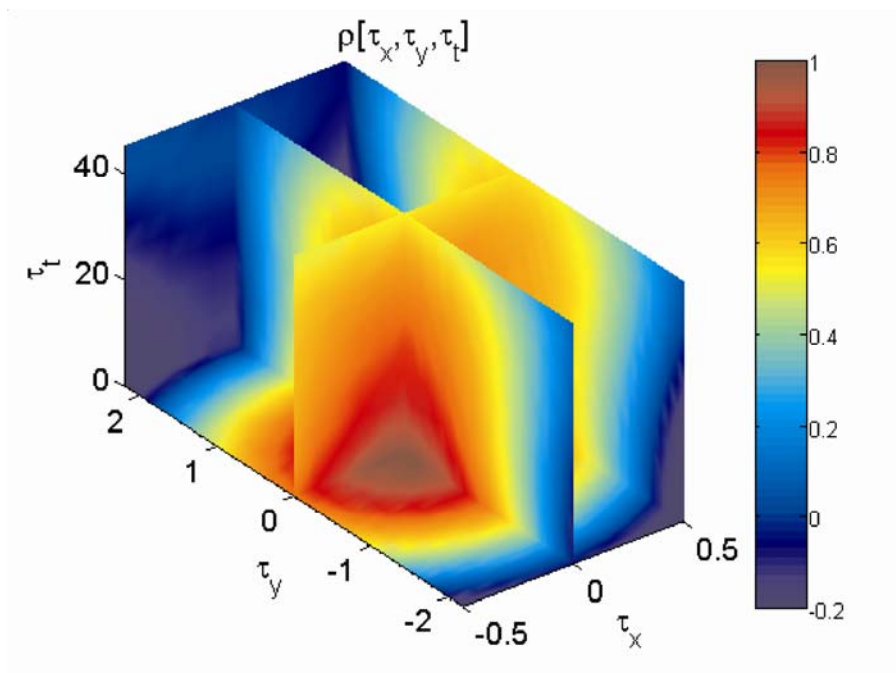
Figure 6.19 Smooth representation of spatio-temporal empirical correlation of data ensemble $v(x_{norm}, y_{norm}, t)$.

175
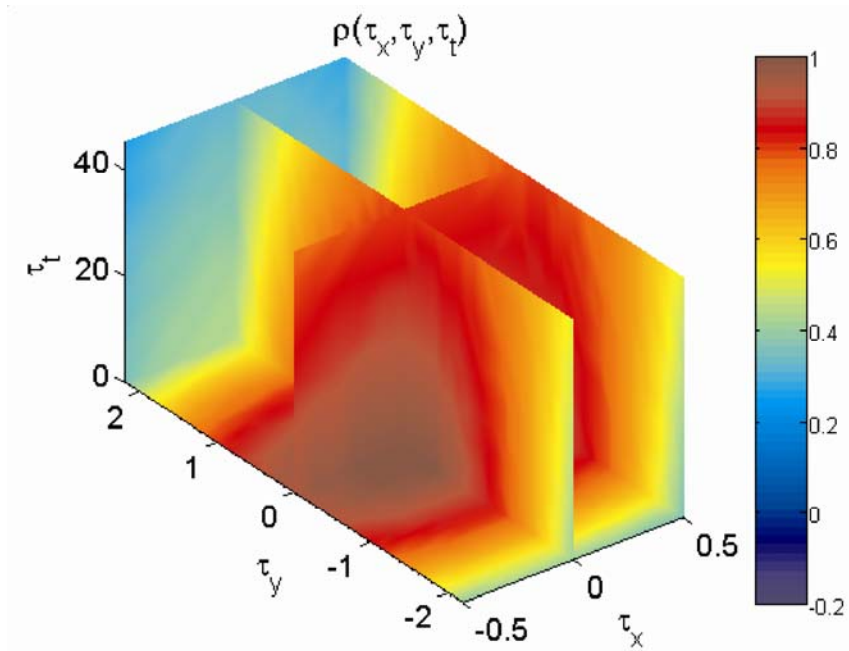
Figure 6.20 Smooth representation of spatio-temporal empirical correlation of data ensemble $w(x_{norm}, y_{norm}, t)$.
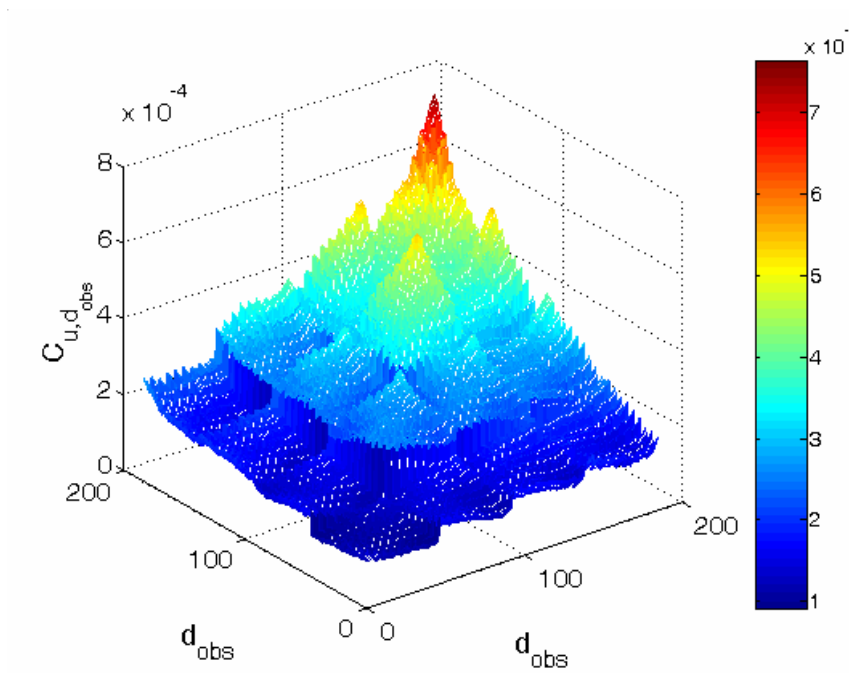
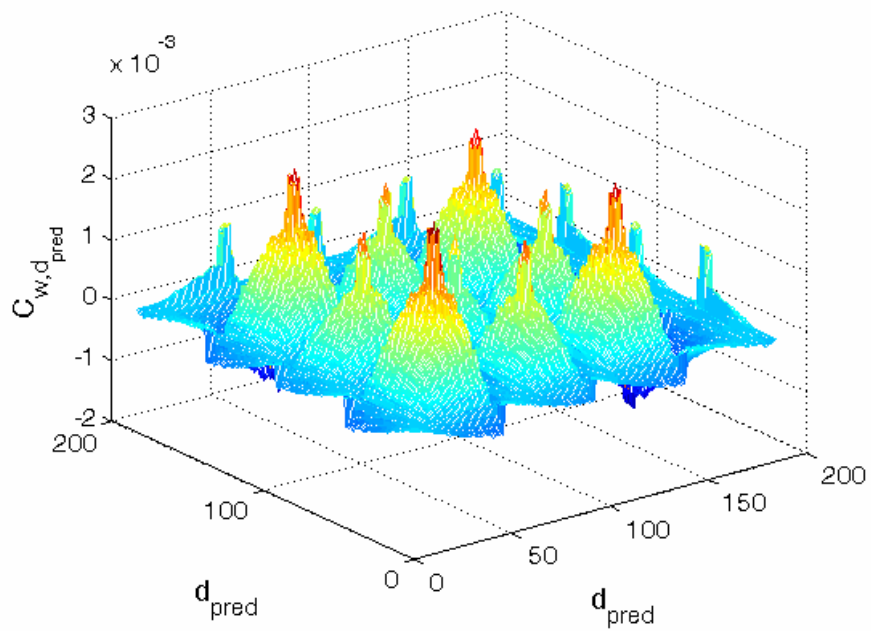**Figure 6.21 Covariance matrix of the *observations*. *u* displacement field.**

176
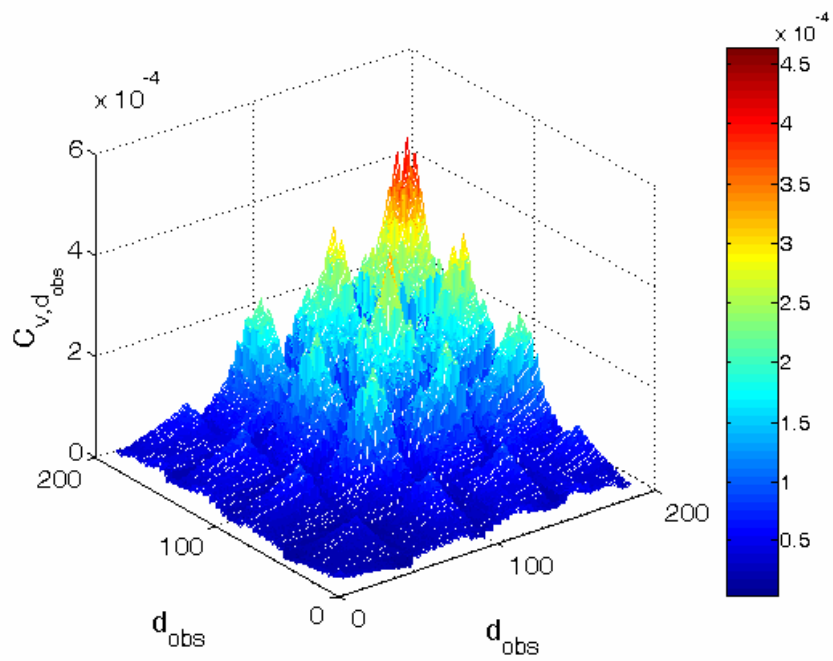
Figure 6.22 Covariance matrix of the *observations*. *v* displacement field.
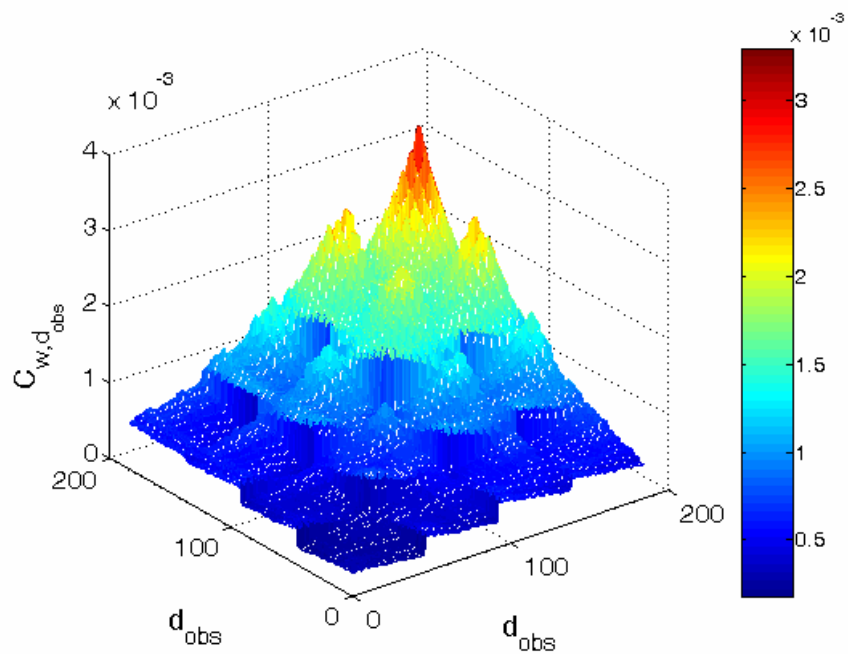
Figure 6.23 Covariance matrix of the *observations*. *w* displacement field.

177
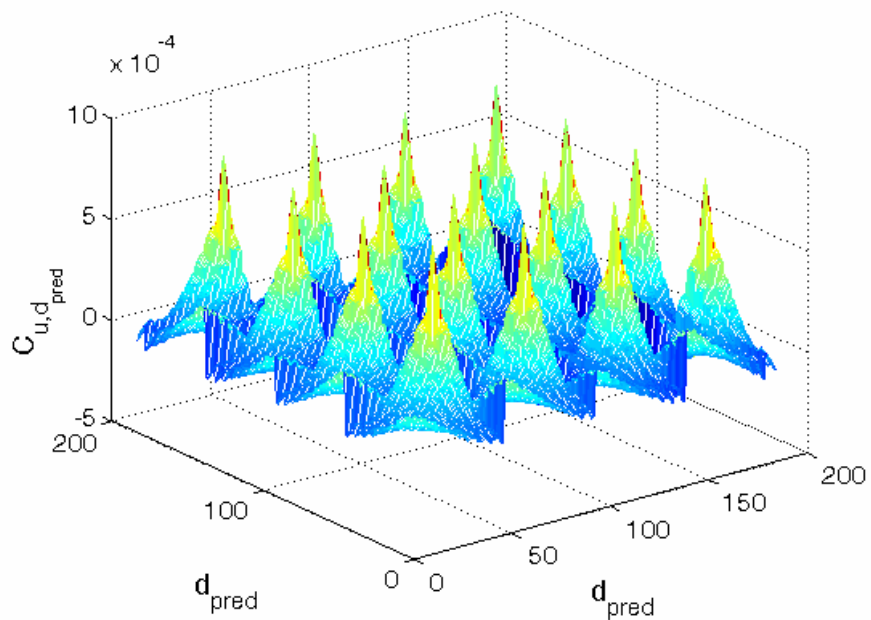
Figure 6.24 Covariance matrix of the *predictions*. *u* displacement field.
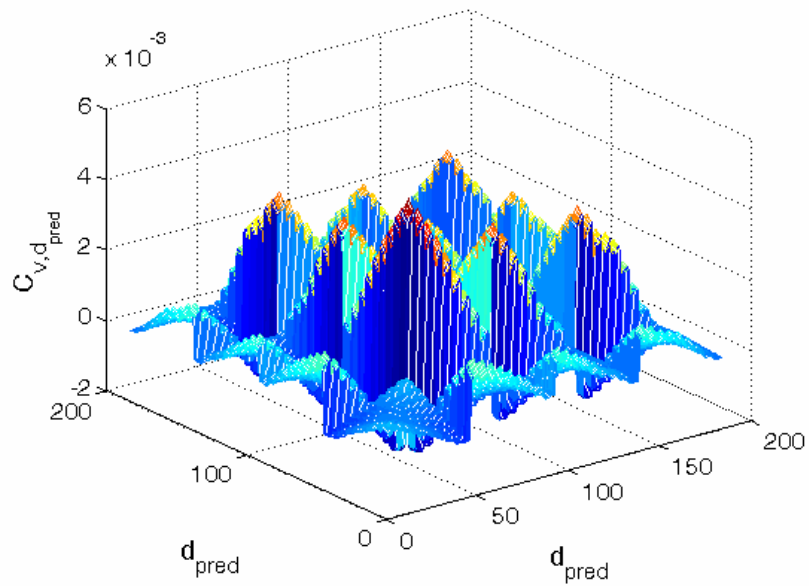
Figure 6.25 Covariance matrix of the *predictions*. *v* displacement field.

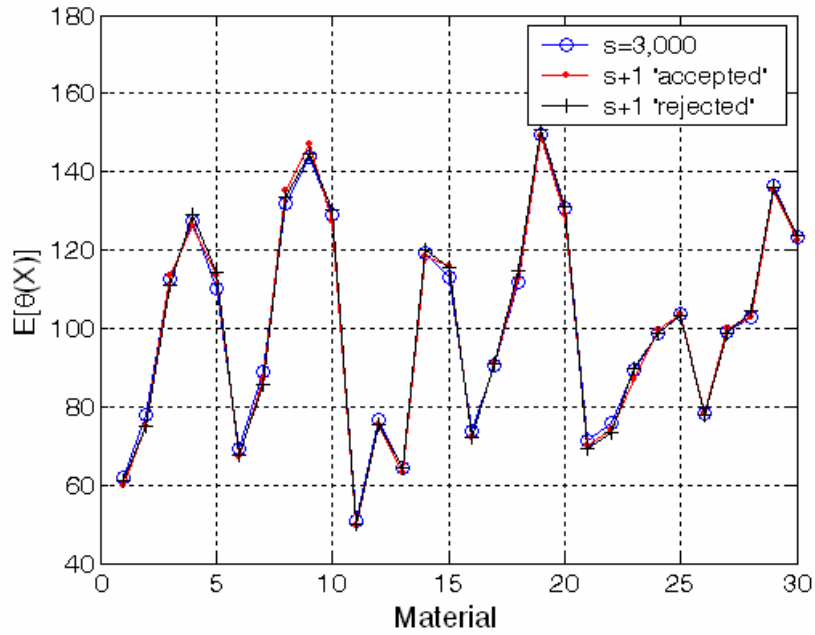**Figure 6.26 Covariance matrix of the *predictions*. *w* displacement field.**
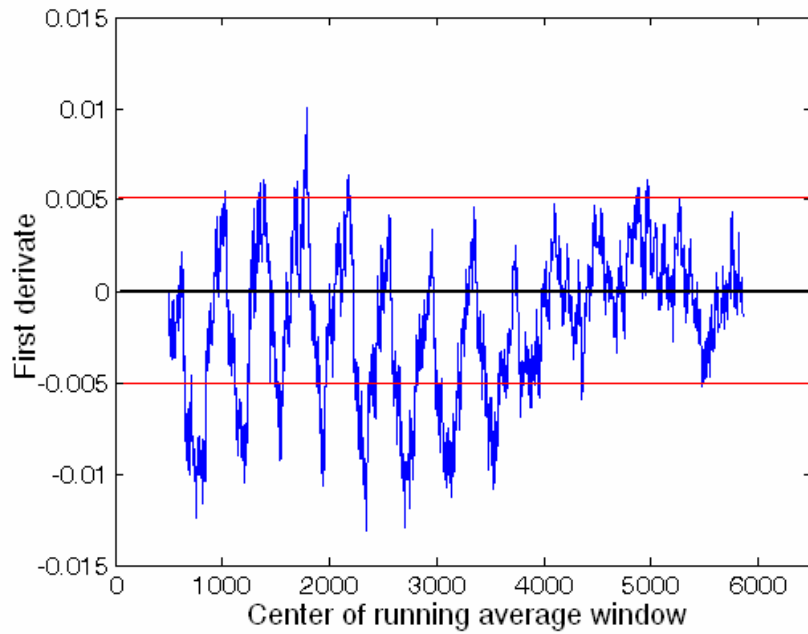
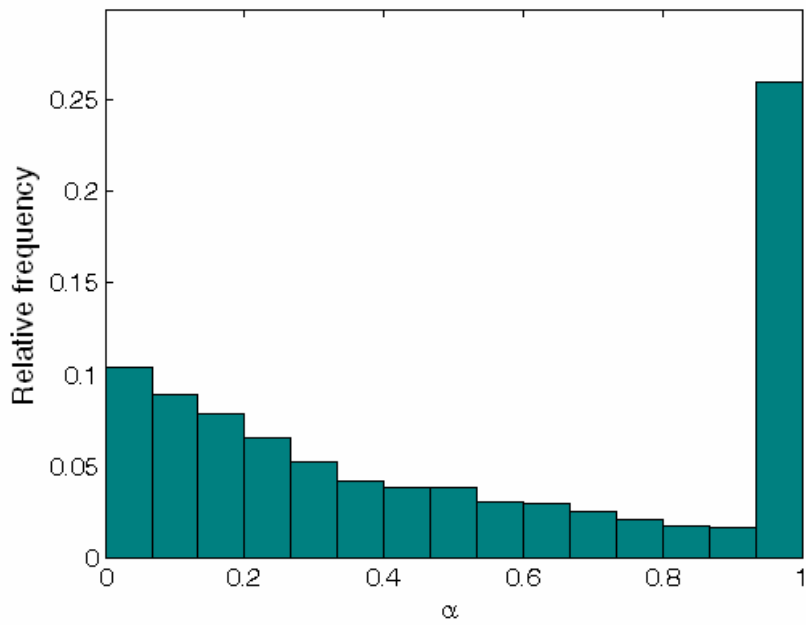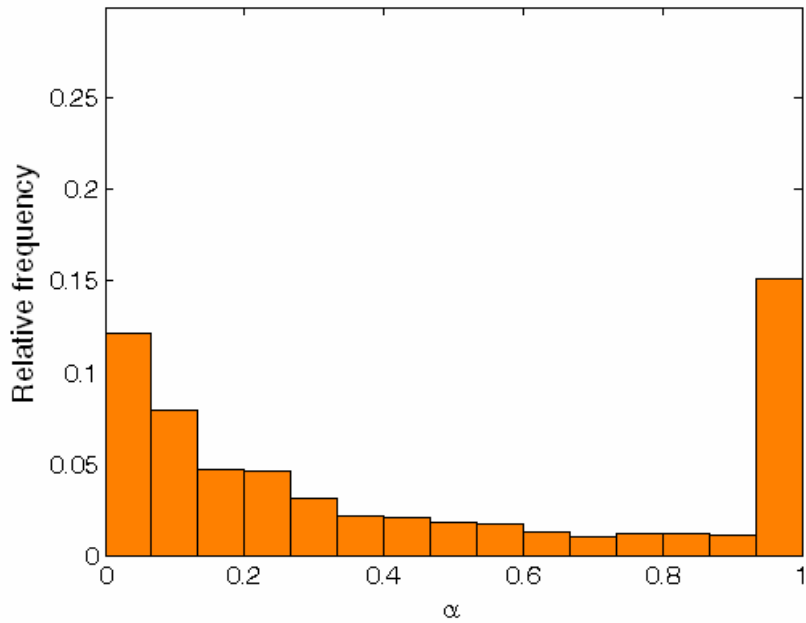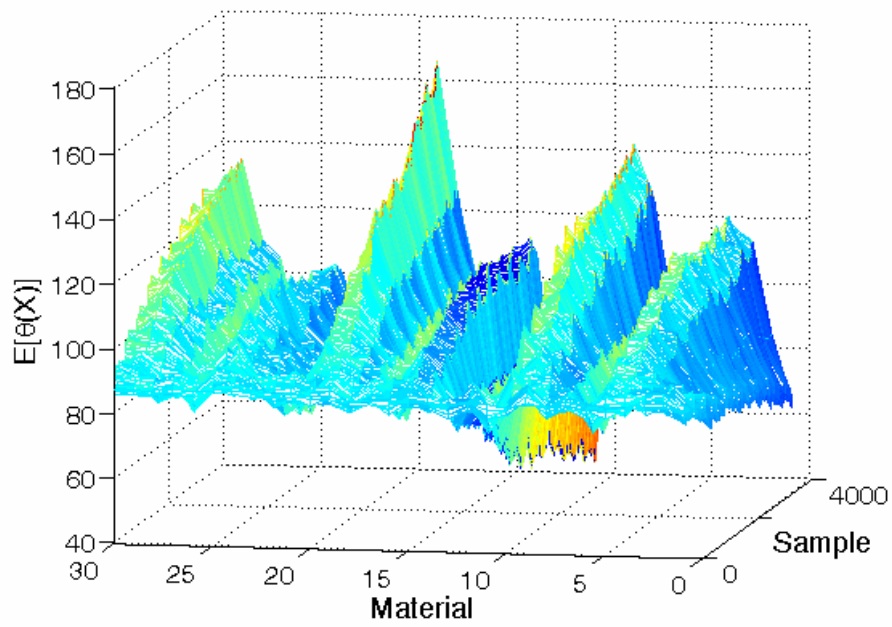**Figure 7.1 Typical sample selection during the MCMC sampling.**

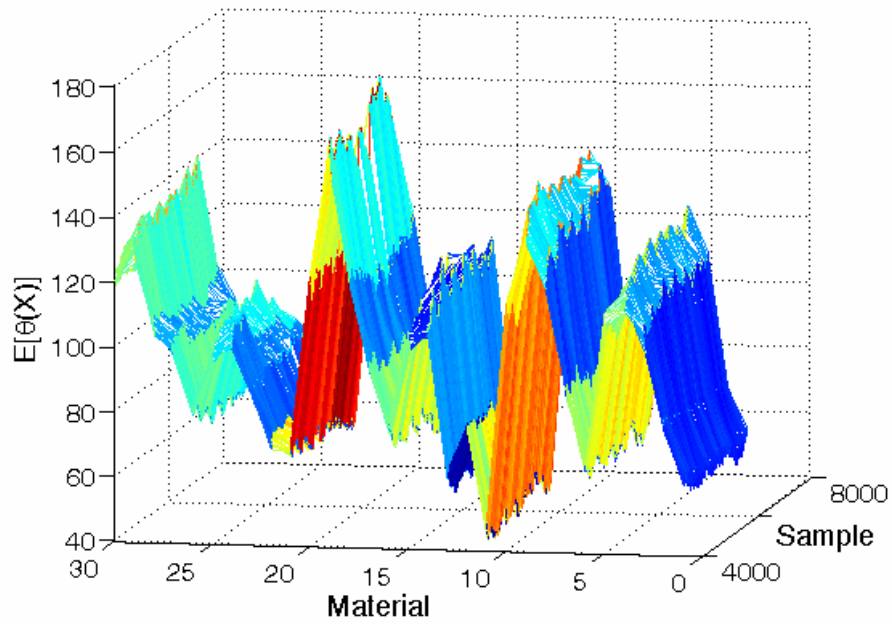
Figure 7.2 MCMC stationarity analysis.

Figure 7.3 Mixing parameter α for the 'burn in' phase.
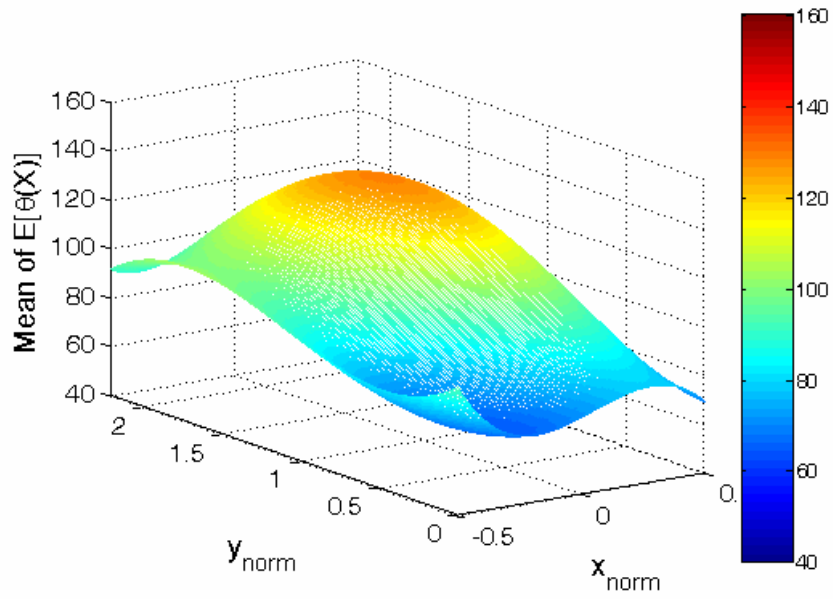

Figure 7.4 Mixing parameter α for the 'stationary' phase.

181

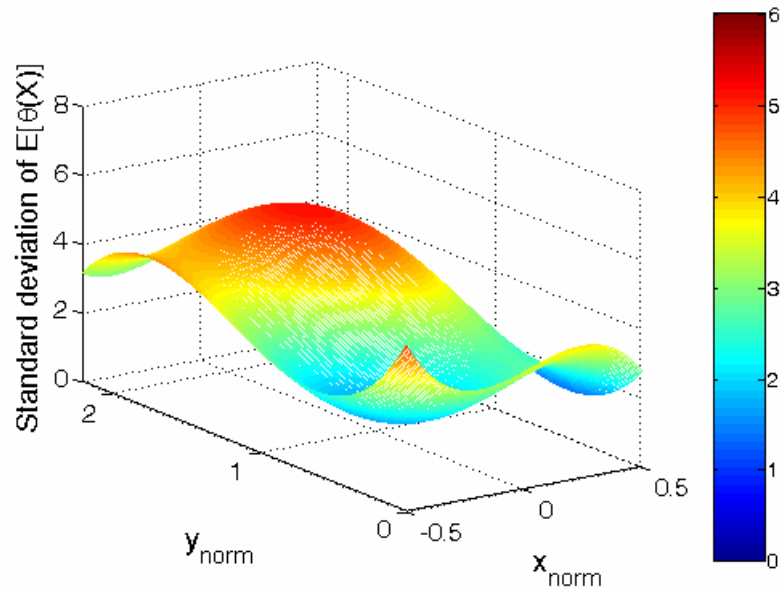**Figure 7.5 MCMC 'burn in' sampling.**

Figure 7.6 MCMC 'stationary' sampling.

182

Figure 7.7 Mean of $E[\theta(X)]$**.**

Figure 7.8 Standard deviation of $E[\theta(X)]$**.**

183
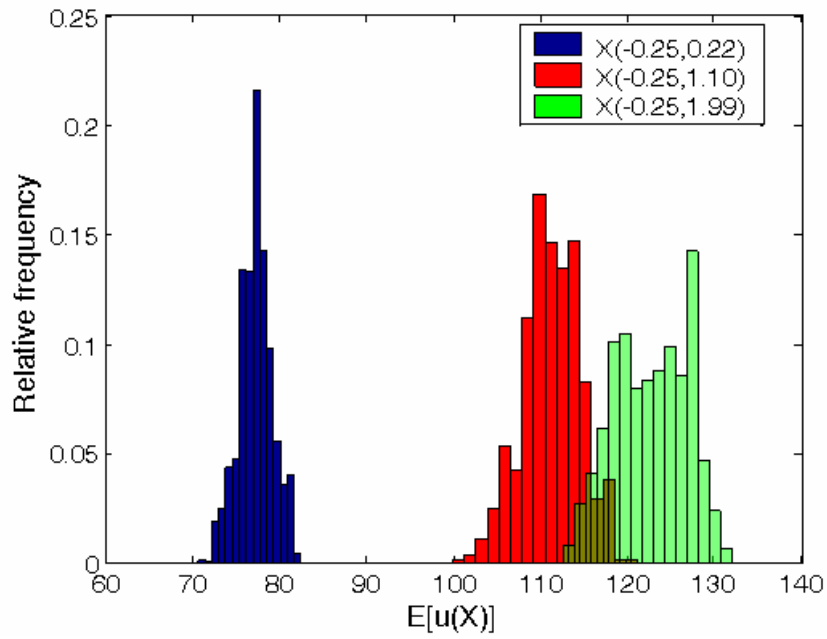
Figure 7.9 Marginal relative frequency histograms of $E[\theta(X)]$ at three control points.

Figure 7.10 Graphical representation of the synthesized correlation matrix of $E[\theta(X)]$.
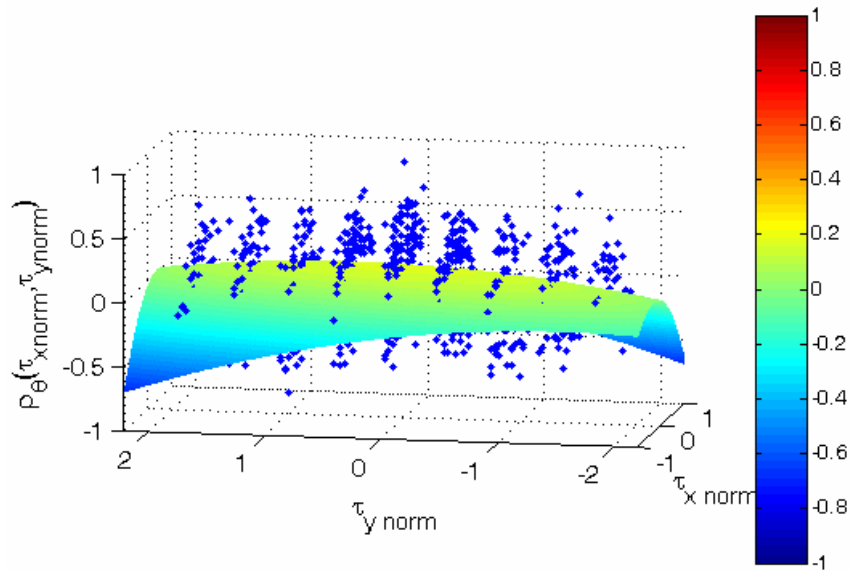
Figure 7.11 Synthesized and fit of covariance function of $E[\theta(X)]$**.**
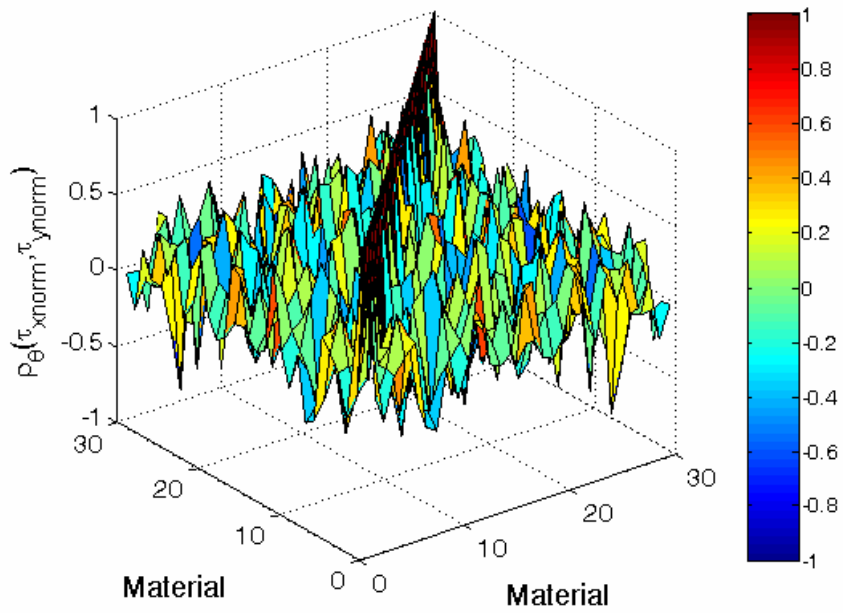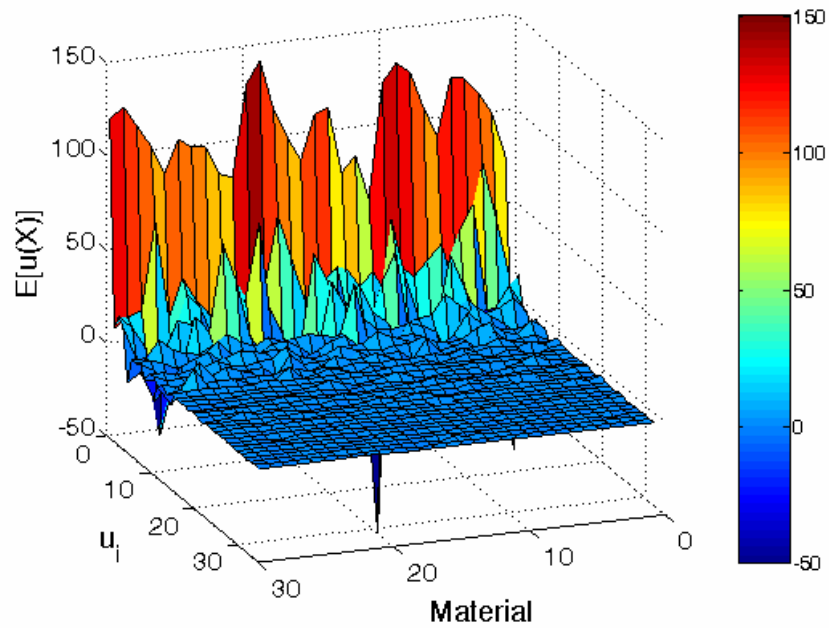

Figure 7.12 Mean $E[u_i(X)]$**.**
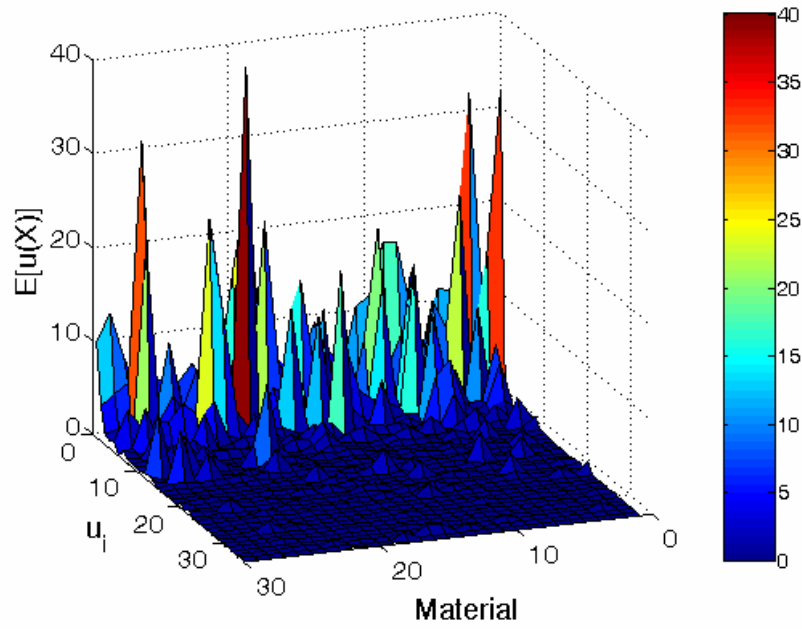
Figure 7.13 Standard deviation of $E[u_i(X)]$**.**
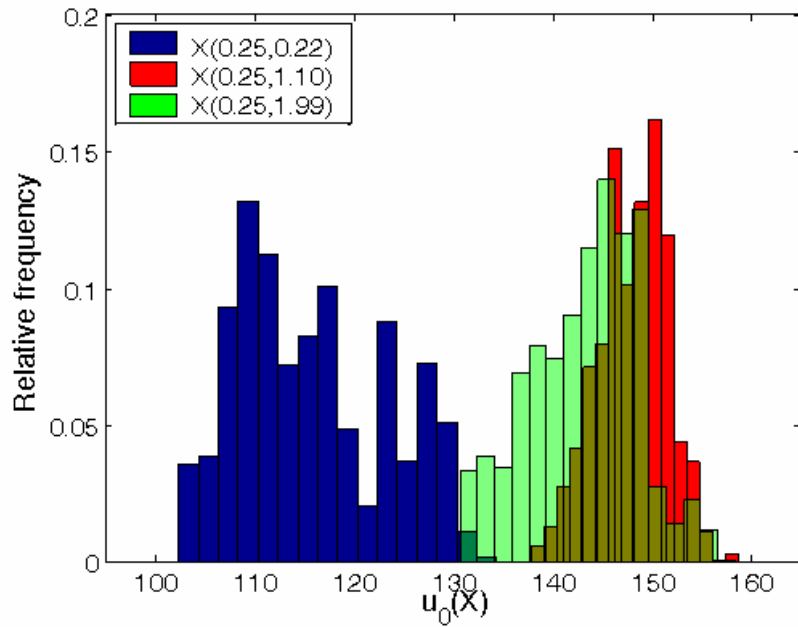
Figure 7.14 Marginal relative frequency histograms of $E[u_0(X)]$ **at three control points.**

186
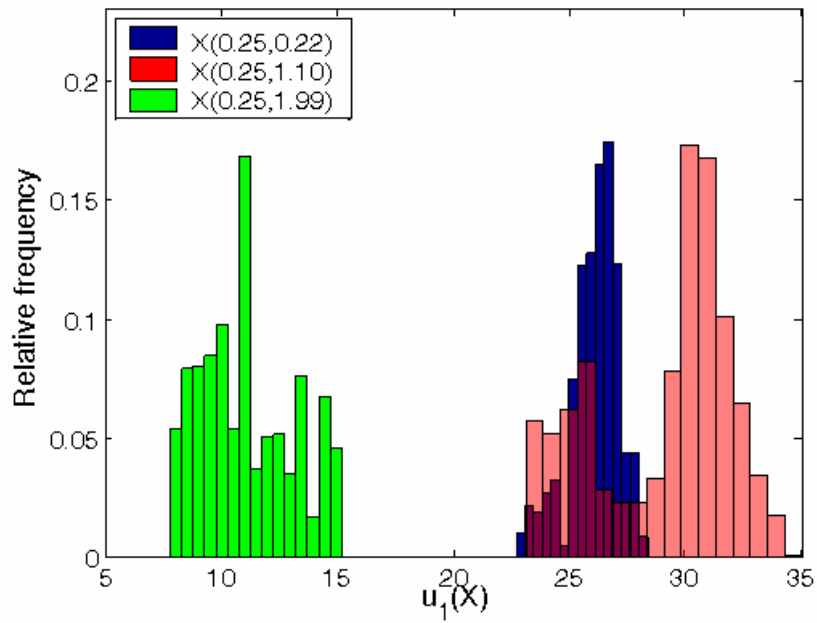
Figure 7.15 Marginal relative frequency histograms of $E[u_1(X)]$ at three control points.
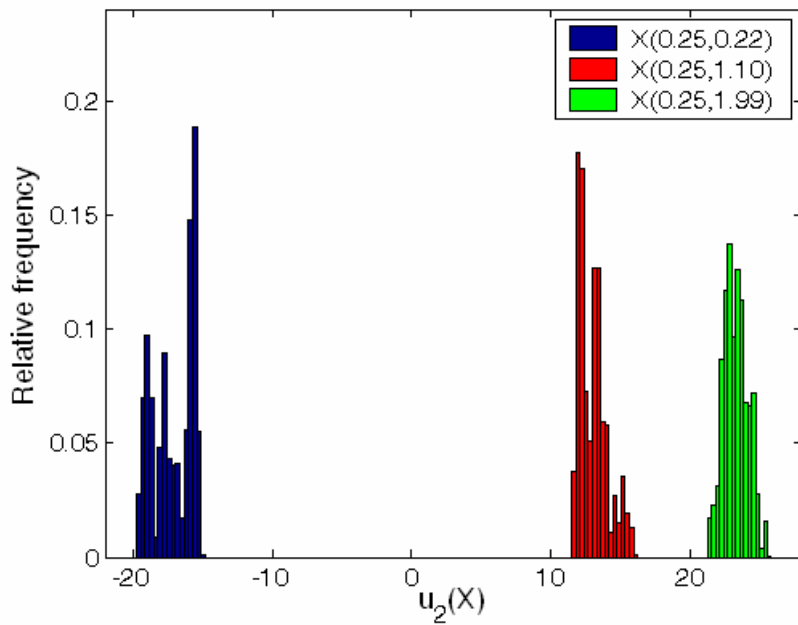
Figure 7.16 Marginal relative frequency histograms of $E[u_2(X)]$ at three control points.

187
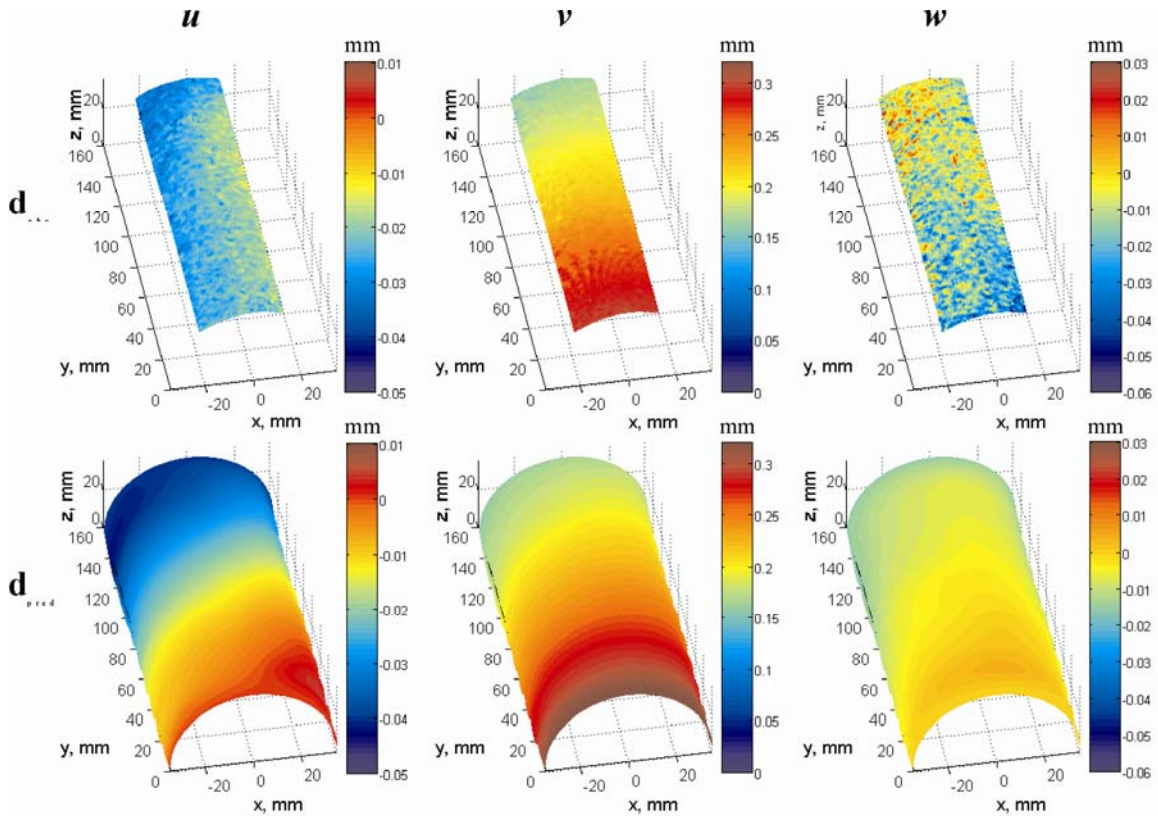
Figure 7.17 Comparison between *observations* and *predictions* obtained with the mean of $E[\theta(X)]$ at 0.2% of axial strain. Test 092903b.

References

Airey D.W. (1991). Finite element analyses of triaxial tests with different end and drainage conditions. *Computer Methods and Advances in Geomechanics*. Beer G., Booker J.R. and Carter J.P. (Eds), Balkema, Rotterdam.

Al-Shibli K., Macari E.J. and Sture S. (1996). Digital imaging techniques for assessment of homogeneity of granular materials. *Transportation Research Record*, 1526, 121-128.

Andrade J.E. and Borja R.I. (2006). Capturing strain localization in dense sands with random density. *International Journal for Numerical Methods in Engineering*, (in press).

Carter J.P. (1982). Predictions of the non-homogeneous behavior of clay in the triaxial test. *Geotechnicque*, 32 (2), 55-58.

Chu T.C., Ranson W.F., Sutton M.A. and Peters W.H. (1985) Applications of digital-image-correlation techniques to experimental mechanics. *Experimental Mechanics*, 25, 232-244.

Cresswell A., Barton M. and Brown R. (1999). Determining the maximum density of sands by pluviation. *Geotechnical Testing Journal*, 22 (4), 324-328.

Correlated Solutions (2004). http://www.correlatedsolutions.com

Dale A.I. (1999). *A History of Inverse Probability. From Thomas Bayes to Karl Pearson*. 2nd Edition. Springer, New York.

Desceliers C., Ghanem R. and Soize C. (2006). Maximum likelihood estimation of stochastic chaos representations from experimental data. *International Journal for Numerical Methods in Engineering*, 66(6), 978-1001.

Desrues J. and Viggiani G. (2004). Strain localization in sand: An overview of the experimental results obtained in Grenoble using stereophotogrammetry. *International Journal for Numerical and Analytical Methods in Geomechanics*, 28 (4), 279 – 321.

Drescher A. and Vardoulakis I. (1982). Geometric softening in triaxial tests on granular material. *Geotechnique*, 32 (4), 291-303.

Desrue J., Chambon R., Mokni M. and Mazerolle F. (1996). Void ratio evolution inside shear bands in triaxial sand specimens studied by computed tomography. *Geotechnique*, 46 (3), 529-546.

Fadale T.D., Nenarokomov A.V. and Emery A.F. (1995). Uncertainties in parameter estimation: The inverse problem. *International Journal of Heat and Mass Transfer*, 38 (3), 511-518.

Finno R.J., Harris W.W., Mooney M.A., Viggiani G. (1997). Shear bands in plane strain compression of loose sand. *Geotechnique*, 47 (1), 149-165.

Fitzpatrick B.G. (1991). Bayesian analysis in inverse problems. *Inverse Problems*, 7, 675-702.

Fourie A.B. (1991). Validity of using triaxial test data for calibration of constitutive relationships. *Computer Methods and Advances in Geomechanics*. Beer G, Booker J.R. and Carter J.P. (Eds), Balkema,, Rotterdam.

Geocomp Corporation (2002). http://www.geocomp.com/

Ghalib A.M. and Hryciw R.D. (1999). Soil particle size distribution by mosaic imaging and watershed analysis. *Journal of Computing in Civil Engineering*, 13 (2), 80-87.

Ghanem R. and Spanos P.D. (2003). *Stochastic Finite Elements: A Spectral Approach,* Revised Edition, Dover Publications, New York.

Ghanem R. and Doostan A. (2006). On the construction and analysis of stochastic models: Characterization and propagation of the errors associated to limited data. *Journal of Computational Physics*, 217, 63-81.

Grigoriu M. (1993). Simulation of stationary processes via the sampling theorem. *Journal of Sound and Vibration*, 166 (22), 301-313.

Grigoriu M. (1995). *Applied Non-Gaussian Processes: Examples, Theory, Simulation, Linear Random Vibration, and Matlab Solutions*. Prentice Hall, New Jersey.

Gudehus G. and Nubel K. (2004). Evolution of shear bands in sand. *Geotechnique*, 54 (3), 187-201.

Hallquist J.O. (1998). *LS-DYNA: Theoretical Manual*. Livermore Software Technology Corporation. Livermore, California.

Jeremic B., Yang Z. and Sture S.(2004). Numerical assessment of the influence of end conditions on constitutive behavior of geomaterials. *Journal of Engineering Mechanics*, 130 (6), 741-745.

Kuo C.Y. and Frost J.D. (1996). Uniformity evaluation of cohesionless specimens using digital image analysis. *Journal of Geotechnical Engineering*, 122 (5), 390-396.

Ladd R.S. (1978). Preparing test specimens using undercompaction. *Geotechnical Testing Journal*. 1(1), 16–23.

Livermore Softare Technology Corporation (2003). http://www.lstc.com

Lo Presti D.C.F., Pedroni S. and Crippa V. (1992). Maximum dry density of cohesionless soils by pluviation and by ASTM D 4253-83: A comparative study. *Geotechnical Testing Journal*. 15 (2), 180-189.

Mahmood A., Mitchell J.K. and Lindblom U. (1976). Effect of specimen preparation method on grain arrangement and compressibility. *Soil Specimen Preparation for Laboratory Testing, ASTM STP 599*, American Society for Testing and Materials, 169-192.

Mathworks (2003). http://www.mathworks.com

McLaughlin D. and Townley L.R. (1996). A reassessment of the groundwater inverse problem. *Water Resources Research*. 32 (5), 1131-1161.

Muhunthan B, Masad E. and Assaad A. (2000). Measurement of uniformity and anisotropy in granular materials. *Geotechnical Testing Journal*. 23 (4), 423-431.

Myers R.H. and Montgomery D.C. (1995). *Response Surface Methodology: Process and Product in Optimization Using Designed Experiments*. John Wiley and Sons Inc. New York.

Naeini S.A. and Baziar M.H. (2000). Effect of sample preparation on steady state. *Geotechnical measurements: Lab and Field. Proceedings of Sessions of Geo-Denver 2000*, Denver CO, Aug 5-8.

Oda M. (1972). Initial fabrics and their relations to mechanical properties of granular material. *Soils and Foundations*, 12 (1), 17-36.

Passalacqua R. (1991). A sand-spreader used for the reconstitution of granular soil models. *Soils and Foundations*, 31 (2), 175-180.

Peters W.H. and Ranson W.F. (1982). Digital imaging techniques in experimental stress analysis. *Optical Engineering*, 21, 427-431.

Press, J. (2003). *Subjective and Objective Bayesian Statistics: Principles, Models, and Applications*, 2nd Edition. Wiley-Inter Science, New Jersey.

Rechenmacher A.L. and Finno, R.J. (2004). Digital image correlation to evaluate shear banding in dilative sands. *Geotechnical Testing Journal*, 27 (1), 1-10.

Rechenmacher A.L. (2006). Grain-scale processes governing shear band initiation and evolution in sands. *Journal of the Mechanics and Physics of Solids*, 54, 22-45.

Rechenmacher A.L. and Medina-Cetina Z. (2006). Calibration of constitutive models with spatially varying parameters. *Journal of Geotechnical and Geoenvironmental Engineering* (Submitted).

Robert C. P. and Casella G. (2005). *Monte Carlo Statistical Methods*. Springer, New York.

Sakamoto S. and Ghanem R. (2002a). Simulation of multi-dimensional non-Gaussian non-stationary random fields. *Probabilistic Engineering Mechanics*, 17 (2), 167-176.

Sakamoto S. and Ghanem R. (2002b). Polynomial chaos decomposition for the simulation of non-Gaussian non-stationary stochastic processes. *Journal of Engineering Mechanics*, 128 (2), 190-201.

Schanz T. and Gussmann P. (1994). The influence of geometry and end restraint on the strength in triaxial compression in numerical simulations. *Numerical Methods in Geotechnical Engineering*. Smith (Ed), Balkema, Rotterdam.

Sheng D., Westerberg B., Mattsson H. and Axelsson K. (1997). Effects of end restraint and strain rate in triaxial tests. *Computers and Geotechnics*, 21 (3) 163-182.

Shinozuka M. and Deodatis G. (1991). Simulation of stochastic processes by spectral representation. *Applied Mechanics Reviews*, 44(4), 191-204.

Sidarta D.E. and Ghaboussi J. (1998). Constitutive modeling of geomaterials from non-uniform material tests. *Computers and Geotechnics*, 22 (1), 53-71.

Snyman J.A. (2000). The LFOPC Leap-Frog algorithm for constrained optimization. *Computers and Mathematics with Applications*. 40, 1085-1096.

Stander N., Eggleston T., Craig K. and Roux W. (2003). LS-OPT User's manual: Design optimization software for the engineering analyst. *Livermore Software Technology Corporation,* Livermore California.

Sutton, M.A., McNeill, S.R., Helm, J.D. and Chao, Y.J. (2000). Advances in two-dimensional and three-dimensional computer vision. *Photomechanics, Topics in Applied Physics*, 77, 323-372.

Tikhonov A.N., Goncharsky A.V., Stepanov V.V. and Yagola A.G. (1995). *Numerical Methods for the Solution of Ill-Posed Problems*. Luwer Academic Publishers, Netherlands.

Triggs B., McLauchlan P., Hartley R. and Fitzgibon A. (2000). Bundle adjustement − A modern synthesis. In: *Vision Algorithms: Theory and Practice*, Triggs W., Zissermann A. and SDzeleski R. (Eds.), Springer Verlag, 298-375.

Vaid Y.P. and Negussey D. (1988). Preparation of reconstituted sand specimens. *Advanced Triaxial Testing of Soil and Rock, ASTM STP 977*. Robert T. Donaghe, Ronald C. Chaney, and Marshal L Silver (Eds.), American Society for Testing and Materials, 405-417.

Van Trees H.L. (2001). *Detection, Estimation, and Modulation Theory. Part I*. John Wiley and Sons Inc., New York.

Wang L.B., Frost J.D., Voyiadjis G.Z. and Harman T.P. (2003). Quantification of damage parameters using X-ray tomography images. *Mechanics of Materials*, 35, 777-790.

Curriculum Vitae

Zenon Medina-Cetina was born in Merida Yucatan Mexico on September 17th of 1971. He graduated with highest honors from the School of Civil Engineering of the Universidad Autonoma de Yucatan in 1994. Soon after, he obtained a National Scholarship from the Mexican Academy of Science to do research on Foundation Engineering at the Instituto de Ingenieria of the Universidad Nacional Autonoma de Mexico UNAM, where he obtained his Master in Science in the field of Soil Mechanics in 2001.

During his stay at the UNAM, he participated in different research projects related to probabilistic applications in geotechnical engineering, including a consultancy for the Geostatistical Characterization of the Site of the Rion-Antirion Bridge in Greece. He also served as Adjunct Professor of the School of Engineering where he taught the Probability and Statistics courses.

Through a Fulbright Scholarship he started his doctoral program at Johns Hopkins in 2001, where he obtained his Master in Science in the field of Stochastic Mechanics in 2005. Before defending his PhD thesis he obtained the Duncan Fund Grant for the Advancement of Research in Statistics from the Department of Applied Mathematics and Statistics AMS, being the first graduate student in the history of the Fund in receiving the Grant as a non-member of the AMS Department.